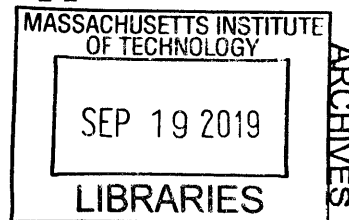


In Vivo Steroid Sensing Using Corona Phase Molecular Recognition: Design, Synthesis, and Applications

Michael A. Lee
B.S.E Chemical Engineering
Princeton University, 2013



SUBMITTED TO THE DEPARTMENT OF CHEMICAL ENGINEERING IN
PARTIAL FULFILLMENT OF THE REQUIREMENTS FOR THE DEGREE OF

DOCTOR OF PHILOSOPHY IN CHEMICAL ENGINEERING AT THE
MASSACHUSETTS INSTITUTE OF TECHNOLOGY

SEPTEMBER 2019

© 2019 Massachusetts Institute of Technology. All rights reserved.

Signature of Author: Signature redacted
Department of Chemical Engineering
August 2019

Certified by: Signature redacted
Michael S. Strano
Professor of Chemical Engineering
Thesis Supervisor

Accepted by: Signature redacted
Patrick S. Doyle
Professor of Chemical Engineering
Chairman, Committee for Graduate Students

In Vivo Steroid Sensing Using Corona Phase Molecular Recognition: Design, Synthesis, and Applications

By

Michael A. Lee

Submitted to the Department of Chemical Engineering on August 23, 2019 in Partial Fulfillment of the Requirements for the Degree of Doctor of Philosophy in Chemical Engineering

Abstract

Steroid hormones dictate a number of underlying biochemical processes controlling human physiology and disease. Changes in steroid hormone concentration and activity are often either indicators or direct causes of disease. In the clinic, steroids are measured as biomarkers of health and have been studied in relation to various diseases, including various cancers, endocrine disorders, and mental illnesses. However, measurements of these important signaling molecules are commonly restricted to the analysis of blood samples using chromatography or immunoassays, which lack temporal resolution and are labor-intensive. Given the dynamic behavior of these steroids, we argue in this thesis that their diagnostic value is highly constrained because of limitations of existing measurement technology. Hence, this thesis explores and develops the engineering tools for the design, synthesis, and application of a continuous biosensor capable of measuring *in vivo* steroid hormones in the human body.

A pharmacokinetic model was developed describing the concentrations of cortisol throughout the body as a function of time under normal physiological conditions. Previous mathematical models and parameters describing cortisol production, circulation, and clearance were compiled and combined in a unified model, and used to describe cortisol values in the adrenal gland, blood, adipose, muscle, and brain. The model was validated against physiological literature and used to tune a theoretical affinity sensor implanted in the interstitial space of adipose in terms of its geometry, sensor site concentration, and binding kinetics/equilibrium. An optimal set of parameters was collected, and the same sensor was shown to operate robustly in both a healthy patient and a patient with Cushing's disease. A major conclusion of this portion of the thesis is that the sensor output of most value for this problem is accurate measurement of the first derivative of concentration.

To address sensor development experimentally, we develop a compositionally controlled templated version of Corona Phase Molecular Recognition (CoPhMoRe) to produce unique molecular recognition sites for steroids. In the CoPhMoRe method, a single-walled carbon nanotube (SWNT) is wrapped with an amphiphilic polymer. The pinned polymers form a corona phase that modulate analyte binding. Upon analyte binding, the fluorescence spectrum may be modified in terms of its intensity and/or peak emission wavelengths. In this work, we synthesized a library of 16 polymers containing various amounts of acrylic acid, styrene, and a template cortisol molecule. The hypothesized mechanism was that the template cortisol monomer would occupy a

free volume within the pinned polymer, which would produce a binding shape in the approximate shape of a steroid, allowing free steroid to competitively displace the template and modulate fluorescence. Selective constructs were found for cortisol and progesterone. The progesterone sensor was translated to an implantable hydrogel form factor. Utilizing the reversibility of the sensor, we performed proof-of-concept experiments demonstrating the functionality of the progesterone sensor in an SKH1-E mouse.

To examine potential application spaces, the feasibility of using CoPhMoRe sensors for aquatic organism biologging was explored. In recent years, biologists have attached sensors to animals to characterize environmental and animal-derived parameters as they behave normally in their environment. By collecting orthogonal datasets describing environmental parameters (e.g. temperature) and animal movement, biologists have elucidated a number of insights regarding migration, predator-prey relationships, reproduction, feeding etc. Currently, however, biochemical information is underutilized and represents a potentially new frontier in biologging. In this study, we examined basic feasibility questions of the use of CoPhMoRe sensors in aquatic biologging. We developed implantation procedures for intramuscular delivery of CoPhMoRe hydrogel sensors and characterized the maximum implantation depth for extraction of the optical signal. Furthermore, we demonstrate that for best fluorescence extraction, hydrogels should be placed into lightly colored tissues. We also demonstrate generally favorable biocompatibility results, with implants causing no observable changes in physiology or behavior.

In both human health and biologging applications, biocompatibility of biomaterials is an important parameter that dictates organisms' tolerance of the material and lifetime of the material. For any long-term use of implantable biosensors, minimizing adverse tissue reactions is critical to prevent chemical modification of the sensor, dislodgement of the sensor from the implantation site, and encapsulation leading to increasing diffusional barriers of analytes from reaching the sensor surface. There have been a number of studies reporting varying degrees of cellular responses depending on SWNT synthesis method, impurity content, SWNT wrapping, and cell type, but the effect of formulation has not been explored systematically. The same parameters that dictate cellular response (e.g. wrapping) also dictate which analytes can be tracked, so discovering orthogonal formulation parameters that can control tissue response while leaving SWNT sensor ability intact is critical. In this study, we tracked tissue responses to five different SWNT-hydrogel formulations to determine design rules to minimize tissue response. Through analysis of the cellular infiltrate, we found that decreasing the hydrogel pore size accelerated the healing process after gel implantation, though all hydrogels were equivalent in inflammatory status by day 28. Furthermore, we demonstrate that the acute inflammatory response has the potential to deactivate hydrogel sensors in a time-dependent manner, pointing to the importance of modulating the tissue response to maximize sensor longevity.

Thesis Supervisor: Michael S. Strano
Title: Carbon P. Dubbs Professor of Chemical Engineering

Acknowledgments

Pursuing my PhD has been the longest, most difficult, and most rewarding part of my life so far, and I would not have been able to make it without the support of so many people. Without their intellectual and emotional support, I would not have been able to complete the program.

First, I'd like to thank Professor Michael Strano for his intellectual and professional guidance these past five years. I joined his research group not only because of the intersection between our research interests but also his infectious enthusiasm for everything scientific. The passion with which he pursues research is truly admirable, and frankly, I really hope to be as passionate about my future career as he is about his research. During my time in his lab, I have grown significantly as a scientist. Comparing myself five years ago to now, I evaluate data more analytically, design experiments more thoughtfully, and propose ideas more creatively. Furthermore, I have also learned how to be an efficient and motivational leader. Because of my time in the Strano Research Group, I am fairly confident that I am armed with the scientific and managerial prowess to be successful in my future ventures. On a side note, I delayed coming to MIT by a year because I wanted to have more international experiences, but really, I probably could have just come to Professor Strano's lab earlier and accomplished the same thing...

I would also like to thank my committee members Dr. Emery Brown, Professor Zachary Smith, and Professor Brad Olsen for their scientific guidance. They provided valuable and diverse perspectives on my projects, which helped me to consider avenues I would not have otherwise considered. Their support has been valuable.

My colleagues in the Strano Research Group have also been wonderful coworkers and friends. From my first to final semesters, I have always felt welcome, even as the old faces moved on and new faces entered. All of you have enriched my experience scientifically and socially, and I hope that did the same for you as well. In particular, I would like to thank Naveed Bakh, who entered the lab at roughly the same time as I and with whom I have worked most closely. Even if you don't express yourself the most delicately at times, you are brilliant, loyal, and empathetic. I'd also like to thank Dan Salem, whom I sat next to and bounced many ideas off of and to whom I asked many questions. You're one of the most consistently hardworking and scientifically rigorous people I have ever met. Other specific people who have been great mentors, colleagues, and friends include Xun Gong, Punit Mehra, Song Wang, Gili Bisker, Freddy Nguyen, Nicole Iverson, Jiyong Ahn, Minkyung Park, Tedrick Lew, and Anton Cottrill. Additionally, I'd like to thank Crystal Pham, Kelvin Jones, Samantha Fletcher, and Cindy Jin for all their help as well.

Outside the lab, I'd like to thank my training partners and instructors at Broadway Jiu-Jitsu. For my first three years in graduate school, I wasn't training and was definitely less emotionally stable at the time. Rediscovering training at such a great gym was definitely a positive turning point in my life, and I'm grateful for all the beatings and camaraderie we've exchanged. With all your guys' help, I can also call myself an undefeated MMA fighter...just kidding.

Most of all, I would like to thank my family and friends for their love and support outside the lab. My parents and brother have supported me throughout my entire life and have continued to support me as I approach my 30s. Even though I am theoretically an independent, self-sufficient adult, I

really appreciate that my family would have my back if I failed and would believe in me even if I did not believe in myself at times. I'd also like to thank my friends at MIT as well. I'm still not fond of the name "Team Celery" to be honest, but we shared some good times. I'd like to thank Christy Chao, especially, who made my time at MIT tolerable when it was tough to be here and amazing every other time. Christy is diligent, witty, and so thoughtful, and I am lucky to have met her at the Chemical Engineering graduate student orientation back in August 2014. Hopefully we can keep the momentum going in whatever city we end up in next!

Table of Contents

Chapter 1 : Introduction	16
References	26
Chapter 2 : A Pharmacokinetic Model of a Tissue Implantable Cortisol Sensor	39
Introduction	39
Model Development	43
Results and Discussion	56
Conclusions	69
References	69
Chapter 3 : Implanted Nanosensors in Marine Organisms for Physiological Biologging: Design, Feasibility, and Species Variability	79
Introduction	79
Methods and Materials	83
Results and Discussion	88
Conclusions	104
References	105
Chapter 4 : In-Vivo Bio-sensing of Human Steroid Hormones using Corona Phase Molecular Recognition (CoPhMoRe) and nIR Fluorescent Single Walled Carbon Nanotubes	116
Introduction	116
Experimental	122
Results and Discussion	146
Conclusions and Future Work	166
References	166
Chapter 5 : Formulation of Hydrogel-Encapsulated Single Walled Carbon Nanotube Sensors Implants to Modulate Inflammation and Foreign-Body Response	178
Introduction	178
Methods and Materials	180
Results and Discussion	183
Conclusions and Future Work	195
References	196
Chapter 6 : Conclusions and Future Work	201

Table of Figures

Figure 1-1: (a) Schematic of the steroidogenesis pathway. Reprinted from Miller et al., *Endocrine Reviews*, 32, 2011, with permission from Oxford University Press. (b-c) Molecular structures of (b) cortisol and (c) progesterone.

..... 18

Figure 1-2: (a) Mechanism of Corona Phase Molecular Recognition (CoPhMoRe). Single-walled carbon nanotubes (SWNT) are wrapped with an amphiphilic polymer that modulates analyte binding. Upon recognition of a molecule, the SWNT fluorescence may change in intensity or in peak wavelength. Adapted from Zhang et al., *Nature Nanotechnology*, 8, 2013, with permission from Springer Nature. (b) Schematic illustrating the roll-up vector and chiral angle combinations forming each SWNT chirality. (c) Band diagram illustrating the electronic transitions leading to SWNT fluorescence. Electrons are excited from v_2 into c_2 , where they relax into c_1 . Upon recombination with a hole in v_1 , photons are emitted with an energy corresponding to the band gap. (b) and (c) reprinted from Weisman, *Optical Spectroscopy of Single-Walled Carbon Nanotubes*, 2008, with permission from Elsevier. 21

Figure 1-3: Previous examples of in vivo SWNT sensors. (a-b) Iverson et al. detected the induction of inflammation in mice treated with RcsX cells in in situ liver. Reprinted from Iverson et al. *Nature Nanotechnology*, 2013, with permission from Springer Nature. (c-d) Galassi et al. detected DNA hybridization events in the IP space of mice using a wavelength shift sensor. Reprinted from Galassi et al., *Science Translational Medicine*, 10, 2018, with permission from AAAS. (e-f) Williams et al. detected the ovarian cancer biomarker HE4 in various mice models. Reprinted from Williams et al., *Science Advances*, 18, 2018, with permission from AAAS. 24

Figure 1-4: Ultimate vision of the CoPhMoRe sensors for steroid hormones. (a) Patients would wear a patch that transmit data wirelessly to an external device illustrating dynamic changes in steroid levels. (b) Underneath the patch would be a subcutaneously implanted hydrogel encapsulating the CoPhMoRe sensors, whose fluorescence would be modulated in response to dynamic changes of steroids in the surrounding tissue. (c) The dermal patch would house the necessary excitation and photodetection optics. Adapted from Bisker et al., *Advanced Healthcare Materials*, 4, 2015, with permission from John Wiley and Sons. 26

Figure 2-1. Schematic of model formulation and structure, which represents the body using various compartments with different volumes (V) and cortisol concentrations (C). Cortisol is secreted in pulses in the adrenal gland (g). Cortisol then passes into the blood by first order kinetics. From the blood, cortisol is cleared by the liver. Concentrations in the blood reservoir (rb) serve as the basis to calculate concentrations in the adipose (a), muscle (m), and brain (b). Each of these compartments is divided into the capillary bed (c) and the interstitial/intracellular space (i). In all compartments, cortisol exists in protein bound and unbound forms. Values for total cortisol (t) and free cortisol (f) are calculated. Only the free fraction can travel between the capillary bed and the interstitium. A hydrogel sensor is placed in the adipose interstitial space with cortisol bound sites (θ_c) and unbound (θ) sites. 44

Figure 2-2: Convergence of solving the hydrogel sensor cortisol profile. Cortisol pulses were predefined for a period of 3 days, and the spatial domain of the sensor hydrogel was split into a number of points. The resulting sensor output was compared to the sensor output with the hydrogel split into 1,000 finite elements. When the hydrogel is split into 40 or more finite elements, the sensor output converges to the same solution. 55

Figure 2-3. Cortisol concentrations throughout the body as predicted by the model. (a) The Faghhi and Brown models were adapted to calculate cortisol levels in the adrenal gland and blood.^{10,37} These calculations were then used to calculate total and free cortisol values in the (b) adipose tissue, (c) muscle tissue, and (d) brain tissue. These three compartments were subdivided into the capillary bed and a lumped interstitial/intracellular space. (e) Intracellular adipose cortisol concentration (blue) and the sensor output (red). The shape of the sensor output maps the transient cortisol profile. (f) Cortisol pulses (blue) and the negative of the derivative of the sensor output (red). There is a correspondence between the number and size of disturbances in the derivative and the number and amplitude of pulses. In this representative data set, only data from $t = 0$ were analyzed to allow the establishment of a proper diurnal cycle and to avoid any slight biases arising from the assumed initial condition of 0 cortisol at 12 am of day -1 ($t = -24$ hours). 60

Figure 2-4: Comparison of adipose interstitial cortisol with (top) and without (bottom) interstitial protein binding. The inclusion of protein binding in the interstitial space dampens the cortisol pulses, such that the peak cortisol concentration is reduced by 10%, peaks occur later by roughly 10 minutes, and the overall profile is smoother.....61

Figure 2-5: Cortisol profile in the adipose tissue following a $25 \mu\text{g dL}^{-1}$ pulse at $t = 500 \text{ min}$. The profile was fit to an exponential function in order to obtain a characteristic time of clearance of 140 minutes and a cortisol half-life of 105 minutes. Clearance was approximated as a first order kinetic process.62

Figure 2-6. Cortisol concentrations throughout a Cushing's disease patient's body as predicted by the model. Values were calculated in the (a) adrenal gland, blood, (b) adipose tissue, (c) muscle tissue, and (d) brain tissue. To obtain similar blood cortisol profiles as the male Cushing's disease patient studied by van den Berg et al.,⁶⁴ pulses of $38 \pm 2.5 \mu\text{g dL}^{-1} \text{ min}^{-1}$ with a $59 \pm 11 \text{ min}$ waiting time between pulses were introduced into the model. (e-f) Sensor output and derivative were also tracked. The sensor showed a flat output relative to that in the normal patient due to the lack of a cortisol diurnal cycle. This output is also close to saturation due to the higher cortisol concentrations. 65

Figure 2-7. Maximum sensor output and time delay as a function of the (a) binding site concentration (θ_T), (b) sensor thickness (L), (c) forward rate binding constant (k_b), and (d) dissociation constant (K_D).67

Figure 3-1: Vision for the future application of CoPhMoRe sensors to physiological biologging of marine organisms. (a) Animals of various sizes and ecological niches tagged with minimally invasive sensors collecting multivariate datasets continuously. (b) Theoretical design of a future biologging system. Hydrogel implants, encapsulating nanoparticles engineered to modulate their fluorescence in response to the local concentration of specific bioanalytes, are injected at a fixed depth in the intramuscular space, where they query biological fluid. Atop the fish's exterior is a flexible, wearable patch that contains embedded optoelectronics to excite and collect hydrogel fluorescence. The elastomer protects the electronic components from the surrounding aquatic environment, as well as conforms to the animal's movements. The device also incorporates other sensors to track animal movement and environmental conditions. The work herein describes the development of the hydrogel component of this theoretical device. (c) Theoretical data output of envisioned device. The device collects biochemical information and other animal-derived and environmental parameters such as velocity, depth, temperature, etc. (d) Visible image of SWNT-gels (scale = 0.5 mm). (e) Overlay of bright field image of sarasa comet goldfish (*Carassius auratus*) and fluorescence image of implanted hydrogel (scale = 10 mm).82

Figure 3-2: In vitro and ex vivo sensor characterization. (a) Normalized UV-Vis-NIR absorption spectra and (b) fluorescence emission spectrum at 785 nm excitation of of ss(AC)₁₅-wrapped (6,5) CoMoCAT SWNT. Spectra were measured for solution phase SWNT and SWNT-gels. The absorption spectrum shows both the excitation (E_{22}) and fluorescence emission peaks (E_{11}) for the corresponding SWNT chiralities given in parentheses. The fluorescence spectrum was decomposed into individual peaks corresponding to the labeled SWNT chiralities. (c-d) Images taken with Raspberry Pi imaging setup (c) without and (d) with a SWNT-gel. (e) Hydrogel fluorescence increased with larger incident excitation power. (f) Fluorescence decreased with stepwise increases in riboflavin concentration between 1 to 100 μM , as measured by a Raspberry Pi camera. (g) Riboflavin calibration curves obtained with an InGaAs camera and the Raspberry Pi camera show good agreement. (h) SWNT-gel response to bolus injection of 100 μM riboflavin while placed 1 mm deep into ex vivo tissue sample of *Stenotomus chrysops*. The fluorescence decreased below the limit of detection of the Raspberry Pi camera.89

Figure 3-3: Photoresponsivity of silicon and InGaAs photodetectors compared to CoMoCAT (6,5) SWNT fluorescence. Photoresponsivity data adapted from ThorLabs products PDA10A2 and PDA015C.^{55,56}.....91

Figure 3-4: Effect of hydrogel implantation depth on fluorescence detection in teleosts (*Sparus aurata* and *Stenotomus chrysops*) and cat shark (*Galeus melastomus*). (a-b) Imaging setup and schematic. A fiber-coupled 561 nm laser fitted with an 850 shortpass filter was used to illuminate the implantation site before and after intramuscular delivery of hydrogels into previously deceased animals via trocar. The signal was collected by a Raspberry Pi camera connected to a 900 longpass filter. The difference in gray values with and without the hydrogel was calculated. (c) In *Sparus aurata*, detectable hydrogel fluorescence decreased as injection depth was increased from just below the skin down to a limit of 0.7 cm. A non-fluorescent hydrogel was injected just superficially below the skin and imaged to give the threshold difference in intensity for the signal to be attributable to the hydrogel and not to other artefacts, such as movement of the fish relative to the laser. (d) A superficially implanted SWNT-gel in

Sparus aurata exhibited a steady fluorescence signal when imaged over 6 minutes. (e) The detection limit of SWNT-gels in Stenotomus chrysops was 0.7 cm. (f) Overlay of brightfield and fluorescence images of a fluorescent hydrogel implanted 0.5 cm below the skin in Galeus melastomus [scale = 20 mm]. (g) SWNT-gels were detected down to a depth of 0.7 cm in Galeus melastomus, as compared to a non-fluorescent hydrogel implanted at a depth of 0.5 cm.97

Figure 3-5: Detection of fluorescent hydrogels implanted superficially in optically heterogeneous tissues. Fluorescent hydrogels were implanted into (a) the scaly legs and (b) softer flesh beneath the neck of a sea turtle (*Caretta caretta*) (scale = 20 mm). (c) Hydrogel fluorescence was detected in the neck but not the scaly legs. SWNT-gels were implanted subcutaneously in (d) dark and (e) white regions of a blue shark (*Prionace glauca*). A non-fluorescent hydrogel was implanted in (f) gray region of the tissue. (g) Fluorescence could be detected underneath white skin but not dark skin. The blank hydrogel in the gray region provided a baseline against which to determine fluorescence detection. Scale in all images is 20 mm.99

Figure 3-6: NIR fluorescent hydrogels implanted in a living European eel (*Anguilla anguilla*), eastern river cooter (*Pseudemmys concinna*), and catshark (*Scyliorhinus stellaris*). (a) Following implantation, attempts were made to track the fluorescence in the eel and turtle confined to a small space. (b-c) Dispersed laser excitation, animal movement, and long exposure times made these attempts unsuccessful in (b) the eel and (c) the turtle. All scalebars are 20 mm. (d) The implantation site fully healed in the catshark by 33 days post-implantation. (e-f) High resolution ultrasound images were taken to examine noninvasively tissue response to the implant 4 weeks after implantation in the (e) eel and (f) catshark (scale = 5 mm). The absence of significant changes in tissue architecture and echogenicity indicates that the hydrogels were well-tolerated in these organisms. (g) The injection site in the turtle did not heal completely 33 days post-implantation. (h) Hydrogels were removed from the turtle after 33 days and were found to be encapsulated by tissue. (i) Histology images from subcutaneous tissue surrounding the hydrogel implant in the turtle indicate a foreign body tissue reaction. 101

Figure 3-7: Quantification of hydrogel implant impact on animal health. (a) Snapshot of the capture video with corresponding sarasa comet goldfish (*Carassius auratus*) movement trajectories included. Blue corresponds to a fish in which a nIR fluorescent hydrogel was implanted, while orange corresponds to a control fish without a hydrogel implant. (b) Trajectories of fish taken for one hour 2 days after a hydrogel was implanted into the subject fish. (c-f) X and Y position histograms for the subject fish (c-d) and control fish (e-f). The subject fish experienced neither impaired movement nor erratic movement due to the hydrogel implant, indicating good tolerance of the implant.103

Figure 4-1: Molecular structures of cortisol (left) and progesterone (right) 118

Figure 4-2: ¹H NMR spectrum of acrylated cortisol. 123

Figure 4-3: Representative ¹H spectrum of p(AA_x-ran-S_y-ran-AC_z) polymers. Peaks used for compositional analysis labeled. Residual diethyl ether, methanol, tetrahydrofuran, and water solvent peaks are labeled as *, **, ***, and ****, respectively. 124

Figure 4-4: Representative GPC trace of p(AA_x-ran-S_y-AC_z). 125

Figure 4-5: Representative FTIR spectrum of p(AA_x-ran-S_y-AC_z). The spectrum qualitatively confirms incorporation of acrylic acid, styrene, and acrylated cortisol. 126

Figure 4-6: Fluorescence spectrum of HiPCO SWNT suspended with P10 (blue). The raw spectrum was decomposed into individual SWNT chiralities using a previously reported method.⁵⁶ 127

Figure 4-7: Semi-rational design for Corona Phase Molecular Recognition sensor for steroid hormone sensing. (a) Proposed mechanism of sensor. The initial configuration of the polymer on the SWNT involves charged hydrophilic groups (blue) extending out into aqueous solution and hydrophobic monomers (orange) anchoring the polymer non-covalently onto the SWNT. A template steroid molecule (orange) is weakly bound to the SWNT, such that exogenously administered steroid molecules (magenta) will displace the appendage, resulting in a polymer configuration change and consequently change in SWNT fluorescence. (b) Polymers were composed of hydrophobic

styrene monomers and alkyl chains (orange), hydrophilic acrylic acid monomers and carboxylic acid groups (blue), and acrylated cortisol (green). (c) Panel of steroid hormones used in the sensor screening, chosen for their physiological and therapeutic significance. 147

Figure 4-8: Summary of polymer library screening results. (a) Heat map showing the fractional fluorescence change, $(I-I_0)/I_0$, of the (9,4) and (7,6) chiralities of each member of the sensor library against 100 μM of each steroid in 2% DMSO and 1x PBS. Red denotes a fluorescence decrease, while blue indicates an increase. P indicates polymers with appendage steroids, while C denotes polymers without appendages. The selective response of P10-(7,6) is boxed in red. The full compositions of each polymer are given in Supporting Information. (b-c) Comparison of composite (9,4) and (7,6) fluorescence response of HiPCO SWNT wrapped with (b) C2, a polymer with 0 appendage units, versus (c) P10, a polymer with 4 appendage units. Increasing the number of appendage units while keeping the number of acrylic acid and styrene relatively fixed at approximately 55 and 25, respectively, increased progesterone selectivity and sensitivity. (d-e) A polymer with (d) 0 mol% styrene, P1, exhibited higher steroid sensitivity but lower selectivity compared to a polymer with (e) higher styrene content at 20 mol%, P13. (f) UV-Vis-NIR absorption spectrum of polymer-suspended HiPCO SWNT, indicating successful suspension of SWNT in the parameter space of the polymer library. The (9,4) and (7,6) channel is indicated with a black arrow, while the red arrow indicates the (6,5) chirality. 149

Figure 4-9: UV-Vis-NIR photoabsorption spectrum of HiPCO SWNT suspended with P1 with 100 μM cortisol and with 2% DMSO as a control. The presence of well-defined peaks before and after analyte additions indicates that nanoparticle aggregation is not the primary mechanism of sensing. 150

Figure 4-10: UV-Vis-NIR photoabsorption spectrum of HiPCO SWNT suspended with P10 with 100 μM progesterone and with 2% DMSO as a control. The presence of well-defined peaks before and after analyte addition indicate that nanoparticle aggregation is not the primary mechanism of sensing. 151

Figure 4-11: Sensor performance in solution phase. (a) The cortisol sensor consists of a low styrene, high template polymer wrapped around (6,5) Comocat SWNT, whose fluorescence increases in response to cortisol. (b) Cortisol induces approximately twice a change in fluorescence intensity magnitude versus the other steroids at the equivalent concentration of 100 μM . (c) Calibration curve showing sensor sensitivity from 20 μM to 100 μM . (d) The progesterone sensor consists of a high styrene, high template polymer wrapped around HiPCO SWNT, whose fluorescence increases in response to progesterone. (e) The progesterone sensor is selective towards progesterone over other steroids by a factor of 2, all tested at 100 μM . (f) The progesterone sensor has a detection range from 10 to 100 μM . (g) (9,4) and (7,6) SWNT wrapped with P10 exhibit selectivity toward progesterone even among other classes of small molecules and large proteins. (h) The progesterone sensing mechanism is not a simple hydrophobicity sensor, indicated by its sensor response relative to its partition coefficient. Progesterone is indicated by the black arrow. (i) The responsivity to each steroid of P10-wrapped SWNT depends on diameter, with an optimum SWNT diameter being observed for progesterone responsivity, as indicated by the arrow. (j-k) Excitation-emission plots of the progesterone sensor (j) before and (k) after the addition of 100 μM progesterone show that the (10,2), (9,4), and (7,6) chiralities are the most sensitive, as indicated by the arrows in orange, red, and white, respectively. 153

Figure 4-12: Molecular dynamics simulations to characterize SWNT corona. (a) Steroids adsorbed on bare (7,6) SWNT to maximize hydrophobic interactions while minimizing unfavorable steric interactions due to protruding methyl groups and contact with polar oxygen groups. (b) Short-range Lennard-Jones potential between steroids and bare (7,6) SWNT. (c) Short-range Lennard-Jones potential per monomer between (7,6) SWNT and poly(acrylic acid) with 20 units, poly(styrene) with 20 units, and poly(acrylated cortisol) with 5 units. (d-f) Snapshots of (d) poly(acrylic acid), (e) polystyrene, and (f) poly(acrylated cortisol) adsorbed onto (7,6) SWNT. (g) Radial distribution functions describing atom distance from surface of (7,6) SWNT for P10 adsorbed onto the SWNT surface. (h) Snapshot of P10 adsorbed on SWNT, demonstrating close proximity of styrene and acrylated cortisol and more distance acrylic acid from the SWNT surface. (i) A snapshot of progesterone (colored purple and indicated by arrow) occupying a binding site consisting of SWNT (silver), styrene (green), acrylic acid (white), and acrylated cortisol (peach). 156

Figure 4-13: Composite (8,3) and (6,5) fluorescence response heat map. P1-(6,5) is marked with a red box. The selective response of P1-(6,5) to cortisol is boxed in red. 157

Figure 4-14: (7,5) fluorescence response heat map.	158
Figure 4-15: (10,2) fluorescence response heat map.	158
Figure 4-16: (12,1) fluorescence response heat map.	159
Figure 4-17: Fluorescence spectrum of P10-suspended HiPCO SWNT encapsulated in PEGDA hydrogel. The hydrogel was fabricated from a solution 10 wt% PEGDA in 1x PBS and 10 mg/L SWNT before cross-linking and swelling.....	160
Figure 4-18: Hydrogel formulation, selection, and performance. (a) SWNT were encapsulated into PEGDA hydrogels, into which analytes diffuse and modulate fluorescence intensity. (b) Fluorescence spectrum of the progesterone sensor in 1x PBS and other commonly used hydrogel polymers before crosslinking. The degree of polymer interaction with SWNT can be seen by the shifting fluorescence spectrum. Among the different hydrogel components, PEG perturbed the sensor baseline fluorescence the least. (c) Sensor response to 100 μ M when also incubated with hydrogel materials. Of the polymers tested, PEG and poly(vinyl pyrrolidone) preserved the sensor response compared to PBS. (d) Progesterone sensor encapsulated in PEGDA hydrogel exposed to varying cycles of 0 (red arrows) and 100 μ M (green arrows) progesterone, showing a stable and reversible response of 18%. (e) Calibration curve of the progesterone sensor hydrogel. (f) The progesterone sensor hydrogel is functional in 10% mouse serum. (g) Excitation-emission plots show that the (9,4) and (7,6) chiralities are most sensitive to progesterone, marked in red and white, respectively.....	161
Figure 4-19: Fluorescence response of P10-SWNT encapsulated in hydrogels with 50 mg/mL 2-methacryloyloxyethyl phosphorylcholine (MPC) and 75 mg/mL PEGDA 8000 to 100 μ M progesterone. (a) Hydrogels were confirmed to response to progesterone upon introduction of 100 μ M progesterone (green arrow) and confirmed to be reversal after changing the concentration to 0 μ M progesterone (red arrow). (b) Non-implanted (NI) controls were compared to hydrogels that had been implanted 1 minute or 2 hours and explanted.....	163
Figure 4-20: FTIR Spectra comparing hydrogels with and without SWNT. Due to their low concentration in the hydrogels, SWNT were not visible.....	164
Figure 4-21 : Proof of concept of in vivo steroid sensor monitoring. (a) Response of sensor hydrogels to 100 μ M progesterone outside of mice. The hydrogels were implanted subcutaneously either directly or inside of 6-8 kDa dialysis bags for varying durations of time and subsequently extracted. Direct implantation leads to deactivation over time, while the use of a dialysis bag slows the deactivation. (b) FTIR spectra do not show any changes in chemical functionalities of the bulk hydrogel material with implantation time. (c) Response of hydrogel inside of dialysis bags to 100 μ M progesterone. (d) Hydrogels inserted into 6-8 kDa dialysis bags (scale = 5 mm). (e) Two hydrogels inside of dialysis bags implanted simultaneously in the dorsal subcutaneous space of SKH1-E mice (scale = 10 mm). One dialysis bag was incubated in 100 μ M progesterone, while the other was incubated in the control buffer. (f) The dialysis bag incubated in progesterone shows a more intense fluorescence decrease over the control bag, as progesterone diffuses outside of the sensor hydrogel. The colored area represents the S.E.M. (n=3). (g) The trend was reproducible in 3 mice, with $p < 0.02$	165
Figure 5-1: (a) Hydrogel pore sizes obtained via swelling experiments. (b) Compressive moduli of hydrogels obtained from the linear regions of dynamic mechanical analysis (inset).	184
Figure 5-2: Images of mice implanted with PEGDA 8000 and PEGDA 1000 hydrogels. Mice with PEGDA 8000 hydrogels showed observable swelling in the vicinity of the implants at day 7, whereas none were noticed with the PEGDA 1000 hydrogels.	187
Figure 5-3:H&E stained tissue samples of SKH1-E taken from implant sites of hydrogels. Hydrogels of formulations 1-5 were explanted days 1, 7, 14, and 28. The hydrogel itself or locations of the hydrogels are marked by arrows. In all formulations, we see heavy neutrophilic infiltration on day 1, with less on day 14, and resolution by day 28. The severity of acute inflammation is higher in formulations 1 and 2 compared to 4 and formulation 3 relative to formulation 5. Formulation 3, however, has neutrophils than formulations 1 and 2. All formulations show an	

increase in, edema, neovascularization, and fibrosis with time. Images were taken at 20x magnification, and gels are indicated by red arrows. Magnification is 4x..... 188

Figure 5-4: H&E stained tissue samples of SKH1-E taken from implant sites of hydrogels. Magnification is 20x. 189

Figure 5-5: Tissue response scores for the (a) implant site, (b) tissue surrounding the implant, (c) fibrosis, (d) edema, (e)neovascularization, and (f)total adverse tissue reaction. The inflammation at and surrounding the implant site, edema, and neovascularization were rated on a scale of 0 to 4: 0 is absent, 1 is minimal, 2 is mild, 3 is moderate, and 4 is severe. Fibrosis was rated on a scale of 1 to 3, with 1 being only a mild fibrous encirclement, 2 being moderate or poorly organized fibrous encirclement, and 3 being a well-organized and epithelioid histiocytic cap. The total adverse tissue reaction was obtained by summing all the components except fibrosis. Fibrosis was omitted from the total because fibrosis limits the inflammatory response and promotes healing, thus being a positive outcome rather than adverse. 190

Figure 5-6: Masson’s Trichrome stained tissue samples imaged at 4x magnification. The progression of healing can be seen by observing the regions of blue, representing fibrous tissue, increasing from day 7 to day 28. Formulations 3-5 appear to have slightly more organized fibrous regions at day 7 compared to formulations 1 and 2, indicating faster healing with smaller pore sizes, as well as lower SWNT concentrations. 191

Figure 5-7: Masson’s Trichrome stained tissue samples imaged at 20x magnification..... 192

Figure 5-8: (a) Summary of the functional and dysfunctional inflammatory cells in five mice lines used in this study. Hydrogel sensors were implanted for a time period (1 min, 2 hours, 24 hours), explanted, and tested outside the mice against 100 μM progesterone. (b) The maximum sensitivity decreased with increasing implantation time in general. (c) For all mice lines, the kinetics of response slowed with longer implantation time. 195

Table of Tables

Table 2-1. Model variables and parameters.....	44
Table 2-2: Parameter values for original blood cortisol concentration model. ¹⁰	48
Table 2-3: Parameter values for cortisol distribution model. ⁴⁰	49
Table 2-4: Parameter values for protein-cortisol binding equilibrium.....	52
Table 2-5: Parameter values for sensor model. ^{[7],[12]}	54
Table 2-6. Comparison of predicted peak cortisol concentrations in compartments to experimental measurements in the literature. Some of the listed studies do not describe the exact timing of cortisol measurements, but the model values generally agree with those reported in the literature. The highest values from each study are compared to daily peak cortisol concentrations calculated by the model. Values from studies are reported either as ranges or confidence intervals based on the original report.	57
Table 2-7. Comparison of peak free cortisol concentrations and time delays in compartments relative to those in the blood. The time delay is defined as the difference in time between the cortisol peak in the blood and the cortisol peak in the compartment.....	58
Table 3-1: Fit parameters for optical penetration depth study in marine organisms.....	96
Table 4-1: Summary of polymer library, detailing composition as calculated by ¹ H NMR and molar mass calculated by ¹ H NMR and GPC.	124
Table 4-2: Bond type parameters added to OPLS-AA force field in GROMACS 4.6.5.	128
Table 4-3: Bond angle type parameters added to OPLS-AA force field in GROMACS 4.6.5.....	128
Table 4-4: Dihedral angle type parameters added to OPLS-AA force field in GROMACS 4.6.5.....	129
Table 4-5: Parameters for styrene atoms.	129
Table 4-6: Bonds in styrene.....	130
Table 4-7: Parameters for acrylic acid atoms.	130
Table 4-8: Bonds in acrylic acid.....	130
Table 4-9: Parameters for atoms in acrylated cortisol as the first monomer in a polymer.....	131
Table 4-10: Parameters for atoms in acrylated cortisol as the middle monomer in a polymer.....	131
Table 4-11: Parameters for atoms in acrylated cortisol as the final monomer in a polymer.....	132
Table 4-12: Bonds in acrylated cortisol as the first monomer in a polymer.	132
Table 4-13: Bonds in acrylated cortisol as a middle monomer in a polymer.....	133
Table 4-14: Bonds in acrylated cortisol as the final monomer in a polymer.	134

Table 4-15: Parameters for atoms in cortisol.....	134
Table 4-16: Bonds in cortisol.....	135
Table 4-17: Parameters for atoms in progesterone.....	135
Table 4-18: Bonds in progesterone.....	136
Table 4-19: Parameters for atoms in testosterone.....	136
Table 4-20: Bonds in testosterone.....	136
Table 4-21: Parameters for atoms in DHEA.....	137
Table 4-22: Bonds in DHEA.....	137
Table 4-23: Parameters for atoms in pregnenolone.....	138
Table 4-24: Bonds in pregnenolone.....	138
Table 4-25: Parameters for atoms in estradiol.....	139
Table 4-26: Bonds in estradiol.....	139
Table 4-27: Parameters for atoms in prednisone.....	139
Table 4-28: Bonds in prednisone.....	140
Table 4-29: Parameters for atoms in corticosterone.....	140
Table 4-30: Bonds in corticosterone.....	141
Table 4-31: Parameters for atoms in cortisone.....	141
Table 4-32: Bonds in cortisone.....	142
Table 4-33: Parameters for atoms in aldosterone.....	142
Table 4-34: Bonds in aldosterone.....	143
Table 4-35: Parameters for atoms in prednisolone.....	143
Table 4-36: Bonds in prednisolone.....	144
Table 37: Hydrogel Formulations.....	182

Chapter 1 : Introduction

Steroid hormones underlie numerous biochemical processes, including macromolecule metabolism,¹ homeostasis,² reproduction,³ inflammation,^{4,5} among many others.⁶ As a therapeutic, steroids can help to reduce inflammation,⁷ manipulate an organism's reproductive potential,⁸ and enhance athletic performance.⁹ With the advancements in sensor technologies in recent decades, there exists a tremendous potential to enhance medical diagnoses and treatments by targeting steroid hormones. By evolving beyond the current paradigm of sampling techniques which provide only a single steroid measurement in time,^{10,11} continuous, *in vivo* sensor technologies may elucidate steroids' biochemical mechanisms in the body; enable earlier, more accurate diagnoses of disease; and enable smarter, more efficient medical treatments through personal data.^{12,13} In this thesis, I explored the use of Corona Phase Molecular Recognition (CoPhMoRe) and polymeric materials to fabricate novel biosensors for steroid hormones that can be implanted into organisms and report local steroid concentrations.

Steroids share the common structural motif of the cyclopentanophenathrene 4-ring backbone.¹⁴ A number of steroids are produced in the adrenal gland, the ovaries, and the testes as part of the steroidogenesis pathway (Figure 1-1a).¹⁴ Due to their hydrophobicity, the majority of steroids in the blood are associated with carrier proteins, including various types of globulins and serum albumin.¹⁵ Free steroids diffuse into cells, where they bind intracellular receptors and are translocated into the nucleus, where they modulate gene expression and consequently protein production.¹⁶ Steroids are typically degraded in the liver and exit the body through urination.¹⁷

Of particular interest to this thesis are cortisol and progesterone. Cortisol is a glucocorticoid most well-known for its role in the stress response, but cortisol also has a number of other functions (Figure 1-1b). It mediates glucose metabolism, blood pressure, and immune responses.¹⁸ Cortisol

also regulates lipid and protein metabolism.¹⁹ Cortisol has also been connected to memory²⁰ and wound healing.²¹ Cortisol has been studied as a potential biomarker in various diseases, including different types of cancers,²²⁻²⁴ mental illnesses,^{23,25-28} and adrenal disorders.^{29,30} Furthermore, the therapeutic equivalent of cortisol, hydrocortisone, is commonly administered for its anti-inflammatory effects and is a common therapeutic in autoimmune disease, osteoarthritis, and immune-related adverse events.^{7,31-33}

Progesterone is one of the primary sex hormones dictating female fertility (Figure 1-1c). It is involved in menstruation, pregnancy, and a number of female cancers.³⁴⁻³⁶ Progesterone levels are often used as a marker for a woman's fertility status.³⁷ Progesterone and its derivatives are often used in contraceptive drugs.³⁸

Because of their importance as both endogenous signaling molecules and exogenously administered therapies, measurements of cortisol and progesterone are often performed as indicators of a patient's health status, as well as the efficacy of therapy.³⁹ The typical method of measurement involves sampling blood, urine, or saliva and utilizing immunoassays, chromatography, or mass spectrometry.¹⁰ These methods provide a single snapshot of steroid concentrations in time. Steroid concentrations, however, vary dynamically, even over the course of a single day as in the case of cortisol.⁴⁰ These sampling methods suffer from the lack of temporal resolution if only single measurements are taken or their labor-intensive nature if multiple measurements are taken over time. Furthermore, steroid concentrations vary significantly in an intraindividual and inter-individual manner. Additionally, immunoassays suffer from a lack of specificity for the steroid hormones,⁴¹ while chromatography and mass spectrometry are expensive and require manual labor in the preparation of samples.

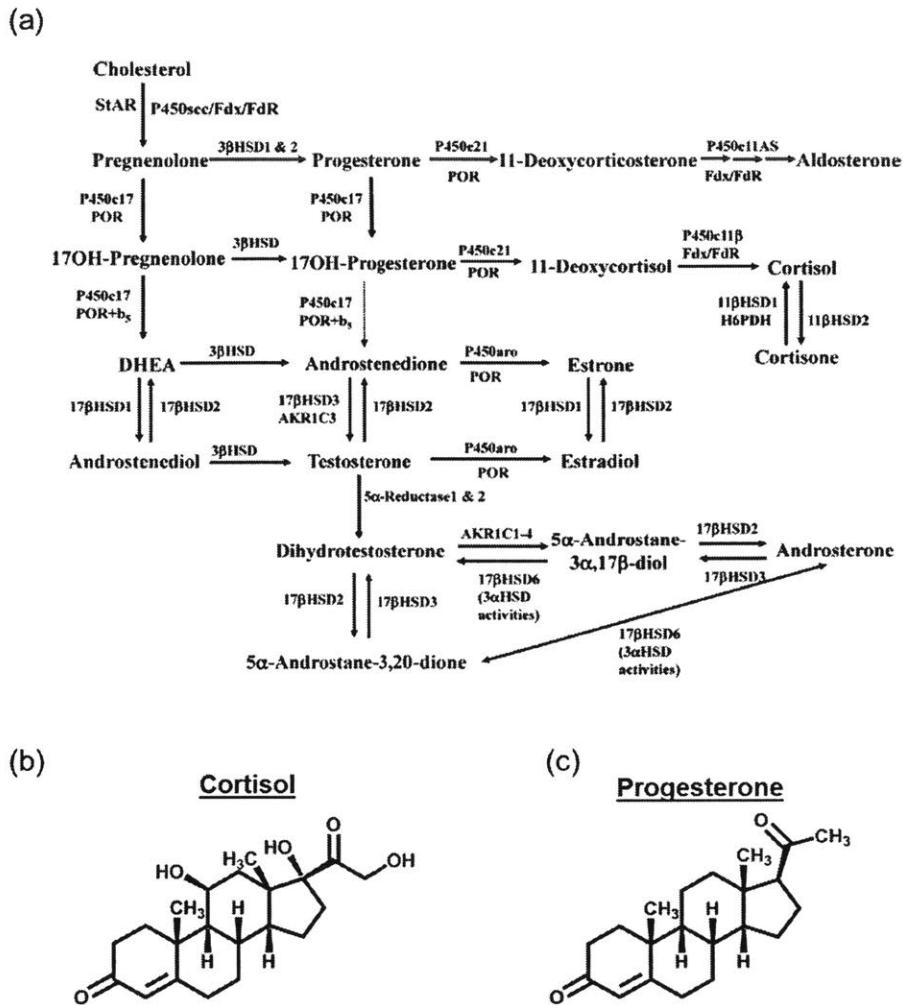


Figure 1-1: (a) Schematic of the steroidogenesis pathway. Reprinted from Miller et al., *Endocrine Reviews*, 32, 2011, with permission from Oxford University Press. (b-c) Molecular structures of (b) cortisol and (c) progesterone.

With advances in sensor technologies, there exists a tremendous potential to transform medical diagnoses and treatment through the continuous monitoring of steroid hormones. At the basis of each type of sensor is the ability to discriminate one specific molecule among the rest in its environment, otherwise labeled molecular recognition. Traditionally, biological structures have been used for various engineering problems utilizing molecular recognition, such as sensors, medicine, enzymatic reactions, and so on. These solutions, which include antibodies,⁴² other proteins,^{43,44} and aptamers,⁴⁵ have numerous advantages, including an exquisite specificity and

selectivity for their targets, easy combinatorial library generation, and established methods for high throughput screening. Molecular recognition sites for steroids have been developed using aptamers⁴⁶ and antibodies.⁴⁷⁻⁵² In recent years with the advent of directed evolution and combinatorial techniques, advances in protein engineering have gained the ability to construct novel antibodies that detect analytes with greater specificity and selectivity than their natural counterparts, revolutionizing molecular recognition.⁵³ Furthermore, other desirable properties besides binding affinity, such as stability and low immunogenicity, can also be engineered.⁵⁴ Such technology has been used to design novel therapeutics and research tools. Despite these advantages, biological units often suffer from chemical and thermal instabilities,⁵⁵ as well as expensive costs of production.⁵⁶

Molecular imprinting circumvents some of these disadvantages by utilizing synthetic materials. In molecular imprinting, monomers are polymerized and cross-linked in the presence of the target analyte of interest. Upon removal of the template, a binding site remains in the shape of the target analyte, forming a selective adsorbent. Various types of molecular imprinting-based binding sites for steroids have been reported and include polymers based on acrylic acid,⁵⁷ methacrylic acid,⁵⁸⁻⁶¹ cyclodextrins,⁶² and N,O-Bismethacryloylethanolamine.⁶³

In addition to the binding site, sensors also require a signal transducer to report and quantify the number of molecular binding events. Commonly, molecular binding sites are coupled to QCM,⁶⁴ optical fibers,⁶⁵ and electrodes.⁶⁶ Generally, molecular recognition sites are developed independently of the transduction site, and coupling strategies have to be explored later. This decoupled approach has several disadvantages, in that the binding site's affinity for its target may be reduced upon immobilization on a substrate by steric hindrance of or conformational changes in the active site, as well as the additional labor.⁶⁷

While a number of point of care devices have been developed for steroid detection,¹⁸ *in vivo* sensors placed directly into the organism have several advantages. Unlike *in vivo* sensors, point-of-care devices require the user to be actively operating either the sampling device or the measurement instrument. As a result, the quality of the data may suffer depending on patient compliance. Conversely, *in vivo* sensors generally have direct access to the biological fluid of the patient, enabling passive data collection. This facilitates long-term, continuous data to be taken remotely while allowing the patient to behave normally. The ability to utilize these sensors outside the clinic is central to their utility, in that these larger datasets paint a more comprehensive picture of the patient's health. With this information, more meaningful diagnoses and therapeutic interventions can be made.

Despite these advantages, very few *in vivo* steroid sensors have been reported in the literature. In farm animals, Cook measured blood cortisol values using an electrochemical immunosensor implanted into the jugular veins.⁶⁸ Cook measured cortisol in the brain of a sheep an antibody-based sensor with a microdialysis instrument.⁶⁹ Takase et al. measured cholesterol in a fish using cholesterol oxidase and an implanted electrode.⁷⁰ Sunwoo et al. implanted an enzyme-conjugated electrode in the adrenal gland of mice and measured cortisol release upon ACTH administration.⁷¹

Corona phase molecular recognition (CoPhMoRe) is an emerging technique for *in vivo* biosensor fabrication that leverages the advantages of synthetic materials while also developing a molecular recognition site automatically coupled to a fluorescent reporter (Figure 1-2a).⁷² In CoPhMoRe, a single-walled carbon nanotube (SWNT) is colloiddally stabilized by an amphiphilic polymer. The pinned configuration of the polymer on the SWNT forms a corona phase, with the

nanoparticle as a whole serving as a synthetic, non-biological antibody. Molecules may interact with the corona phase, changing the local environment of the carbon nanotubes and altering the characteristic fluorescence of the SWNT. In the case of a selective modulation of either the fluorescence intensity or the peak wavelengths toward one specific type of molecule, molecular recognition has taken place. CoPhMoRe has been used to sense many classes of molecules, including neurotransmitters,⁷³ carbohydrates,⁷⁴ proteins,^{75,76} nitric oxide,^{77,78} hydrogen peroxide,⁷⁹ and estrogens.⁷²

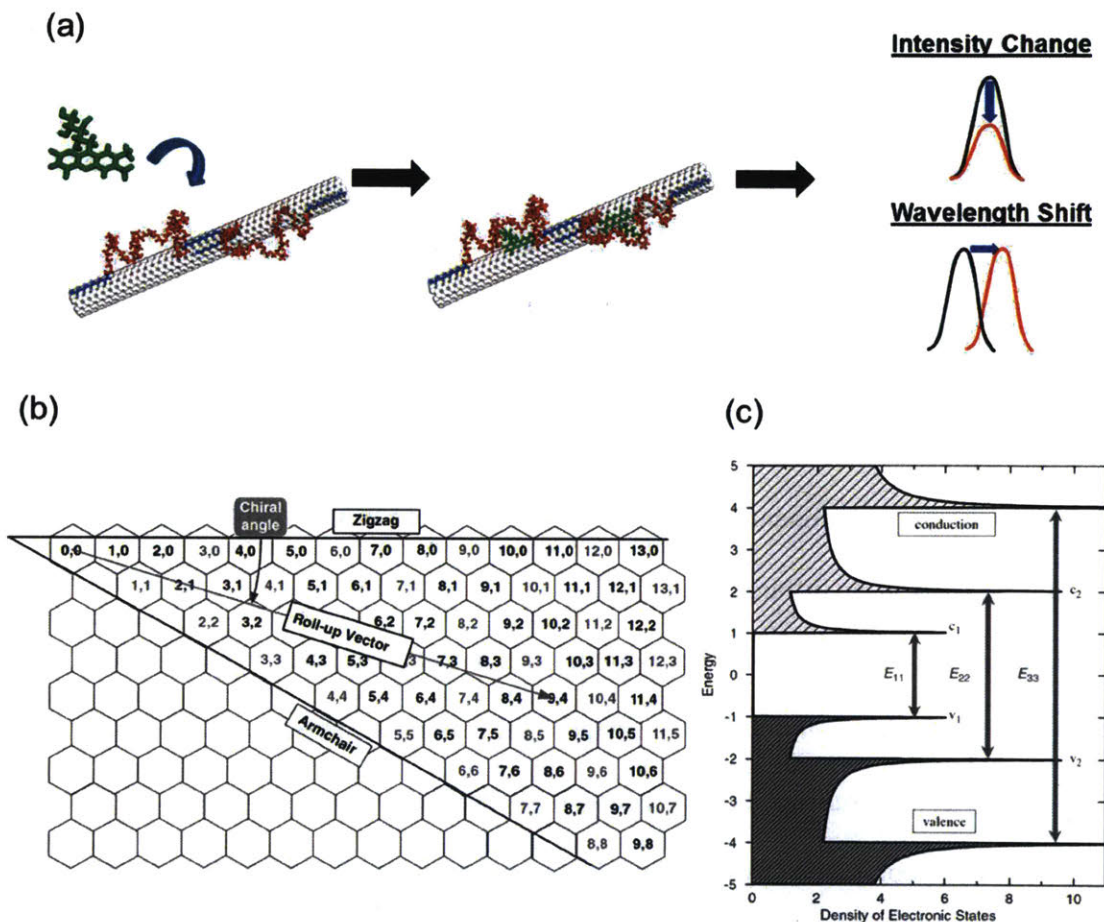


Figure 1-2: (a) Mechanism of Corona Phase Molecular Recognition (CoPhMoRe). Single-walled carbon nanotubes (SWNT) are wrapped with an amphiphilic polymer that modulates analyte binding. Upon recognition of a molecule, the SWNT fluorescence may change in intensity or in peak wavelength. Adapted from Zhang et al., Nature Nanotechnology, 8, 2013, with permission from Springer Nature. (b) Schematic illustrating the roll-up vector and chiral angle combinations forming each SWNT chirality. (c) Band

*diagram illustrating the electronic transitions leading to SWNT fluorescence. Electrons are excited from v_2 into c_2 , where they relax into c_1 . Upon recombination with a hole in v_1 , photons are emitted with an energy corresponding to the band gap. (b) and (c) reprinted from Weisman, *Optical Spectroscopy of Single-Walled Carbon Nanotubes*, 2008, with permission from Elsevier.*

The unique geometrical and electronic properties of SWNT produce this near-infrared fluorescence and is reviewed in Weisman et al.⁸⁰ Briefly, SWNT can be imagined as sheets of graphene that have been rolled up with a specific chiral angle and diameter, described by the chiral indices (n,m) that represent the configuration of folding of a graphene sheet to produce that specific SWNT (Figure 1-2b).⁸⁰ The nanoscale-cylindrical shape of SWNT confines electrons in 1-dimension along its circumference, leading to an electronic density of states exhibiting van Hove singularities. The π electrons exhibit a unique band structure depending on SWNT chirality.⁸¹ SWNT can be metallic or semi-conducting, depending on the size of the bandgap. When n-m is not evenly divisible by 3, the SWNT are semi-conductors and exhibit a band gap. This leads to a band gap between the conduction and valence bands. A band diagram illustrates this fluorescence process. Electrons are excited from the v_2 band to the c_2 band (E_{22} transition), relax to the c_1 band, and fluoresce when they return to the v_1 band (E_{11} transition). (Figure 1-2c). An excitation-emission plot illustrates the distinct electronic properties of each semi-conducting SWNT, with each chirality having a resonant excitation wavelength often in the visible spectrum and a peak emission peak in the near-infrared range.⁸¹

Interactions of target molecules with the corona phase and carbon nanotube can influence SWNT fluorescence in several ways. These mechanisms include solvatochromism, doping, redox reactions, and electron transfer. In the electron transfer mechanism, wrapping/analyte interactions modulate SWNT fluorescence by changing the frequency at which the E_{11} fluorescence transition occurs. In the electron transfer mechanism, electrons that were otherwise allowed to release/prohibited from releasing photons through the E_{11} transition interact with the molecular

orbitals of the analyte to change the frequency of this transition.^{82,83} In solvatochromism, the introduction of analytes changes the local dielectric constant around the SWNT by replacement of solvent molecules, which further modifies the transition energies E11 and E22.⁸⁴ Doping can also change the optical properties of SWNTs, including the width of the bandgap.⁸⁵

The optoelectronic properties of SWNT offer several advantages for *in vivo* monitoring. Unlike traditional organic fluorophores, SWNT exhibit no photobleaching, which allows the fluorescence to be monitored indefinitely.⁸⁶ Additionally, SWNT fluoresce in the near-infrared window, where water and blood absorb light minimally, allowing SWNT fluorescence to penetrate through deeper layers of tissue as opposed to visible light.^{87,88}

SWNT sensors have been used for *in vivo* sensors. Iverson et al. utilized ss(AAAT)₇-wrapped SWNT to detect nitric oxide in mice's livers, as well as in the vicinity of the surgical sites of subcutaneously implanted alginate hydrogels. Furthermore, the fluorescence was confirmed to remain stable over 400 days inside of the mouse.⁷⁸ Using DNA-wrapped SWNT encapsulated in a dialysis bag as an intraperitoneal implant in mice, Harvey et al. detected DNA hybridization events *in vivo*.⁸⁹ Jena et al. detected endolysosomal lipid flux in hepatic macrophages in rodent models for Niemann-Pick disease, atherosclerosis, and nonalcoholic fatty liver disease.^{90,91} Williams et al. encapsulated mAB-conjugated/DNA-wrapped SWNT into dialysis bag and implanted them into the IP space of mice. The sensors measured the ovarian cancer biomarker human epididymis protein 4 in the cases of both exogenous administration and of endogenous production via HE-4 producing mice models.⁹²

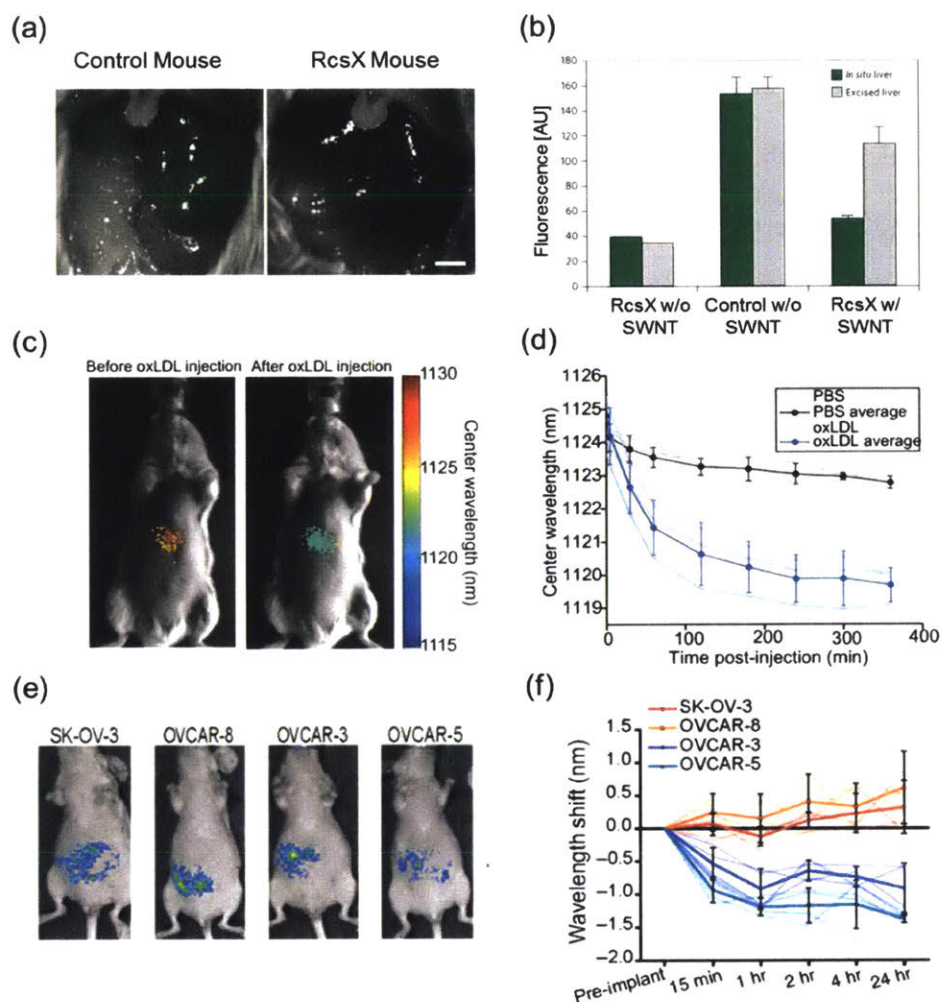


Figure 1-3: Previous examples of *in vivo* SWNT sensors. (a-b) Iverson *et al.* detected the induction of inflammation in mice treated with RcsX cells in *in situ* liver. Reprinted from Iverson *et al.* *Nature Nanotechnology*, 2013, with permission from Springer Nature. (c-d) Galassi *et al.* detected DNA hybridization events in the IP space of mice using a wavelength shift sensor. Reprinted from Galassi *et al.*, *Science Translational Medicine*, 10, 2018, with permission from AAAS. (e-f) Williams *et al.* detected the ovarian cancer biomarker HE4 in various mice models. Reprinted from Williams *et al.*, *Science Advances*, 18, 2018, with permission from AAAS.

Due to the potential of CoPhMoRe sensors for *in vivo* biosensing and the relevance of steroid hormones to human health, this thesis sought to create new CoPhMoRe sensors for steroid hormone monitoring (Figure 1-4). The thesis is structured to present theoretical modeling of sensor operation, actual fabrication and experimental testing of the sensor, and a possible application of steroid monitoring. In Chapter 2, a pharmacokinetic model describing cortisol

dynamics in the body was constructed to answer several questions regarding *in vivo* sensing feasibility: (1) What are the local dynamics that an implanted sensor would see? (2) How do the local values correlated to systemic values? and (3) What design constraints are necessary for the sensor in order to respond robustly to those local dynamics? The computational work elucidated the environment in which the sensor operated and determined ideal geometric and kinetic parameters of the sensor to operate in both a healthy patient and a Cushing's disease patient. In Chapter 3, a future application of steroid hormone monitoring is presented through an orthogonal study in which the feasibility of applying CoPhMoRe sensors to physiological biologging in aquatic organisms was explored. Key accomplishments include the engineering of a portable fluorescence measurement device, the determination of optical penetration depth of the SWNT sensors in fish tissues, the effect of tissue pigmentation on SWNT fluorescence measurements, and tracking of tissue responses in live animals of various species. In Chapter 4, I then discuss the actual fabrication of the CoPhMoRe sensor based on a templated corona phase method. Sensor fabrication and characterization in the colloidal phase is presented, followed by translation into an implanted hydrogel form factor and initial detection of progesterone in SKH1-E mice. In Chapter 5, I present hydrogel formulation strategies to improve biocompatibility and the tissue response to these implanted SWNT-hydrogel sensors. I discuss the sensor deactivation effects possibly caused by the inflammatory response and demonstrate the resolution of the inflammatory response to the SWNT hydrogels within one month. These results may guide future SWNT-hydrogel development for CoPhMoRe sensors.

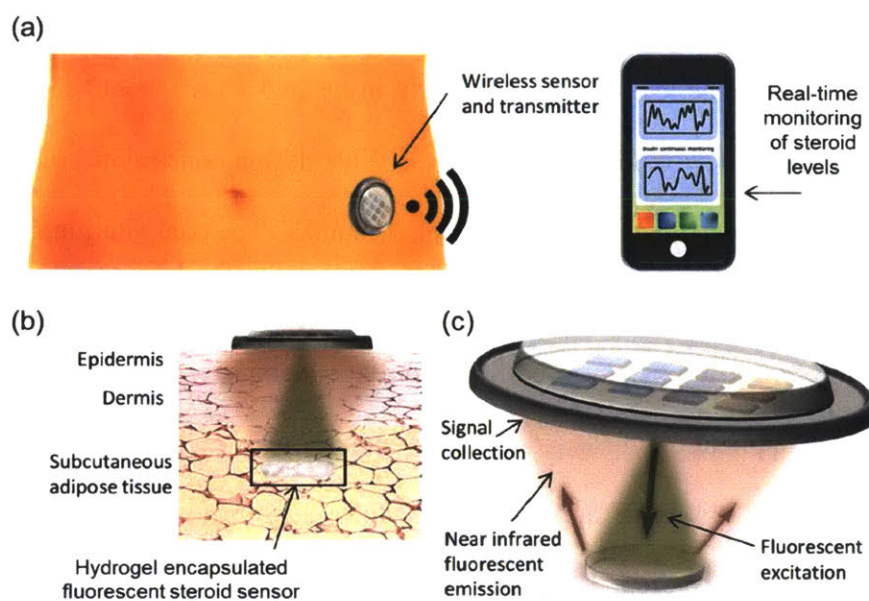


Figure 1-4: Ultimate vision of the CoPhMoRe sensors for steroid hormones. (a) Patients would wear a patch that transmit data wirelessly to an external device illustrating dynamic changes in steroid levels.(b) Underneath the patch would be a subcutaneously implanted hydrogel encapsulating the CoPhMoRe sensors, whose fluorescence would be modulated in response to dynamic changes of steroids in the surrounding tissue. (c) The dermal patch would house the necessary excitation and photodetection optics. Adapted from Bisker et al., *Advanced Healthcare Materials*, 4, 2015, with permission from John Wiley and Sons.

References

- (1) Fernandez-Real, J.-M.; Pugeat, M.; Emptoz-Bonneton, A.; Ricart, W. Study of the effect of changing glucose, insulin, and insulin-like growth factor-I levels on serum corticosteroid binding globulin in lean, obese, and obese subjects with glucose intolerance. *Metabolism* **2001**, *50* (10), 1248–1252 DOI: <https://doi.org/10.1053/meta.2001.25647>.
- (2) de Kloet, E. R.; Vreugdenhil, E.; Oitzl, M. S.; Joëls, M. Brain Corticosteroid Receptor Balance in Health and Disease*. *Endocr. Rev.* **1998**, *19* (3), 269–301 DOI: 10.1210/edrv.19.3.0331.
- (3) Nock, B.; Feder, H. H. Neurotransmitter modulation of steroid action in target cells that mediate reproduction and reproductive behavior. *Neurosci. Biobehav. Rev.* **1981**, *5* (4),

437–447 DOI: [https://doi.org/10.1016/0149-7634\(81\)90014-2](https://doi.org/10.1016/0149-7634(81)90014-2).

- (4) Barnes, P. J.; Adcock, I.; Spedding, M.; Vanhoutte, P. M. Anti-inflammatory actions of steroids: molecular mechanisms. *Trends Pharmacol. Sci.* **1993**, *14* (12), 436–441 DOI: [https://doi.org/10.1016/0165-6147\(93\)90184-L](https://doi.org/10.1016/0165-6147(93)90184-L).
- (5) Sapolsky, R. M.; Romero, L. M.; Munck, A. U. How Do Glucocorticoids Influence Stress Responses? Integrating Permissive, Suppressive, Stimulatory, and Preparative Actions. *Endocr. Rev.* **2000**, *21* (1), 55–89 DOI: 10.1210/edrv.21.1.0389.
- (6) Litwack, G. Steroid Hormones. In *Human Biochemistry*; Litwack, G. B. T.-H. B., Ed.; Academic Press: London, 2018; pp 467–506.
- (7) Cruz-Topete, D.; Cidlowski, J. A. One Hormone, Two Actions: Anti- and Pro-Inflammatory Effects of Glucocorticoids. *Neuroimmunomodulation* **2015**, *22* (1–2), 20–32 DOI: 10.1159/000362724.
- (8) Matzuk, M. M.; Lamb, D. J. The biology of infertility: research advances and clinical challenges. *Nat. Med.* **2008**, *14*, 1197.
- (9) Bhasin, S.; Storer, T. W.; Berman, N.; Callegari, C.; Clevenger, B.; Phillips, J.; Bunnell, T. J.; Tricker, R.; Shirazi, A.; Casaburi, R. The Effects of Supraphysiologic Doses of Testosterone on Muscle Size and Strength in Normal Men. *N. Engl. J. Med.* **1996**, *335* (1), 1–7 DOI: 10.1056/NEJM199607043350101.
- (10) Gatti, R.; Antonelli, G.; Prearo, M.; Spinella, P.; Cappellin, E.; De Palo, E. F. Cortisol assays and diagnostic laboratory procedures in human biological fluids. *Clin. Biochem.* **2009**, *42*, 1205–1217.
- (11) Montskó, G.; Tarjányi, Z.; Mezósi, E.; Kovács, G. L. A validated method for measurement of serum total, serum free, and salivary cortisol, using high-performance liquid

- chromatography coupled with high-resolution ESI-TOF mass spectrometry. *Anal. Bioanal. Chem.* **2014**, *406* (9–10), 2333–2341 DOI: 10.1007/s00216-014-7642-x.
- (12) Soto, R. J.; Hall, J. R.; Brown, M. D.; Taylor, J. B.; Schoenfisch, M. H. In Vivo Chemical Sensors: Role of Biocompatibility on Performance and Utility. *Anal. Chem.* **2017**, *89* (1), 276–299 DOI: 10.1021/acs.analchem.6b04251.
- (13) Rong, G.; Corrie, S. R.; Clark, H. A. In Vivo Biosensing: Progress and Perspectives. *ACS Sensors* **2017**, *2* (3), 327–338 DOI: 10.1021/acssensors.6b00834.
- (14) Miller, W. L.; Auchus, R. J. The Molecular Biology, Biochemistry, and Physiology of Human Steroidogenesis and Its Disorders. *Endocr. Rev.* **2011**, *32* (1), 81–151 DOI: 10.1210/er.2010-0013.
- (15) Anderson, D. C. Sex hormone binding globulin. *Clin. Endocrinol. (Oxf)*. **1974**, *3* (1), 69–96 DOI: 10.1111/j.1365-2265.1974.tb03298.x.
- (16) Defranco, D. B.; Madan, A. P.; Tang, Y.; Chandran, U. R.; Xiao, N.; Yang, J. Nucleocytoplasmic Shuttling of Steroid Receptors; Litwack, G. B. T.-V. & H., Ed.; Academic Press, 1995; Vol. 51, pp 315–338.
- (17) Cameron, C. B. The liver and steroid hormone metabolism. *Br. Med. Bull.* **1957**, *13* (2), 119–125 DOI: 10.1093/oxfordjournals.bmb.a069587.
- (18) Kaushik, A.; Vasudev, A.; Arya, S. K.; Pasha, S. K.; Bhansali, S. Recent advances in cortisol sensing technologies for point-of-care application. *Biosens. Bioelectron.* **2014**, *53*, 499–512 DOI: 10.1016/j.bios.2013.09.060.
- (19) Levine, A.; Zagoory-Sharon, O.; Feldman, R.; Lewis, J. G.; Weller, A. Measuring cortisol in human psychobiological studies. *Physiol. Behav.* **2007**, *90* (1), 43–53 DOI: 10.1016/j.physbeh.2006.08.025.

- (20) Buchanan, T. W.; Lovallo, W. R. Enhanced memory for emotional material following stress-level cortisol treatment in humans. *Psychoneuroendocrinology* **2001**, *26* (3), 307–317 DOI: 10.1016/S0306-4530(00)00058-5.
- (21) Ebrecht, M.; Hextall, J.; Kirtley, L. G.; Taylor, A.; Dyson, M.; Weinman, J. Perceived stress and cortisol levels predict speed of wound healing in healthy male adults. *Psychoneuroendocrinology* **2004**, *29* (6), 798–809 DOI: 10.1016/S0306-4530(03)00144-6.
- (22) Sephton, S. E.; Sapolsky, R. M.; Kraemer, H. C.; Spiegel, D. Diurnal cortisol rhythm as a predictor of breast cancer survival. *J. Natl. Cancer Inst.* **2000**, *92* (12), 994–1000 DOI: 10.1093/JNCI/92.12.994.
- (23) Van Der Pompe, G.; Antoni, M. H.; Heijnen, C. J. Elevated basal cortisol levels and attenuated ACTH and cortisol responses to a behavioral challenge in women with metastatic breast cancer. *Psychoneuroendocrinology* **1996**, *21* (4), 361–374 DOI: 10.1016/0306-4530(96)00009-1.
- (24) Abiven, G.; Coste, J.; Groussin, L.; Anract, P.; Tissier, F.; Legmann, P.; Dousset, B.; Bertagna, X.; Bertherat, J. Clinical and biological features in the prognosis of adrenocortical cancer: Poor outcome of cortisol-secreting tumors in a series of 202 consecutive patients. *J. Clin. Endocrinol. Metab.* **2006**, *91* (7), 2650–2655 DOI: 10.1210/jc.2005-2730.
- (25) Staufenbiel, S. M.; Penninx, B. W. J. H.; Spijker, A. T.; Elzinga, B. M.; van Rossum, E. F. C. Hair cortisol, stress exposure, and mental health in humans: A systematic review. *Psychoneuroendocrinology* **2013**, *38* (8), 1220–1235 DOI: 10.1016/j.psyneuen.2012.11.015.
- (26) Dykens, E. M.; Lambert, W. Trajectories of diurnal cortisol in mothers of children with autism and other developmental disabilities: Relations to health and mental health. *J. Autism*

- Dev. Disord.* **2013**, *43* (10), 2426–2434 DOI: 10.1007/s10803-013-1791-1.Trajectories.
- (27) LeMoult, J.; Joormann, J. Depressive Rumination Alters Cortisol Decline in Major Depressive Disorder. *Biol. Psychol.* **2014**, *100*, 50–55 DOI: 10.1016/j.biotechadv.2011.08.021.Secreted.
- (28) Schulz, P.; Kirschbaum, C.; Prübner, J.; Hellhammer, D. Increased free cortisol secretion after awakening in chronically stressed individuals due to work overload. *Stress Med.* **1998**, *14* (2), 91–97 DOI: 10.1002/(SICI)1099-1700(199804)14:2<91::AID-SMI765>3.0.CO;2-S.
- (29) Nieman, L. K. Diagnosis of Cushing’s Syndrome in the Modern Era. *Endocrinol. Metab. Clin.* **2018**, *47* (2), 259–273 DOI: 10.1016/j.ecl.2018.02.001.
- (30) Napier, C.; Pearce, S. H. S. Current and emerging therapies for Addison’s disease. *Curr. Opin. Endocrinol. Diabetes Obes.* **2014**, *21* (3), 147–153 DOI: 10.1097/MED.0000000000000067.
- (31) Ungaro, R.; Mehandru, S.; Allen, P. B.; Peyrin-Biroulet, L.; Colombel, J.-F. Ulcerative colitis. *Lancet* **2017**, *389* (10080), 1756–1770 DOI: [https://doi.org/10.1016/S0140-6736\(16\)32126-2](https://doi.org/10.1016/S0140-6736(16)32126-2).
- (32) Law, T. Y.; Nguyen, C.; Frank, R. M.; Rosas, S.; McCormick, F. Current concepts on the use of corticosteroid injections for knee osteoarthritis. *Phys. Sportsmed.* **2015**, *43* (3), 269–273 DOI: 10.1080/00913847.2015.1017440.
- (33) Michot, J. M.; Bigenwald, C.; Champiat, S.; Collins, M.; Carbonnel, F.; Postel-Vinay, S.; Berdelou, A.; Varga, A.; Bahleda, R.; Hollebecque, A.; et al. Immune-related adverse events with immune checkpoint blockade: a comprehensive review. *Eur. J. Cancer* **2016**, *54*, 139–148 DOI: <https://doi.org/10.1016/j.ejca.2015.11.016>.
- (34) Bouchard, P. Progesterone and the progesterone receptor. *J. Reprod. Med.* **1999**, *44* (2

- Suppl), 153–157.
- (35) Dinny Graham, J.; Clarke, C. L. Physiological action of progesterone in target tissues. *Endocrine Reviews*. 1997.
- (36) Perkins, M. S.; Toit, R. L.; Africander, D. Hormone therapy and breast cancer: emerging steroid receptor mechanisms. *J. Mol. Endocrinol.* **2018**, *61* (4), R133–R160 DOI: 10.1530/JME-18-0094.
- (37) Bosch, E.; Labarta, E.; Crespo, J.; Simón, C.; Remohí, J.; Jenkins, J.; Pellicer, A. Circulating progesterone levels and ongoing pregnancy rates in controlled ovarian stimulation cycles for in vitro fertilization: analysis of over 4000 cycles. *Hum. Reprod.* **2010**, *25* (8), 2092–2100 DOI: 10.1093/humrep/deq125.
- (38) Rivera, R.; Yacobson, I.; Grimes, D. The mechanism of action of hormonal contraceptives and intrauterine contraceptive devices. *Am. J. Obstet. Gynecol.* **1999**, *181* (5), 1263–1269 DOI: [https://doi.org/10.1016/S0002-9378\(99\)70120-1](https://doi.org/10.1016/S0002-9378(99)70120-1).
- (39) Andrew, R. Clinical measurement of steroid metabolism. *Best Pract. Res. Clin. Endocrinol. Metab.* **2001**, *15* (1), 1–16 DOI: <https://doi.org/10.1053/beem.2001.0116>.
- (40) Brown, E. N.; Meehan, P. M.; Dempster, A. P. A stochastic differential equation model of diurnal cortisol patterns. *Am. J. Physiol. Endocrinol. Metab.* **2001**, *280* (3), E450–E461.
- (41) Stanczyk, F. Z.; Lee, J. S.; Santen, R. J. Standardization of Steroid Hormone Assays: Why, How, and When? *Cancer Epidemiol. Biomarkers & Prev.* **2007**, *16* (9), 1713–1719 DOI: 10.1158/1055-9965.EPI-06-0765.
- (42) Beck, A.; Goetsch, L.; Dumontet, C.; Corvaia, N. Strategies and challenges for the next generation of antibody–drug conjugates. *Nat. Rev. Drug Discov.* **2017**, *16*, 315.
- (43) Docter, D.; Westmeier, D.; Markiewicz, M.; Stolte, S.; Knauer, S. K.; Stauber, R. H. The

- nanoparticle biomolecule corona: lessons learned – challenge accepted? *Chem. Soc. Rev.* **2015**, *44* (17), 6094–6121 DOI: 10.1039/C5CS00217F.
- (44) Skerra, A. Alternative non-antibody scaffolds for molecular recognition. *Curr. Opin. Biotechnol.* **2007**, *18* (4), 295–304 DOI: 10.1016/j.copbio.2007.04.010.
- (45) Dunn, M. R.; Jimenez, R. M.; Chaput, J. C. Analysis of aptamer discovery and technology. *Nat. Rev. Chem.* **2017**, *1*, 76.
- (46) Fernandez, R. E.; Umasankar, Y.; Manickam, P.; Nickel, J. C.; Iwasaki, L. R.; Kawamoto, B. K.; Todoki, K. C.; Scott, J. M.; Bhansali, S. Disposable aptamer-sensor aided by magnetic nanoparticle enrichment for detection of salivary cortisol variations in obstructive sleep apnea patients. *Sci. Rep.* **2017**, *7* (1), 17992 DOI: 10.1038/s41598-017-17835-8.
- (47) Ito, T.; Aoki, N.; Kaneko, S.; Suzuki, K. Highly sensitive and rapid sequential cortisol detection using twin sensor QCM. *Anal. Methods* **2014**, *6* (18), 7469–7474 DOI: 10.1039/c4ay01387e.
- (48) Arya, S. K.; Chornokur, G.; Venugopal, M.; Bhansali, S. Antibody functionalized interdigitated μ -electrode (ID μ E) based impedimetric cortisol biosensor. *Analyst* **2010**, *135* (8), 1941–1946 DOI: 10.1039/c0an00242a.
- (49) Kinnamon, D.; Ghanta, R.; Lin, K.-C.; Muthukumar, S.; Prasad, S. Portable biosensor for monitoring cortisol in low-volume perspired human sweat. *Sci. Rep.* **2017**, *7* (1), 13312 DOI: 10.1038/s41598-017-13684-7.
- (50) Stevens, R. C.; Soelberg, S. D.; Near, S.; Furlong, C. E. Detection of Cortisol in Saliva with a Flow-Filtered, Portable Surface Plasmon Resonance Biosensor System. *Anal. Chem.* **2008**, *80* (17), 6747–6751 DOI: 10.1021/ac800892h.
- (51) Kim, Y.-H.; Lee, K.; Jung, H.; Kang, H. K.; Jo, J.; Park, I.-K.; Lee, H. H. Direct immune-

- detection of cortisol by chemiresistor graphene oxide sensor. *Biosens. Bioelectron.* **2017**, *98*, 473–477 DOI: <https://doi.org/10.1016/j.bios.2017.07.017>.
- (52) Venugopal, M.; Arya, S. K.; Chornokur, G.; Bhansali, S. A realtime and continuous assessment of cortisol in ISF using electrochemical impedance spectroscopy. *Sensors Actuators, A Phys.* **2011**, *172* (1), 154–160 DOI: 10.1016/j.sna.2011.04.028.
- (53) Packer, M. S.; Liu, D. R. Methods for the directed evolution of proteins. *Nat. Rev. Genet.* **2015**, *16*, 379.
- (54) Maynard, J.; Georgiou, G. Antibody Engineering. *Annu. Rev. Biomed. Eng.* **2000**, *2* (1), 339–376 DOI: 10.1146/annurev.bioeng.2.1.339.
- (55) Wang, W.; Singh, S.; Zeng, D. L.; King, K.; Nema, S. Antibody structure, instability, and formulation. *J. Pharm. Sci.* **2007**, *96* (1) DOI: 10.1002/jps.
- (56) Kunert, R.; Reinhart, D. Advances in recombinant antibody manufacturing. *Appl. Microbiol. Biotechnol.* **2016**, *100* (8), 3451–3461 DOI: 10.1007/s00253-016-7388-9.
- (57) Ramström, O.; Ye, L.; Mosbach, K. Artificial antibodies to corticosteroids prepared by molecular imprinting. *Chem. Biol.* **1996**, *3* (6), 471–477 DOI: [https://doi.org/10.1016/S1074-5521\(96\)90095-2](https://doi.org/10.1016/S1074-5521(96)90095-2).
- (58) Cheong, S. H.; McNiven, S.; Rachkov, A.; Levi, R.; Yano, K.; Karube, I. Testosterone Receptor Binding Mimic Constructed Using Molecular Imprinting. *Macromolecules* **1997**, *30* (5), 1317–1322 DOI: 10.1021/ma961014l.
- (59) Szumski, M.; Buszewski, B. Molecularly imprinted polymers: A new tool for separation of steroid isomers. *J. Sep. Sci.* **2004**, *27* (10–11), 837–842 DOI: 10.1002/jssc.200401799.
- (60) Zhou, T.; Shen, X.; Chaudhary, S.; Ye, L. Molecularly imprinted polymer beads prepared by pickering emulsion polymerization for steroid recognition. *J. Appl. Polym. Sci.* **2013**,

131 (1) DOI: 10.1002/app.39606.

- (61) Farber, S.; Green, B. S.; Domb, A. J. Selective 17- β -estradiol molecular imprinting. *J. Polym. Sci. Part A Polym. Chem.* **2009**, *47* (20), 5534–5542 DOI: 10.1002/pola.23604.
- (62) Hishiya, T.; Shibata, M.; Kakazu, M.; Asanuma, H.; Komiyama, M. Molecularly Imprinted Cyclodextrins as Selective Receptors for Steroids. *Macromolecules* **1999**, *32* (7), 2265–2269 DOI: 10.1021/ma9816012.
- (63) Kellens, E.; Bové, H.; Conradi, M.; D’Olieslaeger, L.; Wagner, P.; Landfester, K.; Junkers, T.; Ethirajan, A. Improved Molecular Imprinting Based on Colloidal Particles Made from Miniemulsion: A Case Study on Testosterone and Its Structural Analogues. *Macromolecules* **2016**, *49* (7), 2559–2567 DOI: 10.1021/acs.macromol.6b00130.
- (64) Özgür, E.; Yılmaz, E.; Şener, G.; Uzun, L.; Say, R.; Denizli, A. A new molecular imprinting-based mass-sensitive sensor for real-time detection of 17 β -estradiol from aqueous solution. *Environ. Prog. Sustain. Energy* **2012**, *32* (4), 1164–1169 DOI: 10.1002/ep.11718.
- (65) Usha, S. P.; Shrivastav, A. M.; Gupta, B. D. A contemporary approach for design and characterization of fiber-optic-cortisol sensor tailoring LMR and ZnO/PPY molecularly imprinted film. *Biosens. Bioelectron.* **2017**, *87*, 178–186 DOI: <https://doi.org/10.1016/j.bios.2016.08.040>.
- (66) Manickam, P.; Pasha, S. K.; Snipes, S. A.; Bhansali, S. A Reusable Electrochemical Biosensor for Monitoring of Small Molecules (Cortisol) Using Molecularly Imprinted Polymers. *J. Electrochem. Soc.* **2017**, *164* (2), B54–B59 DOI: 10.1149/2.0781702jes.
- (67) Park, M. Orientation Control of the Molecular Recognition Layer for Improved Sensitivity: a Review. *Biochip J.* **2019**, *13* (1), 82–94 DOI: 10.1007/s13206-019-3103-0.

- (68) Cook, C. J. Real-time measurements of corticosteroids in conscious animals using an antibody-based electrode. *Nat. Biotechnol.* **1997**, *15* (5), 467–471 DOI: 10.1038/nbt0597-467.
- (69) Cook, C. J. Glucocorticoid feedback increases the sensitivity of the limbic system to stress. *Physiol. Behav.* **2002**, *75* (4), 455–464 DOI: [https://doi.org/10.1016/S0031-9384\(02\)00650-9](https://doi.org/10.1016/S0031-9384(02)00650-9).
- (70) Takase, M.; Murata, M.; Hibi, K.; Huifeng, R.; Endo, H. Development of mediator-type biosensor to wirelessly monitor whole cholesterol concentration in fish. *Fish Physiol. Biochem.* **2014**, *40* (2), 385–394 DOI: 10.1007/s10695-013-9851-1.
- (71) Sunwoo, S. H.; Lee, J. S.; Bae, S.; Shin, Y. J.; Kim, C. S.; Joo, S. Y.; Choi, H. S.; Suh, M.; Kim, S. W.; Choi, Y. J.; et al. Chronic and acute stress monitoring by electrophysiological signals from adrenal gland. *Proc. Natl. Acad. Sci.* **2019**, *116* (4), 1146 LP – 1151 DOI: 10.1073/pnas.1806392115.
- (72) Zhang, J.; Landry, M. P.; Barone, P. W.; Kim, J.-H.; Lin, S.; Ulissi, Z. W.; Lin, D.; Mu, B.; Boghossian, A. A.; Hilmer, A. J.; et al. Molecular recognition using corona phase complexes made of synthetic polymers adsorbed on carbon nanotubes. *Nat. Nanotechnol.* **2013**, *8* (12), 959–968 DOI: 10.1038/nnano.2013.236.
- (73) Kruss, S.; Landry, M. P.; Vander Ende, E.; Lima, B. M. a; Reuel, N. F.; Zhang, J.; Nelson, J.; Mu, B.; Hilmer, A.; Strano, M. Neurotransmitter detection using corona phase molecular recognition on fluorescent single-walled carbon nanotube sensors. *J. Am. Chem. Soc.* **2014**, *136* (2), 713–724 DOI: 10.1021/ja410433b.
- (74) Mu, B.; Ahn, J.; McNicholas, T. P.; Strano, M. S. Generating Selective Saccharide Binding Affinity of Phenyl Boronic Acids by using Single-Walled Carbon Nanotube Corona Phases.

Chem. - A Eur. J. **2015**, *21* (12), 4523–4528 DOI: 10.1002/chem.201500175.

- (75) Bisker, G.; Dong, J.; Park, H. D.; Iverson, N. M.; Ahn, J.; Nelson, J. T.; Landry, M. P.; Kruss, S.; Strano, M. S. Protein-targeted corona phase molecular recognition. *Nat. Commun.* **2016**, *7*, 10241 DOI: 10.1038/ncomms10241.
- (76) Bisker, G.; Bakh, N. A.; Lee, M. A.; Ahn, J.; Park, M.; O'Connell, E. B.; Iverson, N. M.; Strano, M. S. Insulin Detection Using a Corona Phase Molecular Recognition Site on Single-Walled Carbon Nanotubes. *ACS Sensors* **2018**, *3* (2), 367–377 DOI: 10.1021/acssensors.7b00788.
- (77) Zhang, J.; Boghossian, A. a.; Barone, P. W.; Rwei, A.; Kim, J. H.; Lin, D.; Heller, D. a.; Hilmer, A. J.; Nair, N.; Reuel, N. F.; et al. Single molecule detection of nitric oxide enabled by d(AT)₁₅ DNA adsorbed to near infrared fluorescent single-walled carbon nanotubes. *J. Am. Chem. Soc.* **2011**, *133* (3), 567–581 DOI: 10.1021/ja1084942.
- (78) Iverson, N. M.; Barone, P. W.; Shandell, M.; Trudel, L. J.; Sen, S.; Sen, F.; Ivanov, V.; Atolia, E.; Farias, E.; McNicholas, T. P.; et al. In vivo biosensing via tissue-localizable near-infrared-fluorescent single-walled carbon nanotubes. *Nat. Nanotechnol.* **2013**, *8* (11), 873–880 DOI: 10.1038/nnano.2013.222.
- (79) Jin, H.; Heller, D. a; Kalbacova, M.; Kim, J.-H.; Zhang, J.; Boghossian, A. a; Maheshri, N.; Strano, M. S. Detection of single-molecule H₂O₂ signalling from epidermal growth factor receptor using fluorescent single-walled carbon nanotubes. *Nat. Nanotechnol.* **2010**, *5* (4), 302–309 DOI: 10.1038/nnano.2010.24.
- (80) Weisman, R. B. Chapter 5 Optical spectroscopy of single-walled carbon nanotubes. In *Carbon Nanotubes: Quantum Cylinders of Graphene*; Saito, S., Zettl, A. B. T.-C. C. of C. M. S., Eds.; Elsevier, 2008; Vol. 3, pp 109–133.

- (81) Bachilo, S. M.; Strano, M. S.; Kittrell, C.; Hauge, R. H.; Smalley, R. E.; Weisman, R. B. Structure-assigned optical spectra of single-walled carbon nanotubes. *Science* **2002**, *298* (5602), 2361–2366 DOI: 10.1126/science.1078727.
- (82) Zhang, J. Q.; Boghossian, A. A.; Barone, P. W.; Rwei, A.; Kim, J. H.; Lin, D. H.; Heller, D. A.; Hilmer, A. J.; Nair, N.; Reuel, N. F.; et al. Single Molecule Detection of Nitric Oxide Enabled by d(AT)(15) DNA Adsorbed to Near Infrared Fluorescent Single-Walled Carbon Nanotubes. *J. Am. Chem. Soc.* **2011**, *133* (3), 567–581 DOI: 10.1021/ja1084942.
- (83) Satishkumar, B. C.; Brown, L. O.; Gao, Y.; Wang, C.-C.; Wang, H.-L.; Doorn, S. K. Reversible fluorescence quenching in carbon nanotubes for biomolecular sensing. *Nat. Nanotechnol.* **2007**, *2* (9), 560–564 DOI: 10.1038/nnano.2007.261.
- (84) Choi, J. H.; Strano, M. S. Solvatochromism in single-walled carbon nanotubes. *Appl. Phys. Lett.* **2007**, *90* (22), 88–91 DOI: 10.1063/1.2745228.
- (85) Ghosh, S.; Bachilo, S. M.; Simonette, R. A.; Beckingham, K. M.; Weisman, R. B. Oxygen Doping Modifies Near-Infrared Band Gaps in Fluorescent Single-Walled Carbon Nanotubes. *Science (80-.)*. **2010**, *330* (6011), 1656–1659 DOI: 10.1126/science.1196382.
- (86) Barone, P. W.; Strano, M. S. Reversible Control of Carbon Nanotube Aggregation for a Glucose Affinity Sensor. *Angew. Chemie* **2006**, *118* (48), 8318–8321 DOI: 10.1002/ange.200603138.
- (87) Welsher, K.; Liu, Z.; Sherlock, S. P.; Robinson, J. T.; Chen, Z.; Daranciang, D.; Dai, H. A route to brightly fluorescent carbon nanotubes for near-infrared imaging in mice. *Nat. Nanotechnol.* **2009**, *4* (11), 773–780 DOI: 10.1038/nnano.2009.294.
- (88) Luo, S.; Zhang, E.; Su, Y.; Cheng, T.; Shi, C. A review of NIR dyes in cancer targeting and imaging. *Biomaterials* **2011**, *32* (29), 7127–7138 DOI: 10.1016/j.biomaterials.2011.06.024.

- (89) Harvey, J. D.; Jena, P. V.; Baker, H. A.; Zerze, G. H.; Williams, R. M.; Galassi, T. V.; Roxbury, D.; Mittal, J.; Heller, D. A. A carbon nanotube reporter of microRNA hybridization events in vivo. *Nat. Biomed. Eng.* **2017**, *1* (4) DOI: 10.1038/s41551-017-0041.
- (90) Jena, P. V.; Roxbury, D.; Galassi, T. V.; Akkari, L.; Horoszko, C. P.; Iaea, D. B.; Budhathoki-Uprety, J.; Pipalia, N.; Haka, A. S.; Harvey, J. D.; et al. A Carbon Nanotube Optical Reporter Maps Endolysosomal Lipid Flux. *ACS Nano* **2017**, *11* (11), 10689–10703 DOI: 10.1021/acsnano.7b04743.
- (91) Galassi, T. V.; Jena, P. V.; Shah, J.; Ao, G.; Molitor, E.; Bram, Y.; Frankel, A.; Park, J.; Jessurun, J.; Ory, D. S.; et al. An optical nanoreporter of endolysosomal lipid accumulation reveals enduring effects of diet on hepatic macrophages in vivo. *Sci. Transl. Med.* **2018**, *10* (461), eaar2680 DOI: 10.1126/scitranslmed.aar2680.
- (92) Williams, R. M.; Lee, C.; Galassi, T. V.; Harvey, J. D.; Leicher, R.; Sirenko, M.; Dorso, M. A.; Shah, J.; Olvera, N.; Dao, F.; et al. Noninvasive ovarian cancer biomarker detection via an optical nanosensor implant. *Sci. Adv.* **2018**, *4* (4), eaaq1090 DOI: 10.1126/sciadv.aaq1090.

Chapter 2 : A Pharmacokinetic Model of a Tissue Implantable Cortisol Sensor

The work, text, and figures presented in this chapter are reproduced with permission from work published in Michael A. Lee et al. *Advanced Healthcare Material*, 5: 3004-3015.

Introduction

Cortisol is a glucocorticoid hormone that has a number of important functions. Cortisol mediates glucose metabolism, blood pressure, and immune responses.¹ Cortisol also regulates lipolysis and proteolysis for energy and biosynthesis,² and has been implicated in memory processes³ and wound healing.⁴ Cortisol is an important biomarker for Post Traumatic Stress Disorder (PTSD),⁵ Cushing's syndrome,⁶ Addison's disease,⁷ and other conditions. Hence, an implantable biosensor capable of real time monitoring of cortisol concentration would be of significant value for diagnosis and treatment of these disorders, as well as general scientific research. In this work, we develop a mathematical model, informed from physiological measurements, to predict dynamic compartmental cortisol concentrations in the human body.

Produced in the adrenal gland, cortisol enters the bloodstream, where approximately 90-95% of cortisol is bound to corticosteroid binding globulin (CBG) and albumin, while the remaining, physiologically active fraction remains free and can circulate to other tissues. CBG has a dissociation constant of 33 nM,⁸ while the dissociation constant of albumin is sensitive to environmental conditions. Previously reported values of albumin K_D values at 37 °C vary between 333 μ M and 810 μ M.^{8,9} Like several other endocrine hormones, cortisol demonstrates pulsatile

release initiated by the hypothalamic-pituitary-adrenal (HPA) axis.¹⁰ On average, there are 15-21 pulses per day with a duration at half maximum of 16 ± 0.61 minutes and amplitudes between 0 to $30 \mu\text{g dL}^{-1} \text{ min}^{-1}$ depending on the timing during the diurnal cycle.^{10,11} Typically, cortisol concentrations peak in the late morning and gradually decrease throughout the day, until reaching a minimum between 8 pm and 2 am.^{10,12}

Cortisol and its therapeutic equivalent, hydrocortisone, are also important molecules in a number of medical conditions. In Addison's disease, the adrenal gland produces low levels of cortisol, which causes various symptoms in patients, including hypotension, vomiting, weight loss, anorexia, fatigue, and increased skin pigmentation. The typical treatment for Addison's disease is ingestion of oral hydrocortisone.⁷ Conversely, excess cortisol, either through endogenous overproduction or overexposure to exogenous glucocorticoid treatment, also has serious consequences.^{13,6} In Cushing's syndrome, high concentrations of cortisol can have several consequences, including muscle weakness, an irregular fat distribution, hypertension, dermatological issues, and higher mortality rates.¹⁴ Other conditions that may be associated with abnormal cortisol levels and production include obesity,^{15,16} memory consolidation,¹⁷ chronic and acute stress,^{18,19} post-traumatic stress disorder,⁵ major depressive disorder,²⁰ bipolar disorder, and schizophrenia.²¹

Given the central role cortisol plays in numerous physiological and pathological processes, cortisol has been utilized as a biomarker for these conditions, primarily quantified using immunoassays and enzyme-linked fluorescent based assays on serum, saliva, urine, and hair samples. Ultrafiltration, equilibrium dialysis, and HPLC-MS have also been used to isolate the free fraction of cortisol in salivary and serum measurements.^{22,23} However, these methods are not currently available as continuous, real time in vivo assays.¹ To construct a continuous cortisol

profile, frequent measurements throughout the day and fitting algorithms are necessary because of the irregular nature of cortisol secretions leading to inter- and intra- personal variation.²⁴ Such measurements are labor intensive and require extensive patient compliance. Additionally, although salivary cortisol is useful for non-invasive cortisol measurements compared to other common cortisol sample sources, disturbances to the sleep-wake cycle may occur during sample collections, complicating data interpretation.²⁵ The more nuanced measurements provided by a continuous, in vivo cortisol sensor would be transformative in the characterization of cortisol dynamics in healthy and unhealthy patients. Additionally, other species have different primary glucocorticoids instead of cortisol, such as corticosterone in amphibians, reptiles, and birds and 1 α -hydroxycorticosterone in sharks and rays.²⁶ To study the physiological role these glucocorticoids play, measurements of these molecules have been taken, but results have been shown to be influenced by sex, seasonal cycles, and diurnal cycles.²⁷ Sensors to measure cortisol, as well as these other glucocorticoids, would be a much needed clinical and scientific tool.

Several efforts to measure cortisol continuously have been made. Venugopal et al. reported a microporation device that detects free cortisol in interstitial fluid based on electrochemical impedance spectroscopy.²⁸ Bhake et al. reported a miniature, wearable automatic sampling device coupled to a microdialysis system that was used to take cortisol samples over 24 hours that could later be analyzed by ELISA.²⁹ However, these technologies have several drawbacks, including the lack of longevity and the difficulty in making such techniques continuous. Our lab has demonstrated sensor platforms such as gel-encapsulated single wall carbon nanotubes (SWNT), whose near infrared fluorescence intensity and wavelength can be engineered to respond to different concentrations of biomolecules.³⁰ This platform may potentially be extended in vivo detection using the tissue transparency to nIR emission.³¹ Recent work from our lab, for example,

has successfully demonstrated estradiol,³² nitric oxide,³³ dopamine,³⁴ fibrinogen,³⁵ and glucose sensors.³⁶ As a starting point for an implantable cortisol sensor, this work seeks to construct a mathematical, dynamic model of cortisol concentrations in the human body, using parameters derived or estimated from physiological measurements. A mathematical model serves to predict local concentrations of cortisol encountered by the sensor, the relationship between these local concentrations and systemic concentrations, and sensor attributes that would enable robust cortisol measurements.

To date, several efforts to model cortisol biodistribution have been advanced. Brown et al. formulated a differential equation model of the infusion of cortisol from the adrenal gland to the bloodstream and its clearance by the liver.³⁷ Faghieh et al. modeled blood cortisol dynamics and the dynamic feedback control between ACTH and cortisol in the HPA axis.^{10,24} Glantz et al. constructed a compartmental cortisol biodistribution model based on interior and exterior volumes.³⁸ Smith et al. constructed a model to predict cortisol concentrations in the four most common locations of cortisol sampling: the blood, saliva, urine, and hair.³⁹ To our knowledge, however, a physiologically based pharmacokinetic model has not been developed that distinguishes individual tissues, an issue important for evaluating a sensor implant. Therefore, using a compartmental approach adopted by Sorensen⁴⁰ and later by our own lab⁴¹ to model glucose and insulin pharmacokinetics in the body, we propose a new model that will differentiate cortisol concentrations in the bloodstream, muscle, adipose, and brain.

First, mass transfer principles and previously proposed models of blood cortisol dynamics were used to construct a model to predict transient cortisol profiles in the adipose, muscle, and brain tissues.^{8,10,37} Waking cortisol values predicted by the model were then verified against experimental values reported in the literature for healthy patients. Then, the underlying blood

cortisol profile was modified to replicate that in a previously studied Cushing's disease patient to predict cortisol values in various tissues. Last, analysis of a theoretical cortisol sensor implanted in the adipose interstitial space was performed. Sensor output values were calculated in both the healthy and Cushing's disease patient. Sensor parameters were tuned to provide a robust sensor response with minimal time lags to enable continuous monitoring in both healthy and diseased patients.

Model Development

Compartmental Descriptions

De novo cortisol synthesis occurs in pulsatile events in the adrenal gland (g) followed by infusion into the blood with first order kinetics. Total cortisol is also eliminated from the blood through first order clearance by the liver. From this blood reservoir (rb), the blood circulates to various parts of the body. In the present model, the muscle (m), adipose (a), and brain (b) compartments have been included. These three compartments are divided into two smaller sub-compartments, the capillary bed (c) and the interstitial/intracellular zone (i). The parenthetical items refer to the subscripts on variables and parameters to be described later. Each compartment is assumed to be well-mixed, and the interstitial and intracellular spaces are lumped together as one compartment. In all compartments, cortisol exists in protein-bound and free forms. There is no clear consensus in the literature about whether cortisol uptake into cells is controlled by passive diffusion through the phospholipid bilayer, carriers through the membrane, or a combination of the two, but for simplicity, passive diffusion was assumed to be the dominant mechanism because of the lipid solubility of cortisol.⁴²⁻⁴⁴ Figure 2-1 illustrates the model structure, while Table 2-1 summarizes the variables.

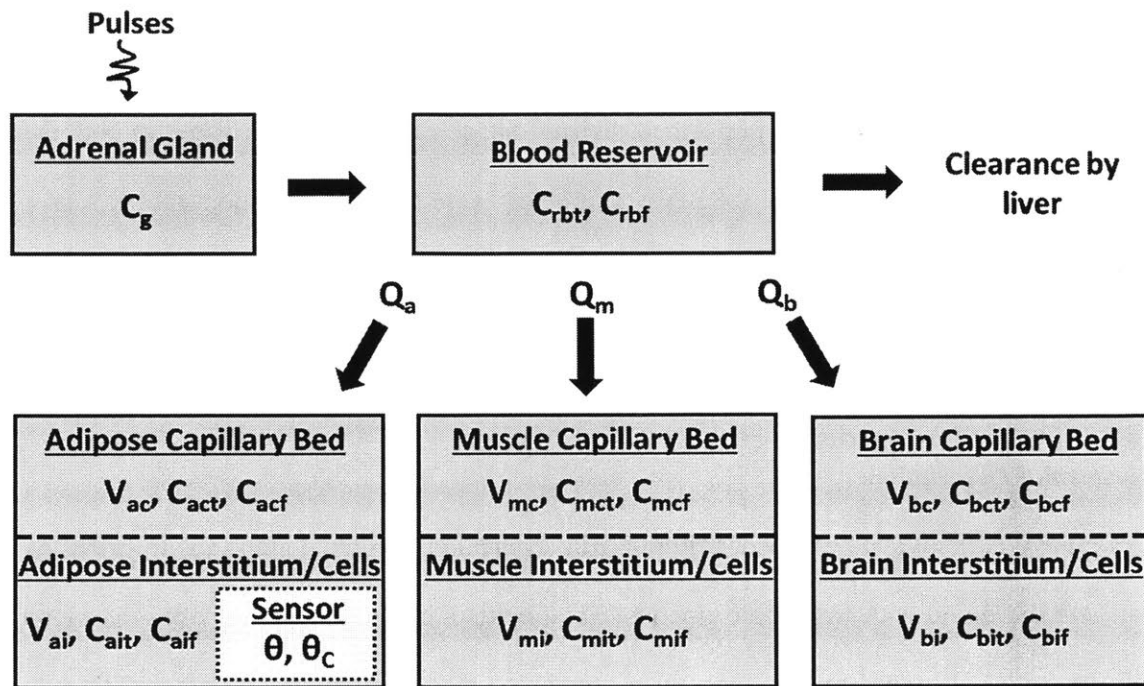


Figure 2-1. Schematic of model formulation and structure, which represents the body using various compartments with different volumes (V) and cortisol concentrations (C). Cortisol is secreted in pulses in the adrenal gland (g). Cortisol then passes into the blood by first order kinetics. From the blood, cortisol is cleared by the liver. Concentrations in the blood reservoir (rb) serve as the basis to calculate concentrations in the adipose (a), muscle (m), and brain (b). Each of these compartments is divided into the capillary bed (c) and the interstitial/intracellular space (i). In all compartments, cortisol exists in protein bound and unbound forms. Values for total cortisol (t) and free cortisol (f) are calculated. Only the free fraction can travel between the capillary bed and the interstitium. A hydrogel sensor is placed in the adipose interstitial space with cortisol bound sites (θ_c) and unbound (θ) sites.

Table 2-1. Model variables and parameters.

Variables		Parameters	
C	Cortisol concentration	r	Cortisol source or sink rate
V	Volume	D	Diffusion coefficient
Q	Blood flowrate	L	Sensor thickness
T	Transcapillary diffusion time	θ_T	Sensor binding site concentration
P	Permeability surface area product	K_D	Equilibrium dissociation constant
θ	Free sensor binding site concentration	k_b	Sensor forward binding rate constant
θ_c	Cortisol bound binding site concentration	β	Sensor output scaling factor
u	Cortisol peak	γ	Cortisol pulse variation scaling factor

q	Cortisol peak amplitude	k_1	Rate constant of cortisol infusion into blood
σ	Cortisol peak amplitude standard deviation	k_2	Rate constant of cortisol clearance by liver
τ	Cortisol peak time	ρ	Compartment density
w	Waiting time between cortisol pulses	K_a	Dissociation constant for albumin-cortisol binding
		K_{cbg}	Dissociation constant for CBG-cortisol binding
		Al	Albumin concentration
		Cbg	Corticosteroid binding concentration
Compartment	First subscript (C, V, T, P, ρ , Al, Cbg, r)	Subcompartment	Second subscript (C, Al, Cbg)
g	Adrenal gland	b	Blood
r	Blood reservoir	c	Capillary bed
a	Adipose	i	Interstitial/intracellular
m	Muscle		
b	Brain		
Cortisol Fraction	Third subscript (C)		
t	Total (bound and unbound)		
f	Free fraction		

Because the original models for total blood cortisol levels by Faghieh and Brown were formulated without consideration of other compartments, the total blood cortisol level is treated as a reservoir, whose concentration does not depend on interaction with the adipose, muscle, and brain compartments.^{10,37} This approximation is justifiable given that the adrenal gland and liver are the major site of cortisol synthesis and metabolism in the body, the Faghieh and Brown models consider both the adrenal gland and liver, and no external administration of cortisol was considered in this work.^{10,37}

Transport of cortisol from the blood to the capillary bed of each compartment occurs by convection. The free fraction of cortisol in the capillary bed can then diffuse into the interstitial compartment with transcapillary diffusion time for compartment k T_k [s], given by:

$$T_k = \frac{V_{ki}}{P_k} \quad (2-1)$$

where P_k [cm^3s^{-1}] is the permeability surface area product and V_{ki} [cm^3] is the volume of the interstitial sub-compartment of compartment k . For the adipose, muscle, and brain compartments, the mass balances for the capillary bed and interstitial space are described by the following equations:

$$V_{kc} \frac{dC_{kct}}{dt} = Q_k (C_{rbt} - C_{kct}) - \frac{V_{ki}}{T_k} (C_{kcf} - C_{kif}) \quad (2-2)$$

$$V_{ki} \frac{dC_{kit}}{dt} = \frac{V_{ki}}{T_k} (C_{kcf} - C_{kif}) + r_k \quad (2-3)$$

where Q is the volumetric flowrate of blood, C is cortisol concentration, t is time, V is volume, and r is the metabolic cortisol source rate. On each variable, the first subscript refers to compartment k . In the adipose, muscle, and brain, the second subscript (c or i) refers to the capillary or the interstitial sub-compartment, while in the blood reservoir, the second subscript (b) refers to blood. The third subscript (t or f) refers to total cortisol or the free fraction of cortisol.

Pulsatile Events

Pulses of cortisol are introduced to the model based on the method of Brown et al.³⁷ The waiting time (w) between each pulsatile event is sampled from a gamma distribution with shape parameter $\alpha = 54$ and inverse scale parameter $\beta = 39$, returning values in the unit of hours, which are then converted to the unit of minutes.

$$\tau_1 = w_1 \quad (2-4)$$

$$\tau_i = \tau_{i-1} + w_i \quad (2-5)$$

where τ_i is the timing of pulsatile event i . The average amplitude of a pulsatile event (\bar{q}) is given for $0 \leq t \leq 1440$ in minutes as:

$$\bar{q}(t) = 6.1 - 4.75 \cos\left(\frac{2\pi t}{1440}\right) + 3.93 \sin\left(\frac{2\pi t}{1440}\right) - 3.76 \cos\left(\frac{4\pi t}{1440}\right) - 2.53 \cos\left(\frac{4\pi t}{1440}\right) \quad (2-6)$$

The standard deviation of the average amplitude is:

$$\sigma_{\bar{q}}(t) = \gamma \sqrt{\bar{q}(t)} \quad (2-7)$$

where γ is a coefficient of variation. In this work, $\gamma = 0.1$, as was used in the Brown model.³⁷ The actual amplitude for each pulse was obtained by sampling from a normal distribution with mean \bar{q} and standard deviation σ calculated at that specific time. During the night hours, if a negative amplitude is returned, a pulse amplitude of $1 \mu\text{g dL}^{-1} \text{min}^{-1}$ is used instead.

Circulation of Cortisol

For the following equations, the initial time point ($t = -24$ hours) corresponds to 12:00 am. Because cortisol levels are physiologically low at this time, all of the compartments are assumed to have an initial cortisol concentration of $0 \mu\text{g dL}^{-1}$.^{10,37} Only values after the first 24 hours of simulation are used for further analysis. This allows the stochastic pulses of cortisol to establish an appropriate diurnal cycle for cortisol levels and also eliminates any biases stemming from the $0 \mu\text{g dL}^{-1}$ cortisol initial condition. The following equations describe the production of cortisol in the adrenal gland, subsequent infusion into the bloodstream, and clearance by the liver:

$$\frac{dC_g(t)}{dt} = -k_1 C_g(t) + u(t) \quad (2-8)$$

$$\frac{dC_{rbt}(t)}{dt} = k_1 C_g(t) - k_2 C_{rbt}(t) \quad (2-9)$$

$$u(t) = \sum_{i=1}^N q_i \delta(t - \tau_i) \quad (2-10)$$

where k_1 is the infusion rate constant of cortisol from the adrenal glands to the blood, and k_2 is the clearance rate constant of cortisol by the liver, whose values are given in Supporting Information

in Table 2-2: Parameter values for original blood cortisol concentration model.¹⁰ The term $u(t)$ is the pulsatile input, and its magnitude q_i is given by sampling from a normal distribution with parameters given by Equation (2-6) and (2-7). N is the total number of pulses.

Parameter	Description	Value [min ⁻¹]
k_1	Infusion Rate Constant	0.0751
k_2	Clearance Rate Constant	0.0086

From the blood reservoir, cortisol is carried to the capillary bed of each compartment. From the capillary bed, the free fraction of cortisol diffuses into the interstitial space according to the following equations:

$$V_{ac} \frac{dC_{act}}{dt} = Q_a (C_{rbt} - C_{act}) - \frac{V_{ai}}{T_a} (C_{acf} - C_{aif}) \quad (2-11)$$

$$V_{ai} \frac{dC_{ait}}{dt} = \frac{V_{ai}}{T_a} (C_{acf} - C_{aif}) + r_{ai} \quad (2-12)$$

$$V_{mc} \frac{dC_{mct}}{dt} = Q_m (C_{rbt} - C_{mct}) - \frac{V_{mi}}{T_m} (C_{mcf} - C_{mif}) \quad (2-13)$$

$$V_{mi} \frac{dC_{mit}}{dt} = \frac{V_{mi}}{T_m} (C_{mcf} - C_{mif}) \quad (2-14)$$

$$V_{bc} \frac{dC_{bct}}{dt} = Q_b (C_{rbt} - C_{bct}) - \frac{V_{bi}}{T_b} (C_{bcf} - C_{bif}) \quad (2-15)$$

$$V_{bi} \frac{dC_{bit}}{dt} = \frac{V_{bi}}{T_b} (C_{bcf} - C_{bif}) \quad (2-16)$$

$$r_{ai} = \frac{1.5 \times 10^{-13} \text{ mol}}{\text{min g tissue}} \rho_{adipose} V_{ai} \quad (2-17)$$

Note that the adipose interstitial compartment includes a term that describes the conversion of cortisone to cortisol, based on previous experimental measurements.⁴⁵ Values for Q_k and V_k were obtained from previously reported values based on a 70 kg man.⁴⁰ T_k values were calculated based on experimentally measured mass transfer rates of steroid hormones across membranes and characteristics of tissues.^{41,46-50} Table 2-3 displays parameter values.

Table 2-3: Parameter values for cortisol distribution model.⁴⁰

Parameter	Description	Units	Adipose	Muscle	Brain	Kidney	Gut
Q_k	Blood Flow Rate	L min ⁻¹	0.5143	1.286	0.7	1.2	1.2
V_k	Volume of Capillary Bed	L	0.36	0.9	0.41	0.68	0.71
	Interstitial Volume	L	1.926	4.81	0.45		
	Intracellular Volume	L	5.61	14.04	0.86		
V_{ki}	Interstitial and Intracellular Volume	L	7.5403	18.85	1.31		
T_k	Transcapillary Diffusion Time	min	15	15	115		
ρ_{ki}	Density	g L ⁻¹	947.5 ⁵¹				

Transcapillary Diffusion Time of Adipose and Muscle

The transcapillary diffusion time is defined in the following way:⁴⁰

$$\frac{V_{ki}}{T_k} = P_k \quad (2-18)$$

where V_{ki} is the volume of the interstitial fluid, T_k is the transcapillary diffusion time, and P_k [cm³s⁻¹] is the permeability surface area product of compartment k , which characterizes the diffusional resistance of capillary walls. P_k was estimated as

$$P_k = A_k K_k \quad (2-19)$$

where A_k is the surface area of the capillary walls [cm^2] and K [cm s^{-1}] is a mass transfer coefficient.

Combining Equation (2-18) and (2-19), T_k is obtained as follows:

$$T_k = \frac{V_k}{A_k K} \quad (2-20)$$

Oren et al. has reported K to be on the order of $2 \times 10^{-5} \text{ cm s}^{-1}$ for progesterone, estradiol, and testosterone transport across biomembranes.⁴⁶ Cortisol has been reported to travel more slowly across membranes than the other steroid hormones, so a value of $5 \times 10^{-6} \text{ cm s}^{-1}$ was used.⁴⁷ Values for the capillary bed surface area to tissue volume ratio for fat tissue range from 51.9 cm^{-1} for well-developed fat tissue and 222.2 cm^{-1} for poorly developed fat tissue.⁴⁸ Thus, as a rough estimate, in minutes:

$$15 \leq T_a \leq 64 \quad (2-21)$$

A value of 15 minutes was selected for the adipose tissue.

Muscle tissue gives similar bounds. Muscle density has been cited as 1.0597 g/cm^3 ,⁴⁹ and the total capillary surface area of EHP muscle in rats is $1.3 - 1.9 \text{ m}^2/100 \text{ g tissue}$.⁵⁰ As a rough estimate, then:

$$16.5 \leq T_m \leq 24.2 \quad (2-22)$$

It was assumed that the muscle and adipose tissue share the same transcapillary diffusion time, as was done in the Bisker pharmacokinetic models for glucose and insulin.⁵²

Transcapillary Diffusion Time for the Brain

The permeability surface area product for cortisol in the brain has been reported to be $0.0084 \text{ mL min}^{-1} \text{ g}^{-1}$.⁵³ Assuming a mass of 1.35 kg for a human brain, and taking both the

interstitial fluid volume and the intracellular fluid volume (0.45 and 0.86 L, respectively),⁴⁰ a characteristic time can be calculated.

$$T_b = \frac{V_b}{P_b} = 115 \text{ min} \quad (2-23)$$

Protein-Cortisol Binding Equilibrium

In all compartments, cortisol exists in both free and protein-bound fractions to either corticosteroid binding globulin or albumin. CBG is the primary binding protein for cortisol with a high affinity, one to one binding stoichiometry but is present in low concentrations. Albumin is an additional binding protein with lower affinity binding with cooperativity effects but is present in higher concentrations.⁸ Dorin et al. reported a cubic equation model that considers equilibrium binding to both CBG and albumin, which was used in the present work to determine free and total fractions of cortisol.⁸ The solution is reproduced below:

$$C_{kif} = \left(2\sqrt{\frac{-a}{3}} \right) \cos\left(\frac{\phi}{3}\right) - \frac{p}{3} \quad (2-24)$$

$$a = \frac{3q - p^2}{3} \quad (2-25)$$

$$b = \frac{2p^3 - 9pq + 27r}{27} \quad (2-26)$$

$$\phi = \cos^{-1}\left(\frac{-b/2}{\sqrt{-a^3/27}}\right) \quad (2-27)$$

$$\frac{b^2}{4} + \frac{a^3}{27} < 0 \quad (2-28)$$

$$p = Al_{kj} + Cbg_{kj} - C_{kjt} + K_a + K_{cbg} \quad (2-29)$$

$$q = Al_{kj}K_{cbg} + Cbg_{kj}K_a - C_{kjt}(K_a + K_{cbg}) + K_aK_{cbg} \quad (2-30)$$

$$r = -K_a K_{cbg} C_{kjt} \quad (2-31)$$

where Al is albumin concentration, Cbg is corticosteroid binding concentration, K_a is the dissociation constant for albumin binding, K_{cbg} is the dissociation constant for corticosteroid binding globulin binding, and subscripts k and j refer to compartments and sub-compartments, respectively. Albumin concentrations in the blood, the interstitial fluid of muscle and adipose, and cerebrospinal fluid have previously been measured.^{8,54,55} CBG concentrations have also been reported for the blood and cerebrospinal fluid,^{8,55} but to the best of our knowledge, no such measurements are reported specifically for CBG in the interstitial fluid of muscle and adipose. As an assumption, the ratio of CBG to albumin in the blood is kept constant in the muscle and adipose tissues and used to calculate protein bound cortisol in the interstitial spaces based on previously measured albumin concentrations in those spaces. The dissociation constants are assumed to remain the same among all the compartments. Parameter values are given in Table 2-4.

Table 2-4: Parameter values for protein-cortisol binding equilibrium.

Parameter	Description	Value in Blood [M] ⁸	Value in interstitial adipose [M] ^{8,54}	Value in interstitial muscle [M] ⁵⁴	Value in interstitial brain [M] ^{8,55}
Cbg_k	total CBG concentration	6.25×10^{-7}	9.38×10^{-8}	1.69×10^{-7}	5.1×10^{-10}
Al_k	total albumin concentration	5.76×10^{-4}	8.64×10^{-5}	1.56×10^{-4}	2.24×10^{-6}
K_{cbg}	dissociation constant for CBG	3.3×10^{-8}	3.3×10^{-8}	3.3×10^{-8}	3.3×10^{-8}
K_a	dissociation constant for albumin	1.378×10^{-4}	1.378×10^{-4}	1.378×10^{-4}	1.378×10^{-4}

Sensor Description and Formulation

A hydrogel sensor of a disk shape and thickness L is placed in the interstitial sub-compartment of the adipose tissue for the simulations. The thickness of the hydrogel is assumed to be much smaller than its diameter, such that only one spatial dimension must be considered. From the interstitial fluid, free cortisol diffuses into the hydrogel and binds reversibly to sensor binding sites dispersed throughout the gel. The sensor output then changes as a function of the concentration of hydrogel-bound cortisol.

The hydrogel is represented with the transient one-dimensional reaction-diffusion equation:

$$\frac{\partial C}{\partial t} = D \frac{\partial^2 C}{\partial x^2} + r_s \quad (2-32)$$

$$r_s = K_D k_b \theta_c - k_b \theta C \quad (2-33)$$

$$\theta + \theta_c = \theta_t \quad (2-34)$$

where x describes axial position along the hydrogel, t is time, k_b is the forward rate binding constant to sensor binding sites, K_D is the corresponding dissociation constant, θ is the free binding site concentration, θ_c is the bound cortisol concentration, θ_t is the total binding site concentration, and r_s is the net rate of cortisol unbinding from the hydrogel. The values for k_b and K_D are estimated from the binding properties of cortisol to the glucocorticoid receptor.⁵⁶ The partial differential equation was solved using the method of lines, which is described in detail in Supporting Information. The adipose interstitial cortisol concentration serves as the boundary condition on both ends of the hydrogel. The hydrogel was assumed to contain no cortisol at $t = -24$ hours, which is a close approximation of the nighttime condition. The sensor response is assumed to be a turn-off fluorescence sensor with the following mathematical form:³²

$$\text{sensor output} = \frac{\bar{F} - F_0}{F_0} = -\beta \frac{\bar{\theta}_c}{\theta_T} \quad (2-35)$$

where β is a scaling factor for the sensor response, $\bar{\theta}_c$ is the average bound cortisol concentration within the hydrogel, and θ_T is the total concentration of binding sites. \bar{F} and F_0 are the average fluorescence and original fluorescence of the nanosensors encapsulated within the hydrogel, respectively. The parameter values are listed in Table 2-5.

Table 2-5: Parameter values for sensor model.^{[7], [12]}

Parameter	Description	Units	Value
L	Length	m	5×10^{-4}
D	Diffusion rate constant	$\text{m}^2 \text{min}^{-1}$	1.8×10^{-8}
θ_T	Total concentration of binding sites	M	2×10^{-7}
k_b	Forward rate binding constant	$\text{M}^{-1} \text{min}^{-1}$	10^7
K_D	Dissociation equilibrium constant	M^{-1}	3.4×10^{-8}
β	Sensor response scaling factor		1

Solving the partial differential equations describing the sensor

The hydrogel is represented with the transient reaction-diffusion equation in one dimension:

$$\frac{\partial C}{\partial t} = D \frac{\partial^2 C}{\partial x^2} + r_s \quad (2-36)$$

$$r_s = K_D k_b \theta_c - k_b \theta C \quad (2-37)$$

$$\theta + \theta_c = \theta_T \quad (2-38)$$

To solve the PDE, the method of lines is used by partitioning the spatial domain into 60 points and solving the resulting ODEs. The following equations are used to calculate the concentration profile in time.

$$\frac{dC(x_1,t)}{dt} = D \frac{C(x_2,t) - 2C(x_1,t) + C(x_0,t)}{(\Delta x)^2} - k_b \theta(x_1,t) C(x_1,t) + k_b K_D (\theta_T - \theta(x_1,t)) \quad (2-39)$$

$$\frac{dC(x_i,t)}{dt} = D \frac{C(x_{i+1},t) - 2C(x_i,t) + C(x_{i-1},t)}{(\Delta x)^2} - k_b \theta(x_i,t) C(x_i,t) + k_b K_D (\theta_T - \theta(x_i,t)) \quad (2-40)$$

$$\frac{dC(x_L,t)}{dt} = D \frac{C(x_{L+1},t) - 2C(x_L,t) + C(x_{L-1},t)}{(\Delta x)^2} - k_b \theta(x_L,t) C(x_L,t) + k_b K_D (\theta_T - \theta(x_L,t)) \quad (2-41)$$

where $C(x_0,t)$ and $C(x_{L+1},t)$ are the interstitial adipose cortisol concentration at time t , acting as the boundary condition for the hydrogel.

To ensure that the spatial grid was partitioned into a sufficient number of points, the convergence of the solution was checked for a pre-defined set of cortisol pulses. The spatial domain of the hydrogel was split from 2 to 200 finite elements and compared to the solution calculated from a grid with 1000 elements. When the spatial domain is split into 40 or greater units, the solution of the PDE converges, as shown in Figure 2-2.

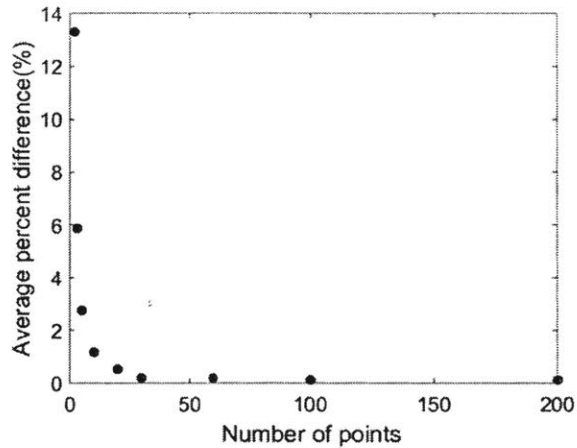


Figure 2-2: Convergence of solving the hydrogel sensor cortisol profile. Cortisol pulses were predefined for a period of 3 days, and the spatial domain of the sensor hydrogel was split into a number of points. The resulting sensor output was compared to the sensor output with the hydrogel split into 1,000 finite elements. When the hydrogel is split into 40 or more finite elements, the sensor output converges to the same solution.

Sensor Optimization

To characterize and optimize the sensor response, sensor design parameters were changed over several orders of magnitude, including the hydrogel thickness (L), the total binding site concentration (θ_T), the forward rate binding constant (k_b), and the dissociation constant (K_D). To extract details about sensor characteristics, a single pulse of $25 \mu\text{g dL}^{-1}$ was introduced to the adrenal gland and allowed to propagate according to the equations described above. The maximum sensor output was recorded, and the delay time of the peak sensor output value was calculated relative to the peak value in the interstitial adipose compartment.

Results and Discussion

Model Validation

The model was validated by comparing daily peak cortisol values predicted by the model to daily peak values reported in the literature for various compartments in healthy patients (Table 2-6).^{10,28,29,55,57-60} The total cortisol levels in the blood correspond well with those measured by Faghih et al. over 24 hours.¹⁰ As the cited studies measured free cortisol values in the subcutaneous space and interstitial fluid measurements, those values were compared against free cortisol in the muscle and adipose interstitial concentrations predicted by the model. To the best of our knowledge, there are no studies measuring protein bound cortisol in the adipose and muscle interstitial fluid against which we could validate our calculations. The total cortisol concentration in the brain interstitial concentration in the model was compared to reported measurements in cerebrospinal fluid, as at least one study explicitly mentions measuring both free and protein bound fractions.⁵⁵ Not all of the studies shown in Table 2-6 reported timing of the measurements in

relation to the circadian cycle of cortisol, but the waking values predicted by the model agree with the maximums of reported experimental values to an order of magnitude.

Table 2-6. Comparison of predicted peak cortisol concentrations in compartments to experimental measurements in the literature. Some of the listed studies do not describe the exact timing of cortisol measurements, but the model values generally agree with those reported in the literature. The highest values from each study are compared to daily peak cortisol concentrations calculated by the model. Values from studies are reported either as ranges or confidence intervals based on the original report.

Model Compartment	Model Value [$\mu\text{g/dL}$]	Reported Compartment	Study	Reported Value [$\mu\text{g/dL}$]
Blood	17 – 27	Blood – Total Cortisol	Faghih (2015) ¹⁰	15 – 25
Interstitial Adipose	1.30 – 1.89	Interstitial Fluid – Free Cortisol	Venugopal (2011) ²⁸	1.00 – 1.45
			Cohen (2009) ⁵⁷	0.1 – 0.3
			Bhake (2013) ²⁹	0.54 – 3.62
Interstitial Brain	1.07 – 1.57	Cerebrospinal Fluid – Total Cortisol	Mehta (2015) ⁵⁸	1.05 \pm 0.67
			Holub (2007) ⁵⁹	0.29 – 0.43
			Santarsieri (2014) ⁶⁰	0.45 \pm 0.04
			Schwarz (1992) ⁵⁵	0.94 \pm 0.18

Cortisol Dynamics

The cortisol levels for normal patients in the adrenal gland, blood reservoir, adipose tissue, muscle tissue, and brain tissue are shown in

Figure 2-3. Cortisol concentrations peak around waking time, which is assumed to be approximately 8 am in this model. The concentrations of cortisol in all areas are in a physiologically feasible range for normal patients. Note that only data starting from $t = 0$ were used in analyses. For the same representative dataset, **Table 2-7** compares peak blood free cortisol concentrations and timing to free cortisol concentration and timing in the other compartments. A particular focus was placed on free cortisol because it is the physiologically active fraction.⁸ Total cortisol concentration profiles are almost identical between the capillary beds of the various compartments and the blood reservoir because roughly 92-98% is bound to serum proteins and

unavailable for diffusion outside of blood vessels. The ratios of free cortisol in the capillary beds to free cortisol in the blood reservoir are all greater than 0.9. Conversely, the interstitial spaces exhibit much lower total cortisol concentrations than the total blood concentration because only the free fraction of cortisol is available for diffusion into the interstitial space. The adipose and muscle interstitial space peak free cortisol concentrations represent roughly 90% and 80% of the peak free cortisol concentration in the blood, respectively, while that in the brain represents roughly 70%.

Table 2-7. Comparison of peak free cortisol concentrations and time delays in compartments relative to those in the blood. The time delay is defined as the difference in time between the cortisol peak in the blood and the cortisol peak in the compartment.

Compartment	Ratio to Free Peak	Time Delay of Peak [min]
Blood	1	0
Adipose Capillary	0.95	3
Adipose Intracellular	0.90	35
Muscle Capillary	0.93	3
Muscle Intracellular	0.80	40
Brain Capillary	0.93	1
Brain Intracellular	0.70	70
Sensor Output		40

Two factors largely determine the transport of cortisol from the blood into the surrounding compartments: the binding equilibrium of cortisol and its proteins in the blood and the transcapillary diffusion time. As discussed previously, the binding equilibrium determines the fraction of cortisol that is available for diffusion, while the transcapillary diffusion time characterizes the resistance to diffusion into the surrounding tissues, which in turn affects the peak concentrations and the time delay in each compartment. The muscle and adipose intracellular spaces have identical transcapillary diffusion times and consequently very close transient cortisol

profiles, with the differences being the conversion of cortisone to cortisol in the adipose tissue and different concentrations of CBG and albumin. The brain, which has a transcapillary diffusion time that is larger by almost an order of magnitude compared to the muscle and adipose tissues, possesses several noticeable characteristics because of its longer transcapillary diffusion time: lower peak cortisol concentrations, delay, and smoothing of the cortisol peaks. In the adipose and muscle intracellular compartments, the transcapillary diffusion time is sufficiently small to distinguish individual pulses.

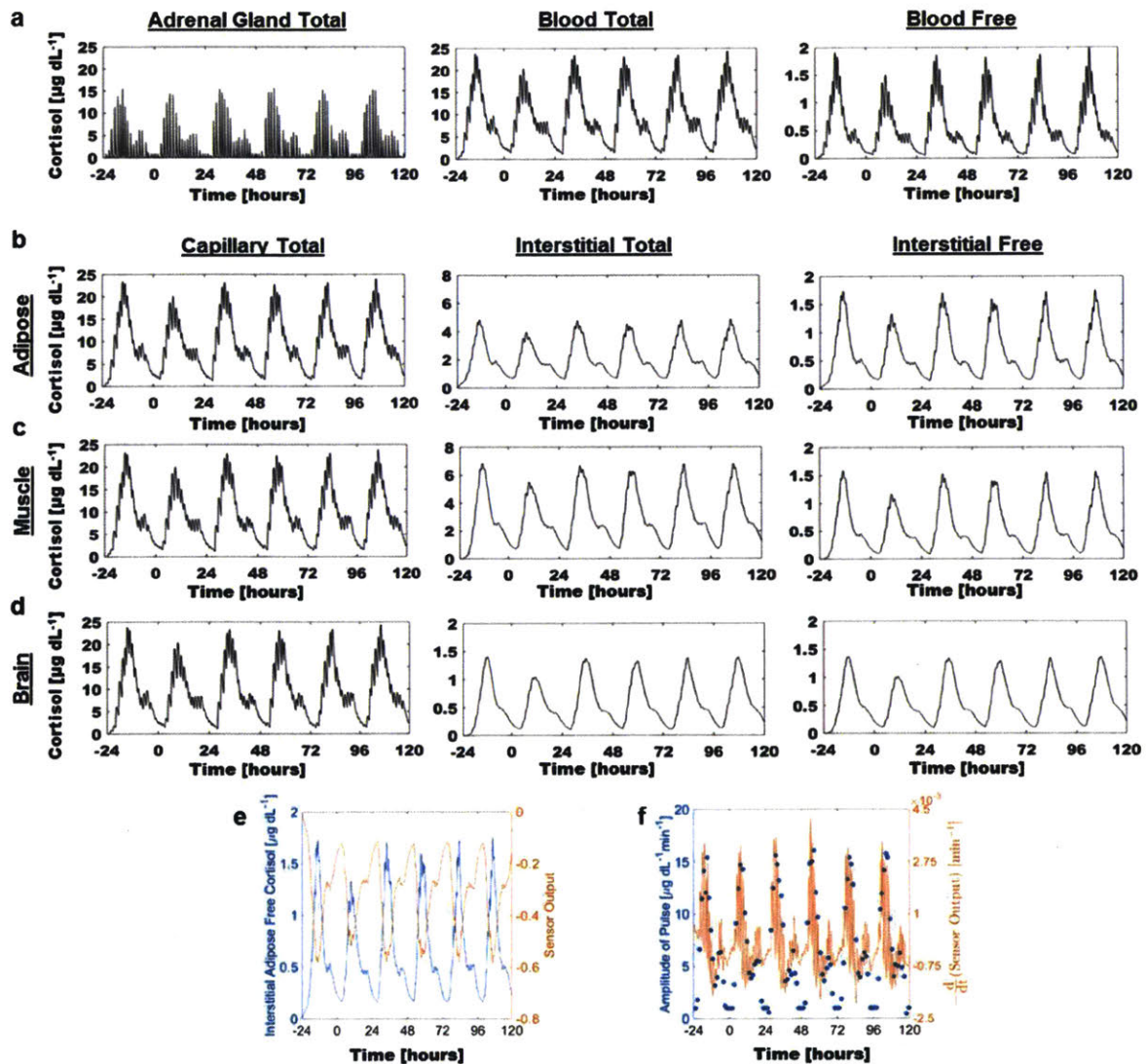


Figure 2-3. Cortisol concentrations throughout the body as predicted by the model. (a) The Faghih and Brown models were adapted to calculate cortisol levels in the adrenal gland and blood.^{10,37} These calculations were then used to calculate total and free cortisol values in the (b) adipose tissue, (c) muscle tissue, and (d) brain tissue. These three compartments were subdivided into the capillary bed and a lumped interstitial/intracellular space. (e) Intracellular adipose cortisol concentration (blue) and the sensor output (red). The shape of the sensor output maps the transient cortisol profile. (f) Cortisol pulses (blue) and the negative of the derivative of the sensor output (red). There is a correspondence between the number and size of disturbances in the derivative and the number and amplitude of pulses. In this representative data set, only data from $t = 0$ were analyzed to allow the establishment of a proper diurnal cycle and to avoid any slight biases arising from the assumed initial condition of 0 cortisol at 12 am of day -1 ($t = -24$ hours).

The effects of interstitial protein binding of cortisol were also investigated in more detail. Because each interstitial sub-compartment contains different concentrations of CBG and albumin, the proportion of free cortisol relative to the total varies among the compartments. Within a compartment, however, interstitial protein binding has some small effects on the timing and magnitude of peak cortisol values (Figure 2-4). When interstitial protein concentrations are set to 0 for an identical set of cortisol pulses, free cortisol peaks in the adipose interstitial space occur roughly 10 minutes earlier and are more pronounced. The presence of interstitial protein binding dampens cortisol pulses. However, since the mass transfer driving forces described in Equation (2-11)-(2-16) are based on free cortisol values, the difference in peak values is relatively small at less than 10%. In other words, larger variations in free cortisol concentration result from the stochastic pulsatile input in the adrenal gland compared to the inclusion of interstitial protein binding.

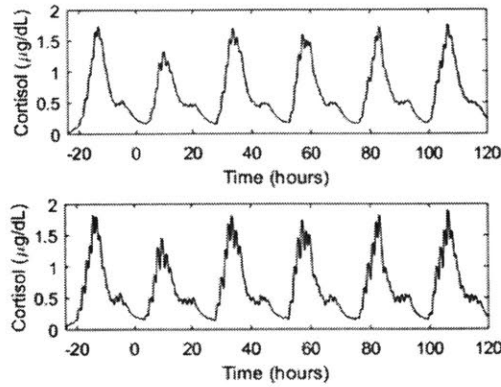


Figure 2-4: Comparison of adipose interstitial cortisol with (top) and without (bottom) interstitial protein binding. The inclusion of protein binding in the interstitial space dampens the cortisol pulses, such that the peak cortisol concentration is reduced by 10%, peaks occur later by roughly 10 minutes, and the overall profile is smoother.

Differences in the cortisol profile between compartments have significant implications for the placement of the sensor. Using the parameters listed in Table S4, the sensor itself has roughly a 5 minute time lag compared to its compartment and a decreased cortisol concentration due to transport barriers. As such, the sensor should be placed in a location with minimal time lag itself. Additionally, the sensitivity of the tissue to each pulse of cortisol is important if the sensor is to be used to correlate local cortisol concentrations with systemic cortisol concentrations. With these considerations in mind, further analyses of the hypothetical sensor were performed under the assumption of implantation in the adipose interstitial compartment, which showed sufficient sensitivity in distinguishing individual peaks of cortisol, as well as smaller time delays relative to the muscle and brain. The adipose is also likely the most accessible region of implantation and signal measurement. In order to obtain an approximate time scale of adipose tissue clearance of cortisol, an exponential curve was fit to the transient cortisol profile in the adipose tissue compartment following a single pulse of cortisol of 25 µg/dL, as shown in Figure 2-5. The profile was fit to the following form:

$$C = C_0 e^{-\frac{t}{\tau_{\text{tissue}}}} \tag{2-42}$$

$$\tau_{tissue} = 140 \text{ min} \quad (2-43)$$

This fit approximates cortisol clearance as a first order kinetic process in order to calculate τ_{tissue} , a characteristic time of adipose tissue clearance

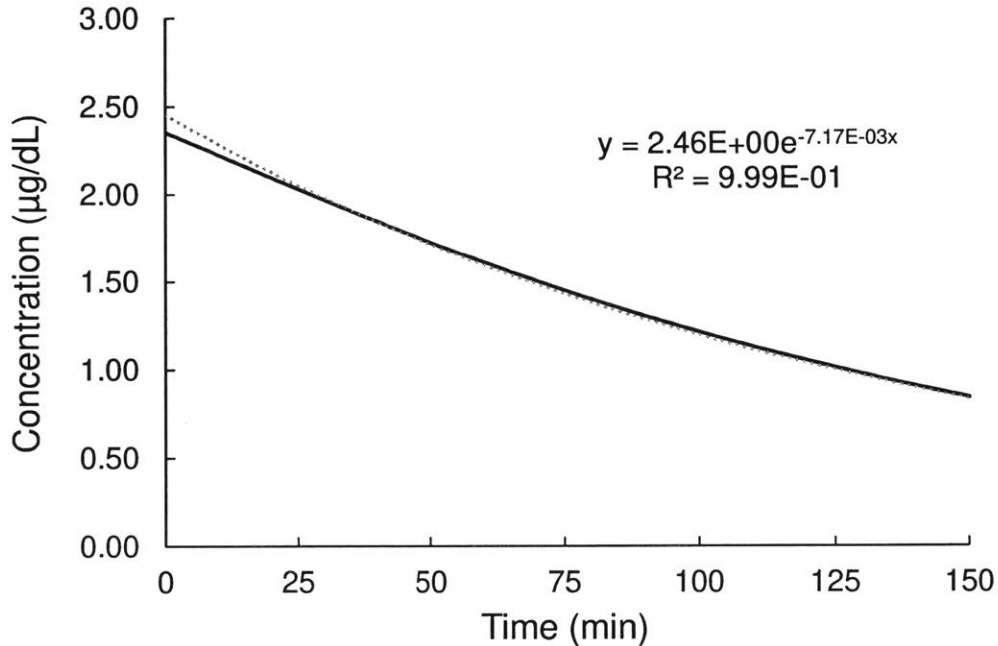


Figure 2-5: Cortisol profile in the adipose tissue following a $25 \mu\text{g dL}^{-1}$ pulse at $t = 500 \text{ min}$. The profile was fit to an exponential function in order to obtain a characteristic time of clearance of 140 minutes and a cortisol half-life of 105 minutes. Clearance was approximated as a first order kinetic process.

Sensor Response

The hypothetical sensor is modeled by considering a prototypical SWNT sensor used by our group. As in the Bisker model for an implantable insulin sensor,⁴¹ the total concentration of binding sites was calculated by assuming a hydrogel concentration of 10 mg/L of SWNTs, an individual SWNT length of 1 μm and binding site separation of 50 nm. This leads to an overall SWNT binding site concentration of 200 nM. The rate constant for cortisol binding (k_b) and dissociation constant (K_D) for the SWNT constructs – $0.01 \text{ nM}^{-1} \text{ min}^{-1}$ and 34 nM, respectively –

were estimated by comparison to previously reported values for a model of cortisol binding to glucocorticoid binding receptor.⁵⁶ Although SWNT sensors are used as the basis of this calculation, the model is equally applicable to other sensors whose binding site concentrations and kinetic parameters are known. The hydrogel was assumed to have a thickness of 0.5 mm, and the diffusion coefficient of cortisol within the gel (D) was estimated as $3 \times 10^{-10} \text{ m}^2\text{s}^{-1}$.⁶¹ The characteristic times of diffusion (τ_D), binding (τ_b), and unbinding (τ_u) can then be calculated in the following way:

$$\tau_D = \frac{L^2}{D} = 13.9 \text{ min} \quad (2-44)$$

$$\tau_b = \frac{1}{k_b \theta_r} = 0.5 \text{ min} \quad (2-45)$$

$$\tau_u = \frac{1}{k_u K_D} = 2.94 \text{ min} \quad (2-46)$$

Because τ_{tissue} is greater than τ_D , τ_b , and τ_u , the encapsulation of the sensor and the binding kinetics do not limit the sensor response, as the dynamics of the sensor-cortisol interactions are faster than cortisol dynamics in the adipose tissue.

In order to visualize *in vivo* cortisol dynamics with the finest detail, the sensor should be placed in a location that preserves the cortisol profile.

Figure 2-3e shows a representative interstitial adipose cortisol profile and the corresponding sensor response. Because the sensor response resembles the underlying profile of its compartment, sensor placement is critical. Thus, placing the sensor in the adipose or the muscle as opposed to the brain allows for more fine information to be extracted, which can then be used to correlate to the blood levels for a sense of the systemic cortisol levels.

Tracking the cortisol concentration over a period of days yields valuable information about baseline cortisol values at different times of day, which may inform medical treatment for people with various conditions such as PTSD.^{5,62} Additionally, due to the pulsatile nature of cortisol release, the derivative of the sensor output allows clearer visualization of the number of pulses occurring within a time interval.

Figure 2-3f shows the negative of the derivative of the sensor response over a period of five days. The derivative can directly inform the user about the frequency and amplitude of the pulses throughout the day. Information about the frequency of pulses can inform sensor users about possible issues of hyposensitivity to stress, hypersensitivity to stress, unusual exposures to stress, and other similar issues. Altogether, with the information of the frequency and amplitude of the pulses from the derivative and information about baseline values from the actual response, a comprehensive picture of the underlying transient cortisol profile can be pieced together, making a continuous cortisol sensor valuable.

Application of Model to Cushing's Disease Patient

Previous studies have measured 24 hour blood cortisol profiles in patients with excess cortisol concentrations. Linkowski et al. measured higher cortisol concentrations in patients with major depressive illnesses and attributed hypercortisolism to higher cortisol pulses amplitudes.⁶³ In another study, van den Berg et al. detected higher cortisol pulse amplitude and frequency in patients suffering from Cushing's disease.⁶⁴ As a model case, we simulated cortisol pharmacokinetics based on the blood cortisol levels of the male Cushing's disease patient studied in the van den Berg experiments. This patient has blood cortisol levels between 50 to 100 $\mu\text{g}/\text{dL}$ with no obvious diurnal pattern. To obtain the same general pattern of total blood cortisol, pulses of $38 \pm 2.5 \mu\text{g dL}^{-1} \text{ min}^{-1}$ with a $59 \pm 11 \text{ min}$ waiting time between pulses were introduced into the

pharmacokinetic model. Again, initial conditions of 0 $\mu\text{g/dL}$ cortisol were used in all compartments. The total blood cortisol concentrations resembled that of the van den Berg patient, and the corresponding compartmental concentrations, as well as theoretical sensor output, were calculated (Figure 2-6).

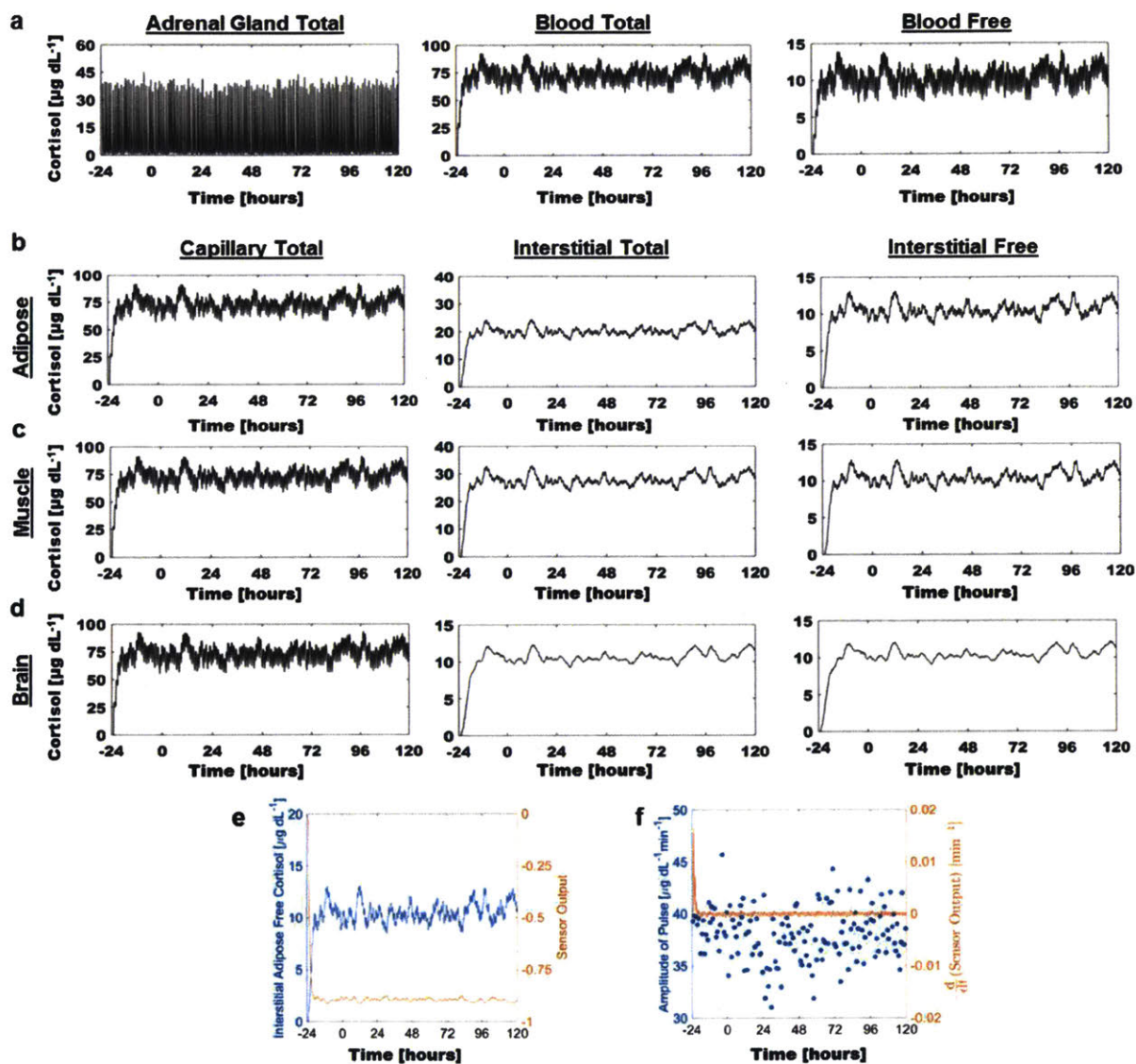


Figure 2-6. Cortisol concentrations throughout a Cushing's disease patient's body as predicted by the model. Values were calculated in the (a) adrenal gland, blood, (b) adipose tissue, (c) muscle tissue, and (d) brain tissue. To obtain similar blood cortisol profiles as the male Cushing's disease patient studied by van den Berg et al.,⁶⁴ pulses of $38 \pm 2.5 \mu\text{g dL}^{-1} \text{min}^{-1}$ with a $59 \pm 11 \text{ min}$ waiting time between pulses were introduced into the model. (e-f) Sensor output and derivative were also tracked. The sensor showed a flat output relative to that in the normal patient due to the lack of a cortisol diurnal cycle. This output is also close to saturation due to the higher cortisol concentrations.

The data show several distinctive features of Cushing's disease patients. Patients with hypercortisolism exhibiting this particular blood cortisol profile have adipose, muscle, and brain interstitial space free cortisol concentrations that are commensurate with total blood cortisol concentrations in healthy patients, as well as a higher proportion of free cortisol concentrations in the blood. The lack of a diurnal cycle also allows the cortisol concentrations in the interstitial adipose, muscle, and brain compartments to be roughly equal, as time delays no longer prevent the brain interstitial space from reaching the same cortisol concentrations as the adipose and muscle. Additionally, using the parameters given by Table S4, the theoretical sensor exhibits an output that falls within a much narrower range than that in the healthy patient and is almost saturated, showing the utility of an affinity based sensor in distinguishing between healthy and Cushing's disease patients and indicating the need for appropriate sensor design to avoid sensor output saturation. To predict biodistribution of cortisol in other types of disorders and determine necessary sensor parameters for continuous monitoring, this model may be extended by introducing appropriate patterns of cortisol secretory events.

Sensor Optimization

In order to characterize an ideal continuous cortisol sensor, four parameters were varied individually to see the effect on the maximal sensor response and the time delay of the response. These parameters include the sensor thickness, the forward binding constant, the dissociation constant, and the concentration of binding sites within the hydrogel implant (Figure 2-7).

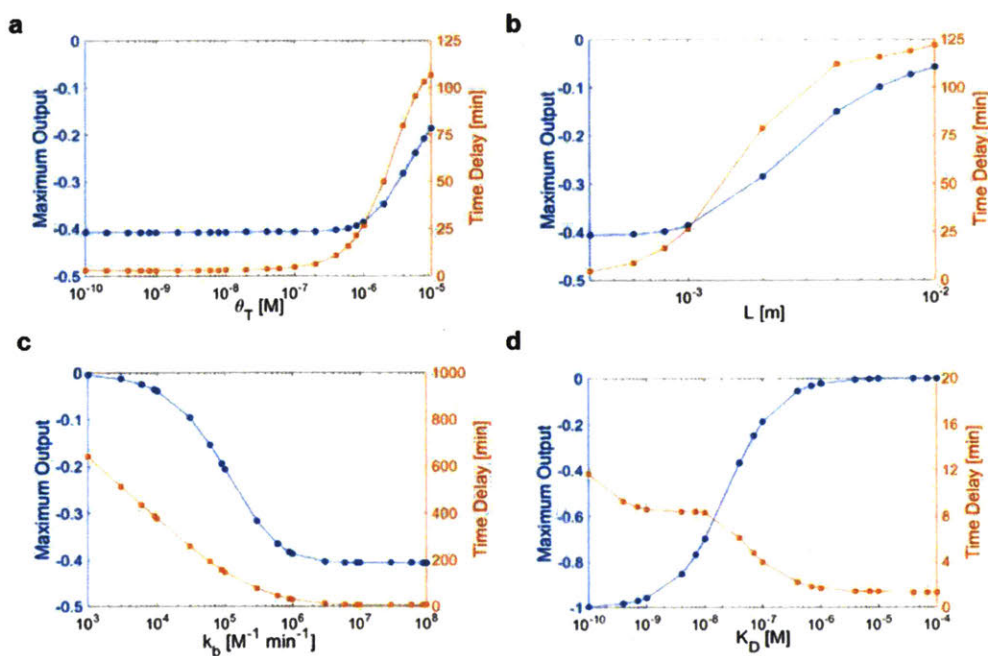


Figure 2-7. Maximum sensor output and time delay as a function of the (a) binding site concentration (θ_T), (b) sensor thickness (L), (c) forward rate binding constant (k_b), and (d) dissociation constant (K_D).

The maximal sensor response and the time delay are largely invariant over 4 orders of magnitude of sensor binding site concentration from 10^{-10} to 10^{-7} M (Figure 2-7a). However, both the time delay and the maximal response decreased with increasing concentration of binding sites, presumably a consequence of roughly the same level of cortisol reacting with what represents a smaller fraction of the total population of binding sites. The maximum output decreased from 50% to 20%, while the time delay increased from 3 minutes to 105 minutes. Given the concentration of free cortisol in the adipose tissue (~ 50 nM in healthy patients according to the model), a low concentration of binding sites renders the sensor more sensitive to changes in cortisol concentration. Additionally, lower concentrations of binding sites would be easier to achieve in practice, as sensor material could simply be diluted to the appropriate values. However, using an excessively low concentration of sensor binding sites may result in sensor output saturation, as was almost the case in the model Cushing's disease patient.

The sensor thickness was varied from 0.4 mm to 1 cm (Figure 2-7b). The maximum output decreased from 40% to 7%, while the time delay increased from 5 minutes to 122 minutes. Overall, the sensor was more sensitive and robust with smaller dimensions, but in practice, a larger sensor thickness is easier to construct and less subject to noise in the measurements.⁴¹ A balance, therefore, would have to be achieved. A 1 mm thickness offers a time delay of roughly 24 minutes, which provides enough responsivity to distinguish individual cortisol pulses. Using thinner thicknesses, however, reduces diffusional barriers to increase sensor responsivity.

Increasing k_b from 10^3 to 10^8 $\text{M}^{-1}\text{min}^{-1}$ while keeping K_D constant increases the maximal output from 0% to 40% and decreases the time delay from 640 to 5 minutes (Figure 2-7c). Increasing K_D from 10^{-10} to 10^{-4} M while keeping k_b constant decreases the delay time but also reduces the maximum response from 100% to 0% (Figure 2-7d). Both extremes represent nearly irreversible binding and no binding at all, respectively. To accurately monitor increases and decreases of cortisol concentration throughout the diurnal cycle, the sensor should exhibit neither extreme.

From this analysis, then, we propose constructing a sensor with the following design. Sensors should have roughly 1 mm or lower thickness, a dissociation constant of 100 nM, and a binding site concentration with the value of 200 nM, such that cortisol can readily bind and unbind sensor sites to induce changes in sensor output. When sensor output is linearly dependent on the fractional binding site coverage, as was assumed in Equation (2-35), the binding site concentration should lie close but higher than the dynamic cortisol concentrations encountered in the implantation site in vivo. In the case of the Cushing's disease patient examined in this study, a θ_T value of 200 nM allows the sensor to provide an unsaturated output, while still being able to provide a range of outputs reflecting the diurnal cycle of cortisol in a normal patient. The kinetics

of binding and unbinding necessitate that K_D and θ_T have values of the same order of magnitude. As can be calculated by Equation (2-44)-(2-46), a design with such K_D and θ_T allows the characteristic time of binding and unbinding to be close in value, such that the sensor respond to both low and high values of cortisol, which is paramount for robustly monitoring the diurnal cycle. When K_D and θ_T have close values, k_b should be as high as possible to maximize sensor output and minimize delay time. Changes in the value of k_b do not change the ratio of the characteristic times of binding and unbinding. Altogether, such a design can provide a robust response to cortisol dynamics while avoiding output saturation, diffusion-limited regimes, and significant delay times in response.

Conclusions

In this work, a compartmental model to connect adipose, muscle, and brain tissue cortisol concentrations with blood cortisol concentrations was formulated and verified against reported cortisol measurements. The model was used to calculate cortisol biodistribution in a Cushing's disease patient previous studied by van den Berg et al and compared against a normal patient's pharmacokinetics.⁶⁴ Furthermore, the model was used to examine a theoretical affinity sensor implanted in the interstitial space of the adipose tissue. Sensor properties, including concentration, geometry, binding kinetics, and binding equilibrium were varied, and their effects on sensor output were calculated to estimate workable parameter values. We conclude that the compartmental representation of the human body is a valuable approach to model cortisol pharmacokinetics and that implantable affinity sensors for continuous cortisol measurements are theoretically possible.

References

- (1) Kaushik, A.; Vasudev, A.; Arya, S. K.; Pasha, S. K.; Bhansali, S. Recent advances in

- cortisol sensing technologies for point-of-care application. *Biosens. Bioelectron.* **2014**, *53*, 499–512 DOI: 10.1016/j.bios.2013.09.060.
- (2) Levine, A.; Zagoory-Sharon, O.; Feldman, R.; Lewis, J. G.; Weller, A. Measuring cortisol in human psychobiological studies. *Physiol. Behav.* **2007**, *90* (1), 43–53 DOI: 10.1016/j.physbeh.2006.08.025.
 - (3) Buchanan, T. W.; Lovallo, W. R. Enhanced memory for emotional material following stress-level cortisol treatment in humans. *Psychoneuroendocrinology* **2001**, *26* (3), 307–317 DOI: 10.1016/S0306-4530(00)00058-5.
 - (4) Ebrecht, M.; Hextall, J.; Kirtley, L. G.; Taylor, A.; Dyson, M.; Weinman, J. Perceived stress and cortisol levels predict speed of wound healing in healthy male adults. *Psychoneuroendocrinology* **2004**, *29* (6), 798–809 DOI: 10.1016/S0306-4530(03)00144-6.
 - (5) Yahyavi, S. T.; Zarghami, M.; Naghshvar, F.; Danesh, A. Relationship of cortisol, norepinephrine, and epinephrine levels with war-induced posttraumatic stress disorder in fathers and their offspring. *Rev. Bras. Psiquiatr.* **2015**, *37* (2), 93–98 DOI: 10.1590/1516-4446-2014-1414.
 - (6) Gupta, S. K.; Dubé, M. P. Exogenous cushing syndrome mimicking human immunodeficiency virus lipodystrophy. *Clin. Infect. Dis.* **2002**, *35* (6), E69-71 DOI: 10.1086/342562.
 - (7) Napier, C.; Pearce, S. H. S. Current and emerging therapies for Addison’s disease. *Curr. Opin. Endocrinol. Diabetes Obes.* **2014**, *21* (3), 147–153 DOI: 10.1097/MED.0000000000000067.
 - (8) Dorin, R. I.; Pai, H. K.; Ho, J. T.; Lewis, J. G.; Torpy, D. J.; Urban, F. K.; Qualls, C. R. Validation of a simple method of estimating plasma free cortisol: Role of cortisol binding

- to albumin. *Clin. Biochem.* **2009**, *42* (1–2), 64–71 DOI: 10.1016/j.clinbiochem.2008.09.115.
- (9) McCarty, G.; Schwartz, B. Reduced plasma cortisol binding to albumin in ocular hypertension and primary open-angle glaucoma. *Curr. Eye Res.* **1999**, *18* (6), 467–476.
- (10) Faghieh, R. T.; Dahleh, M. A.; Adler, G. K.; Klerman, E. B.; Brown, E. N. Deconvolution of serum cortisol levels by using compressed sensing. *PLoS One* **2014**, *9* (1), 1–12 DOI: 10.1371/journal.pone.0085204.
- (11) Veldhuis, J. D.; Iranmanesh, A.; Lizarralde, G.; Johnson, M. L. Amplitude modulation of a burstlike mode of cortisol secretion subserves the circadian glucocorticoid rhythm. *Am. J. Physiol.* **1989**, *257* (14), E6–E14.
- (12) Faghieh, R. T.; Savla, K.; Dahleh, M. A.; Brown, E. N. A feedback control model for cortisol secretion. *2011 Annu. Int. Conf. IEEE Eng. Med. Biol. Soc.* **2011**, 716–719 DOI: 10.1109/IEMBS.2011.6090162.
- (13) van Heerden, J. A.; Young, W. F.; Grant, C. S.; Carpenter, P. C. Adrenal surgery for hypercortisolism—surgical aspects. *Surgery* **1995**, *117* (4), 466–472 DOI: 10.1016/S0039-6060(05)80069-8.
- (14) Nieman, L. K. Cushing’s syndrome: update on signs, symptoms and biochemical screening. *Eur. J. Endocrinol.* **2015**, *173* (4), M33–M38 DOI: 10.1530/EJE-15-0464.
- (15) Björntorp, P.; Rosmond, R. Obesity and cortisol. *Nutrition* **2000**, *16* (10), 924–936 DOI: 10.1016/S0899-9007(00)00422-6.
- (16) Sharp, D. S.; Andrew, M. E.; Fekedulegn, D. B.; Burchfiel, C. M.; Violanti, J. M.; Wactawski-Wende, J.; Miller, D. B. The cortisol response in policemen: Intraindividual variation, not concentration level, predicts truncal obesity. *Am. J. Hum. Biol.* **2013**, *25* (4), 499–507 DOI: 10.1002/ajhb.22397.

- (17) Van Marle, H. J. F.; Hermans, E. J.; Qin, S.; Overeem, S.; Fernández, G. The effect of exogenous cortisol during sleep on the behavioral and neural correlates of emotional memory consolidation in humans. *Psychoneuroendocrinology* **2013**, *38* (9), 1639–1649 DOI: 10.1016/j.psyneuen.2013.01.009.
- (18) Gonzalez-Cabrera, J.; Fernandez-Prada, M.; Iribar-Ibabe, C.; Peinado, J. M. Acute and chronic stress increase salivary cortisol: A study in the real-life setting of a national examination undertaken by medical graduates. *Stress* **2014**, *17* (2), 149–156 DOI: 10.3109/10253890.2013.876405.
- (19) Schulz, P.; Kirschbaum, C.; Prübner, J.; Hellhammer, D. Increased free cortisol secretion after awakening in chronically stressed individuals due to work overload. *Stress Med.* **1998**, *14* (2), 91–97 DOI: 10.1002/(SICI)1099-1700(199804)14:2<91::AID-SMI765>3.0.CO;2-S.
- (20) LeMoult, J.; Joormann, J. Depressive rumination alters cortisol decline in Major Depressive Disorder. *Biol. Psychol.* **2014**, *100*, 50–55 DOI: 10.1016/j.biopsycho.2014.05.001.
- (21) Steen, N. E.; Methlie, P.; Lorentzen, S.; Dieset, I.; Aas, M.; Nerhus, M.; Haram, M.; Agartz, I.; Melle, I.; Berg, J. P.; et al. Altered systemic cortisol metabolism in bipolar disorder and schizophrenia spectrum disorders. *J. Psychiatr. Res.* **2014**, *52*, 57–62 DOI: 10.1016/j.jpsychires.2014.01.017.
- (22) Gatti, R.; Antonelli, G.; Prearo, M.; Spinella, P.; Cappellin, E.; De Palo, E. F. Cortisol assays and diagnostic laboratory procedures in human biological fluids. *Clin. Biochem.* **2009**, *42*, 1205–1217.
- (23) Montskó, G.; Tarjányi, Z.; Mezősi, E.; Kovács, G. L. A validated method for measurement of serum total, serum free, and salivary cortisol, using high-performance liquid chromatography coupled with high-resolution ESI-TOF mass spectrometry. *Anal. Bioanal.*

- Chem.* **2014**, *406* (9–10), 2333–2341 DOI: 10.1007/s00216-014-7642-x.
- (24) Faghieh, R.; Dahleh, M.; Adler, G.; Klerman, E.; Brown, E. Quantifying Pituitary-Adrenal Dynamics and Deconvolution of Concurrent Cortisol and Adrenocorticotrophic Hormone Data by Compressed Sensing. *IEEE Trans. Biomed. Eng.* **2015**, *9294* (c), 1–1 DOI: 10.1109/TBME.2015.2427745.
- (25) Carroll, T.; Raff, H.; Findling, J. W. Late-night salivary cortisol measurement in the diagnosis of Cushing’s syndrome. *Nat. Clin. Pract. Endocrinol. Metab.* **2008**, *4* (6), 344–350 DOI: 10.1038/ncpendmet0837.
- (26) Sheriff, M. J.; Dantzer, B.; Delehanty, B.; Palme, R.; Boonstra, R. Measuring stress in wildlife: techniques for quantifying glucocorticoids. *Oecologia* **2011**, *166*, 869–887 DOI: 10.1007/s00442-011-1943-y.
- (27) Manire, C. A.; Rasmussen, L. E. L.; Maruska, K. P.; Tricas, T. C. Sex, seasonal , and stress-related variations in elasmobranch corticosterone concentrations. *Comp. Biochem. Physiology* **2007**, *148*, 926–935 DOI: 10.1016/j.cbpa.2007.09.017.
- (28) Venugopal, M.; Arya, S. K.; Chornokur, G.; Bhansali, S. A realtime and continuous assessment of cortisol in ISF using electrochemical impedance spectroscopy. *Sensors Actuators, A Phys.* **2011**, *172* (1), 154–160 DOI: 10.1016/j.sna.2011.04.028.
- (29) Bhake, R. C.; Leendertz, J. A.; Linthorst, A. C. E.; Lightman, S. L. Automated 24-hours sampling of subcutaneous tissue free cortisol in humans. *J. Med. Eng. Technol.* **2013**, *37* (3), 180–184 DOI: 10.3109/03091902.2013.773096.
- (30) Iverson, N. M.; Bisker, G.; Farias, E.; Ivanov, V.; Ahn, J.; Wogan, G. N.; Strano, M. S. Quantitative Tissue Spectroscopy of Near Infrared Fluorescent Nanosensor Implants. *J. Biomed. Nanotechnol.* **2016**, *12* (5), 1035–1047 DOI: 10.1166/jbn.2016.2237.

- (31) Landry, M. P.; Kruss, S.; Nelson, J. T.; Bisker, G.; Iverson, N. M.; Reuel, N.; Strano, M. Experimental Tools to Study Molecular Recognition within the Nanoparticle Corona. *Sensors* **2014**, *14* (9), 16196–16211 DOI: 10.3390/s140916196.
- (32) Zhang, J.; Landry, M. P.; Barone, P. W.; Kim, J.-H.; Lin, S.; Ulissi, Z. W.; Lin, D.; Mu, B.; Boghossian, A. A.; Hilmer, A. J.; et al. Molecular recognition using corona phase complexes made of synthetic polymers adsorbed on carbon nanotubes. *Nat. Nanotechnol.* **2013**, *8* (12), 959–968 DOI: 10.1038/nnano.2013.236.
- (33) Iverson, N. M.; Barone, P. W.; Shandell, M.; Trudel, L. J.; Sen, S.; Sen, F.; Ivanov, V.; Atolia, E.; Farias, E.; McNicholas, T. P.; et al. In vivo biosensing via tissue-localizable near-infrared-fluorescent single-walled carbon nanotubes. *Nat. Nanotechnol.* **2013**, *8* (11), 873–880 DOI: 10.1038/nnano.2013.222.
- (34) Kruss, S.; Landry, M. P.; Vander Ende, E.; Lima, B. M. A.; Reuel, N. F.; Zhang, J.; Nelson, J.; Mu, B.; Hilmer, A.; Strano, M. Neurotransmitter detection using corona phase molecular recognition on fluorescent single-walled carbon nanotube sensors. *J. Am. Chem. Soc.* **2014**, *136* (2), 713–724 DOI: 10.1021/ja410433b.
- (35) Bisker, G.; Dong, J.; Park, H. D.; Iverson, N. M.; Ahn, J.; Nelson, J. T.; Landry, M. P.; Kruss, S.; Strano, M. S. Protein-targeted corona phase molecular recognition. *Nat. Commun.* **2016**, *7*, 10241 DOI: 10.1038/ncomms10241.
- (36) Mu, B.; Ahn, J.; McNicholas, T. P.; Strano, M. S. Generating Selective Saccharide Binding Affinity of Phenyl Boronic Acids by using Single-Walled Carbon Nanotube Corona Phases. *Chem. - A Eur. J.* **2015**, *21* (12), 4523–4528 DOI: 10.1002/chem.201500175.
- (37) Brown, E. N.; Meehan, P. M.; Dempster, A. P. A stochastic differential equation model of diurnal cortisol patterns. *Am. J. Physiol. Endocrinol. Metab.* **2001**, *280* (3), E450–E461.

- (38) Glantz, S. A.; Luetscher, J. A.; Day, R. P.; Perloff, M. Compartment Description for Cortisol Secretion, Distribution, Binding, and Metabolism in Man. *IEEE Trans. Biomed. Eng.* **1976**, *BME-23* (1), 36–44 DOI: 10.1109/TBME.1976.324613.
- (39) Smith, M. N.; Griffith, W. C.; Beresford, S. A. A.; Vredevoogd, M.; Vigoren, E. M.; Faustman, E. M. Using a biokinetic model to quantify and optimize cortisol measurements for acute and chronic environmental stress exposure during pregnancy. *J. Expo. Sci. Environ. Epidemiol.* **2013**, No. October, 1–7 DOI: 10.1038/jes.2013.86.
- (40) Sorensen, J. T. A Physiological Model of Glucose Metabolism in Man and its Use to Design and Assess Insulin Therapies for Diabetes. *MIT PhD Thesis* **1985**.
- (41) Bisker, G.; Iverson, N. M.; Ahn, J.; Strano, M. S. A Pharmacokinetic Model of a Tissue Implantable Insulin Sensor. *Adv. Healthc. Mater.* **2015**, *4* (1), 87–97 DOI: 10.1002/adhm.201400264.
- (42) Rao, G. S.; Schulze-Hagen, K.; Rao, M. L.; Breuer, H. Kinetics of steroid transport through cell membranes: comparison of the uptake of cortisol by isolated rat liver cells with binding of cortisol to rat liver cytosol. *J. Steroid Biochem.* **1976**, *7* (11–12), 1123–1129 DOI: 10.1016/0022-4731(76)90043-1.
- (43) Rao, G. S. Mode of entry of steroid and thyroid hormones into cells. *Mol. Cell. Endocrinol.* **1981**, *21* (2), 97–108 DOI: 10.1016/0303-7207(81)90047-2.
- (44) Lan, N. C.; Karin, M.; Nguyen, T.; Weisz, A.; Birnbaum, M. J.; Eberhardt, N. L.; Baxter, J. D. Mechanisms of glucocorticoid hormone action. *J. Steroid Biochem.* **1984**, *20* (1), 77–88 DOI: 10.1016/0022-4731(84)90192-4.
- (45) Stimson, R. H.; Andersson, J.; Andrew, R.; Redhead, D. N.; Karpe, F.; Hayes, P. C.; Olsson, T.; Walker, B. R. Cortisol release from adipose tissue by 11beta-hydroxysteroid

- dehydrogenase type 1 in humans. *Diabetes* **2009**, *58* (1), 46–53 DOI: 10.2337/db08-0969.
- (46) Oren, I.; Fleishman, S. J.; Kessel, A.; Ben-Tal, N. Free diffusion of steroid hormones across biomembranes: a simplex search with implicit solvent model calculations. *Biophys. J.* **2004**, *87* (2), 768–779 DOI: 10.1529/biophysj.103.035527.
- (47) Bleau, G.; Roberts, K. D.; Chapdelaine, A. The in vitro and in vivo uptake and metabolism of steroids in human adipose tissue. *J. Clin. Endocrinol. Metab.* **1974**, *39* (2), 236–246 DOI: 10.1210/jcem-39-2-236.
- (48) Gersh, I.; Still, M. A. BLOOD VESSELS IN FAT TISSUE. RELATION TO PROBLEMS OF GAS EXCHANGE. *J. Exp. Med.* **1945**, *81* (2), 219–232 DOI: 10.1084/jem.81.2.219.
- (49) Ward, S. R.; Lieber, R. L. Density and hydration of fresh and fixed human skeletal muscle. *J. Biomech.* **2005**, *38* (11), 2317–2320 DOI: 10.1016/j.jbiomech.2004.10.001.
- (50) Myrhaage, R.; Hudlická, O. The microvascular bed and capillary surface area in rat extensor hallucis proprius muscle (EHP). *Microvasc. Res.* **1976**, *11* (3), 315–323 DOI: 10.1016/0026-2862(76)90061-3.
- (51) Martin, A. D.; Daniel, M. Z.; Drinkwater, D. T.; Clarys, J. P. Adipose tissue density, estimated adipose lipid fraction and whole body adiposity in male cadavers. *Int. J. Obes. Relat. Metab. Disord.* **1994**, *18* (2), 79–83.
- (52) Bisker, G.; Iverson, N. M.; Ahn, J.; Strano, M. S. A Pharmacokinetic Model of a Tissue Implantable Insulin Sensor. *Adv. Healthc. Mater.* **2015**, *4* (1), 87–97 DOI: 10.1002/adhm.201400264.
- (53) Pardridge, W. M.; Mietus, L. J. Transport of Steroid Hormones through the Rat Blood-Brain Barrier. *J. Clin. Invest.* **1979**, *64* (1), 145–154 DOI: 10.1172/JCI109433.
- (54) Ellmerer, M.; Schaupp, L.; Brunner, G. A.; Sendlhofer, G.; Wutte, A.; Wach, P.; Pieber, T.

- R. Measurement of interstitial albumin in human skeletal muscle and adipose tissue by open-flow microperfusion. *Am. J. Physiol. Endocrinol. Metab.* **2000**, 278 (2), E352-6 DOI: 10.3389/fnins.2011.00005.
- (55) Schwarz, S.; Pohl, P. Steroid Hormones and Steroid Hormone Binding Globulins in Cerebrospinal Fluid Studied in Individuals with Intact and with Disturbed Blood-Cerebrospinal Fluid Barrier. *Neuroendocrinology* **1992**, 55 (2), 174–182.
- (56) Munck, A.; Holbrook, N. J. Glucocorticoid-receptor complexes in rat thymus cells. *J. Biol. Chem.* **1984**, 259 (2), 820–831.
- (57) Cohen, J.; Deans, R.; Dalley, A.; Lipman, J.; Roberts, M. S.; Venkatesh, B. Measurement of tissue cortisol levels in patients with severe burns: a preliminary investigation. *Crit. Care* **2009**, 13 (6), R189 DOI: 10.1186/cc8184.
- (58) Mehta, A.; Mahale, R. R.; Sudhir, U.; Javali, M.; Srinivasa, R. Utility of cerebrospinal fluid cortisol level in acute bacterial meningitis. *Ann. Indian Acad. Neurol.* **2015**, 18 (2), 210 DOI: 10.4103/0972-2327.150626.
- (59) Holub, M.; Beran, O.; Džupová, O.; Hnyková, J.; Lacinová, Z.; Příhodová, J.; Procházka, B.; Helcl, M. Cortisol levels in cerebrospinal fluid correlate with severity and bacterial origin of meningitis. *Crit. Care* **2007**, 11 (2), R41 DOI: 10.1186/cc5729.
- (60) Santarsieri, M.; Niyonkuru, C.; McCullough, E. H.; Dobos, J. A.; Dixon, C. E.; Berga, S. L.; Wagner, A. K. Cerebrospinal fluid cortisol and progesterone profiles and outcomes prognostication after severe traumatic brain injury. *J. Neurotrauma* **2014**, 31 (8), 699–712 DOI: 10.1089/neu.2013.3177.
- (61) Gordic, M. Theoretical Modeling of Cortisol Sensor. *Univ. South Florida Masters Thesis* **2008**.

- (62) Delaney, E. The Relationship between Traumatic Stress, PTSD and Cortisol. *Nav. Cent. Combat Oper. Stress Control* **2013**.
- (63) Linkowski, P.; Mendlewicz, J.; Leclercq, R.; Brasseur, M.; Hubain, P.; Golstein, J.; Copinschi, G.; Cauter, E. Van. The 24-Hour Profile of Adrenocorticotropin and Cortisol in Major Depressive Illness*. *J. Clin. Endocrinol. Metab.* **1985**, *61* (3), 429–438 DOI: 10.1210/jcem-61-3-429.
- (64) van den Berg, G.; Frolich, M.; Veldhuis, J. D.; Roelfsema, F. Combined amplification of the pulsatile and basal modes of adrenocorticotropin and cortisol secretion in patients with Cushing's disease: Evidence for decreased responsiveness of the adrenal glands. *J. Clin. Endocrinol. Metab.* **1995**, *80* (12), 3750–3757 DOI: 10.1210/jc.80.12.3750.

Chapter 3 : Implanted Nanosensors in Marine Organisms for Physiological Biologging: Design, Feasibility, and Species Variability

The work, text, and figures presented in this chapter are reproduced with permission from work published in Michael A. Lee et al. *ACS Sensors*, 4,1, 32-43.

Introduction

In recent decades, the biologging community has attached various types of sensors to animals to characterize animal behavior in the context of their environments.¹ These studies have produced key insights into a wide range of ecological phenomena, including the metabolic energy balance,² predator-prey relationships,³ the ecological effects of climate change,⁴ the impact of human activity on animals,⁵ and other behaviors related to feeding,⁶ migration,⁷ and reproduction.⁸ However, deployed sensors have largely been limited to environmental parameter sensors (temperature, pressure, and salinity), movement and location sensors (accelerometers and GPS), and vital sign sensors, such as heart rate monitors.² Notably missing from these tools are chemical sensors. These may be outward-facing, measuring analytes in the local environment around the animal, or inward-facing, measuring biochemical signaling pathways within the animal. The advent of novel technologies capable of real-time, continuous chemical sensing, such as those enabled by Corona Phase Molecular Recognition (CoPhMoRe), may enable access to this information and thereby significantly advance biologging studies.⁹ Herein, we explore, for the first time, several design and operation issues associated with implantable sensors of this type for biologging applications, using near infrared (nIR) fluorescent carbon nanotube sensors as a model

for marine organisms to address aspects of feasibility. For this study and purpose, we have assembled a unique team of marine biologists, sensor developers, and engineers to address this challenge, as co-authors of this study.

Recent developments in *in vivo* sensing technologies offer tremendous opportunities for biologists to probe the chemical network underpinning animal behaviors. As many excellent reviews have reported, *in vivo* sensors operating in several modalities – including optical and electrochemical – have been developed to measure a variety of biomarkers, including ions, reactive oxygen species, redox active molecules, oxygen, metals, and macromolecules, among many others.¹⁰⁻¹⁸ Recently, Sun et al. measured glucose in mice using oxygen-sensitive polymer dots and a smartphone,¹⁹ Measurements of hypochlorous acid and pH been performed in zebrafish and their embryos.^{20,21} Ferreira et al. modified carbon fiber microelectrodes and simultaneously measured ascorbate and glutamate in the hippocampi of anesthetized rats.²² Despite these advances, the continuous glucose monitor remains one of the few technologies to be adopted due to stringent analytical and biocompatibility requirements for sensor integrity in *in vivo* environments.^{13,14} Although biologically derived units such as antibodies, aptamers, and enzymes have traditionally been used for chemical sensing,²³ they may lose their capability for molecular recognition when conjugated to other sensor components and may also suffer from limited thermal and chemical stability, restricting their use *in vivo* to short periods of time.²⁴

Synthetic sensing approaches have overcome some of these disadvantages. Our group has developed Corona Phase Molecular Recognition (CoPhMoRe), which uses a nIR fluorescent nanoparticle that acts as both the molecular recognition unit and the reporter of binding events.⁹ An amphiphilic polymer or surfactant adsorbs onto singly dispersed single wall carbon nanotubes (SWNT) via hydrophobic interactions. The hydrophilic groups on the polymer provide the

dispersion colloidal stability in aqueous solutions, where a majority of bioanalytes exist. The conformation of the adsorbed phase, or the corona, modulates analyte binding to the nanoparticle and provides selectivity. Upon analyte binding, the fluorescence intensity and/or peak wavelength may change. To date, CoPhMoRe sensors have been fabricated for a variety of molecules, including nitric oxide,²⁵ hydrogen peroxide,²⁶ riboflavin, L-thyroxine, estradiol,⁹ dopamine,^{27,28} fibrinogen,²⁴ and insulin.²⁹ The nitric oxide sensor has been demonstrated *in vivo* and shown to have a fluorescence stability of over 400 days within the body of a mouse.³⁰

The challenge facing researchers is to now incorporate these new types of physiological sensors into biologging devices.³¹ In the past, the biologging community has traditionally focused on sensors that describe the behaviors, external environments, and location of animals. Accelerometers, depth, and temperature sensors and Argos satellite-linked and GPS tags have been central to this task.³² For example, using accelerometers, Wilson et al. studied the significance of neck length in swimming and foraging behaviors in Imperial cormorants and Megallanic penguins,³³ Hays et al. used records from satellite tagging of thousands of sea turtles to compare their migration distances with those of other similarly-sized marine animals,⁷ and Meekan et al. used a combination of an accelerometer, magnetometer, GPS, and depth sensors to study the energy efficiency of whale shark movement patterns.³⁴

The combination of sensors that collect datasets of movement, location, and relevant biochemical parameters (such as glucose, dopamine, and cortisol)^{28,29,35} into biologging tags potentially offers unprecedented insights into the behavior, ecology, and condition of animals. To date, physiological data in biologging tags has mostly been obtained from electromyogram (EMG) and heart rate sensors.² Although there have been a few examples of bioanalyte measurements in extracted blood,³⁶⁻³⁸ the measurement of biomarkers in sampled fluid *ex vivo* offers limited

information and may introduce artefacts due to the capture and restraint of the animal.³⁵ CoPhMoRe sensors incorporated into animal-borne sensor tags have the potential to transform biologging studies by giving researchers continuous and real-time access to biomarkers reflecting the condition of free-living animals (Figure 3-1).^{39,40}

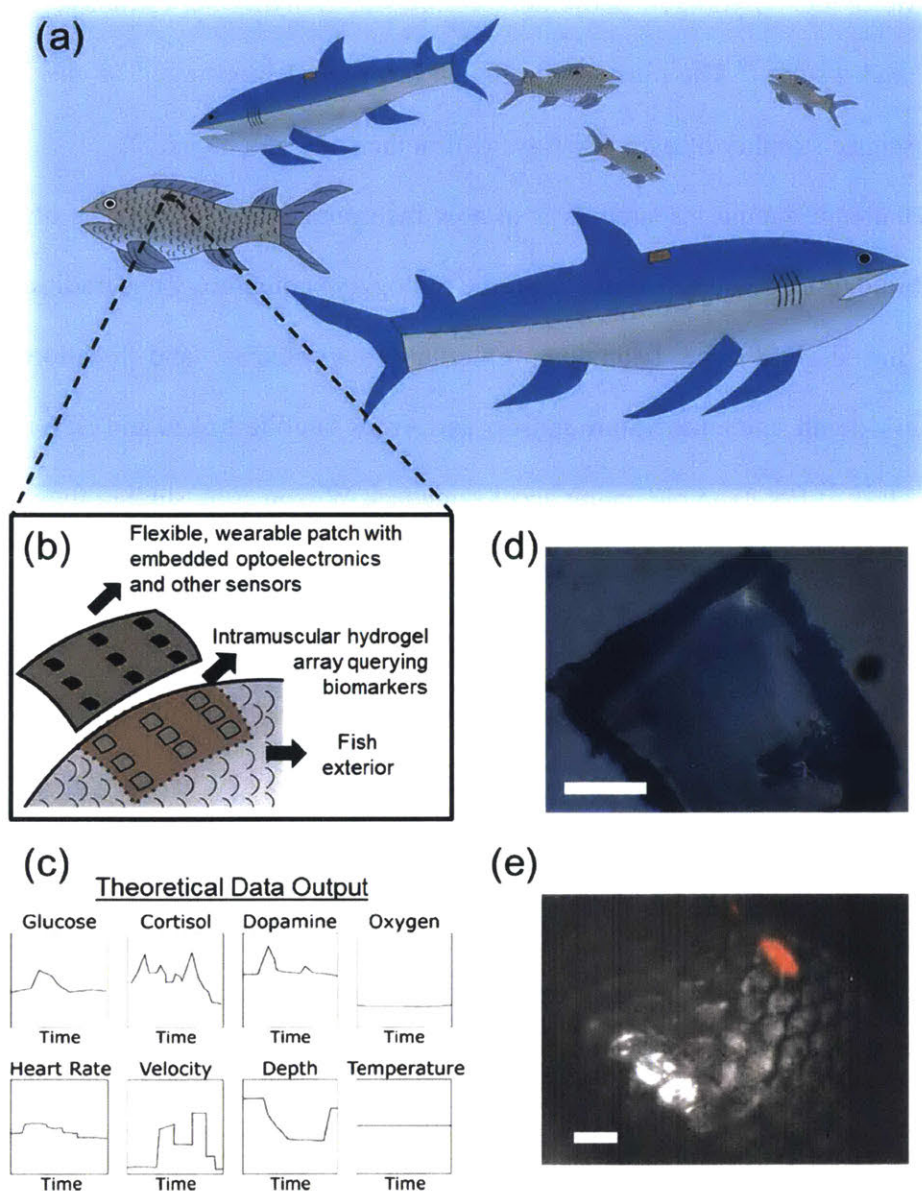


Figure 3-1: Vision for the future application of CoPhMoRe sensors to physiological biologging of marine organisms. (a) Animals of various sizes and ecological niches tagged with minimally invasive sensors collecting multivariate datasets continuously. (b) Theoretical design of a future biologging system. Hydrogel implants, encapsulating nanoparticles engineered to modulate their fluorescence in response to the local concentration of specific bioanalytes, are injected at a fixed depth in the intramuscular space, where they query biological fluid. Atop the fish's exterior is a flexible, wearable patch that contains embedded optoelectronics to

*excite and collect hydrogel fluorescence. The elastomer protects the electronic components from the surrounding aquatic environment, as well as conforms to the animal's movements. The device also incorporates other sensors to track animal movement and environmental conditions. The work herein describes the development of the hydrogel component of this theoretical device. (c) Theoretical data output of envisioned device. The device collects biochemical information and other animal-derived and environmental parameters such as velocity, depth, temperature, etc. (d) Visible image of SWNT-gels (scale = 0.5 mm). (e) Overlay of bright field image of sarasa comet goldfish (*Carassius auratus*) and fluorescence image of implanted hydrogel (scale = 10 mm).*

In this work, as a model sensor implant, we use DNA-wrapped SWNT that we have fabricated and encapsulated into a biocompatible poly(ethylene glycol diacrylate) (PEGDA) hydrogel and calibrated against riboflavin, an essential nutrient involved in oxidative phosphorylation.⁴¹ *In vitro* characterization and experiments with two species of marine organisms were performed at MIT, whereas experiments with an additional seven species were performed at Oceanogràfic in Valencia, Spain from January 30 – February 1, 2018. The implants were delivered via trocar to both recently deceased and living animals. The hydrogel detection limit with injection depth was determined, and the effects of tissue heterogeneity on fluorescence detection were explored. The three living animals showed no external signs of adverse health or behavioral changes one month after implantation. However, in the case of the turtle, some tissue reaction was detected upon dissection and histopathology. At MIT, analysis of goldfish swimming patterns indicated that the hydrogel implants do not impair animal movement. All together, these data indicate the feasibility of using CoPhMoRe sensors for marine organism biologging with further improvements to sensor detection limits, normalization of sensor signal to account for individual tissue optical properties, and wearable fluorescence device design.

Methods and Materials

Materials

(6,5)-enriched SWNTs produced by the CoMoCAT process (lot # MKBZ1159V) were purchased from Sigma Aldrich. Single-stranded (AC)₁₅ was purchased from Integrated DNA

Technologies, while PEGDA ($M_n = 8000$) was purchased from Alfa Aesar. Unless otherwise noted, other reagents were purchased from Sigma Aldrich.

Sensor fabrication

SWNT (1 mg/mL) and ss(AC)₁₅ (2 mg/mL) were mixed in 2 mL of 100 mM sodium chloride. The mixture was bath sonicated for 10 minutes, followed by sonication with a 3 mm probe at 4 W for 20 minutes (QSonica). The suspension was centrifuged at 32,000 rcf for 3 hours, and the top 80% of the supernatant was collected for further use. Free DNA was removed using 100 kDa MWCO centrifugal filters (Merck Millipore) with 5 volumetric replacements with 1x phosphate buffered saline (PBS). UV-Vis-NIR absorption spectra were collected to verify successful suspension. The SWNT mass concentration was calculated using the absorption value at 632 nm.

ssDNA-SWNT (0.1 mg/mL), PEGDA (100 mg/mL), and 2-hydroxy-4'-(2-hydroxyethoxy)-2-methylpropiophenone (0.175 mg/mL) were mixed in 1x PBS, cast into glass molds, and incubated for 30 minutes under a nitrogen atmosphere. The samples were then illuminated under 365 nm ultraviolet radiation (UVP Blak-Ray XX-15BLB, 15 W) for 60 minutes. The hydrogels were removed from the molds and incubated in excess 1x PBS for 48 hours to remove unreacted monomers and unencapsulated SWNT. The hydrogels were then incubated in fresh 1x PBS until further use.

In vitro characterization

UV-Vis-NIR absorption spectra were measured for both solution phase and hydrogel encapsulated ssDNA-SWNT (Shimadzu UV-3101PC). Fluorescence spectra were measured in a custom-built NIR microscope. Samples were illuminated using a 785 nm photodiode laser (B&W Tek. Inc.) and imaged using a Zeiss AxioVision inverted microscope with appropriate optical

filters. The fluorescence was passed through a Princeton Instruments Acton SP2500 spectrometer and measured using a liquid nitrogen cooled Princeton Instruments InGaAs 1D detector.

Riboflavin was used as a model analyte to test hydrogel chemical sensitivity *in vitro* and *ex vivo*. Hydrogels were cut into 5 x 5 x 1 mm sections and placed inside perfusion channels (ibidi μ -Slide III 3D Perfusion). Hydrogel fluorescence was monitored while varying the concentration of riboflavin in 1x PBS between 0 – 100 μ M at a flowrate of 0.3 mL/min. Fluorescence images were taken using a liquid nitrogen cooled Princeton Instruments InGaAs 2D detector. These measurements were also performed on a 5 x 5 x 2 mm section of hydrogel placed 1 mm below the surface of skin and muscle tissue of *Stenotomus chrysops*. A 500 μ L bolus of 100 μ M riboflavin was introduced atop of the hydrogel.

In vivo implantation

All procedures described below were approved by the animal ethics committee of the Fundaci3n Oceanogr3fic de la Comunitat Valenciana and performed at Oceanogr3fic over the duration of the experiments.

Prior to implantation, hydrogels were illuminated by UV light for 15 minutes and handled in a biological hood (Telstar AV-100) thereafter to ensure sterility. Hydrogels were cut to a 1 x 5 x 1 mm block and loaded into 12 gauge transponder needles from which the microchips were removed (Avid Suds Monoject).

The implantation procedure varied depending on the target organism. In the case of deceased animals, all animals were injected without further treatment of the skin. Hydrogels were placed at the desired location and penetration depth by using the needle length and angle of insertion as a guide.

A live European eel (*Anguilla anguilla*) was anesthetized prior to injection by submersion in a 70 mg/L benzocaine solution. When the eel was non-responsive, the injection site on the dorsal side was washed with sterile saline, and the hydrogel was injected. The eel was moved to new water and allowed to recover prior to further handling.

A live eastern river cooter (*Pseudemys concinna*) and catshark (*Scyliorhinus stellaris*) were restrained by animal care personnel for hydrogel implantations. The skin of the shark was washed with sterile saline, whereas the skin of the turtle was disinfected with iodopovidone. The hydrogel was injected subcutaneously in the dorsal area of the shark at the level of the second dorsal fin and in the dorsal part of the cranial tram of the turtle's neck.

After implantation, the animals were monitored for 2 months to determine tolerance to the implants and changes in swimming and feeding behavior. High-resolution ultrasound images of the implantation site were used to non-invasively study the impacts of implantation on tissues. After one month, the turtle was euthanized (for reasons not related to this study), allowing biopsies of the implantation site to be collected for histopathology.

Imaging using Raspberry Pi

The imaging system consisted of a Raspberry Pi 3 (Adafruit) with a 5 MP camera with the IR filter removed (SainSmart). The camera was placed inside of a 1 inch lens tube. The camera was used without further modification when taking brightfield images. The Picamera software package was used to control the camera.

When taking fluorescence images, the hydrogels were illuminated with a 200 mW 561 nm laser (Opto Engine LLC) passing through a collimator. Fluorescence passed through a 900 longpass filter prior to collection by the camera. Fluorescence was quantified by taking two images before and after hydrogel placement and calculating the difference in gray value in the region of

interest. For all images, the auto-white balance gains, exposure times, and shutter speed were set manually. The analog and digital gains were kept constant by equilibration of the camera for a one minute period.

Goldfish hydrogel implantations and motion tracking

All experimental details below and associated husbandry procedures were reviewed and approved by the Committee on Animal Care at MIT.

Two sarasa comet goldfish (*Carassius auratus*) were purchased from LiveAquaria, housed in a 110 liter glass aquarium with dimensions of 76 x 42 x 30 cm (length x width x height), and allowed to acclimate for at least two weeks prior to experimental manipulation. The water was maintained at 24 °C, and the aquarium was lit daily for 10 hours. Fish were fed daily with flake foods (TetraFin).

Prior to implantation, hydrogels were treated under UV light for 15 minutes and handled in a biological hood thereafter to ensure sterility. Hydrogels were cut to a 1 x 3 x 1 mm shape and loaded into 16 gauge needles. Fish were anesthetized in a solution of 60 mg/L tricaine methanesulfonate. When the fish were non-responsive to handling and a fin pinch, the hydrogels were injected into muscle just below the dorsal fin. The fish were allowed to recover in a holding tank before being returned to the home tank.

To determine the impact of the hydrogel implant on the animal's health, its movements were recorded using a surveillance system consisting of the Raspberry Pi 2 computer with a Raspberry Pi Camera Board v2. Fish movements were extracted using the Kinovea software.

After the experimental lifetime, the fish were euthanized by submersion into a 500 mg/L solution of tricaine methanesulfonate.

Results and Discussion

Sensor fabrication and in vitro optical characterization

DNA-wrapped SWNT have been utilized in many studies due to their high wrapping efficiency^{42,43} and flexibility in selective sensing of different analytes.^{25–27,30,44} The UV-Vis-NIR absorption spectrum (Figure 3-2a) shows distinct peaks, indicating successful nanoparticle suspension. Mass concentration of total carbon in the solution was estimated using an extinction coefficient of $\epsilon_{632\text{ nm}} = 0.036 \text{ (mg/L)}^{-1}\text{cm}^{-1}$.⁴⁵ Singly dispersed ss(AC)₁₅-SWNT nanoparticles were produced at a 36% yield based on a carbon mass balance. Peak position and relative peak intensities of ss(AC)₁₅-SWNT in solution phase or encapsulated in the hydrogel (SWNT-gel) were identical in both the absorption spectra and fluorescence emission spectra (Figure 3-2b), indicating that the dielectric environments surrounding the SWNT were nearly identical.^{46,47} The absorption spectrum of the SWNT-gel indicated a final concentration of 33 mg/L SWNT. However, the fluorescence intensity of the SWNT-gel was only 50% of the intensity in the equivalent concentration in solution phase. Sample geometry contributed to this decrease, as the hydrogels are only 1 mm in thickness, whereas liquid samples were typically 1 cm in height. Additionally, the chemical environment of the sensors in the hydrogel is different, in that the SWNT are diffusionally constrained by a polymer matrix. Free radicals that are generated during the photopolymerization of the hydrogel may have also chemically altered the DNA on the SWNT surface.

Characterization of SWNT-gel pore size

The hydrogel pore size formed by the spacing between cross-linked polymer chains is a critical parameter that controls sensor functionality and environment. The pores in the gel determine the size of the analyte that is permitted to enter the network, as well its rate of diffusion,

thereby affecting sensor response time.⁴⁸ The pore size can also be used to exclude large molecular weight interfering molecules to improve sensor selectivity. Furthermore, the hydrogel's pore diameter relative to nanoparticle size dictates the degree of nanoparticle entrapment.⁴⁹

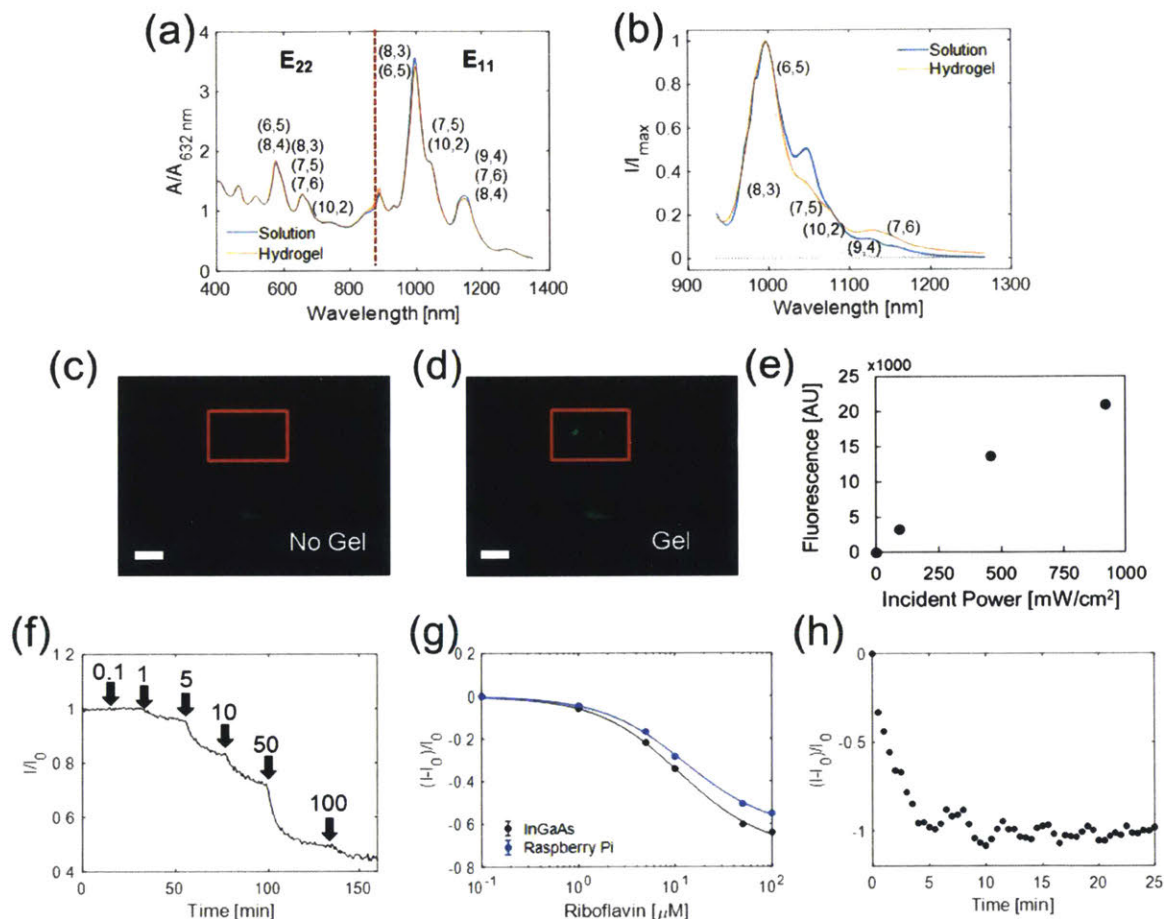


Figure 3-2: *In vitro* and *ex vivo* sensor characterization. (a) Normalized UV-Vis-NIR absorption spectra and (b) fluorescence emission spectrum at 785 nm excitation of ss(AC)₁₅-wrapped (6,5) CoMoCAT SWNT. Spectra were measured for solution phase SWNT and SWNT-gels. The absorption spectrum shows both the excitation (E₂₂) and fluorescence emission peaks (E₁₁) for the corresponding SWNT chiralities given in parentheses. The fluorescence spectrum was decomposed into individual peaks corresponding to the labeled SWNT chiralities. (c-d) Images taken with Raspberry Pi imaging setup (c) without and (d) with a SWNT-gel. (e) Hydrogel fluorescence increased with larger incident excitation power. (f) Fluorescence decreased with stepwise increases in riboflavin concentration between 1 to 100 μM, as measured by a Raspberry Pi camera. (g) Riboflavin calibration curves obtained with an InGaAs camera and the Raspberry Pi camera show good agreement. (h) SWNT-gel response to bolus injection of 100 μM riboflavin while placed 1 mm deep into *ex vivo* tissue sample of *Stenotomus chrysops*. The fluorescence decreased below the limit of detection of the Raspberry Pi camera.

Swelling experiments were performed in 1x PBS to obtain the average SWNT-gel pore size from the polymer network. The swelling ratio was determined using the following equation

$$Q = \frac{m_{\text{swollen}}}{m_{\text{dry}}} = \alpha^{-1} \quad (3-1)$$

where Q is the hydrogel swelling ratio and m is the hydrogel mass. Q can then be used to calculate the average pore diameter:^{50,51}

$$\bar{M}_c^{-1} = \frac{2}{\bar{M}_n} - \frac{(\bar{v}/V_2) [\ln(1-\alpha) + \alpha + \chi\alpha^2]}{\alpha^{1/3} - (2/\theta)\alpha} \quad (3-2)$$

$$\xi = \alpha^{-1/3} \left(\frac{2C_\infty l^2 \bar{M}_c}{M_0} \right)^{1/2} \quad (3-3)$$

where \bar{M}_c is the molecular weight between cross links, \bar{M}_n is the molecular weight of the polymers without crosslinking (=8000), \bar{v} is the specific volume of the polymer (=0.903 mL/g), V_2 is the specific volume of water (=18.01 mL/mol), χ is the Flory-Huggins parameter (=0.3765), θ is the functionality of PEGDA (= 4), ξ is the average mesh side, C_∞ is the Flory characteristic ratio (=6.9), l is the carbon-carbon bond length (=0.154 nm), and M_0 is the molar mass of the repeat unit (=44.05 g/mol). The Flory parameter was obtained from a previous study of PEG polymers.⁵² The average pore size was estimated to be 15 nm.

Raspberry Pi Imaging Systems

To understand the range of organism-environment interactions and document variation among individuals and populations, some biologging studies have deployed sensors on anywhere from dozens to hundreds of animals.^{7,53} To this end, some laboratory instruments are not practical due to their prohibitive cost for large-scale deployment, immobility, and fragility on a moving animal in its natural environment. For example, InGaAs cameras typically used to measure near infrared fluorophores can weigh on the order of 5 kg and can cost thousands of dollars.^{9,24,29} Consequently, we chose to use inexpensive and portable Raspberry Pi computers and cameras

which costs on the order of tens of dollars. In the real application, the components of a Raspberry Pi imaging system can be readily incorporated into a miniaturized sensor suite. Recently, Göröcs et al. incorporated a similar CMOS image sensor into a portable imaging device weighing less than 40 grams.⁵⁴

Because the optical sensors on the cameras are fabricated from silicon, which have limited sensitivity (< 0.1 A/W above 980 nm) to the near infrared fluorescence of SWNT (Figure 3-3), we first verified that the hydrogels could be visualized by our system (Figure 3-2c-d). Analysis showed a linear trend of hydrogel fluorescence with incident laser power density (Figure 3-2e).

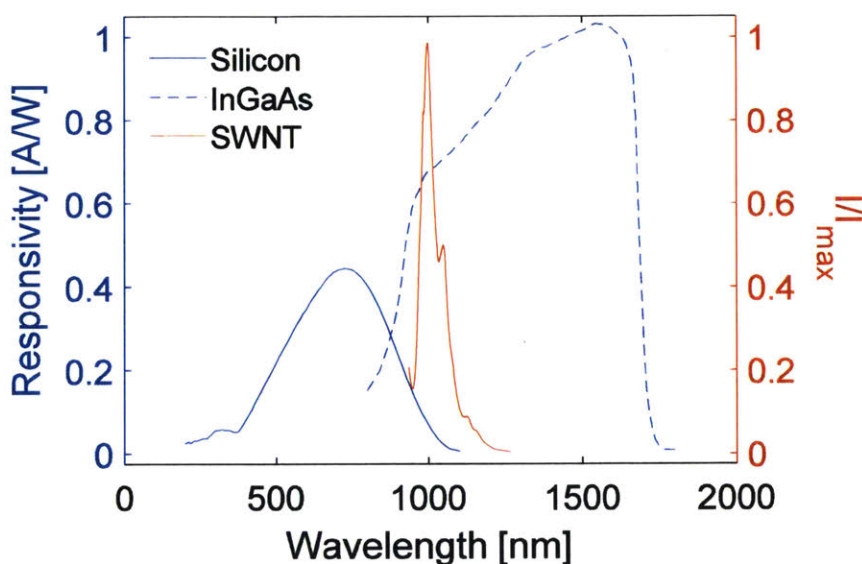


Figure 3-3: Photoresponsivity of silicon and InGaAs photodetectors compared to CoMoCAT (6,5) SWNT fluorescence. Photoresponsivity data adapted from ThorLabs products PDA10A2 and PDA015C.^{55,56}

Riboflavin as a model analyte for chemical sensing *in vitro* and *ex vivo*

Riboflavin plays a key role in the recycling of FADH and FAD⁺ in oxidative phosphorylation and is an essential nutrient in a fish's diet.^{41,57} Riboflavin exists in plasma typically between 1- 100 nM.^{58,59} Furthermore, DNA oligonucleotides of various sequences, when complexed to SWNTs, allow for a nIR fluorescence modulation in response to riboflavin binding via both intensity quenching and wavelength shifts,⁹ making it an ideal model analyte to evaluate *in vivo* sensing feasibility.

The SWNT-gels showed stepwise decreases in fluorescence with stepwise increases in surrounding riboflavin concentration, with sensitivity from 1- 100 μM (Figure 3-2f). The calibration curves were fit to the following functional form:

$$\text{Response} = \frac{I - I_0}{I_0} = \beta \frac{C}{C + K_D} \quad (3-4)$$

where β is the gain, C is the riboflavin concentration, and K_D is the equilibrium dissociation constant. To evaluate the performance of the Raspberry Pi relative to typical laboratory equipment, we compared results obtained with a Princeton Instrument 2D InGaAs camera. The calibration curves showed good agreement (Figure 3-2g). For the InGaAs camera, β was -0.72, and K_D was 11.3 μM , while the corresponding values were -0.63 and 12.7 μM for the Raspberry Pi. The difference in maximum response is a product of higher background signal in the Raspberry Pi, which partially masked the fluorescence quenching of the riboflavin. Future versions of the sensor tag will be designed to eliminate such interference by optimizing optical configurations and increase the sensitivity to detect physiological levels of riboflavin.

Furthermore, the fluorescence of the SWNT-gels decreased in response to a bolus of 100 μM when placed in a 1 mm thick skin and muscle tissue sample of *Stenotomus chrysops* (Figure 3-2h). The fluorescence decreased below the detection limit of the Raspberry Pi camera.

Optical Penetration Depth

We constructed a simplified, 1-D mathematical model to describe the effects of material, tissue, and equipment properties on the optical signal from a sensor implanted into tissue. Incident excitation light is partially reflected from the epidermal interface:

$$I_0 = I_i (1 - r_{ex}) \quad (3-5)$$

where I_i and I_o are the incident and transmitted excitation fluences, respectively, and r_{ex} is the epidermal reflectivity at the excitation wavelength. Tissue further attenuates excitation light according to the Beer-Lambert law:

$$\log\left(\frac{I_o}{I}\right) = \gamma_{ex} d \quad (3-6)$$

where I is the fluence at the implantation site, γ_{ex} is the tissue extinction coefficient at the excitation wavelength, and d is distance through tissue. The fluorescence intensity of the hydrogel at the implantation site is described by

$$\log\left(1 - \frac{F_o}{\eta IA}\right) = -\epsilon_{ex} ct \quad (3-7)$$

where F_o is the fluorescence intensity at the implantation site, η is the quantum efficiency of SWNT, A is the cross-sectional area of the hydrogel, ϵ_{ex} is the extinction coefficient of SWNT at the excitation wavelength, c is the concentration of SWNT in the hydrogel, and t is the hydrogel thickness. The thickness of the hydrogel is assumed to be negligible compared to the implantation depth. The fluorescence reaching the surface of the epidermis is given by the following equation:

$$\log\left(\frac{F_o}{F}\right) = \gamma_{em} d \quad (3-8)$$

where F is the fluorescence reaching the epidermal interface, γ_{em} is the tissue extinction coefficient at the emission wavelength. Back-reflection of fluorescence may occur at the epidermal interface:

$$F_f = F(1 - r_{em}) \quad (3-9)$$

where F_f is the fluorescence exiting the tissue and r_{em} is the reflectivity at the fluorescent wavelength. Assuming minimal scattering and absorption between the epidermal surface and the photodetector, the measured signal is described by

$$S = F_f R \quad (3-10)$$

where S is the signal, and R is the responsivity of the camera. Combining Eqs. 5-10 yields

$$\log\left(\frac{S}{\eta A R I_i (1-r_{ex})(1-r_{em})}\right) = \log(1-10^{\epsilon_{ex} c t}) - d(\gamma_{ex} + \gamma_{em}) \quad (3-11)$$

The terms in Eq. (3-11) can be classified into material, tissue, and equipment properties and tunable engineering parameters. The specific fluorophore dictates the value of η and ϵ_{ex} . Different tissues attenuate light transmission to varying extents and consequently have unique values of γ , which may be measured in a future study via light transmission measurements. Both absorption and scattering contribute to the extinction coefficient. Scattering decreases with increasing incident wavelength,⁶⁰ while absorption is largely determined by water and blood absorption, which is minimal in the SWNT fluorescent region.⁶¹ Furthermore, unlike organic fluorophores, SWNT do not photobleach and thus exhibit a constant c as long as the implant maintains its integrity. Thus, the near infrared fluorescence of SWNT is ideal for an *in vivo* optical biosensor due to the lack of photobleaching and the transparency of the near infrared window.^{62,63} Controllable parameters include I_i , A , c , t , r , and d . Increased hydrogel thickness, fluorophore concentration, equipment responsivity, and excitation power and decreased implantation depth increase the fluorescence signal. In a previous study, Iverson et al. measured the fluorescence of an alginate hydrogel with 10 mg/L SWNT to a depth of 5 mm in tissue phantoms using a hyperspectral CRI Maestro system.⁶⁴

For this application, consideration of the marine organism tissue properties is critical. Many fish species, including teleosts, have evolved skin containing significant amounts of reflective guanine crystals in the stratum argenteum and underneath the scales, which may camouflage the animal against predators.⁶⁵ The reflective spectra of such biomaterials have been

thoroughly characterized in previous work.⁶⁶ These different skin types will affect the penetration of light through tissue. Others, such as sharks and marine reptiles, have evolved thick, mechanically stiff skin and/or scales as protection against environmental hazards, which may require specialized methods of placing implantable devices.⁶⁷ All together, these factors suggest that each species should be considered individually when using implantable nIR fluorescent hydrogel sensors for biologging.

Two deceased teleosts (*Sparus aurata* and *Stenotomus chrysops*), a female adult catshark (*Galeus melastormus*) were used for the nIR penetration versus depth study. The teleosts were chosen because over 32,500 species exist, making them the largest category of vertebrates.⁶⁸ Furthermore, catsharks comprise over 10% of extant cartilaginous fish.⁶⁹ Images were taken of the fish before and after placement of the hydrogel using the Raspberry Pi camera system (Figure 3-4a-b). Movement of the animal relative to the imaging setup was minimized such that differences in signal between the two images is predominantly the hydrogel, not position change. In *Sparus aurata*, the nIR fluorescent SWNT-gels were detected up to a depth of 7 mm (Figure 3-4c). Injection of sham non-fluorescent hydrogels using the same method verified that the difference in signal due to movement was negligible compared to the additional signal from the fluorescence. The residual signal is a small change in laser reflection from a small shift in position of the fish tissue. The SWNT-gels also exhibited stable fluorescence (Figure 3-4d). This stability is critical, so that perturbations can be attributed solely to changes in analyte concentrations. For *Stenotomus chrysops* and *Galeus melastormus* (Figure 3-4e-g), the SWNT-gels were detected again to a depth of 7 mm over a minimum signal difference threshold determined by injection of a non-fluorescent hydrogel (Figure 3-4g). A simplified version of eqn. (3-11) was used to fit the data and reproduced the trends.

$$S = a \cdot 10^{b \cdot d + c} \quad (3-12)$$

where S is the signal, t is the tissue thickness, and the fit parameters are a , b , and c . The fit parameters are reported in Table 3-1.

Table 3-1: Fit parameters for optical penetration depth study in marine organisms.

Species	a	b	c
<i>Sparus aurata</i>	6.5	-0.96	5.2
<i>Galeus melastomus</i>	1.6	-0.48	6.2
<i>Stenotomus chrysops</i>	47.5	-0.12	5.1

As can be seen in Figure 3-4c, Figure 3-4e, and Figure 3-4g, there was not a monotonic decrease in fluorescence with increasing depth. We attribute the noise to variations in hydrogel thickness, cross-sectional area, placement at the intended depth, and position relative to the excitation source. As illustrated by Eqn. (3-11), variations in geometry and placement of the SWNT-gels necessarily change the signal by reducing the excitation power incident on the hydrogel and changing the attenuation distance of the excitation and fluorescence through tissue.

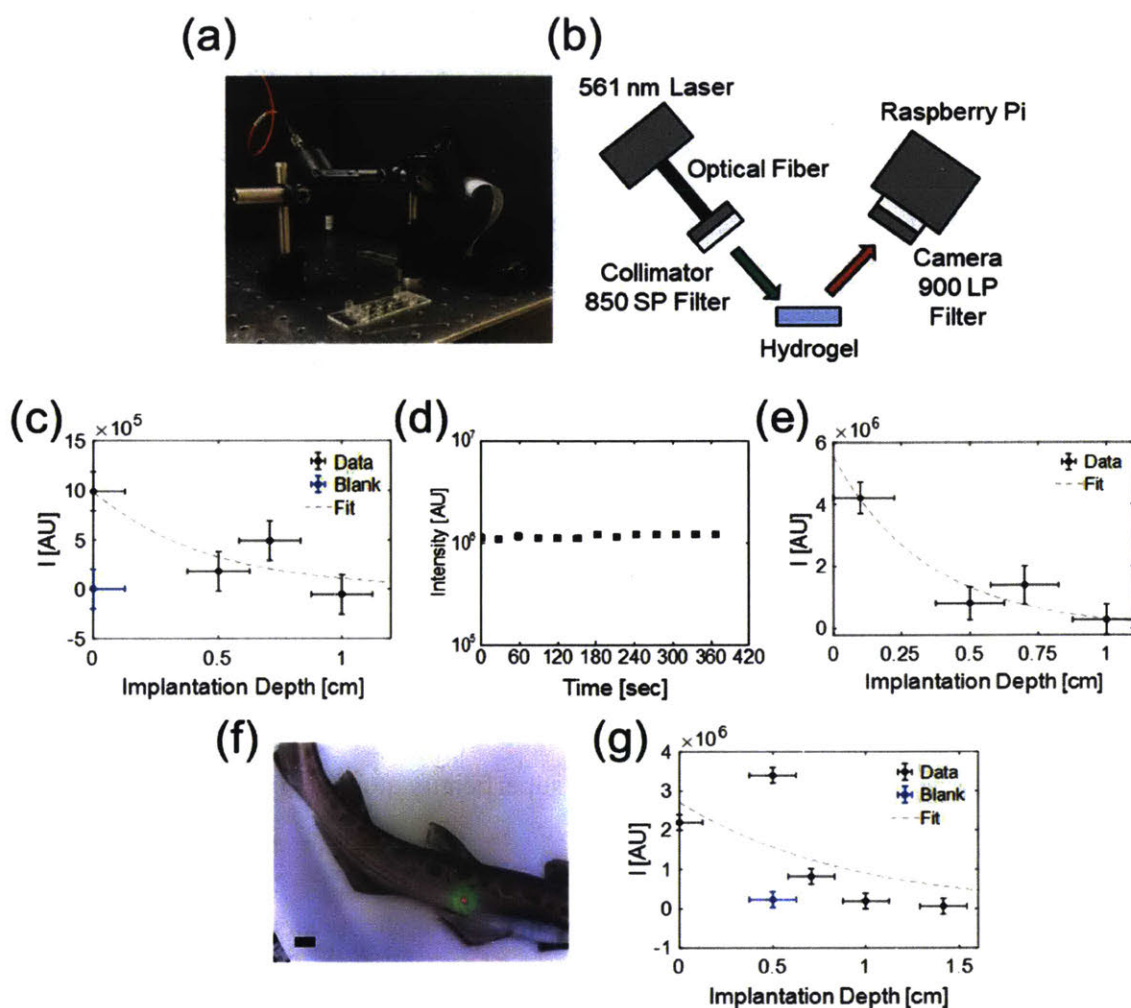


Figure 3-4: Effect of hydrogel implantation depth on fluorescence detection in teleosts (*Sparus aurata* and *Stenotomus chrysops*) and cat shark (*Galeus melastomus*). (a-b) Imaging setup and schematic. A fiber-coupled 561 nm laser fitted with an 850 shortpass filter was used to illuminate the implantation site before and after intramuscular delivery of hydrogels into previously deceased animals via trocar. The signal was collected by a Raspberry Pi camera connected to a 900 longpass filter. The difference in gray values with and without the hydrogel was calculated. (c) In *Sparus aurata*, detectable hydrogel fluorescence decreased as injection depth was increased from just below the skin down to a limit of 0.7 cm. A non-fluorescent hydrogel was injected just superficially below the skin and imaged to give the threshold difference in intensity for the signal to be attributable to the hydrogel and not to other artefacts, such as movement of the fish relative to the laser. (d) A superficially implanted SWNT-gel in *Sparus aurata* exhibited a steady fluorescence signal when imaged over 6 minutes. (e) The detection limit of SWNT-gels in *Stenotomus chrysops* was 0.7 cm. (f) Overlay of brightfield and fluorescence images of a fluorescent hydrogel implanted 0.5 cm below the skin in *Galeus melastomus* [scale = 20 mm]. (g) SWNT-gels were detected down to a depth of 0.7 cm in *Galeus melastomus*, as compared to a non-fluorescent hydrogel implanted at a depth of 0.5 cm.

Although the penetration depth of the SWNT sensors in the target species were similar to that of previous studies,⁶⁴ the maximum depth can be increased using several approaches. First, the excitation and fluorescence detection equipment can be optimized specifically for SWNT-

based biosensors. An InGaAs photodetector, which has almost an order of magnitude higher photoresponsivity (0.67 A/W at 1000 nm) may replace the silicon-based camera (0.067 A/W at 1000 nm) used in this study (Figure 3-3). This equipment, along with other optical components such as lenses, can be attached directly to the animal instead of being placed at standoff distances, thus reducing the optical path length, optimizing excitation and fluorescence collection, and increasing signal. Alternatively, optical fibers may be implanted transdermally, in the form of an optode, to couple the excitation source directly with the hydrogel and the hydrogel with the photodetector.⁷⁰

Ultimately, placement of the sensor could be influenced by other factors in addition to optical penetration depth, including local analyte concentration and sensor sensitivity. Many analytes of interest, such as glucose, cortisol, and vitamins, exist in interstitial fluids and can be theoretically queried with a hydrogel implanted superficially atop the hypodermis.⁷¹

Tissue Heterogeneity

Different color patterns of tissue and mechanically distinct exteriors may exist on the skin of the same animal, which may affect hydrogel implantation and/or fluorescence visibility. To examine this issue, we implanted hydrogels in different skin tissues of a juvenile female sea turtle (*Caretta caretta*) and a juvenile male blue shark (*Prionace glauca*). The sea turtle had both scaly and fleshy regions of the skin,⁶⁷ whereas the blue shark had distinctly colored regions ranging from dark blue to white.⁷²

SWNT-gels were delivered in both the front right leg and the flesh centered underneath the neck of the sea turtle (Figure 3-5a-b). As the needle could not pierce the scales, it was inserted between them. The neck flesh was stretched prior to hydrogel placement to prevent folding of additional skin on top of the implant, avoiding artificial increases in the optical path length. The

hydrogel was not visible beneath the scales but was visible beneath the fleshy skin of the neck (Figure 3-5c). SWNT-gel sensors were placed underneath the white and dark sections of shark's epidermis, and a non-fluorescent hydrogel was placed into a gray area to provide a baseline against which nIR fluorescent hydrogels could be compared (Figure 3-5d-f). The nIR fluorescent hydrogel was visible beneath the white but not the dark-colored epidermis (Figure 3-5g).

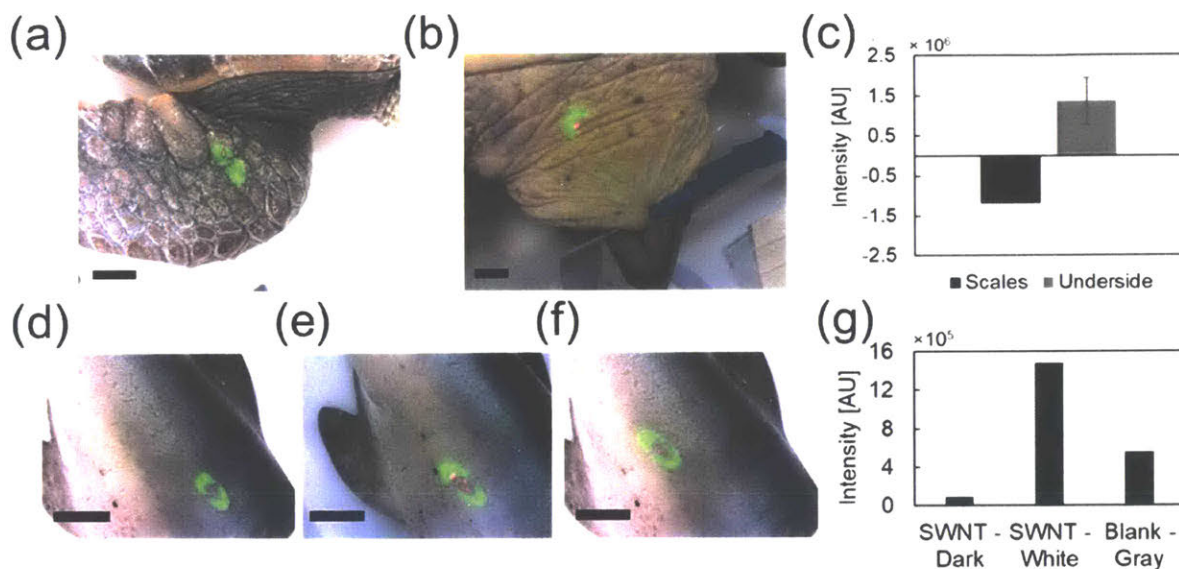


Figure 3-5: Detection of fluorescent hydrogels implanted superficially in optically heterogeneous tissues. Fluorescent hydrogels were implanted into (a) the scaly legs and (b) softer flesh beneath the neck of a sea turtle (*Caretta caretta*) (scale = 20 mm). (c) Hydrogel fluorescence was detected in the neck but not the scaly legs. SWNT-gels were implanted subcutaneously in (d) dark and (e) white regions of a blue shark (*Prionace glauca*). A non-fluorescent hydrogel was implanted in (f) gray region of the tissue. (g) Fluorescence could be detected underneath white skin but not dark skin. The blank hydrogel in the gray region provided a baseline against which to determine fluorescence detection. Scale in all images is 20 mm.

In both organisms, dark sections of tissue masked the nIR fluorescence of the sensor implants. Increased melanin levels in the epidermis result in higher absorption coefficients up to 1100 nm^{73,74} resulting in less excitation of the hydrogel and transmission of (6,5) SWNT fluorescence by increasing the values of γ_{ex} and γ_{em} in Eqn. 11. UV-Vis-NIR absorption measurements of tissue samples can quantify these wavelength / tissue dependent effects in a future study.

These results indicate two additional requirements for nIR fluorescent biosensors for *in vivo* applications. First, to maximize the signal-to-noise ratio, sensors should be delivered to tissues that are as optically transparent as possible for both the excitation and emission wavelengths. Furthermore, sensor fluorescence may have to be normalized against an invariant internal standard to eliminate the effects of tissue heterogeneity.⁴⁴ Second, to deliver hydrogels via a minimally invasive injection, some tissue sections will be inaccessible due to their mechanical strength and rigidity.

Imaging and sensor operation in live animals

Several questions regarding tolerance/biocompatibility of the implant and its effects on behavior can only be answered using living animals. A moving animal also adds greater complexity when imaging which may require reconfigurations of the sensor.

A female adult European eel (*Anguilla anguilla*), a female adult eastern river cooter (*Pseudemmys concinna*), and a juvenile male catshark (*Scyliorhinus stellaris*) were tagged with sensor hydrogels and monitored for up to 2 months. We attempted to image the eel and turtle in a small bucket from a distance of 0.5 m, but were unsuccessful for several reasons (Figure 3-6a-c). First, the camera and excitation sources were moved farther away to image the entire field of view. This reduced both the excitation power density incident upon the surface of the epidermis from 150 to 0.3 mW/cm² and consequently the fluorescence upon the camera's sensor by a factor of at least 500, according to Eqn. (3-11). Furthermore, the combination of a long exposure time and animal movement apparently blurred the images.

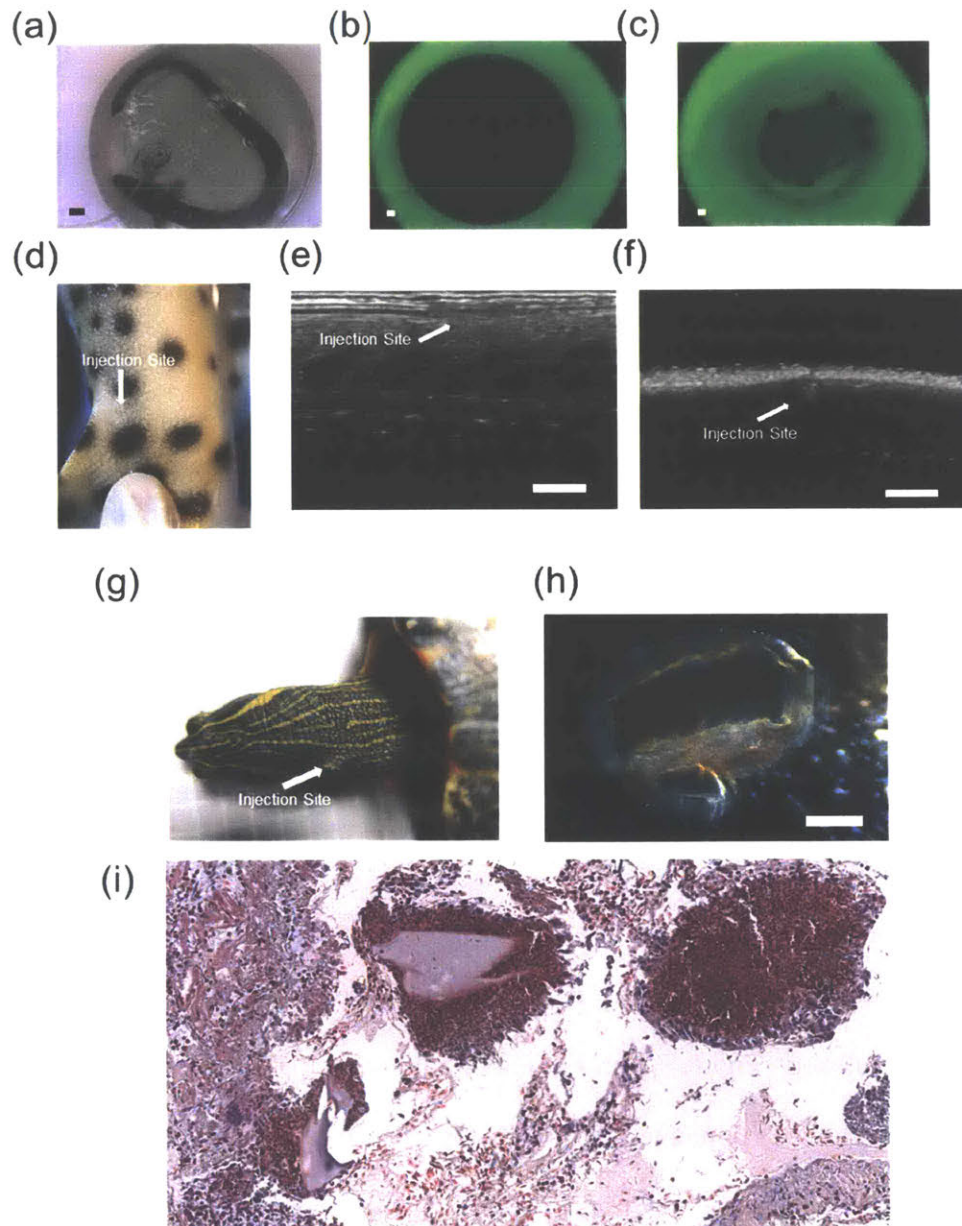


Figure 3-6: NIR fluorescent hydrogels implanted in a living European eel (*Anguilla anguilla*), eastern river cooter (*Pseudemmys concinna*), and catshark (*Scyliorhinus stellaris*). (a) Following implantation, attempts were made to track the fluorescence in the eel and turtle confined to a small space. (b-c) Dispersed laser excitation, animal movement, and long exposure times made these attempts unsuccessful in (b) the eel and (c) the turtle. All scalebars are 20 mm. (d) The implantation site fully healed in the catshark by 33 days post-implantation. (e-f) High resolution ultrasound images were taken to examine noninvasively tissue response to the implant 4 weeks after implantation in the (e) eel and (f) catshark (scale = 5 mm). The absence of significant changes in tissue architecture and echogenicity indicates that the hydrogels were well-tolerated in these organisms. (g) The injection site in the turtle did not heal completely 33 days post-implantation. (h) Hydrogels were removed from the turtle after 33 days and were found to be encapsulated by tissue. (i) Histology images from subcutaneous tissue surrounding the hydrogel implant in the turtle indicate a foreign body tissue reaction.

Engineering Design for nIR Fluorescent Hydrogel Implants

A central goal of the current work is to utilize these findings to design sensing hydrogel implants. A wearable fluorescence reader that conforms to the animal's body as it moves is necessary.⁷⁵ Fixing the position of the measurement unit relative to the SWNT-gels eliminates changes in hydrogel fluorescence due to a changing excitation field and/or misalignment of the hydrogel and camera. Furthermore, placing the measurement device directly on top of the hydrogel reduces the optical path length, increasing the signal-to-noise ratio. As such, the miniaturization into and attachment methods of a flexible form factor are critical next steps.

Biocompatibility of the hydrogel was favorable in two of the three animals. We found no changes in movement or feeding behavior of the eel and catshark for two months post-implantation (Figure 3-6d). In the ultrasound images, the implantation site was identified via a slight change in tissue structure and echogenicity, but the surrounding tissue was completely normal (Figure 3-6e-f). In the case of a significant foreign body reaction, larger changes in architecture and echogenicity would be found in the periphery of the implant as it becomes encapsulated.^{76,77} In contrast, histopathology suggested that the turtle experienced some reaction to the implant. The injection site did not heal cleanly (Figure 3-6g). It is important to note that there may have been an infection of the wound following implantation, precluding clean healing. Granules containing hydrogel fragments were extracted from the implantation site one month after the procedure (Figure 3-6h). H&E stained tissue sections showed infiltration of inflammatory cells into the deep dermis, hypodermis, and cutaneous muscle. The infiltrate consisted of heterophiles, macrophages, and several multinucleated giant cells, consistent with panniculitis and a foreign body reaction to the implant (Figure 3-6i). However, no behavioral changes were noted in the turtle.

A similar implantation procedure was performed on adult Sarasa comet goldfish (*Carassius auratus*), and its movement patterns were analyzed relative to a control goldfish without an implant (Figure 3-7a). Animal trajectories and position histograms did not differ significantly between the two animals, indicating that the hydrogel implants do not adversely impact animal health (Figure 6b-f). During times of stress or infections, the fish may swim violently or erratically. In the case of serious illness, fish movement would slow severely.^{78,79} The video data and position histograms (Figure 3-7c-f) show that the subject fish showed neither erratic movement nor stationary behavior relative to the control. The absence of other abnormalities, such as damaged fins, disinterest in food, and discoloration, further indicate that the fish tolerated the implant well.⁸⁰ Furthermore, goldfish were maintained up to six months with the hydrogel implant, indicating long-term biocompatibility.

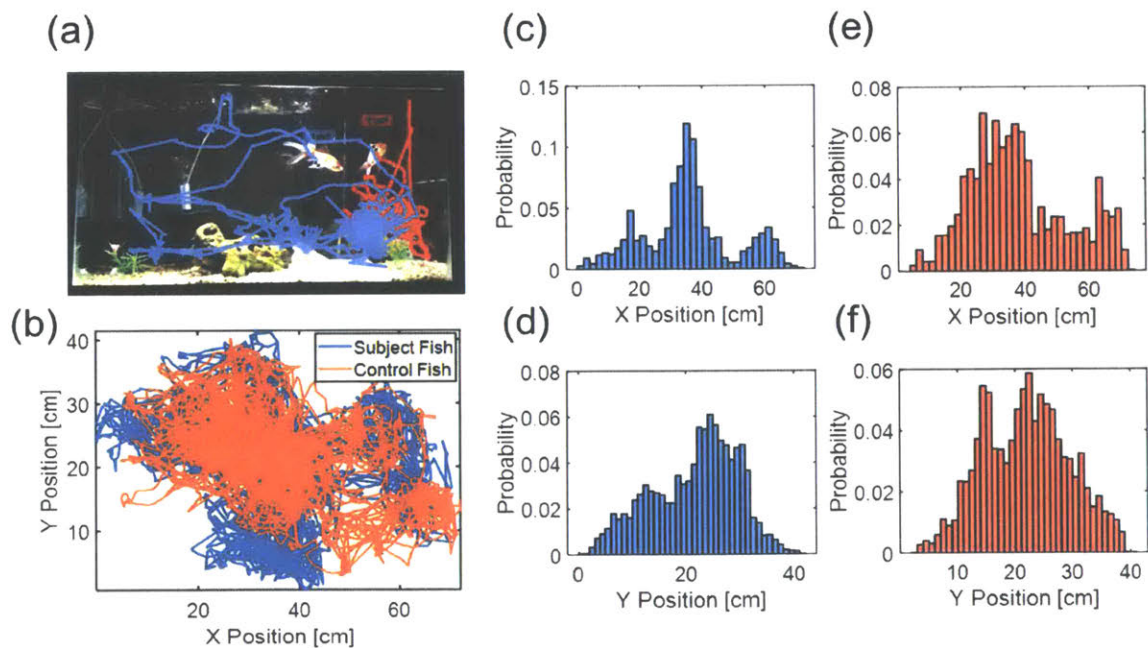


Figure 3-7: Quantification of hydrogel implant impact on animal health. (a) Snapshot of the capture video with corresponding sarasa comet goldfish (*Carassius auratus*) movement trajectories included. Blue corresponds to a fish in which a nIR fluorescent hydrogel was implanted, while orange corresponds to a control fish without a hydrogel implant. (b) Trajectories of fish taken for one hour 2 days after a hydrogel was implanted into the subject fish. (c-d) X and Y position histograms for the subject fish (c-d) and control fish (e-f). The subject fish experienced neither impaired movement nor erratic movement due to the hydrogel implant, indicating good tolerance of the implant.

These results effectively form a pilot study that can be used to direct and prioritize future work involving larger sample sizes, a greater diversity of species, optimization of the hydrogel and delivery method, and development of a wearable fluorescence reader.

Conclusions

In summary, the feasibility of applying CoPhMoRe sensors for the physiological biologging of marine organisms was demonstrated in nine species of aquatic vertebrates. Future work will perform similar tissue penetration, tissue heterogeneity, and biocompatibility studies with a larger number of animals to probe phenotypic diversity. Strategies to normalize sensor signals against individual implant site optical properties and internal fluorescent standards will be explored to create absolute inter-species calibrations. Ratiometric approaches to optical sensing will mitigate movement and other artefacts that may confound the signal.⁴⁴ The successful measurement of the fluorescent hydrogels using an inexpensive, field portable Raspberry Pi imaging setup motivates further efforts to design a wearable, flexible sensor tag that integrates optoelectronic components tailored for physiological biologging using SWNT-gels. These technical improvements may improve the signal-to-noise ratio, time resolution of the measurements, and stability of the signal when attached to a moving animal. In parallel, the underlying SWNT nanosensors may be engineered to be sensitive to a wider range of bioanalytes to investigate a wider range of physiological states. The detection range of the riboflavin sensor described herein will be further improved to be sensitive to the physiologically relevant range. This work advances the application of biosensors into animals beyond the commonly used rodent and zebrafish models and carves a path towards the physiological biologging of aquatic organisms.

References

- (1) McIntyre, T. Trends in tagging of marine mammals: a review of marine mammal biologging studies. *African J. Mar. Sci.* **2014**, *36* (4), 409–422 DOI: 10.2989/1814232X.2014.976655.
- (2) Cooke, S. J.; Brownscombe, J. W.; Raby, G. D.; Broell, F.; Hinch, S. G.; Clark, T. D.; Semmens, J. M. Remote bioenergetics measurements in wild fish: Opportunities and challenges. *Comp. Biochem. Physiol. -Part A Mol. Integr. Physiol.* **2016**, *202*, 23–37 DOI: 10.1016/j.cbpa.2016.03.022.
- (3) Watanabe, Y. Y.; Ito, M.; Takahashi, A. Testing optimal foraging theory in a penguin–krill system. *Proc. R. Soc. B Biol. Sci.* **2014**, *281* (1779), 20132376.
- (4) Amélineau, F.; Fort, J.; Mathewson, P. D.; Speirs, D. C.; Courbin, N.; Perret, S.; Porter, W. P.; Wilson, R. J.; Grémillet, D. Energyscapes and prey fields shape a North Atlantic seabird wintering hotspot under climate change. *R. Soc. Open Sci.* **2018**, *5*, 171883 DOI: 10.1098/rsos.171883.
- (5) Barnett, A.; Payne, N. L.; Semmens, J. M.; Fitzpatrick, R. Ecotourism increases the field metabolic rate of whitetip reef sharks. *Biol. Conserv.* **2016**, *199*, 132–136 DOI: 10.1016/j.biocon.2016.05.009.
- (6) Baylis, A. M. M.; Orben, R. A.; Arnould, J. P. Y.; Peters, K.; Knox, T.; Costa, D. P.; Staniland, I. J. Diving deeper into individual foraging specializations of a large marine predator, the southern sea lion. *Oecologia* **2015**, *179* (4), 1053–1065 DOI: 10.1007/s00442-015-3421-4.
- (7) Hays, G. C.; Scott, R. Global patterns for upper ceilings on migration distance in sea turtles and comparisons with fish, birds and mammals. *Funct. Ecol.* **2013**, *27* (3), 748–756 DOI: 10.1111/1365-2435.12073.

- (8) Yasuda, T.; Kawabe, R.; Takahashi, T.; Murata, H.; Kurita, Y.; Nakatsuka, N.; Arai, N. Habitat shifts in relation to the reproduction of Japanese flounder *Paralichthys olivaceus* revealed by a depth-temperature data logger. *J. Exp. Mar. Bio. Ecol.* **2010**, *385* (1–2), 50–58 DOI: 10.1016/j.jembe.2010.02.001.
- (9) Zhang, J.; Landry, M. P.; Barone, P. W.; Kim, J.-H.; Lin, S.; Ulissi, Z. W.; Lin, D.; Mu, B.; Boghossian, A. A.; Hilmer, A. J.; et al. Molecular recognition using corona phase complexes made of synthetic polymers adsorbed on carbon nanotubes. *Nat. Nanotechnol.* **2013**, *8* (12), 959–968 DOI: 10.1038/nnano.2013.236.
- (10) Wu, D.; Sedgwick, A. C.; Gunnlaugsson, T.; Akkaya, E. U.; Yoon, J.; James, T. D. Fluorescent chemosensors: the past, present and future. *Chem. Soc. Rev.* **2017**, *46* (23), 7105–7123 DOI: 10.1039/C7CS00240H.
- (11) Xiao, T.; Wu, F.; Hao, J.; Zhang, M.; Yu, P.; Mao, L. In Vivo Analysis with Electrochemical Sensors and Biosensors. *Anal. Chem.* **2017**, *89* (1), 300–313 DOI: 10.1021/acs.analchem.6b04308.
- (12) Sun, W.; Guo, S.; Hu, C.; Fan, J.; Peng, X. Recent Development of Chemosensors Based on Cyanine Platforms. *Chem. Rev.* **2016**, *116* (14), 7768–7817 DOI: 10.1021/acs.chemrev.6b00001.
- (13) Soto, R. J.; Hall, J. R.; Brown, M. D.; Taylor, J. B.; Schoenfisch, M. H. In Vivo Chemical Sensors: Role of Biocompatibility on Performance and Utility. *Anal. Chem.* **2017**, *89* (1), 276–299 DOI: 10.1021/acs.analchem.6b04251.
- (14) Rong, G.; Corrie, S. R.; Clark, H. A. In Vivo Biosensing: Progress and Perspectives. *ACS Sensors* **2017**, *2* (3), 327–338 DOI: 10.1021/acssensors.6b00834.
- (15) Howes, P. D.; Chandrawati, R.; Stevens, M. M. Colloidal nanoparticles as advanced

- biological sensors. *Science* (80-.). **2014**, *346* (6205), 1247390 DOI: 10.1126/science.1247390.
- (16) Carter, K. P.; Young, A. M.; Palmer, A. E. Fluorescent sensors for measuring metal ions in living systems. *Chem. Rev.* **2014**, *114* (8), 4564–4601 DOI: 10.1021/cr400546e.
- (17) Scholten, K.; Meng, E. A review of implantable biosensors for closed-loop glucose control and other drug delivery applications. *Int. J. Pharm.* **2018**, *544* (2), 319–334 DOI: <https://doi.org/10.1016/j.ijpharm.2018.02.022>.
- (18) Cotruvo Joseph A., J.; Aron, A. T.; Ramos-Torres, K. M.; Chang, C. J. Synthetic fluorescent probes for studying copper in biological systems. *Chem. Soc. Rev.* **2015**, *44* (13), 4400–4414 DOI: 10.1039/C4CS00346B.
- (19) Sun, K.; Yang, Y.; Zhou, H.; Yin, S.; Qin, W.; Yu, J.; Chiu, D. T.; Yuan, Z.; Zhang, X.; Wu, C. Ultrabright Polymer-Dot Transducer Enabled Wireless Glucose Monitoring via a Smartphone. *ACS Nano* **2018**, *12* (6), 5176–5184 DOI: 10.1021/acsnano.8b02188.
- (20) Deng, B.; Ren, M.; Kong, X.; Zhou, K.; Lin, W. Development of an enhanced turn-on fluorescent HOCl probe with a large Stokes shift and its use for imaging HOCl in cells and zebrafish. *Sensors Actuators B Chem.* **2018**, *255*, 963–969 DOI: <https://doi.org/10.1016/j.snb.2017.08.146>.
- (21) Gurkov, A.; Sadovoy, A.; Shchapova, E.; Teh, C.; Meglinski, I.; Timofeyev, M. Microencapsulated fluorescent pH probe as implantable sensor for monitoring the physiological state of fish embryos. *PLoS One* **2017**, *12* (10), e0186548.
- (22) Ferreira, N. R.; Ledo, A.; Laranjinha, J.; Gerhardt, G. A.; Barbosa, R. M. Simultaneous measurements of ascorbate and glutamate in vivo in the rat brain using carbon fiber nanocomposite sensors and microbiosensor arrays. *Bioelectrochemistry* **2018**, *121*, 142–

150 DOI: <https://doi.org/10.1016/j.bioelechem.2018.01.009>.

- (23) Mehrotra, P. Biosensors and their applications - A review. *J. Oral Biol. Craniofacial Res.* **2016**, *6* (2), 153–159 DOI: 10.1016/j.jobcr.2015.12.002.
- (24) Bisker, G.; Dong, J.; Park, H. D.; Iverson, N. M.; Ahn, J.; Nelson, J. T.; Landry, M. P.; Kruss, S.; Strano, M. S. Protein-targeted corona phase molecular recognition. *Nat. Commun.* **2016**, *7*, 10241 DOI: 10.1038/ncomms10241.
- (25) Zhang, J. Q.; Boghossian, A. A.; Barone, P. W.; Rwei, A.; Kim, J. H.; Lin, D. H.; Heller, D. A.; Hilmer, A. J.; Nair, N.; Reuel, N. F.; et al. Single Molecule Detection of Nitric Oxide Enabled by d(AT)(15) DNA Adsorbed to Near Infrared Fluorescent Single-Walled Carbon Nanotubes. *J. Am. Chem. Soc.* **2011**, *133* (3), 567–581 DOI: 10.1021/ja1084942.
- (26) Jin, H.; Heller, D. a; Kalbacova, M.; Kim, J.-H.; Zhang, J.; Boghossian, A. a; Maheshri, N.; Strano, M. S. Detection of single-molecule H₂O₂ signalling from epidermal growth factor receptor using fluorescent single-walled carbon nanotubes. *Nat. Nanotechnol.* **2010**, *5* (4), 302–309 DOI: 10.1038/nnano.2010.24.
- (27) Kruss, S.; Landry, M. P.; Vander Ende, E.; Lima, B. M. A.; Reuel, N. F.; Zhang, J.; Nelson, J.; Mu, B.; Hilmer, A.; Strano, M. Neurotransmitter detection using corona phase molecular recognition on fluorescent single-walled carbon nanotube sensors. *J. Am. Chem. Soc.* **2014**, *136* (2), 713–724 DOI: 10.1021/ja410433b.
- (28) Kruss, S.; Salem, D. P.; Vuković, L.; Lima, B.; Vander Ende, E.; Boyden, E. S.; Strano, M. S. High-resolution imaging of cellular dopamine efflux using a fluorescent nanosensor array. *Proc. Natl. Acad. Sci.* **2017**, *114* (8), 1789–1794 DOI: 10.1073/pnas.1613541114.
- (29) Bisker, G.; Bakh, N. A.; Lee, M. A.; Ahn, J.; Park, M.; O’Connell, E. B.; Iverson, N. M.; Strano, M. S. Insulin Detection Using a Corona Phase Molecular Recognition Site on

- Single-Walled Carbon Nanotubes. *ACS Sensors* **2018**, *3* (2), 367–377 DOI: 10.1021/acssensors.7b00788.
- (30) Iverson, N. M.; Barone, P. W.; Shandell, M.; Trudel, L. J.; Sen, S.; Sen, F.; Ivanov, V.; Atolia, E.; Farias, E.; McNicholas, T. P.; et al. In vivo biosensing via tissue-localizable near-infrared-fluorescent single-walled carbon nanotubes. *Nat. Nanotechnol.* **2013**, *8* (11), 873–880 DOI: 10.1038/nnano.2013.222.
- (31) Hays, G. C.; Ferreira, L. C.; Sequeira, A. M. M.; Meekan, M. G.; Duarte, C. M.; Bailey, H.; Bailleul, F.; Bowen, W. D.; Caley, M. J.; Costa, D. P.; et al. Key Questions in Marine Megafauna Movement Ecology. *Trends Ecol. Evol.* **2016**, *31* (6), 463–475 DOI: 10.1016/j.tree.2016.02.015.
- (32) Payne, N. L.; Taylor, M. D.; Watanabe, Y. Y.; Semmens, J. M. From physiology to physics: are we recognizing the flexibility of biologging tools? *J. Exp. Biol.* **2014**, *217* (3), 317–322 DOI: 10.1242/jeb.093922.
- (33) Wilson, R. P.; Gómez-Laich, A.; Sala, J. E.; Dell’Omo, G.; Holton, M. D.; Quintana, F. Long necks enhance and constrain foraging capacity in aquatic vertebrates. *Proc. R. Soc. B Biol. Sci.* **2017**, *284* (1867), 20172072 DOI: 10.1098/rspb.2017.2072.
- (34) Meekan, M. G.; Fuiman, L. A.; Davis, R.; Berger, Y.; Thums, M. Swimming strategy and body plan of the world’s largest fish: implications for foraging efficiency and thermoregulation. *Front. Mar. Sci.* **2015**, *2*, 64 DOI: 10.3389/fmars.2015.00064.
- (35) Lee, M. A.; Bakh, N.; Bisker, G.; Brown, E. N.; Strano, M. S. A Pharmacokinetic Model of a Tissue Implantable Cortisol Sensor. *Adv. Healthc. Mater.* **2016**, *5* (23), 3004–3015 DOI: 10.1002/adhm.201600650.
- (36) Pon, L. B.; Hinch, S. G.; Cooke, S. J.; Patterson, D. A.; Farrell, A. P. Physiological,

- energetic and behavioural correlates of successful fishway passage of adult sockeye salmon *Oncorhynchus nerka* in the Seton River, British Columbia. *J. Fish Biol.* **2009**, *74* (6), 1323–1336 DOI: 10.1111/j.1095-8649.2009.02213.x.
- (37) Crossin, G. T.; Takahashi, A.; Sakamoto, K. Q.; Trathan, P. N.; Williams, T. D. Habitat selection by foraging macaroni penguins correlates with hematocrit, an index of aerobic condition. *Mar. Ecol. Prog. Ser.* **2015**, *530*, 163–176 DOI: 10.3354/meps11320.
- (38) O’Toole, A. C.; Dechraoui Bottein, M. Y.; Danylchuk, A. J.; Ramsdell, J. S.; Cooke, S. J. Linking ciguatera poisoning to spatial ecology of fish: A novel approach to examining the distribution of biotoxin levels in the great barracuda by combining non-lethal blood sampling and biotelemetry. *Sci. Total Environ.* **2012**, *427–428*, 98–105 DOI: 10.1016/j.scitotenv.2011.11.053.
- (39) Kruss, S.; Hilmer, A. J.; Zhang, J.; Reuel, N. F.; Mu, B.; Strano, M. S. Carbon nanotubes as optical biomedical sensors. *Adv. Drug Deliv. Rev.* **2013**, *65* (15), 1933–1950 DOI: 10.1016/j.addr.2013.07.015.
- (40) Bisker, G.; Iverson, N. M.; Ahn, J.; Strano, M. S. A pharmacokinetic model of a tissue implantable insulin sensor. *Adv. Healthc. Mater.* **2015**, *4* (1), 87–97 DOI: 10.1002/adhm.201400264.
- (41) Massey, V. The Chemical and Biological Versatility of Riboflavin. *Biochem. Soc. Trans.* **2000**, *28* (4), 283–296 DOI: 10.1042/bst0280283.
- (42) Nakashima, N.; Okuzono, S.; Murakami, H.; Nakai, T.; Yoshikawa, K. DNA Dissolves Single-walled Carbon Nanotubes in Water. *Chem. Lett.* **2003**, *32* (5), 456–457 DOI: 10.1246/cl.2003.456.
- (43) Zheng, M.; Jagota, A.; Semke, E. D.; Diner, B. A.; McLean, R. S.; Lustig, S. R.; Richardson,

- R. E.; Tassi, N. G. DNA-assisted dispersion and separation of carbon nanotubes. *Nat. Mater.* **2003**, *2* (5), 338–342 DOI: 10.1038/nmat877.
- (44) Giraldo, J. P.; Landry, M. P.; Kwak, S. Y.; Jain, R. M.; Wong, M. H.; Iverson, N. M.; Ben-Naim, M.; Strano, M. S. A Ratiometric Sensor Using Single Chirality Near-Infrared Fluorescent Carbon Nanotubes: Application to in Vivo Monitoring. *Small* **2015**, *11* (32), 3973–3984 DOI: 10.1002/smll.201403276.
- (45) Zhang, J.; Kruss, S.; Hilmer, A. J.; Shimizu, S.; Schmois, Z.; De La Cruz, F.; Barone, P. W.; Reuel, N. F.; Heller, D. A.; Strano, M. S. A Rapid, Direct, Quantitative, and Label-Free Detector of Cardiac Biomarker Troponin T Using Near-Infrared Fluorescent Single-Walled Carbon Nanotube Sensors. *Adv. Healthc. Mater.* **2014**, *3* (3), 412–423 DOI: 10.1002/adhm.201300033.
- (46) Larsen, B. A.; Deria, P.; Holt, J. M.; Stanton, I. N.; Heben, M. J.; Therien, M. J.; Blackburn, J. L. Effect of solvent polarity and electrophilicity on quantum yields and solvatochromic shifts of single-walled carbon nanotube photoluminescence. *J. Am. Chem. Soc.* **2012**, *134* (30), 12485–12491 DOI: 10.1021/ja2114618.
- (47) Choi, J. H.; Strano, M. S. Solvatochromism in single-walled carbon nanotubes. *Appl. Phys. Lett.* **2007**, *90* (22), 88–91 DOI: 10.1063/1.2745228.
- (48) Tokarev, I.; Minko, S. Stimuli-responsive porous hydrogels at interfaces for molecular filtration, separation, controlled release, and gating in capsules and membranes. *Adv. Mater.* **2010**, *22* (31), 3446–3462 DOI: 10.1002/adma.201000165.
- (49) Zhao, F.; Yao, D.; Guo, R.; Deng, L.; Dong, A.; Zhang, J. Composites of Polymer Hydrogels and Nanoparticulate Systems for Biomedical and Pharmaceutical Applications. *Nanomaterials* **2015**, *5* (4), 2054–2130 DOI: 10.3390/nano5042054.

- (50) Peppas, N. A.; Huang, Y.; Torres-Lugo, M.; Ward, J. H.; Zhang, J. Physicochemical Foundations and Structural Design of Hydrogels in Medicine and Biology. *Annu. Rev. Biomed. Eng.* **2000**, *2* (1), 9–29 DOI: 10.1146/annurev.bioeng.2.1.9.
- (51) Peppas, N. A.; Hilt, J. Z.; Khademhosseini, A.; Langer, R. Hydrogels in biology and medicine: From molecular principles to bionanotechnology. *Adv. Mater.* **2006**, *18* (11), 1345–1360 DOI: 10.1002/adma.200501612.
- (52) Pedersen, J. S.; Sommer, C. Temperature dependence of the virial coefficients and the chi parameter in semi-dilute solutions of PEG. *Prog. Colloid Polym. Sci.* **2005**, *130*, 70–78 DOI: 10.1007/b107350.
- (53) Hays, G. C.; Bastian, T.; Doyle, T. K.; Fossette, S.; Gleiss, A. C.; Gravenor, M. B.; Hobson, V. J.; Humphries, N. E.; Lilley, M. K. S.; Pade, N. G.; et al. High activity and Levy searches: jellyfish can search the water column like fish. *Proc. R. Soc. B Biol. Sci.* **2012**, *279* (1728), 465–473 DOI: 10.1098/rspb.2011.0978.
- (54) Göröcs, Z.; Rivenson, Y.; Ceylan Koydemir, H.; Tseng, D.; Troy, T. L.; Demas, V.; Ozcan, A. Quantitative Fluorescence Sensing Through Highly Autofluorescent, Scattering, and Absorbing Media Using Mobile Microscopy. *ACS Nano* **2016**, *10* (9), 8989–8999 DOI: 10.1021/acsnano.6b05129.
- (55) ThorLabs. PDA10A2 - Si Fixed Gain Detector
<https://www.thorlabs.com/thorproduct.cfm?partnumber=PDA10A2> (accessed May 1, 2018).
- (56) ThorLabs. PDA015C - InGaAs Fixed Gain Amplified Detector
<https://www.thorlabs.com/thorproduct.cfm?partnumber=PDA015C> (accessed May 1, 2018).

- (57) Lim, C.; Leamaster, B.; Brock, J. A. Riboflavin Requirement of Fingerling Red Hybrid Tilapia Grown in Seawater. *J. World Aquac. Soc.* **1993**, *24* (4), 451–458 DOI: 10.1111/j.1749-7345.1993.tb00573.x.
- (58) Petteys, B. J.; Frank, E. L. Rapid determination of vitamin B2 (riboflavin) in plasma by HPLC. *Clin. Chim. Acta* **2011**, *412* (1), 38–43 DOI: <https://doi.org/10.1016/j.cca.2010.08.037>.
- (59) Yao, Y.; Yonezawa, A.; Yoshimatsu, H.; Omura, T.; Masuda, S.; Matsubara, K. Involvement of riboflavin transporter RFVT2/Slc52a2 in hepatic homeostasis of riboflavin in mice. *Eur. J. Pharmacol.* **2013**, *714* (1), 281–287 DOI: <https://doi.org/10.1016/j.ejphar.2013.07.042>.
- (60) Bashkatov, A. N.; Genina, E. A.; Kochubey, V. I.; Tuchin, V. V. Optical properties of human skin, subcutaneous and mucous tissues in the wavelength range from 400 to 2000 nm. *J. Phys. D. Appl. Phys.* **2005**, *38* (15), 2543–2555 DOI: 10.1088/0022-3727/38/15/004.
- (61) Smith, A. M.; Mancini, M. C.; Nie, S. Bioimaging: Second window for in vivo imaging. *Nature Nanotechnology*. 2009, pp 710–711.
- (62) Welsher, K.; Liu, Z.; Sherlock, S. P.; Robinson, J. T.; Chen, Z.; Darancioglu, D.; Dai, H. A route to brightly fluorescent carbon nanotubes for near-infrared imaging in mice. *Nat. Nanotechnol.* **2009**, *4* (11), 773–780 DOI: 10.1038/nnano.2009.294.
- (63) Luo, S.; Zhang, E.; Su, Y.; Cheng, T.; Shi, C. A review of NIR dyes in cancer targeting and imaging. *Biomaterials* **2011**, *32* (29), 7127–7138 DOI: 10.1016/j.biomaterials.2011.06.024.
- (64) Iverson, N. M.; Bisker, G.; Farias, E.; Ivanov, V.; Ahn, J.; Wogan, G. N.; Strano, M. S. Quantitative tissue spectroscopy of near infrared fluorescent nanosensor implants. *J. Biomed. Nanotechnol.* **2016**, *12* (5), 1035–1047 DOI: 10.1166/jbn.2016.2237.

- (65) Hawkes, J. W. The structure of fish skin. *Cell Tissue Res.* **1974**, *149* (713), 147–158 DOI: 10.1007/BF00222271.
- (66) Jordan, T. M.; Partridge, J. C.; Roberts, N. W. Non-polarizing broadband multilayer reflectors in fish. *Nat. Photonics* **2012**, *6* (11), 759–763 DOI: 10.1038/nphoton.2012.260.
- (67) Spotila, J. R. *Sea Turtles: A Complete Guide to Their Biology, Behavior, and Conservation*; Johns Hopkins University Press: Baltimore, 2004.
- (68) Ng, K.-C. C.; Ooi, A.-C. P. A review of fish taxonomy conventions and species identification techniques. *J. Surv. Fish. Sci.* **2017**, *4* (1), 54–93 DOI: 10.18331/SFS2017.4.1.6.
- (69) Human, B. A.; Owen, E. P.; Compagno, L. J. V; Harley, E. H. Testing morphologically based phylogenetic theories within the cartilaginous fishes with molecular data, with special reference to the catshark family (Chondrichthyes; Scyliorhinidae) and the interrelationships within them. *Mol. Phylogenet. Evol.* **2006**, *39* (2), 384–391 DOI: 10.1016/j.ympev.2005.09.009.
- (70) Kosoglu, M. A.; Hood, R. L.; Chen, Y.; Xu, Y.; Rylander, M. N.; Rylander, C. G. Fiber Optic Microneedles for Transdermal Light Delivery: Ex Vivo Porcine Skin Penetration Experiments. *J. Biomech. Eng.* **2010**, *132* (9), 91014–91017.
- (71) Matzeu, G.; Florea, L.; Diamond, D. Advances in wearable chemical sensor design for monitoring biological fluids. *Sensors Actuators, B Chem.* **2015**, *211*, 403–418 DOI: 10.1016/j.snb.2015.01.077.
- (72) Allaby, M. Carcharhinidae. In *A Dictionary of Zoology*; Oxford University Press, 2009.
- (73) Jacques, S. L. Optical properties of biological tissues: A review. *Phys. Med. Biol.* **2013**, *58* (11) DOI: 10.1088/0031-9155/58/11/R37.

- (74) Anderson, R. R.; Parrish, J. A. The optics of human skin. *J. Invest. Dermatol.* **1981**, *77* (1), 13–19 DOI: 10.1111/1523-1747.ep12479191.
- (75) Nassar, J. M.; Khan, S. M.; Velling, S. J.; Diaz-Gaxiola, A.; Shaikh, S. F.; Gerald, N. R.; Torres Sevilla, G. A.; Duarte, C. M.; Hussain, M. M. Compliant lightweight non-invasive standalone “Marine Skin” tagging system. *npj Flex. Electron.* **2018**, *2* (1), 13 DOI: 10.1038/s41528-018-0025-1.
- (76) Ando, A.; Hatori, M.; Hagiwara, Y.; Isefuku, S.; Itoi, E. Imaging features of foreign body granuloma in the lower extremities mimicking a soft tissue neoplasm. *Ups. J. Med. Sci.* **2009**, *114* (1), 46–51 DOI: 10.1080/03009730802602455.
- (77) Anderson, J. M.; Rodriguez, A.; Chang, D. T. Foreign body reaction to biomaterials. *Semin. Immunol.* **2008**, *20* (2), 86–100 DOI: 10.1016/j.smim.2007.11.004.
- (78) Adelman, J. S.; Martin, L. B. Vertebrate sickness behaviors: Adaptive and integrated neuroendocrine immune responses. *Integr. Comp. Biol.* **2009**, *49* (3), 202–214.
- (79) Ashley, P. J.; Sneddon, L. U. Pain and Fear in Fish. In *Fish Welfare*; Branson, E. J., Ed.; Blackwell, 2008; pp 49–77.
- (80) Stoskopf, M. K. Biology and Management of Laboratory Fishes. In *Laboratory Animal Medicine*; Anderson, L. C., Otto, G. M., Pritchett-Corning, K. R., Whary, M. T. B. T., Eds.; Academic Press: Boston, 2015; pp 1063–1086.

Chapter 4 : In-Vivo Bio-sensing of Human Steroid Hormones using Corona Phase Molecular Recognition (CoPhMoRe) and nIR Fluorescent Single Walled Carbon Nanotubes

This chapter is adapted from a manuscript in preparation.

Introduction

Steroid signaling pathways control critical aspects of human physiology, including cortisol for the stress response, progesterone for female fertility, and testosterone for androgenic traits. Steroid hormones are also implicated in a broad array of medical conditions and pathologies, including cortisol in Cushing's disease and mental illnesses and aldosterone for adrenal cancer and irregular blood pressure. Real time, dynamic measurements of these important analytes *in vivo* may significantly deepen our understanding of steroid biochemistry, leading to new diagnoses and therapeutic approaches, but these measurements are limited by the availability of specific molecular recognition sites for sensor development. In this work, we apply a synthetic approach of Corona Phase Molecular Recognition (CoPhMoRe) to generate near infrared fluorescent sensors for progesterone and cortisol based on selection from a styrene and acrylic acid copolymer library augmented with an acrylated steroid, shown to self-template the corona phase as a novel CoPhMoRE strategy introduced in this work. Sensors exhibit excellent stability in sensor response from 1 to 200 μM with reversibility upon repeated analyte cycling, yielding K_D values of 100 for progesterone. We show that molecular recognition using such constructs is possible even *in vivo* after sensor implantation into a murine model by employing a poly(ethylene glycol) diacrylate

(PEGDA) hydrogel and porous cellulose interface to limit non-specific absorption. The results demonstrate that synthetic molecular recognition strategies such as CoPhMoRe are sufficiently robust to enable a new class of continuous, *in vivo* biosensors for insight into steroid signaling, potentially enabling new diagnostic and therapeutic approaches.

Steroid hormones are essential components in numerous metabolic pathways dictating macromolecule metabolism,¹ homeostasis,² reproduction,³ inflammation,^{4,5} among many others.⁶ Consequently, dysfunction in the synthesis, signaling pathways, and degradation of these molecules are key mechanisms by which various diseases act.^{7,8} Steroid hormone levels are often measured as biomarkers for these diseases,⁹ though the exact biochemical mechanisms remain a central focus of basic research.¹⁰⁻¹⁴ Furthermore, steroids are regularly administered as therapeutics, requiring specific dosage amounts and timing based on individual patient characteristics.⁶ *In vivo* sensors capable of providing real-time information on steroid levels could enable faster, more accurate medical diagnoses, elucidate biochemical mechanisms of disease, and enhance therapeutic interventions through real-time feedback on efficacy. Such sensors necessarily require molecular recognition sites that remains stable within the harsh implant environment. It remains an open question whether synthetic molecular recognition constructs can demonstrate such stability to address this problem. In this work, we focus our study on newly synthesized interfaces for cortisol and progesterone recognition using Corona Phase Molecular Recognition, showing that they enable steroid detection *in vivo* within a mouse model.

As regulators of gene expression, steroids control a number of processes dictating physiological and pathological mechanisms in the human body. Steroids exist in the blood between 0-500 nM, with roughly 90% of the steroids being bound to carrier proteins such as corticosteroid binding globulin (transcortin),¹⁵ sex-binding globulin,¹⁶ and serum albumin.¹⁷ Free steroids

passively diffuse from the circulation into the interstitial spaces and eventually the intracellular space, where they bind to their receptors and act as transcription factors.⁶ In these compartments, steroids typically exist at 0-50 nM.¹⁵ Steroids may also induce non-genomic effects by interaction with membrane proteins.¹⁸

Among the most important steroids include cortisol and progesterone (Figure 4-1). Cortisol is the primary stress hormone that plays a key role in the stress response, macromolecular metabolism, and inflammation.¹⁵ Cortisol is a key marker for various diseases, including Cushing's syndrome, Addison's disease, and various types of cancers.^{19,20} Furthermore, cortisol has been studied as a possible biomarker for neuropsychiatric diseases, including major depression,²¹ post-traumatic stress disorder,²² and bipolar disorder.²³ The World Health Organization reports that approximately 300 million people worldwide suffered from depression in 2015.²⁴ A variety of assays are being developed for cortisol, including a recently reported point-of-care lateral flow assay utilizing aptamer-conjugated gold nanoparticles.²⁵ Progesterone dictates processes regarding female sexual traits, including differentiation, fertility, menstruation, and pregnancy.²⁶ The dysregulation of progesterone signaling pathways delineates certain classes of female cancers, including breast.²⁷ These diseases are both deadly and widespread, occurring in approximately 1 in 8 women with a mortality rate of 40,000 per year.²⁸ Progesterone has also been a target for sensor development, including a recently reported amperometric sensor based on multi-layer graphene covered tungsten trioxide nanoball electrodes.²⁹

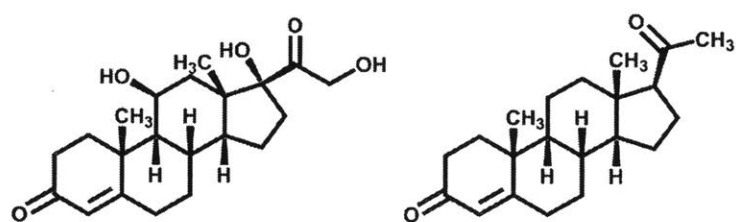


Figure 4-1: Molecular structures of cortisol (left) and progesterone (right)

Measurements of steroids are central to the treatment of these diseases and others. Initial diagnosis involves the identification of aberrant steroid levels. Subsequent measurements determine the efficacy and dictate further course of treatment. For example, immunotherapies have emerged as promising candidates for the treatment of various types of cancer.³⁰ However, the administration of such drugs may cause undesired immune-related adverse events (IRAEs),³¹ such as hepatitis, auto-immune diabetes, and hypothyroidism, which are subsequently treated by anti-inflammatory glucocorticoids. The glucocorticoids are typically administered over several weeks, with the dosages adjusted over time to account for individual patient traits and the stage of therapy.³² However, a balance exists between tempering the immune response enough to resolve the IRAEs but not excessively such that the immunotherapy becomes ineffective.³¹ To account for tumor and patient heterogeneity, this balance would be facilitated by quantitative feedback with high temporal resolution, motivating an *in vivo* sensor in order to manipulate dosages as needed.

In another example, patients with adrenal insufficiency consume glucocorticoid replacement drugs multiple times daily, with each dose being slightly different to account for the natural diurnal pattern of cortisol.³³ Over-replacement and under-replacement are possible outcomes of erroneous dosages, resulting in undesired conditions such as exogenous Cushing's syndrome.³⁴ Glucocorticoids are also used to treat osteoarthritis, various autoimmune diseases such as ulcerative colitis, and other inflammatory disorders.³⁵⁻³⁷ Additionally, steroids other than glucocorticoids are being investigated for their therapeutic potential, including sex hormones for lung diseases,³⁸ Alzheimer's disease,³⁹ and various types of cancers.⁴⁰⁻⁴²

Clearly, smarter drug delivery schemes, in which dosage timing and size are controlled by existing levels of steroids in the body and consider the patients themselves, require real-time *in vivo* sensors continuously querying and reporting the levels of biomarkers. The current standard

of measurement involves sampling blood and using chromatography or immunoassays.⁴³ However, these methods are too labor-intensive, costly, and lack the temporal resolution for real-time feedback.⁴⁴ Furthermore, in the case of cortisol, endogenous production involve a diurnal pattern, as well as stochastic release, such that single measurements fail to capture the complete profile.¹⁵

New technologies for point-of-care steroids have been developed extensively. We point readers to excellent reviews regarding sensors based on molecular imprinting, aptamers, and antibodies.⁴⁴⁻⁴⁸ While point-of-care sensors have their utility in a number of important medical applications, the lack of direct access to the *in vivo* environment represents significant delay time and inconvenience to the patient. Such configurational weaknesses reduce the temporal resolution of the measurements and may also adversely affect patient compliance with the measurement protocols.¹⁵

Conversely, in the literature, there exist only a few examples of true *in vivo* steroid/steroid derivative sensors, which have direct access to biological fluids through either an injection or implantation. Takase et al. coupled cholesterol oxidase and an implantable electrode to monitor the cholesterol level in eye interstitial fluid in fish for 48 hours.⁴⁹ Cook measured cortisol in sheep and cattle using an electrochemical immunosensor implanted into the jugular veins.⁵⁰ Cook also used a microdialysis probe coupled to an immunosensor implanted in the amygdala of sheep to measure cortisol.⁵¹ Sunwoo et al. implanted an enzyme-conjugated electrode into mice's adrenal glands to measure cortisol.⁵²

In vivo steroid detection remains a challenging problem, but Corona Phase Molecular Recognition (CoPhMoRe) has emerged as a promising solution to create implantable nanosensors capable of *in vivo* measurements. In this technique, synthetic molecular recognition sites are created by non-covalently dispersing fluorescent single walled carbon nanotubes (SWNT) with

polymers of controlled composition, whose configuration on the nanoparticle excludes most molecules from interacting with the SWNT. Signal transduction is built into the nanoparticle as changes in the SWNT fluorescence spectrum. SWNT are particularly advantageous for long-term, spatiotemporal monitoring because they fluoresce in the tissue transparency window and do not have photobleaching.⁵³ Furthermore, the selectivity of the sensors can be tuned by modifying the suspending polymer. Previous CoPhMoRe sensors have included dopamine,^{54,55} riboflavin, L-thyroxine, estradiol,⁵⁶ nitric oxide,^{57,58} fibrinogen,⁵⁹ and insulin.⁶⁰ The nitric oxide sensor has been used *in vivo* and shown to maintain its fluorescence stability over 400 days⁵³

CoPhMoRe has shown its versatility in the recognition of various classes of molecules with remarkable structural diversity, which make the technique an appealing choice for a steroid sensor. Some questions remain, however. While there have been some efforts to establish design principles between polymer dispersant structure and corresponding CoPhMoRe sensor structure,⁶¹⁻⁶³ to date, CoPhMoRe sensors have been discovered empirically, utilizing dispersants known to suspend SWNT well but not with a clear structural correlate to the target analyte. Furthermore, while CoPhMoRe has been shown to differentiate between molecules with wildly different structures, it has not yet been used within a class of molecules that have only slight variations on a structural motif. Last, a CoPhMoRe sensor based on synthetic polymers has not yet been taken from the first step of design to the end of an *in vivo* demonstration. The work in this chapter addresses all of these questions. We introduce novel CoPhMoRe sensors for steroids that were fabricated by non-covalently functionalizing SWNT with polymers incorporating template steroid molecules in a semi-rational manner. Compositional variants of the styrene, acrylic acid, template steroid polymers were synthesized, coupled to SWNT, and screened against a panel of steroid hormone chosen for their physiological and/or therapeutic significance. Selective fluorescent responses are

found for cortisol and progesterone. The progesterone sensor was encapsulated into a poly(ethylene glycol) diacrylate (PEGDA) hydrogel which is formulated to optimize sensitivity and binding kinetics. The sensor hydrogels are deactivated when directly implanted subcutaneously into mice, so they were further encapsulated into dialysis bags. This configuration allows the sensors to respond to local progesterone levels while in the subcutaneous space of the mouse.

Experimental

Materials. Raw single wall carbon nanotubes (SWNT) produced by the HiPCO process were purchased from NanoIntegris and used without further processing (Batch HR27-104). Poly(ethylene glycol) diacrylate (PEGDA) ($M_n = 8000$) was purchased from Alfa Aesar. All other chemicals were purchased from Sigma Millipore.

Acrylation of Cortisol. Cortisol (2 grams, 1 equiv.) and triethylamine (850 mL, 1.1 equiv.) was dissolved in 50 mL tetrahydrofuran (THF). The solution was placed in an ice-bath under magnetic stirring. Acryloyl chloride (0.5 mL, 1.1 equiv.) diluted in THF at 10 vol% was added dropwise to the solution. The reaction proceeded at 0 °C for 1 hour and at room temperature thereafter for two days. The solution was decanted from the HCl-TEA salts. THF was removed by rotary evaporation. The product was reconstituted in 50 mL dichloromethane (DCM), washed thrice with 0.5 M HCl, twice with 5 wt% NaHCO₃, and once with saturated aqueous NaCl. The solution was dried using anhydrous Na₂SO₄. DCM was removed by rotary evaporation. 1.2 grams of product was obtained. The structure was confirmed using ¹H NMR using a Bruker AVANCE III -400 NMR Spectrometer (Figure 4-2)

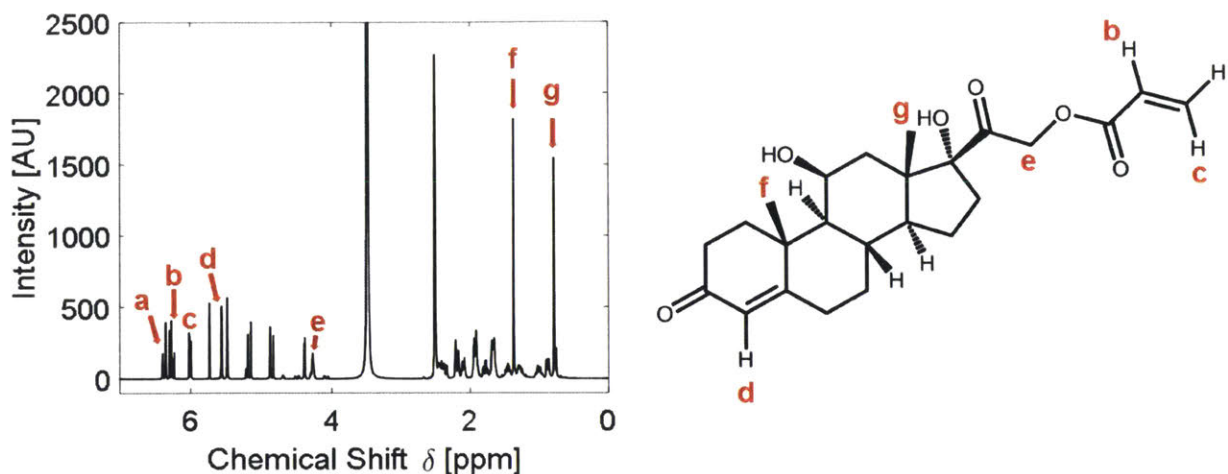


Figure 4-2: ^1H NMR spectrum of acrylated cortisol.

Polymer Library Synthesis. Varying amounts of styrene (S), acrylic acid (AA), and acrylated cortisol (AC) monomers were dissolved in 10 mL 1,4-dioxane according to the specific polymer design (Figure 4-3, Table 4-1). MEHQ in acrylic acid and 4-*tert*-butylcatechol in styrene were removed by passing the reagents through columns packed with inhibitor removers. 2-(Dodecylthiocarbonothioylthio)-2-methylpropionic acid (1 equiv.) and 2,2'-Azobis(2-methylpropionitrile) (0.2 equiv.) were added to each reaction mixture. The solution was sparged with N_2 for 30 minutes and sealed in the nitrogen environment throughout the reaction. The reaction was conducted at 70 °C for 24 hours. After the reaction, the mixture was precipitated in 300 mL diethyl ether. The polymer was redissolved in THF and re-precipitated in diethyl ether twice more to remove unreacted monomer. The polymer was dried under vacuum for 3 days and stored at -20 °C until further use.

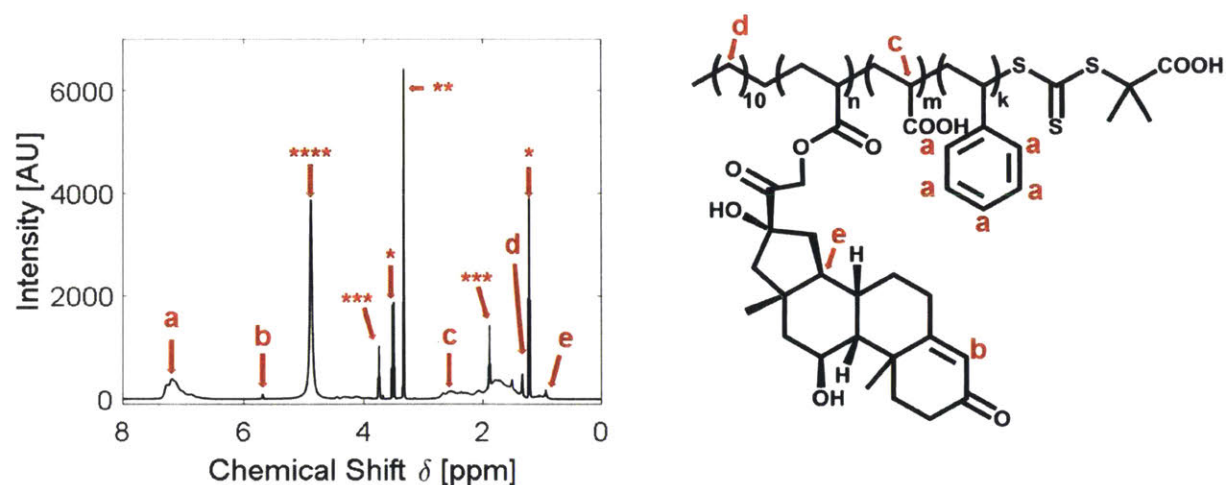


Figure 4-3: Representative ^1H spectrum of $p(\text{AA}_x\text{-ran-S}_y\text{-ran-AC}_z)$ polymers. Peaks used for compositional analysis labeled. Residual diethyl ether, methanol, tetrahydrofuran, and water solvent peaks are labeled as *, **, ***, and ****, respectively.

Polymer	Acrylic Acid Units	Styrene Units	Acrylated Cortisol Units	Chain Transfer Agent	M_n (NMR)	M_n (GPC)	PDI
P1	197	0	4.7	1	16500	17400	1.16
P2	144	1.8	5.0	1	13000	15900	1.18
P3	165	3.7	5.5	1	15000	16000	1.19
P4	166	6.3	5.4	1	15300	16100	1.16
P5	137.9	8.5	1	1	11600	18000	1.17
P6	83.8	17.3	1.3	1	8800	12900	1.12
P7	55.1	25.2	1.4	1	7600	8900	1.24
P8	44.4	32.0	1.3	1	7500	5300	1.56
P9	59.2	24.1	2.6	1	8300	8200	1.29
P10	53.7	21.8	3.7	1	8100	6600	1.41
P11	109.2	15.3	5	1	12000	13300	1.20
P12	54.0	27.1	3.8	1	8700	4500	1.49
P13	78.3	21.1	7.7	1	11500	6700	1.37
C1	87.5	17.2	0	1	8500	11800	1.11
C2	55.1	28.6	0	1	7300	7400	1.31
C3	63.4	45.9	0	1	9700	6400	1.35

Table 4-1: Summary of polymer library, detailing composition as calculated by ^1H NMR and molar mass calculated by ^1H NMR and GPC.

Polymer Characterization. NMR spectra were obtained by dissolving polymers at 30 mg/mL in methanol- d_4 . Molecular weight distributions were obtained using gel permeation chromatography on an Agilent Infinity 1260 equipped with a PL Aquagel-OH 30 column (Figure

4-4). The mobile phase was an aqueous solution of 0.2 M NaNO₃ and 0.01 M NaH₂PO₄ eluted at a flowrate of 0.5 mL/min. Samples were dissolved at 5 mg/mL, adjusted to pH 7, and filtered through a 0.22 μm membrane prior to the run. The molar mass was calibrated against PEG standards ranging from 106 to 30,310 Da. FTIR spectra were measured from 500 – 4000 cm⁻¹ with a Nicolet 4700 (Thermo Scientific) (Figure 4-5).

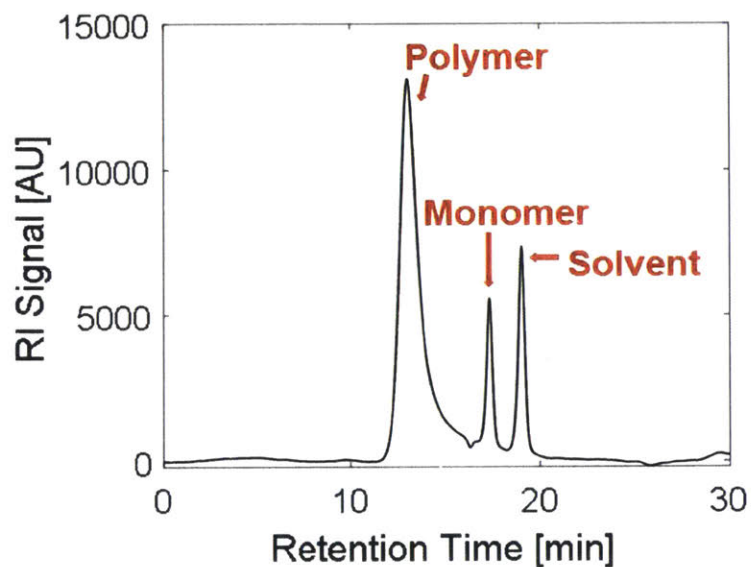


Figure 4-4: Representative GPC trace of $p(AA_x\text{-ran-}S_y\text{-}AC_z)$.

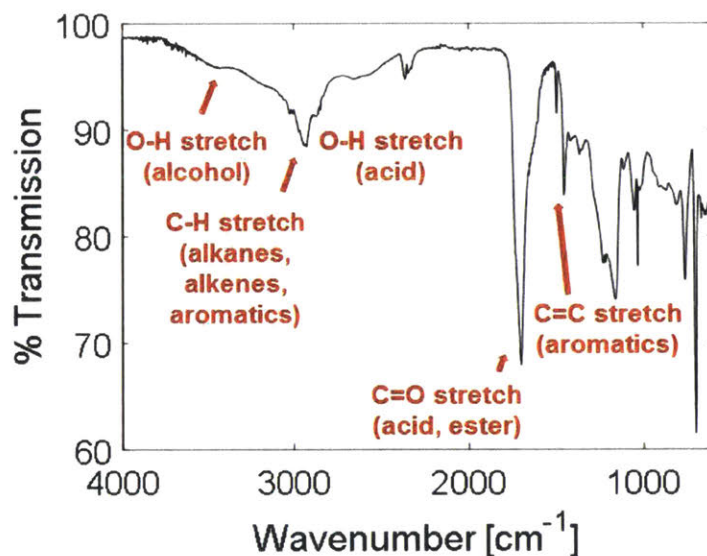


Figure 4-5: Representative FTIR spectrum of $p(AA_x\text{-}ran\text{-}S_y\text{-}AC_z)$. The spectrum qualitatively confirms incorporation of acrylic acid, styrene, and acrylated cortisol.

SWNT Suspension. In 5 mL of 1x PBS, 5 mg HiPCO SWNT and 50 mg of polymers were mixed. The solution was adjusted to a final pH of 7.4 using 2 M NaOH. The mixture was bath sonicated for 10 minutes and ultrasonicated using a 6 mm probe at a power of 10 W for 1 hour (QSonica). The resulting suspension was ultracentrifuged at 155,000 rcf for four hours. The top 80% of the suspension was reserved for further use, while the remaining 20% was discarded. Free polymer was removed from the suspension by dialysis against 1x PBS over 5 days using 100 kDa cutoff Float-a-Lyzer devices (Spectrum Labs) with buffer replacements thrice daily. UV-Vis-NIR absorption spectroscopy was used to confirm successful suspensions and obtain the mass concentration of the nanoparticles using an extinction coefficient of $\epsilon_{632} = 0.036 \text{ mg}/(\text{L cm})$.⁶⁴

Sensor Screening. High throughput screening of the sensor library against the steroid panel was performed using a customized nIR microscope, which consists of a Zeiss Axio Vision inverted Microscope body with a 20x objective, coupled to a Acton SP2500 spectrometer and liquid nitrogen cooled InGaAs 1D detector (Princeton Instruments). In a 96 well plate, one SWNT

sensor (1 mg/L) and one steroid (100 μ M) were mixed in a final volume of 150 μ L in 1x PBS with 2 vol% DMSO and incubated for 1 hour in each well. The samples were then illuminated by a 150 mW 785 nm photodiode laser (B&W Tek Inc.), and fluorescence emission spectra were collected from 950 to 1250 nm. The fluorescence spectra were deconvoluted into individual peaks corresponding to single SWNT chiralities according to a previously reported algorithm (Figure 4-6).⁵⁶ Peak position and intensities of each sensor-steroid pair were compared to a sensor-blank control to calculate the sensor response. The most promising candidates were identified and studied further.

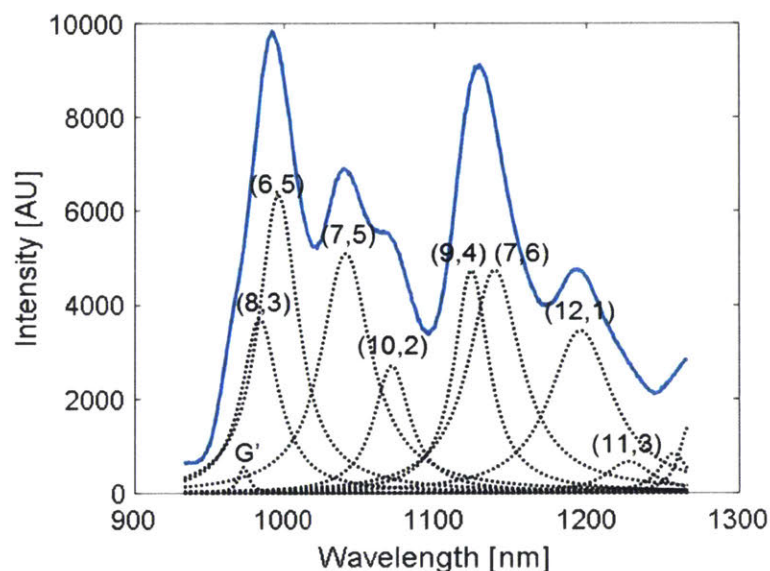


Figure 4-6: Fluorescence spectrum of HiPCO SWNT suspended with P10 (blue). The raw spectrum was decomposed into individual SWNT chiralities using a previously reported method.⁵⁶

Molecular Dynamics (MD) Simulations. MD simulations were performed in GROMACS 4.6.5. Simulations were performed on (7,6) SWNT interacting with steroids and polymers containing various combinations of acrylic acid, styrene, and acrylated cortisol. SWNT, steroids, and polymers were created in Materials Studio 8.0. The OPLS-AA force field was used in the simulations. Parameters describing the bonds, bond angles, and dihedral angles of the monomers

not in the original force field were obtained by using values from similar chemical structures already included, listed below. SWNT were centered in a 10 nm x 10 nm 4.8 nm box with the interacting molecule to be studied placed parallel to the SWNT. The box was hydrated using the TIP4P water model, and charges were neutralized using Na⁺ counterions. Energy was minimized, and the system was equilibrated for 100 ps each under NVT and NPT ensembles. For steroids, a production run of 10 ns was conducted, while polymers were simulated using a production run of 200 ns. All simulations were performed at 300 K and with a 2 fs time step. Equilibration was confirmed by monitoring the polymer radius of gyration and the drift in the average Lennard-Jones potential.

i	j	func	b0	kb
C_2	C_2	1	0.146	322168

Table 4-2: Bond type parameters added to OPLS-AA force field in GROMACS 4.6.5.

i	j	k	func	th0	cth
CM	C_2	CM	1	117.2	669.44
C_2	C_2	HC	1	116	669.44
HC	C_2	HC	1	117	292.88
OS	C_2	C_2	1	111.4	677.808
CT	C_2	CM	1	117.2	669.44

Table 4-3: Bond angle type parameters added to OPLS-AA force field in GROMACS 4.6.5.

i	j	k	l	func	c1	c2	c3	c4	c5	c6
C_2	C_2	CT	HC	3	-0.2092	-0.6276	0	0.8368	0	0
CA	CA	CA	CA	3	30.334	0	-30.334	0	0	0
C_2	CT	CT	C_2	3	-4.23421	7.22159	1.9079	-4.89528	0	0
C_2	CT	CT	CM	3	-4.23421	7.22159	1.9079	-4.89528	0	0
C_2	OS	CT	C_2	3	1.71544	2.84512	1.046	-5.60656	0	0
CM	CM	C_2	CT	3	-10.8784	-1.6736	12.552	0	0	0
CM	CM	C_2	CM	3	-10.8784	-1.6736	12.552	0	0	0
CM	CM	C_2	O_2	3	30.334	-5.23	-25.104	0	0	0
CM	CM	CT	CM	3	0.52719	-6.39734	-1.69452	7.56467	0	0
CM	CM	C_2	HC	3	-0.77822	-2.33467	0	3.1129	0	0
CM	C_2	CT	CT	3	0.52719	-6.39734	-1.69452	7.56467	0	0
CM	C_2	CT	HC	3	-0.77822	-2.33467	0	3.1129	0	0
CM	C_2	CM	HC	3	-0.77822	-2.33467	0	3.1129	0	0

C_2	CT	OH	HO	3	-1.8828	1.8828	0	0	0	0
C_2	C_2	CT	CT	3	-4.23421	7.22159	1.9079	-4.89528	0	0
CT	C_2	CM	HC	3	58.576	0	-58.576	0	0	0
CT	CM	CT	CM	3	6.32202	-2.4853	0.7071	-4.54382	0	0
CT	C_2	C_2	OS	3	-1.15688	-3.47063	0	4.6275	0	0
CT	C_2	C_2	O_2	3	3.10662	-3.77606	-5.13795	5.80739	0	0
C_2	C_2	OS	CT	3	31.20637	-9.76754	-21.4388	0	0	0
HC	CM	C_2	O_2	3	0	0	0	0	0	0
HC	CM	CT	CT	3	0.66525	1.99576	0	-2.66102	0	0
HC	CM	CT	CM	3	0.66525	1.99576	0	-2.66102	0	0
HC	C_2	C_2	OS	3	0.27615	0.82844	0	-1.10458	0	0
HC	C_2	C_2	O_2	3	0	0	0	0	0	0
O_2	C_2	CT	X	3	0	0	0	0	0	0
HC	CM	CM	C_2	3	58.576	0	-58.576	0	0	0
CT	C_2	CT	OH	3	2.87441	0.58158	2.092	-5.54799	0	0
CT	C_2	CT	OS	3	2.87441	0.58158	2.092	-5.54799	0	0

Table 4-4: Dihedral angle type parameters added to OPLS-AA force field in GROMACS 4.6.5.

First Monomer			Middle Monomer			Final Monomer		
C1	opls_135	-0.17647	C1	opls_136	-0.11625	C1	opls_136	-0.12
C2	opls_149	-0.00147	C2	opls_149	-0.00125	C2	opls_149	-0.005
C3	opls_145	-0.11147	C3	opls_145	-0.11125	C3	opls_145	-0.115
C4	opls_145	-0.11147	C4	opls_145	-0.11125	C4	opls_145	-0.115
C5	opls_145	-0.11147	C5	opls_145	-0.11125	C5	opls_145	-0.115
C6	opls_145	-0.11147	C6	opls_145	-0.11125	C6	opls_145	-0.115
C7	opls_145	-0.11147	C7	opls_145	-0.11125	C7	opls_145	-0.115
C8	opls_145	-0.11147	C8	opls_145	-0.11125	C8	opls_145	-0.115
H11	opls_140	0.063529	H11	opls_140	0.06375	H11	opls_140	0.06
H12	opls_140	0.063529	H12	opls_140	0.06375	H12	opls_140	0.06
H13	opls_140	0.063529	H21	opls_140	0.06375	H21	opls_140	0.06
H21	opls_140	0.063529	H41	opls_146	0.11875	H22	opls_140	0.06
H41	opls_146	0.118529	H51	opls_146	0.11875	H41	opls_146	0.115
H51	opls_146	0.118529	H61	opls_146	0.11875	H51	opls_146	0.115
H61	opls_146	0.118529	H71	opls_146	0.11875	H61	opls_146	0.115
H71	opls_146	0.118529	H81	opls_146	0.11875	H71	opls_146	0.115
H81	opls_146	0.118529				H81	opls_146	0.115

Table 4-5: Parameters for styrene atoms.

First Monomer	Middle Monomer	Final Monomer
-C1 C2	-C1 C2	C1 C2
C1 C2	C1 C2	C1 H11
C1 H11	C1 H11	C1 H12
C1 H12	C1 H12	C2 C3

C1 H13		C2 C3		C2 H21
C2 C3		C2 H21		C2 H22
C2 H21		C3 C4		C3 C4
C3 C4		C3 C8		C3 C8
C3 C8		C4 C5		C4 C5
C4 C5		C4 H41		C4 H41
C4 H41		C5 C6		C5 C6
C5 C6		C5 H51		C5 H51
C5 H51		C6 C7		C6 C7
C6 C7		C6 H61		C6 H61
C6 H61		C7 C8		C7 C8
C7 C8		C7 H71		C7 H71
C7 H71		C8 H81		C8 H81
C8 H81				

Table 4-6: Bonds in styrene.

First Monomer			Middle Monomer			Final Monomer		
C1	opls_135	-0.18	C1	opls_136	-0.12	C1	opls_136	-0.12
C2	opls_275	-0.16	C2	opls_275	-0.16	C2	opls_274	-0.22
C3	opls_271	0.7	C3	opls_271	0.7	C3	opls_271	0.7
H11	opls_140	0.06	H11	opls_140	0.06	H11	opls_140	0.06
H12	opls_140	0.06	H12	opls_140	0.06	H12	opls_140	0.06
H13	opls_140	0.06	H21	opls_282	0.06	H21	opls_282	0.06
H21	opls_282	0.06	O31	opls_272	-0.8	H22	opls_282	0.06
O31	opls_272	-0.8	O32	opls_272	-0.8	O31	opls_272	-0.8
O32	opls_272	-0.8				O32	opls_272	-0.8

Table 4-7: Parameters for acrylic acid atoms.

First Monomer	Middle Monomer	Final Monomer
-C1 C2	-C1 C2	C1 C2
C1 C2	C1 C2	C1 H11
C1 H11	C1 H11	C1 H12
C1 H12	C1 H12	C2 C3
C1 H13	C2 C3	C2 H21
C2 C3	C2 H21	C2 H22
C2 H21	C3 O31	C3 O31
C3 O31	C3 O32	C3 O32
C3 O32		

Table 4-8: Bonds in acrylic acid.

C1	opls_135	-0.18762	C22	opls_136	-0.12762	HOD	opls_155	0.410381
C2	opls_280	0.462381	C23	opls_280	0.462381	HE1	opls_140	0.052381
C3	opls_465	0.502381	C24	opls_142	-0.12262	HF1	opls_140	0.052381

C4	opls_468	0.152381		H11	opls_140	0.052381		HG1	opls_140	0.052381
C5	opls_280	0.462381		H12	opls_140	0.052381		HG2	opls_140	0.052381
C6	opls_159	0.257381		H13	opls_140	0.052381		HH1	opls_140	0.052381
C7	opls_136	-0.12762		H21	opls_282	0.052381		HH2	opls_140	0.052381
C8	opls_136	-0.12762		H41	opls_469	0.022381		HK1	opls_140	0.052381
C9	opls_137	-0.06762		H42	opls_469	0.022381		HK2	opls_140	0.052381
C10	opls_139	-0.00762		H06	opls_155	0.410381		HK3	opls_140	0.052381
C11	opls_135	-0.18762		H71	opls_140	0.052381		HL1	opls_140	0.052381
C12	opls_136	-0.12762		H72	opls_140	0.052381		HL2	opls_140	0.052381
C13	opls_158	0.197381		H81	opls_140	0.052381		HM1	opls_140	0.052381
C14	opls_137	-0.06762		H82	opls_140	0.052381		HM2	opls_140	0.052381
C15	opls_137	-0.06762		H91	opls_140	0.052381		HP1	opls_144	0.107381
C16	opls_136	-0.12762		HB1	opls_140	0.052381		O31	opls_466	-0.43762
C17	opls_136	-0.12762		HB2	opls_140	0.052381		O32	opls_467	-0.33762
C18	opls_141	-0.00762		HB3	opls_140	0.052381		O51	opls_281	-0.47762
C19	opls_139	-0.00762		HC1	opls_140	0.052381		O61	opls_154	-0.69062
C20	opls_135	-0.18762		HC2	opls_140	0.052381		OD1	opls_154	-0.69062
C21	opls_136	-0.12762		HD1	opls_156	0.032381		ON1	opls_281	-0.47762

Table 4-9: Parameters for atoms in acrylated cortisol as the first monomer in a polymer.

C1	opls_136	-0.12774		C22	opls_136	-0.12774		HE1	opls_140	0.052258
C2	opls_280	0.462258		C23	opls_280	0.462258		HF1	opls_140	0.052258
C3	opls_465	0.502258		C24	opls_142	-0.12274		HG1	opls_140	0.052258
C4	opls_468	0.152258		H11	opls_140	0.052258		HG2	opls_140	0.052258
C5	opls_280	0.462258		H12	opls_140	0.052258		HH1	opls_140	0.052258
C6	opls_159	0.257258		H21	opls_282	0.052258		HH2	opls_140	0.052258
C7	opls_136	-0.12774		H41	opls_469	0.022258		HK1	opls_140	0.052258
C8	opls_136	-0.12774		H42	opls_469	0.022258		HK2	opls_140	0.052258
C9	opls_137	-0.06774		H06	opls_155	0.410258		HK3	opls_140	0.052258
C10	opls_139	-0.00774		H71	opls_140	0.052258		HL1	opls_140	0.052258
C11	opls_135	-0.18774		H72	opls_140	0.052258		HL2	opls_140	0.052258
C12	opls_136	-0.12774		H81	opls_140	0.052258		HM1	opls_140	0.052258
C13	opls_158	0.197258		H82	opls_140	0.052258		HM2	opls_140	0.052258
C14	opls_137	-0.06774		H91	opls_140	0.052258		HP1	opls_144	0.107258
C15	opls_137	-0.06774		HB1	opls_140	0.052258		O31	opls_466	-0.43774
C16	opls_136	-0.12774		HB2	opls_140	0.052258		O32	opls_467	-0.33774
C17	opls_136	-0.12774		HB3	opls_140	0.052258		O51	opls_281	-0.47774
C18	opls_141	-0.00774		HC1	opls_140	0.052258		O61	opls_154	-0.69074
C19	opls_139	-0.00774		HC2	opls_140	0.052258		OD1	opls_154	-0.69074
C20	opls_135	-0.18774		HD1	opls_156	0.032258		ON1	opls_281	-0.47774
C21	opls_136	-0.12774		HOD	opls_155	0.410258				

Table 4-10: Parameters for atoms in acrylated cortisol as the middle monomer in a polymer.

C1	opls_136	-0.12857		C22	opls_136	-0.12857		HOD	opls_155	0.409429
C2	opls_280	0.461429		C23	opls_280	0.461429		HE1	opls_140	0.051429

C3	opls_465	0.501429		C24	opls_142	-0.12357		HF1	opls_140	0.051429
C4	opls_468	0.151429		H11	opls_140	0.051429		HG1	opls_140	0.051429
C5	opls_280	0.461429		H12	opls_140	0.051429		HG2	opls_140	0.051429
C6	opls_159	0.256429		H21	opls_282	0.051429		HH1	opls_140	0.051429
C7	opls_136	-0.12857		H22	opls_282	0.051429		HH2	opls_140	0.051429
C8	opls_136	-0.12857		H41	opls_469	0.021429		HK1	opls_140	0.051429
C9	opls_137	-0.06857		H42	opls_469	0.021429		HK2	opls_140	0.051429
C10	opls_139	-0.00857		HO6	opls_155	0.409429		HK3	opls_140	0.051429
C11	opls_135	-0.18857		H71	opls_140	0.051429		HL1	opls_140	0.051429
C12	opls_136	-0.12857		H72	opls_140	0.051429		HL2	opls_140	0.051429
C13	opls_158	0.196429		H81	opls_140	0.051429		HM1	opls_140	0.051429
C14	opls_137	-0.06857		H82	opls_140	0.051429		HM2	opls_140	0.051429
C15	opls_137	-0.06857		H91	opls_140	0.051429		HP1	opls_144	0.106429
C16	opls_136	-0.12857		HB1	opls_140	0.051429		O31	opls_466	-0.43857
C17	opls_136	-0.12857		HB2	opls_140	0.051429		O32	opls_467	-0.33857
C18	opls_141	-0.00857		HB3	opls_140	0.051429		O51	opls_281	-0.47857
C19	opls_139	-0.00857		HC1	opls_140	0.051429		O61	opls_154	-0.69157
C20	opls_135	-0.18857		HC2	opls_140	0.051429		OD1	opls_154	-0.69157
C21	opls_136	-0.12857		HD1	opls_156	0.031429		ON1	opls_281	-0.47857

Table 4-11: Parameters for atoms in acrylated cortisol as the final monomer in a polymer.

-C1 C2	C8 H82	C17 C18
C1 C2	C9 C10	C17 HH1
C1 H11	C9 C15	C17 HH2
C1 H12	C9 H91	C18 C19
C1 H13	C10 C11	C18 C24
C2 C3	C10 C12	C19 C20
C2 H21	C11 HB1	C19 C21
C3 O31	C11 HB2	C20 HK1
C3 O32	C11 HB3	C20 HK2
C4 O32	C12 C13	C20 HK3
C4 C5	C12 HC1	C21 C22
C4 H41	C12 HC2	C21 HL1
C4 H42	C13 C14	C21 HL2
C5 C6	C13 HD1	C22 C23
C5 O51	C13 OD1	C22 HM1
C6 C7	C14 C15	C22 HM2
C6 C10	C14 C19	C23 C24
C6 O61	C14 HE1	C23 ON1
C7 C8	C15 C16	C24 HP1
C7 H71	C15 HF1	O61 HO6
C7 H72	C16 C17	OD1 HOD
C8 C9	C16 HG1	
C8 H81	C16 HG2	

Table 4-12: Bonds in acrylated cortisol as the first monomer in a polymer.

-C1 C2	C9 C10	C17 HH1
C1 C2	C9 C15	C17 HH2
C1 H11	C9 H91	C18 C19
C1 H12	C10 C11	C18 C24
C2 C3	C10 C12	C19 C20
C2 H21	C11 HB1	C19 C21
C3 O31	C11 HB2	C20 HK1
C3 O32	C11 HB3	C20 HK2
C4 O32	C12 C13	C20 HK3
C4 C5	C12 HC1	C21 C22
C4 H41	C12 HC2	C21 HL1
C4 H42	C13 C14	C21 HL2
C5 C6	C13 HD1	C22 C23
C5 O51	C13 OD1	C22 HM1
C6 C7	C14 C15	C22 HM2
C6 C10	C14 C19	C23 C24
C6 O61	C14 HE1	C23 ON1
C7 C8	C15 C16	C24 HP1
C7 H71	C15 HF1	O61 HO6
C7 H72	C16 C17	OD1 HOD
C8 C9	C16 HG1	
C8 H81	C16 HG2	
C8 H82	C17 C18	

Table 4-13: Bonds in acrylated cortisol as a middle monomer in a polymer.

C1 C2	C9 C10	C17 HH1
C1 H11	C9 C15	C17 HH2
C1 H12	C9 H91	C18 C19
C2 C3	C10 C11	C18 C24
C2 H21	C10 C12	C19 C20
C2 H22	C11 HB1	C19 C21
C3 O31	C11 HB2	C20 HK1
C3 O32	C11 HB3	C20 HK2
C4 O32	C12 C13	C20 HK3
C4 C5	C12 HC1	C21 C22
C4 H41	C12 HC2	C21 HL1
C4 H42	C13 C14	C21 HL2
C5 C6	C13 HD1	C22 C23
C5 O51	C13 OD1	C22 HM1
C6 C7	C14 C15	C22 HM2
C6 C10	C14 C19	C23 C24
C6 O61	C14 HE1	C23 ON1
C7 C8	C15 C16	C24 HP1

C7 H71	C15 HF1	O61 HO6
C7 H72	C16 C17	OD1 HOD
C8 C9	C16 HG1	
C8 H81	C16 HG2	
C8 H82	C17 C18	

Table 4-14: Bonds in acrylated cortisol as the final monomer in a polymer.

C4	opls_157	0.146071	C24	opls_142	-0.11393	HG2	opls_140	0.061071
C5	opls_280	0.471071	HO3	opls_155	0.419071	HH1	opls_140	0.061071
C6	opls_159	0.266071	H41	opls_156	0.041071	HH2	opls_140	0.061071
C7	opls_136	-0.11893	H42	opls_156	0.041071	HK1	opls_140	0.061071
C8	opls_136	-0.11893	HO6	opls_155	0.419071	HK2	opls_140	0.061071
C9	opls_137	-0.05893	H71	opls_140	0.061071	HK3	opls_140	0.061071
C10	opls_139	0.001071	H72	opls_140	0.061071	HL1	opls_140	0.061071
C11	opls_135	-0.17893	H81	opls_140	0.061071	HL2	opls_140	0.061071
C12	opls_136	-0.11893	H82	opls_140	0.061071	HM1	opls_140	0.061071
C13	opls_158	0.206071	H91	opls_140	0.061071	HM2	opls_140	0.061071
C14	opls_137	-0.05893	HB1	opls_140	0.061071	HP1	opls_144	0.116071
C15	opls_137	-0.05893	HB2	opls_140	0.061071	O32	opls_154	-0.68193
C16	opls_136	-0.11893	HB3	opls_140	0.061071	O51	opls_281	-0.46893
C17	opls_136	-0.11893	HC1	opls_140	0.061071	O61	opls_154	-0.68193
C18	opls_141	0.001071	HC2	opls_140	0.061071	OD1	opls_154	-0.68193
C19	opls_139	0.001071	HD1	opls_156	0.041071	ON1	opls_281	-0.46893
C20	opls_135	-0.17893	HOD	opls_155	0.419071			
C21	opls_136	-0.11893	HE1	opls_140	0.061071			
C22	opls_136	-0.11893	HF1	opls_140	0.061071			
C23	opls_280	0.471071	HG1	opls_140	0.061071			

Table 4-15: Parameters for atoms in cortisol.

C4 O32	C11 HB1	C18 C19
C4 C5	C11 HB2	C18 C24
C4 H41	C11 HB3	C19 C20
C4 H42	C12 C13	C19 C21
C5 C6	C12 HC1	C20 HK1
C5 O51	C12 HC2	C20 HK2
C6 C7	C13 C14	C20 HK3
C6 C10	C13 HD1	C21 C22
C6 O61	C13 OD1	C21 HL1
C7 C8	C14 C15	C21 HL2
C7 H71	C14 C19	C22 C23
C7 H72	C14 HE1	C22 HM1
C8 C9	C15 C16	C22 HM2
C8 H81	C15 HF1	C23 C24
C8 H82	C16 C17	C23 ON1
C9 C10	C16 HG1	C24 HP1

C9 C15	C16 HG2	O32 HO3
C9 H91	C17 C18	O61 HO6
C10 C11	C17 HH1	OD1 HOD
C10 C12	C17 HH2	C18 C19

Table 4-16: Bonds in cortisol.

C4	opls_135	-0.18	C22	opls_136	-0.12	HD2	opls_140	0.06
C5	opls_280	0.47	C23	opls_280	0.47	HE1	opls_140	0.06
C6	opls_137	-0.06	C24	opls_142	-0.115	HF1	opls_140	0.06
C7	opls_136	-0.12	H41	opls_140	0.06	HG1	opls_140	0.06
C8	opls_136	-0.12	H42	opls_140	0.06	HG2	opls_140	0.06
C9	opls_137	-0.06	H43	opls_140	0.06	HH1	opls_140	0.06
C10	opls_139	0	H61	opls_140	0.06	HH2	opls_140	0.06
C11	opls_135	-0.18	H71	opls_140	0.06	HK1	opls_140	0.06
C12	opls_136	-0.12	H72	opls_140	0.06	HK2	opls_140	0.06
C13	opls_136	-0.12	H81	opls_140	0.06	HK3	opls_140	0.06
C14	opls_137	-0.06	H82	opls_140	0.06	HL1	opls_140	0.06
C15	opls_137	-0.06	H91	opls_140	0.06	HL2	opls_140	0.06
C16	opls_136	-0.12	HB1	opls_140	0.06	HM1	opls_140	0.06
C17	opls_136	-0.12	HB2	opls_140	0.06	HM2	opls_140	0.06
C18	opls_141	0	HB3	opls_140	0.06	HP1	opls_144	0.115
C19	opls_139	0	HC1	opls_140	0.06	O51	opls_281	-0.47
C20	opls_135	-0.18	HC2	opls_140	0.06	ON1	opls_281	-0.47
C21	opls_136	-0.12	HD1	opls_140	0.06			

Table 4-17: Parameters for atoms in progesterone.

C4 C5	C10 C12	C17 HH1
C4 H41	C11 HB1	C17 HH2
C4 H42	C11 HB2	C18 C19
C4 H43	C11 HB3	C18 C24
C5 C6	C12 C13	C19 C20
C5 O51	C12 HC1	C19 C21
C6 C7	C12 HC2	C20 HK1
C6 C10	C13 C14	C20 HK2
C6 H61	C13 HD1	C20 HK3
C7 C8	C13 HD2	C21 C22
C7 H71	C14 C15	C21 HL1
C7 H72	C14 C19	C21 HL2
C8 C9	C14 HE1	C22 C23
C8 H81	C15 C16	C22 HM1
C8 H82	C15 HF1	C22 HM2
C9 C10	C16 C17	C23 C24
C9 C15	C16 HG1	C23 ON1
C9 H91	C16 HG2	C24 HP1

C10 C11	C17 C18	
---------	---------	--

Table 4-18: Bonds in progesterone.

C6	opls_159	0.264184	C23	opls_280	0.469184	HF1	opls_140	0.059184
C7	opls_136	-0.12082	C24	opls_142	-0.11582	HG1	opls_140	0.059184
C8	opls_136	-0.12082	H61	opls_156	0.039184	HG2	opls_140	0.059184
C9	opls_137	-0.06082	HO6	opls_155	0.417184	HH1	opls_140	0.059184
C10	opls_139	-0.00082	H71	opls_140	0.059184	HH2	opls_140	0.059184
C11	opls_135	-0.18082	H72	opls_140	0.059184	HK1	opls_140	0.059184
C12	opls_136	-0.12082	H81	opls_140	0.059184	HK2	opls_140	0.059184
C13	opls_136	-0.12082	H82	opls_140	0.059184	HK3	opls_140	0.059184
C14	opls_137	-0.06082	H91	opls_140	0.059184	HL1	opls_140	0.059184
C15	opls_137	-0.06082	HB1	opls_140	0.059184	HL2	opls_140	0.059184
C16	opls_136	-0.12082	HB2	opls_140	0.059184	HM1	opls_140	0.059184
C17	opls_136	-0.12082	HB3	opls_140	0.059184	HM2	opls_140	0.059184
C18	opls_141	-0.00082	HC1	opls_140	0.059184	HP1	opls_144	0.114184
C19	opls_139	-0.00082	HC2	opls_140	0.059184	O61	opls_154	-0.68382
C20	opls_135	-0.18082	HD1	opls_140	0.059184	ON1	opls_281	-0.47082
C21	opls_136	-0.12082	HD2	opls_140	0.059184			
C22	opls_136	-0.12082	HE1	opls_140	0.059184			

Table 4-19: Parameters for atoms in testosterone.

C6 C7	C12 C13	C18 C24
C6 C10	C12 HC1	C19 C20
C6 H61	C12 HC2	C19 C21
C6 O61	C13 C14	C20 HK1
C7 C8	C13 HD1	C20 HK2
C7 H71	C13 HD2	C20 HK3
C7 H72	C14 C15	C21 C22
C8 C9	C14 C19	C21 HL1
C8 H81	C14 HE1	C21 HL2
C8 H82	C15 C16	C22 C23
C9 C10	C15 HF1	C22 HM1
C9 C15	C16 C17	C22 HM2
C9 H91	C16 HG1	C23 C24
C10 C11	C16 HG2	C23 ON1
C10 C12	C17 C18	C24 HP1
C11 HB1	C17 HH1	O61 HO6
C11 HB2	C17 HH2	
C11 HB3	C18 C19	

Table 4-20: Bonds in testosterone.

C6	opls_280	0.470408	C23	opls_158	0.205408	HG2	opls_140	0.060408
C7	opls_136	-0.11959	C24	opls_136	-0.11959	HH1	opls_144	0.115408
C8	opls_136	-0.11959	H71	opls_140	0.060408	HK1	opls_140	0.060408
C9	opls_137	-0.05959	H72	opls_140	0.060408	HK2	opls_140	0.060408

C10	opls_139	0.000408	H81	opls_140	0.060408	HK3	opls_140	0.060408
C11	opls_135	-0.17959	H82	opls_140	0.060408	HL1	opls_140	0.060408
C12	opls_136	-0.11959	H91	opls_140	0.060408	HL2	opls_140	0.060408
C13	opls_136	-0.11959	HB1	opls_140	0.060408	HM1	opls_140	0.060408
C14	opls_137	-0.05959	HB2	opls_140	0.060408	HM2	opls_140	0.060408
C15	opls_137	-0.05959	HB3	opls_140	0.060408	HN1	opls_156	0.040408
C16	opls_136	-0.11959	HC1	opls_140	0.060408	HON	opls_155	0.418408
C17	opls_142	-0.11459	HC2	opls_140	0.060408	HP1	opls_140	0.060408
C18	opls_141	0.000408	HD1	opls_140	0.060408	HP2	opls_140	0.060408
C19	opls_139	0.000408	HD2	opls_140	0.060408	O61	opls_281	-0.46959
C20	opls_135	-0.17959	HE1	opls_140	0.060408	ON1	opls_154	-0.68259
C21	opls_136	-0.11959	HF1	opls_140	0.060408			
C22	opls_136	-0.11959	HG1	opls_140	0.060408			

Table 4-21: Parameters for atoms in DHEA.

C6 C7	C12 HC1	C19 C21
C6 C10	C12 HC2	C20 HK1
C6 O61	C13 C14	C20 HK2
C7 C8	C13 HD1	C20 HK3
C7 H71	C13 HD2	C21 C22
C7 H72	C14 C15	C21 HL1
C8 C9	C14 C19	C21 HL2
C8 H81	C14 HE1	C22 C23
C8 H82	C15 C16	C22 HM1
C9 C10	C15 HF1	C22 HM2
C9 C15	C16 C17	C23 C24
C9 H91	C16 HG1	C23 HN1
C10 C11	C16 HG2	C23 ON1
C10 C12	C17 C18	ON1 HON
C11 HB1	C17 HH1	C24 HP1
C11 HB2	C18 C19	C24 HP2
C11 HB3	C18 C24	
C12 C13	C19 C20	

Table 4-22: Bonds in DHEA.

C4	opls_135	-0.17964	C23	opls_158	0.205364	HF1	opls_140	0.060364
C5	opls_280	0.470364	C24	opls_136	-0.11964	HG1	opls_140	0.060364
C6	opls_137	-0.05964	H41	opls_140	0.060364	HG2	opls_140	0.060364
C7	opls_136	-0.11964	H42	opls_140	0.060364	HH1	opls_144	0.115364
C8	opls_136	-0.11964	H43	opls_140	0.060364	HK1	opls_140	0.060364
C9	opls_137	-0.05964	H61	opls_140	0.060364	HK2	opls_140	0.060364
C10	opls_139	0.000364	H71	opls_140	0.060364	HK3	opls_140	0.060364
C11	opls_135	-0.17964	H72	opls_140	0.060364	HL1	opls_140	0.060364
C12	opls_136	-0.11964	H81	opls_140	0.060364	HL2	opls_140	0.060364

C13	opls_136	-0.11964		H82	opls_140	0.060364		HM1	opls_140	0.060364
C14	opls_137	-0.05964		H91	opls_140	0.060364		HM2	opls_140	0.060364
C15	opls_137	-0.05964		HB1	opls_140	0.060364		HN1	opls_156	0.040364
C16	opls_136	-0.11964		HB2	opls_140	0.060364		HON	opls_155	0.418364
C17	opls_142	-0.11464		HB3	opls_140	0.060364		HP1	opls_140	0.060364
C18	opls_141	0.000364		HC1	opls_140	0.060364		HP2	opls_140	0.060364
C19	opls_139	0.000364		HC2	opls_140	0.060364		O51	opls_281	-0.46964
C20	opls_135	-0.17964		HD1	opls_140	0.060364		ON1	opls_154	-0.68264
C21	opls_136	-0.11964		HD2	opls_140	0.060364				
C22	opls_136	-0.11964		HE1	opls_140	0.060364				

Table 4-23: Parameters for atoms in pregnenolone.

C4 C5	C11 HB1	C18 C24
C4 H41	C11 HB2	C19 C20
C4 H42	C11 HB3	C19 C21
C4 H43	C12 C13	C20 HK1
C5 C6	C12 HC1	C20 HK2
C5 O51	C12 HC2	C20 HK3
C6 C7	C13 C14	C21 C22
C6 C10	C13 HD1	C21 HL1
C6 H61	C13 HD2	C21 HL2
C7 C8	C14 C15	C22 C23
C7 H71	C14 C19	C22 HM1
C7 H72	C14 HE1	C22 HM2
C8 C9	C15 C16	C23 C24
C8 H81	C15 HF1	C23 ON1
C8 H82	C16 C17	C23 HN1
C9 C10	C16 HG1	ON1 HON
C9 C15	C16 HG2	C24 HP1
C9 H91	C17 C18	C24 HP2
C10 C11	C17 HH1	
C10 C12	C18 C19	

Table 4-24: Bonds in pregnenolone.

C6	opls_159	0.265455		C22	opls_145	-0.11455		HD1	opls_140	0.060455
C7	opls_136	-0.11955		C23	opls_166	0.150455		HD2	opls_140	0.060455
C8	opls_136	-0.11955		C24	opls_145	-0.11455		HE1	opls_140	0.060455
C9	opls_137	-0.05955		H61	opls_156	0.040455		HF1	opls_140	0.060455
C10	opls_139	0.000455		HO6	opls_155	0.418455		HG1	opls_140	0.060455
C11	opls_135	-0.17955		H71	opls_140	0.060455		HG2	opls_140	0.060455
C12	opls_136	-0.11955		H72	opls_140	0.060455		HH1	opls_140	0.060455
C13	opls_136	-0.11955		H81	opls_140	0.060455		HH2	opls_140	0.060455
C14	opls_149	-0.00455		H82	opls_140	0.060455		HL1	opls_146	0.115455
C15	opls_137	-0.05955		H91	opls_140	0.060455		HM1	opls_146	0.115455

C16	opls_136	-0.11955		HB1	opls_140	0.060455		HON	opls_168	0.435455
C17	opls_149	-0.00455		HB2	opls_140	0.060455		HP1	opls_146	0.115455
C18	opls_145	-0.11455		HB3	opls_140	0.060455		O61	opls_154	-0.68255
C19	opls_145	-0.11455		HC1	opls_140	0.060455		ON1	opls_167	-0.58455
C21	opls_145	-0.11455		HC2	opls_140	0.060455				

Table 4-25: Parameters for atoms in estradiol.

C6 C7	C11 HB2	C17 C18
C6 C10	C11 HB3	C17 HH1
C6 H61	C12 C13	C17 HH2
C6 O61	C12 HC1	C18 C19
C7 C8	C12 HC2	C18 C24
C7 H71	C13 C14	C19 C20
C7 H72	C13 HD1	C19 C21
C8 C9	C13 HD2	C21 C22
C8 H81	C14 C15	C21 HL1
C8 H82	C14 C19	C22 C23
C9 C10	C14 HE1	C22 HM1
C9 C15	C15 C16	C23 C24
C9 H91	C15 HF1	C23 ON1
C10 C11	C16 C17	C24 HP1
C10 C12	C16 HG1	O61 HO6
C11 HB1	C16 HG2	ON1 HON

Table 4-26: Bonds in estradiol.

C4	opls_157	0.146111		C22	opls_142	-0.11389		HOD	opls_155	0.419111
C5	opls_280	0.471111		C23	opls_280	0.471111		HE1	opls_140	0.061111
C6	opls_159	0.266111		C24	opls_142	-0.11389		HF1	opls_140	0.061111
C7	opls_136	-0.11889		HO3	opls_155	0.419111		HG1	opls_140	0.061111
C8	opls_136	-0.11889		H41	opls_156	0.041111		HG2	opls_140	0.061111
C9	opls_137	-0.05889		H42	opls_156	0.041111		HH1	opls_140	0.061111
C10	opls_139	0.001111		HO6	opls_155	0.419111		HH2	opls_140	0.061111
C11	opls_135	-0.17889		H71	opls_140	0.061111		HK1	opls_140	0.061111
C12	opls_136	-0.11889		H72	opls_140	0.061111		HK2	opls_140	0.061111
C13	opls_158	0.206111		H81	opls_140	0.061111		HK3	opls_140	0.061111
C14	opls_137	-0.05889		H82	opls_140	0.061111		HL1	opls_144	0.116111
C15	opls_137	-0.05889		H91	opls_140	0.061111		HM1	opls_144	0.116111
C16	opls_136	-0.11889		HB1	opls_140	0.061111		HP1	opls_144	0.116111
C17	opls_136	-0.11889		HB2	opls_140	0.061111		O32	opls_154	-0.68189
C18	opls_141	0.001111		HB3	opls_140	0.061111		O51	opls_281	-0.46889
C19	opls_139	0.001111		HC1	opls_140	0.061111		O61	opls_154	-0.68189
C20	opls_135	-0.17889		HC2	opls_140	0.061111		OD1	opls_154	-0.68189
C21	opls_142	-0.11389		HD1	opls_156	0.041111		ON1	opls_281	-0.46889

Table 4-27: Parameters for atoms in prednisone.

C4 O32	C10 C12	C17 HH1
C4 C5	C11 HB1	C17 HH2
C4 H41	C11 HB2	C18 C19
C4 H42	C11 HB3	C18 C24
C5 C6	C12 C13	C19 C20
C5 O51	C12 HC1	C19 C21
C6 C7	C12 HC2	C20 HK1
C6 C10	C13 C14	C20 HK2
C6 O61	C13 HD1	C20 HK3
C7 C8	C13 OD1	C21 C22
C7 H71	C14 C15	C21 HL1
C7 H72	C14 C19	C22 C23
C8 C9	C14 HE1	C22 HM1
C8 H81	C15 C16	C23 C24
C8 H82	C15 HF1	C23 ON1
C9 C10	C16 C17	C24 HP1
C9 C15	C16 HG1	O32 HO3
C9 H91	C16 HG2	O61 HO6
C10 C11	C17 C18	OD1 HOD

Table 4-28: Bonds in prednisone.

C4	opls_157	0.146404	C23	opls_158	0.206404	HF1	opls_140	0.061404
C5	opls_280	0.471404	C24	opls_142	-0.1136	HG1	opls_140	0.061404
C6	opls_137	-0.0586	HO3	opls_155	0.419404	HG2	opls_140	0.061404
C7	opls_136	-0.1186	H41	opls_156	0.041404	HH1	opls_140	0.061404
C8	opls_136	-0.1186	H42	opls_156	0.041404	HH2	opls_140	0.061404
C9	opls_137	-0.0586	H61	opls_140	0.061404	HK1	opls_140	0.061404
C10	opls_139	0.001404	H71	opls_140	0.061404	HK2	opls_140	0.061404
C11	opls_135	-0.1786	H72	opls_140	0.061404	HK3	opls_140	0.061404
C12	opls_136	-0.1186	H81	opls_140	0.061404	HL1	opls_140	0.061404
C13	opls_158	0.206404	H82	opls_140	0.061404	HL2	opls_140	0.061404
C14	opls_137	-0.0586	H91	opls_140	0.061404	HM1	opls_140	0.061404
C15	opls_137	-0.0586	HB1	opls_140	0.061404	HM2	opls_140	0.061404
C16	opls_136	-0.1186	HB2	opls_140	0.061404	HN1	opls_156	0.041404
C17	opls_136	-0.1186	HB3	opls_140	0.061404	HON	opls_155	0.419404
C18	opls_141	0.001404	HC1	opls_140	0.061404	HP1	opls_144	0.116404
C19	opls_139	0.001404	HC2	opls_140	0.061404	O32	opls_154	-0.6816
C20	opls_135	-0.1786	HD1	opls_156	0.041404	O51	opls_281	-0.4686
C21	opls_136	-0.1186	HOD	opls_155	0.419404	OD1	opls_154	-0.6816
C22	opls_136	-0.1186	HE1	opls_140	0.061404	ON1	opls_154	-0.6816

Table 4-29: Parameters for atoms in corticosterone.

C4 O32	C11 HB1	C18 C19
C4 C5	C11 HB2	C18 C24
C4 H41	C11 HB3	C19 C20

C4 H42	C12 C13	C19 C21
C5 C6	C12 HC1	C20 HK1
C5 O51	C12 HC2	C20 HK2
C6 C7	C13 C14	C20 HK3
C6 C10	C13 HD1	C21 C22
C6 H61	C13 OD1	C21 HL1
C7 C8	C14 C15	C21 HL2
C7 H71	C14 C19	C22 C23
C7 H72	C14 HE1	C22 HM1
C8 C9	C15 C16	C22 HM2
C8 H81	C15 HF1	C23 C24
C8 H82	C16 C17	C23 HN1
C9 C10	C16 HG1	C23 ON1
C9 C15	C16 HG2	C24 HP1
C9 H91	C17 C18	O32 HO3
C10 C11	C17 HH1	OD1 HOD
C10 C12	C17 HH2	ON1 HON

Table 4-30: Bonds in corticosterone.

C4	opls_157	0.263519	C22	opls_136	-0.12148	HF1	opls_140	0.058519
C5	opls_280	0.468519	C23	opls_280	0.468519	HG1	opls_140	0.058519
C6	opls_159	0.263519	C24	opls_142	-0.11648	HG2	opls_140	0.058519
C7	opls_136	-0.12148	HO3	opls_155	0.416519	HH1	opls_140	0.058519
C8	opls_136	-0.12148	H41	opls_156	0.038519	HH2	opls_140	0.058519
C9	opls_137	-0.06148	H42	opls_156	0.038519	HK1	opls_140	0.058519
C10	opls_139	-0.00148	HO6	opls_155	0.416519	HK2	opls_140	0.058519
C11	opls_135	-0.18148	H71	opls_140	0.058519	HK3	opls_140	0.058519
C12	opls_136	-0.12148	H72	opls_140	0.058519	HL1	opls_140	0.058519
C13	opls_280	0.468519	H81	opls_140	0.058519	HL2	opls_140	0.058519
C14	opls_137	-0.06148	H82	opls_140	0.058519	HM1	opls_140	0.058519
C15	opls_137	-0.06148	H91	opls_140	0.058519	HM2	opls_140	0.058519
C16	opls_136	-0.12148	HB1	opls_140	0.058519	HP1	opls_144	0.113519
C17	opls_136	-0.12148	HB2	opls_140	0.058519	O32	opls_154	-0.68448
C18	opls_141	-0.00148	HB3	opls_140	0.058519	O51	opls_281	-0.47148
C19	opls_139	-0.00148	HC1	opls_140	0.058519	O61	opls_154	-0.68448
C20	opls_135	-0.18148	HC2	opls_140	0.058519	OD1	opls_281	-0.47148
C21	opls_136	-0.12148	HE1	opls_140	0.058519	ON1	opls_281	-0.47148

Table 4-31: Parameters for atoms in cortisone.

C4 O32	C10 C12	C17 HH2
C4 C5	C11 HB1	C18 C19
C4 H41	C11 HB2	C18 C24
C4 H42	C11 HB3	C19 C20
C5 C6	C12 C13	C19 C21
C5 O51	C12 HC1	C20 HK1

C6 C7	C12 HC2	C20 HK2
C6 C10	C13 C14	C20 HK3
C6 O61	C13 OD1	C21 C22
C7 C8	C14 C15	C21 HL1
C7 H71	C14 C19	C21 HL2
C7 H72	C14 HE1	C22 C23
C8 C9	C15 C16	C22 HM1
C8 H81	C15 HF1	C22 HM2
C8 H82	C16 C17	C23 C24
C9 C10	C16 HG1	C23 ON1
C9 C15	C16 HG2	C24 HP1
C9 H91	C17 C18	O32 HO3
C10 C11	C17 HH1	O61 HO6

Table 4-32: Bonds in cortisone.

C4	opls_157	0.146111	C22	opls_136	-0.11889	HF1	opls_140	0.061111
C5	opls_280	0.471111	C23	opls_280	0.471111	HG1	opls_140	0.061111
C6	opls_137	-0.05889	C24	opls_142	-0.11389	HG2	opls_140	0.061111
C7	opls_136	-0.11889	HO3	opls_155	0.419111	HH1	opls_140	0.061111
C8	opls_136	-0.11889	H41	opls_156	0.041111	HH2	opls_140	0.061111
C9	opls_137	-0.05889	H42	opls_156	0.041111	HK1	opls_140	0.061111
C10	opls_139	0.001111	H61	opls_140	0.061111	HK2	opls_140	0.061111
C11	opls_277	0.451111	H71	opls_140	0.061111	HK3	opls_140	0.061111
C12	opls_136	-0.11889	H72	opls_140	0.061111	HL1	opls_140	0.061111
C13	opls_158	0.206111	H81	opls_140	0.061111	HL2	opls_140	0.061111
C14	opls_137	-0.05889	H82	opls_140	0.061111	HM1	opls_140	0.061111
C15	opls_137	-0.05889	H91	opls_140	0.061111	HM2	opls_140	0.061111
C16	opls_136	-0.11889	HB1	opls_279	0.001111	HP1	opls_144	0.116111
C17	opls_136	-0.11889	HC1	opls_140	0.061111	O32	opls_154	-0.68189
C18	opls_141	0.001111	HC2	opls_140	0.061111	O51	opls_281	-0.46889
C19	opls_139	0.001111	HD1	opls_156	0.041111	OB1	opls_278	-0.44889
C20	opls_135	-0.17889	HOD	opls_155	0.419111	OD1	opls_154	-0.68189
C21	opls_136	-0.11889	HE1	opls_140	0.061111	ON1	opls_281	-0.46889

Table 4-33: Parameters for atoms in aldosterone.

C4 O32	C10 C12	C17 HH2
C4 C5	C11 OB1	C18 C19
C4 H41	C11 HB1	C18 C24
C4 H42	C12 C13	C19 C20
C5 C6	C12 HC1	C19 C21
C5 O51	C12 HC2	C20 HK1
C6 C7	C13 C14	C20 HK2
C6 C10	C13 HD1	C20 HK3
C6 H61	C13 OD1	C21 C22
C7 C8	C14 C15	C21 HL1

C7 H71	C14 C19	C21 HL2
C7 H72	C14 HE1	C22 C23
C8 C9	C15 C16	C22 HM1
C8 H81	C15 HF1	C22 HM2
C8 H82	C16 C17	C23 C24
C9 C10	C16 HG1	C23 ON1
C9 C15	C16 HG2	C24 HP1
C9 H91	C17 C18	O32 HO3
C10 C11	C17 HH1	OD1 HOD

Table 4-34: Bonds in aldosterone.

C4	opls_157	0.145769	C22	opls_142	-0.11423	HF1	opls_140	0.060769
C5	opls_280	0.470769	C23	opls_280	0.470769	HG1	opls_140	0.060769
C6	opls_159	0.265769	C24	opls_142	-0.11423	HG2	opls_140	0.060769
C7	opls_136	-0.11923	HO3	opls_155	0.418769	HH1	opls_140	0.060769
C8	opls_136	-0.11923	H41	opls_156	0.040769	HH2	opls_140	0.060769
C9	opls_137	-0.05923	H42	opls_156	0.040769	HK1	opls_140	0.060769
C10	opls_139	0.000769	HO6	opls_155	0.418769	HK2	opls_140	0.060769
C11	opls_135	-0.17923	H71	opls_140	0.060769	HK3	opls_140	0.060769
C12	opls_136	-0.11923	H72	opls_140	0.060769	HL1	opls_144	0.115769
C13	opls_280	0.470769	H81	opls_140	0.060769	HM1	opls_144	0.115769
C14	opls_137	-0.05923	H82	opls_140	0.060769	HP1	opls_144	0.115769
C15	opls_137	-0.05923	H91	opls_140	0.060769	O32	opls_154	-0.68223
C16	opls_136	-0.11923	HB1	opls_140	0.060769	O51	opls_281	-0.46923
C17	opls_136	-0.11923	HB2	opls_140	0.060769	O61	opls_154	-0.68223
C18	opls_141	0.000769	HB3	opls_140	0.060769	OD1	opls_281	-0.46923
C19	opls_139	0.000769	HC1	opls_140	0.060769	ON1	opls_281	-0.46923
C20	opls_135	-0.17923	HC2	opls_140	0.060769			
C21	opls_142	-0.11423	HE1	opls_140	0.060769			

Table 4-35: Parameters for atoms in prednisolone.

C4 O32	C10 C12	C17 HH2
C4 C5	C11 HB1	C18 C19
C4 H41	C11 HB2	C18 C24
C4 H42	C11 HB3	C19 C20
C5 C6	C12 C13	C19 C21
C5 O51	C12 HC1	C20 HK1
C6 C7	C12 HC2	C20 HK2
C6 C10	C13 C14	C20 HK3
C6 O61	C13 OD1	C21 C22
C7 C8	C14 C15	C21 HL1
C7 H71	C14 C19	C22 C23
C7 H72	C14 HE1	C22 HM1
C8 C9	C15 C16	C23 C24

C8 H81	C15 HF1	C23 ON1
C8 H82	C16 C17	C24 HP1
C9 C10	C16 HG1	O32 HO3
C9 C15	C16 HG2	O61 HO6
C9 H91	C17 C18	
C10 C11	C17 HH1	

Table 4-36: Bonds in prednisolone.

Molecular Probe Adsorption (MPA) Surface Area. The free surface area of the polymer-wrapped SWNT was estimated using a molecular probe adsorption technique. Fluorescence calibration curves of riboflavin from 0 to 5 μM were measured using a Thermo VarioSkan Plate Reader. Riboflavin were excited at 460 nm, and emission were collected from 510 to 540 nm. Deflections of the riboflavin fluorescence were taken in the presence of 10 mg/mL polymer and a solution of 10 mg/L SWNT with 10 mg/mL polymer. The surface area was estimated according to Park et al.⁶⁵

Hydrogel Fabrication and Characterization. SWNT were encapsulated in a hydrogel matrix using a modified version of a previously reported protocol.⁶⁶ Briefly PEGDA (100 mg/L), dispersed SWNT (10 mg/L), and 2-hydroxy-4'-(2-hydroxyethoxy)-2-methylpropiophenone (0.175 mg/mL) were mixed in 1x PBS. The mixture was placed into glass molds. After a 30 minute incubation in a nitrogen atmosphere, the molds were crosslinked under 365 nm ultraviolet light (UVP Blak-Ray XX-15BLB, 15 W) for 1 hour. The hydrogels were incubated in 1x PBS, with a replacement with fresh 1x PBS after 48 hours to remove unencapsulated SWNT and excess polymer.

Hydrogels were cut to 5 x 5 x 1 mm sections. Hydrogels were either used directly after fabrication or were placed into 6-8 kDa dialysis bags with a volume of 300 μL 1x PBS.

Fluorescence imaging on hydrogels were performed using a 2D InGaAs camera (Princeton Instruments) coupled to a Nikon AF Micro-Nikkor 60 mm 4/2.8D lens. The hydrogels were

illuminated under a 785 nm Invictus laser (Kaiser). The optical window from 1075 – 1200 nm was monitored using a 1075 nm longpass filter and 1200 nm shortpass filter (Edmund Optics). To test progesterone responsivity, unencapsulated hydrogels were placed in 6-well plates and exposed to varying concentrations of progesterone. Hydrogels encapsulated in 6-8 kDa dialysis bags (Spectrum Labs) were imaged inside of transparent, 20 mL scintillation vials with 100 μ M progesterone solution in 2% DMSO and 1x PBS.

Excitation-emission maps were constructed by tracking the fluorescence spectrum from 950 – 1250 nm while stepping the excitation from 500 – 800 nm in 5 nm increments. A 1 W broadband white laser (NKT Photonics) was coupled to a tunable filter with a 2 nm bandwidth (Photon Etc.) and fed to the aforementioned custom built NIR microscope array.

In vivo implantation and imaging. These procedures were reviewed and approved by the Committee on Animal Care at MIT. Prior to implantation, hydrogels were incubated in 2% DMSO and 1x PBS, with or without 100 μ M progesterone for three hours. The hydrogels were then sterilized under 365 nm UV light (UVP Blak-Ray XX-15BLB, 15 W) for 10 minutes.

Female 7 week old SKH-1E mice (Charles River Laboratory) were anesthetized under 2% isoflurane gas for 15 minutes. Once unresponsive to a toe pinch, the implantation site was sterilized using alternating washes with iopovidone and 70% ethanol repeated thrice. Hydrogels were placed subcutaneously in the dorsal side of the animal. The wound was closed with nylon sutures. Animals were imaged under 2% isoflurane using a 2D InGaAs camera coupled to a Nikon AF Micro-Nikkor 60 mm 4/2.8D lens, 1075 nm longpass filter, and 1200 nm shortpass filter. The mice were illuminated under a 785 nm Invictus laser dispersed over the surface of the animal to a power density of 10 mW/cm². After their experimental lifetime, mice were euthanized by CO₂ asphyxiation.

Results and Discussion

Polymer Library Design. Central to the synthetic strategy of the **Corona Phase Molecular Recognition (CoPhMoRe)** technique is a polymer adsorbed and pinned into a configuration onto a nanoparticle surface, which together also act as a sensor transducer for the reporting of molecular binding^{54,56,59,60}. Computational models can be used to predict the underlying corona phase structures and necessary binding constants for robust functioning in *in vivo* environments.^{15,61,67} In this work, we explore a synthetic approach whereby a chemical appendage off of the backbone of the polymer, similar in molecular weight and chemical structure to the target analyte (Figure 4-7a) creates a reversible binding pocket within the corona phase. The rationale is that as the polymer adsorbs and becomes the nanoparticle corona, the appendage self-templates the corona, creating an encapsulating binding pocket ideal for analyte recognition. We hypothesize that the appendage should reversibly adsorb, while still attached to the backbone, such that the vacancy produced is capable of recognizing molecules of similar size and molecular weight. This templating could be considered a corona phase analog of the molecular imprinting technique, except that the analyte template is never removed, but remains bound to the backbone, and no-cross-linking is required.⁶⁸⁻
⁷⁴ A clear advantage is that this gives the newly created binding site direct access to the underlying transducer, which can remain nanometer in scale. The bound appendage should be reversibly displaced upon addition of a more strongly adsorbing analyte. We observe that this is the case for two important steroid sensors: a cortisol sensor, P1-(6,5), and the progesterone sensor, P10-(7,6), as discussed in-depth below.

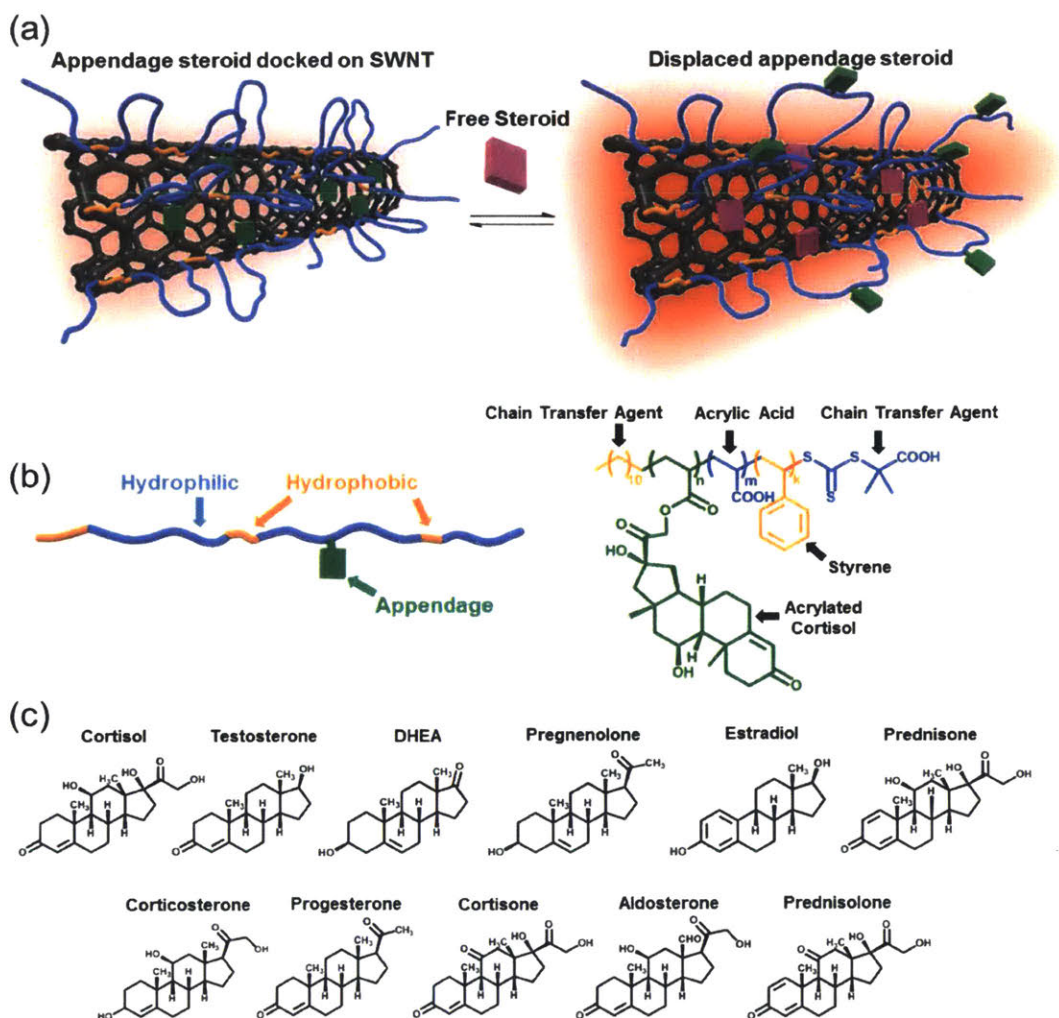


Figure 4-7: Semi-rational design for Corona Phase Molecular Recognition sensor for steroid hormone sensing. (a) Proposed mechanism of sensor. The initial configuration of the polymer on the SWNT involves charged hydrophilic groups (blue) extending out into aqueous solution and hydrophobic monomers (orange) anchoring the polymer non-covalently onto the SWNT. A template steroid molecule (orange) is weakly bound to the SWNT, such that exogenously administered steroid molecules (magenta) will displace the appendage, resulting in a polymer configuration change and consequently change in SWNT fluorescence. (b) Polymers were composed of hydrophobic styrene monomers and alkyl chains (orange), hydrophilic acrylic acid monomers and carboxylic acid groups (blue), and acrylated cortisol (green). (c) Panel of steroid hormones used in the sensor screening, chosen for their physiological and therapeutic significance.

The corona phase library was generated using RAFT polymerization to generate low polydispersity, random copolymers consisting of acrylic acid, styrene, and acrylated cortisol, the chemical appendage. The acrylic acid portion of the backbone provides the hydrophilic units and colloidal stability at physiological pH. The hydrophobic styrene units serve as anchor points for

the polymer backbone onto the SWNT (Figure 4-7b). The unit composition of the polymers was varied to produce structurally diverse corona phases to sample a range of free-volumes and relative strengths of dynamic binding/unbinding of the appendage. In total, we explore 80 unique corona phases in this work based on 16 polymer backbones to suspend five sets of SWNT chiralities grouped by emission maximum wavelengths: (8,3) and (6,5); (7,5); (10,2); (9,4) and (7,6); and (12,1). These SWNT span a range from 0.75 to 1.0 nm in diameter. These were tested against a panel of 11 steroids, chosen for their physiological and therapeutic significance (Figure 4-7c).

The near-IR fluorescence response of each SWNT wrapped in a distinct polymer corona phase was measured using a solution of 1 mg/L SWNT/corona exposed to 100 μ M steroid in 1x PBS containing 2% DMSO for analyte solubility (Figure 4-8a). The resulting heat map of binding shows several important trends with varying polymer composition. A comparison between self-templated and non-templated polymers demonstrates increased affinity toward progesterone with greater appendage content in the polymers (Figure 4-8b-c), supporting this templating approach. As expected, a one-to-one correspondence between appendage structure and analyte selectivity is not observed. The appendage is based around the molecular structure of cortisol – which shares the three concatenated, 6-membered rings with one pentamer ring with the entire steroidal set considered in this work. The resulting selectivity for progesterone suggests that it has a stronger affinity for the resulting cavity upon appendage desorption. The screening results in Figure 4-8 point to two corona phases of particular interest in this current study.

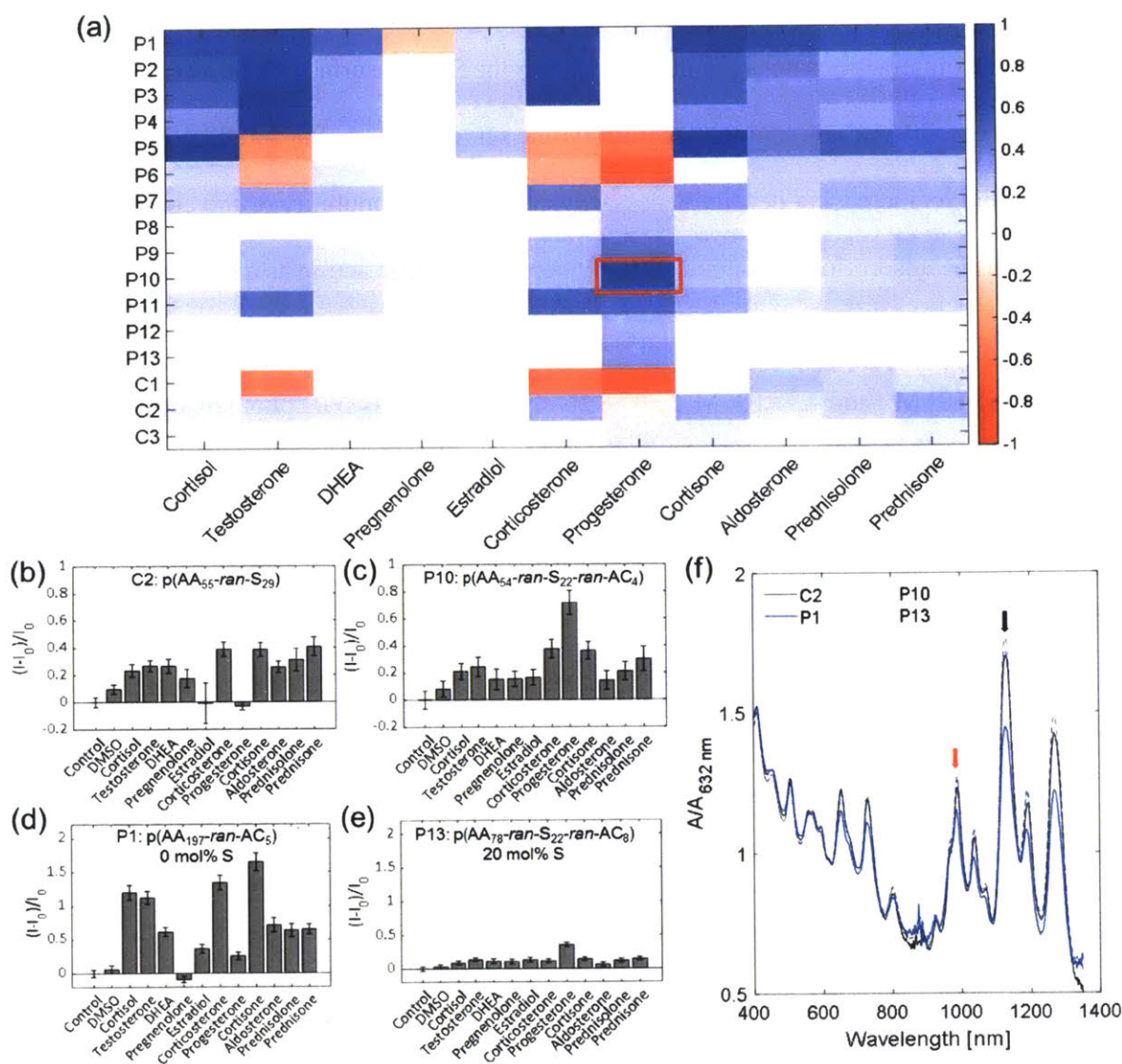


Figure 4-8: Summary of polymer library screening results. (a) Heat map showing the fractional fluorescence change, $(I-I_0)/I_0$, of the (9,4) and (7,6) chiralities of each member of the sensor library against 100 μM of each steroid in 2% DMSO and 1x PBS. Red denotes a fluorescence decrease, while blue indicates an increase. P indicates polymers with appendage steroids, while C denotes polymers without appendages. The selective response of P10-(7,6) is boxed in red. The full compositions of each polymer are given in Supporting Information. (b-c) Comparison of composite (9,4) and (7,6) fluorescence response of HiPCO SWNT wrapped with (b) C2, a polymer with 0 appendage units, versus (c) P10, a polymer with 4 appendage units. Increasing the number of appendage units while keeping the number of acrylic acid and styrene relatively fixed at approximately 55 and 25, respectively, increased progesterone selectivity and sensitivity. (d-e) A polymer with (d) 0 mol% styrene, P1, exhibited higher steroid sensitivity but lower selectivity compared to a polymer with (e) higher styrene content at 20 mol%, P13. (f) UV-Vis-NIR absorption spectrum of polymer-suspended HiPCO SWNT, indicating successful suspension of SWNT in the parameter space of the polymer library. The (9,4) and (7,6) channel is indicated with a black arrow, while the red arrow indicates the (6,5) chirality.

We find that increasing styrene content systemically decreases the nIR fluorescence response to analyte binding for the entire steroid library (Figure 4-8d-e). As an anchor for the

polymer corona, styrene is shown to influence the responsivity in two ways. Styrene itself can sterically block interactions between the analyte and the SWNT surface by occupying surface area otherwise accessible for adsorption. Second, styrene serves as an anchor for the polymer backbone by design, and its increasing density necessarily constrains the mobility of the corona phase. The molecular probe adsorption technique strongly supports styrene acting as a blocker of the SWNT surface area, as P1-(6,5) with 0 mol% styrene and P10-(7,6) with 27.5 mol% styrene showed q/K_d values of $2.9 \times 10^3 \text{ M}^{-1}$ and $4.7 \times 10^2 \text{ M}^{-2}$, respectively. The UV-Vis-NIR photoabsorption spectra of the SWNT/corona systems that comprise the heat map of responses show well-resolved E_{11} and E_{22} photoabsorption transitions, consistent with colloidal dispersion in contrast to aggregation (Figure 4-8f, Figure 4-9, Figure 4-10), without an increase in the full-width at half maximum of the peaks.⁷⁵ SWNT aggregation also causes nIR fluorescence quenching.⁷⁶

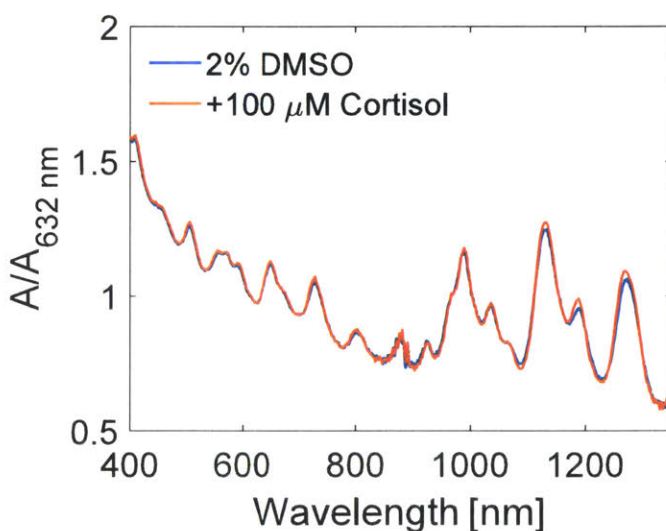


Figure 4-9: UV-Vis-NIR photoabsorption spectrum of HiPCO SWNT suspended with P1 with 100 μM cortisol and with 2% DMSO as a control. The presence of well-defined peaks before and after analyte additions indicates that nanoparticle aggregation is not the primary mechanism of sensing.

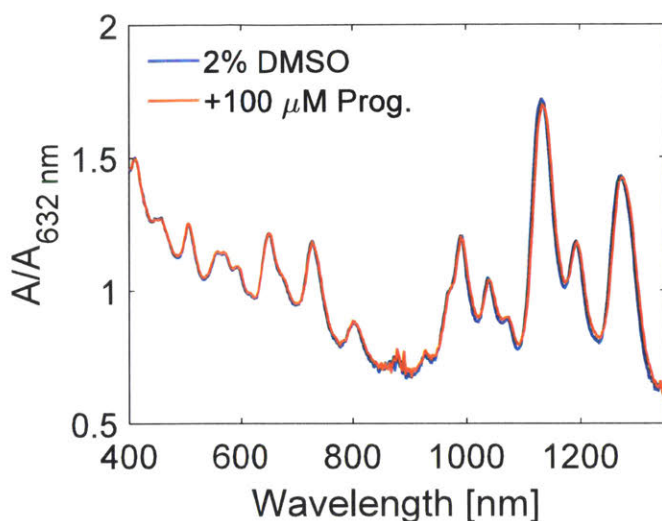


Figure 4-10: UV-Vis-NIR photoabsorption spectrum of HiPCO SWNT suspended with P10 with 100 μM progesterone and with 2% DMSO as a control. The presence of well-defined peaks before and after analyte addition indicate that nanoparticle aggregation is not the primary mechanism of sensing.

We examine two SWNT corona phases with high selectivity: P1-(6,5) for cortisol and P10-(7,6) for progesterone. The first, P1-(6,5) consists of a (6,5) chirality SWNT wrapped by p(AA₁₉₇-ran-AC₅) polymers and exhibit a 90% turn-on fluorescence response to cortisol (Figure 4-11a), whereas the magnitude of the second highest response is 57% at 100 μM (Figure 4-11b). The sensor was exposed to varying cortisol concentrations, and the response was fit to the following functional form:

$$\frac{I - I_0}{I_0} = \beta \frac{C}{C + K_D} \quad (4-1)$$

Where I is the fluorescence intensity after steroid addition, I_0 is the original intensity, β is the proportionality factor between analyte occupancy and fluorescence intensity change, C is the steroid concentration, and K_D is the equilibrium dissociation constant (Figure 4-11c). A solution of 1 mg/L SWNT is responsive between 10 – 200 μM . The calibration curve was not extended beyond 200 μM due to solubility, which precluded a meaningful K_D value from being calculated.

The second corona phase, P10-(7,6), is selective to progesterone and comprised of a SWNT wrapped with p(AA₅₃-ran-S₂₂-ran-AC₄) polymer (Figure 4-11d). The response appears strongly chirality dependent, with the (9,4) and (7,6) fluorescence peaks having the strongest response at 72%, while the remaining chiralities exhibit a less intense turn-on response. The sensor exhibits some selectivity with the next highest responses inducing only a 38% fluorescence increase at 100 μ M (Figure 4-11e). The calibration curve shows sensor responses between 5-100 μ M and a K_D of 100 μ M (Figure 4-11f). P10-(7,6) exhibited selectivity toward progesterone even with an expanded analyte list including small molecules of acyclic and cyclic structures and large molecular weight proteins (Figure 4-11g). Despite the common structural features among the steroids, no trends were observed when considering the oxidation state of each steroid, as well as the spatial distribution of oxygen groups on the backbone. Furthermore, we rule out the possibility of a non-specific hydrophobic interaction, as progesterone appears as an outlier when considering its response vs. its logP value (Figure 4-11h).

These results strongly support that the corona phase itself discriminates between steroids based on their specific molecular shape and chemical display. The curvature of the SWNT surface appears to influence the resulting corona phase binding, with the (10,2), (9,4), and (7,6) chiralities wrapped with P10 being the most sensitive to progesterone and the (6,5) chirality being non-selective (Figure 4-11i). An nIR fluorescence excitation-emission map taken before and after the addition of 100 μ M confirms that the (9,4) and (7,6) chiralities are the most sensitive to progesterone (Figure 4-11j-k).

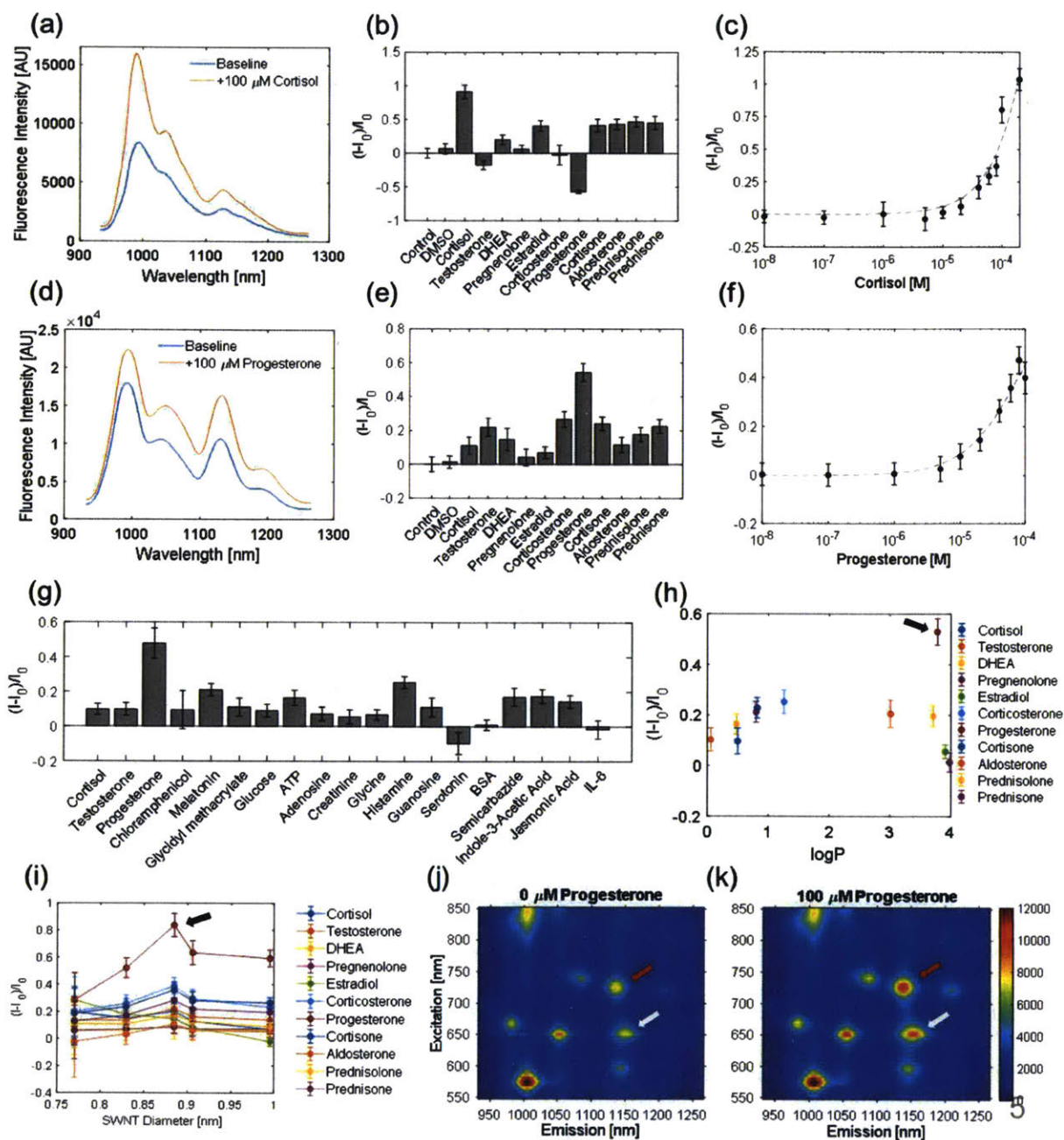


Figure 4-11: Sensor performance in solution phase. (a) The cortisol sensor consists of a low styrene, high template polymer wrapped around (6,5) Comocat SWNT, whose fluorescence increases in response to cortisol. (b) Cortisol induces approximately twice a change in fluorescence intensity magnitude versus the other steroids at the equivalent concentration of 100 μM . (c) Calibration curve showing sensor sensitivity from 20 μM to 100 μM . (d) The progesterone sensor consists of a high styrene, high template polymer wrapped around HiPCO SWNT, whose fluorescence increases in response to progesterone. (e) The progesterone sensor is selective towards progesterone over other steroids by a factor of 2, all tested at 100 μM . (f) The progesterone sensor has a detection range from 10 to 100 μM . (g) (9,4) and (7,6) SWNT wrapped with P10 exhibit selectivity toward progesterone even among other classes of small molecules and large proteins. (h) The progesterone sensing mechanism is not a simple hydrophobicity sensor, indicated by its sensor response relative to its partition coefficient. Progesterone is indicated by the black arrow. (i) The responsiveness to each steroid of P10-wrapped SWNT depends on diameter, with an optimum SWNT diameter being observed for progesterone responsivity, as indicated by the arrow. (j-k) Excitation-emission plots of the progesterone sensor (j) before and (k)

after the addition of 100 μ M progesterone show that the (10,2), (9,4), and (7,6) chiralities are the most sensitive, as indicated by the arrows in orange, red, and white, respectively.

Molecular dynamics simulations were performed in GROMACS to characterize the mechanism of molecular recognition and the structure of the binding site. In the absence of a corona on the SWNT, steroids adsorb onto the surface to maximize the surface contact of its alkyl rings onto the SWNT surface, while minimizing unfavorable steric interactions due to protruding methyl groups and interactions with hydrophilic oxygen groups (Figure 4-12a). Short-range Lennard-Jones potentials did not vary significantly among steroids, with a range of -79 kJ/mol to -93 kJ/mol. Progesterone was ranked second-highest with a LJ potential of -90 kJ/mol (Figure 4-12b). To quantify the relative energetic contributions of each monomer in P10 to the interaction with SWNT, simulations were conducted using poly(acrylic acid)₂₀, poly(styrene)₂₀, and poly(acrylated cortisol)₅. The Lennard-Jones potential was -12.5 kJ/monomer, -17.3 kJ/monomer, and -81.4 kJ/monomer, for acrylic acid, styrene, and acrylated cortisol, respectively. We observe that poly(acrylic acid) wraps around SWNT with the alkyl backbone adsorbed and its charged carboxylate groups pointing away (Figure 4-12d). Poly(styrene) interacts primarily through π - π stacking, with the phenyl ring interacting with SWNT in T-shaped, sandwich, and parallel-displaced configurations (Figure 4-12e). It is noteworthy that the relatively short distance (1 carbon-carbon bond) between the phenyl group and alkyl backbone leads to inflexibility forcing some phenyl groups on the homopolymer to extend away from the SWNT. In the random copolymer with lower mol. percent of styrene, we expect this effect to be less pronounced. Poly(acrylated cortisol) wraps around the SWNT to maximize binding between the steroidal rings, as described above (Figure 4-12f). Unlike styrene, however, there are 3 carbon-carbon bonds separating the rings from the alkyl chain, so all the monomers can wrap around the SWNT due to greater chain flexibility. When simulating the full P10 polymer, radial distribution functions

confirm that on average styrene and acrylated cortisol equilibrate more closely to the SWNT compared to acrylic acid, supporting our intuitive picture of the styrene and acrylated cortisol units acting as anchors and the acrylic acid units extended out into solution (Figure 4-12g). These anchor-loop conformations were observed in simulation (Figure 4-12h).

The selectivity to small differences in steroid structure observed experimentally may be attributed to the overall conformation of the SWNT, P10, and steroid complexes. Acrylic acid is capable of hydrogen bonding with hydroxyls and carbonyl groups on steroids, with smaller amounts of anchoring styrene monomers decreasing the spatial proximity of these H-bonding groups to each other and distance from the SWNT surface. Furthermore, the tethered appendages interact with the SWNT via hydrophobic interactions and with acrylic acids via H-bonding. The same polymer will adopt a different conformation on each SWNT chirality due to local curvature. Taken together, each corona is distinct and will interact with each steroid to a different degree. While the steroids share the same overall 4-alkyl ring backbone, they are distinct in the distribution of hydroxyl groups, carbonyls, and alkyl chains. Therefore, each steroid has a unique shape on the SWNT surface, which dictates the extent it can fit into a given corona phase and consequently selectivity. All together, the steroid occupies a binding pocket comprised of the SWNT, acrylic acid, styrene, and acrylated cortisol components, with the exact shape dictated by SWNT chirality and polymer composition (Figure 4-12i)

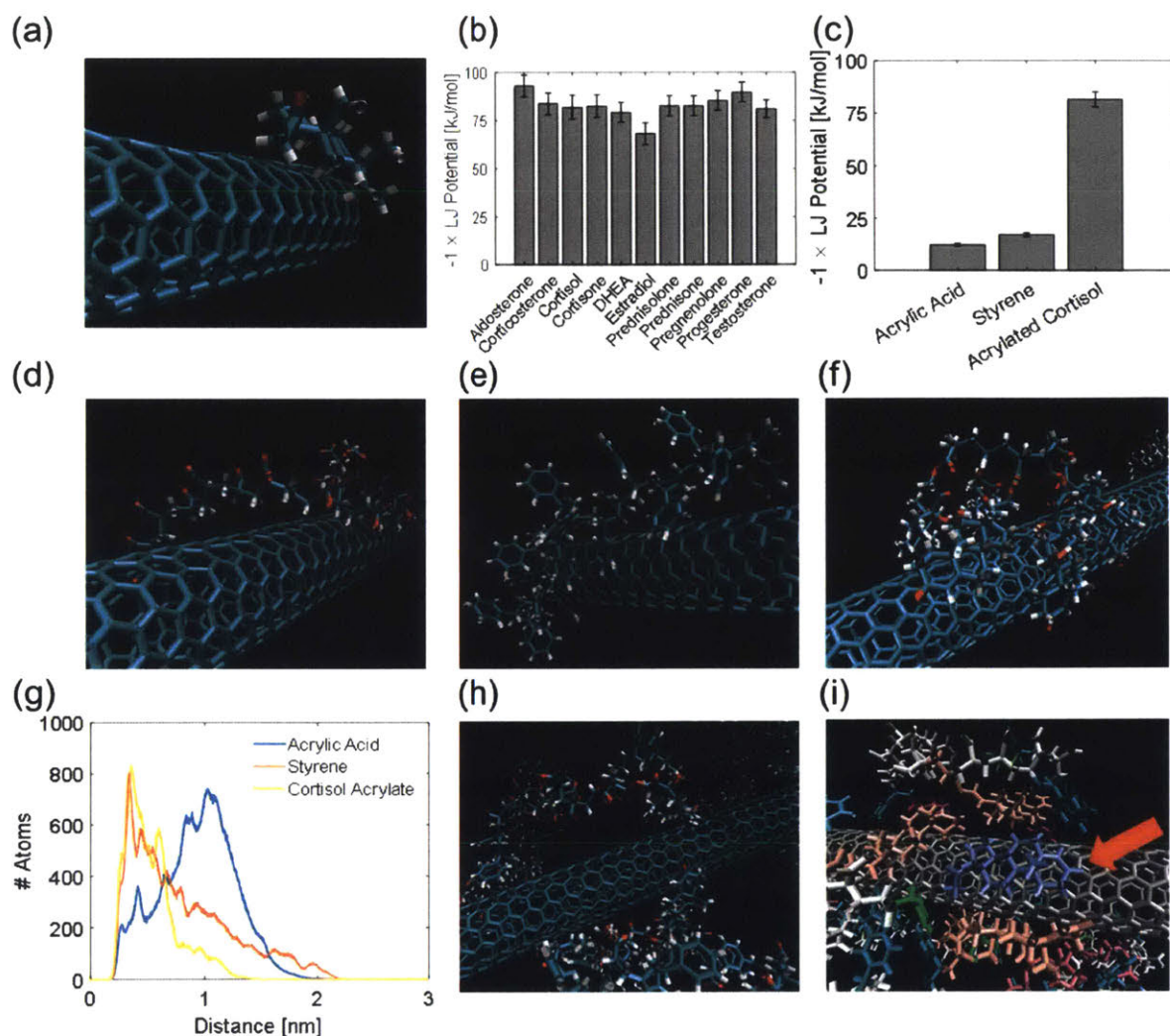


Figure 4-12: Molecular dynamics simulations to characterize SWNT corona. (a) Steroids adsorbed on bare (7,6) SWNT to maximize hydrophobic interactions while minimizing unfavorable steric interactions due to protruding methyl groups and contact with polar oxygen groups. (b) Short-range Lennard-Jones potential between steroids and bare (7,6) SWNT. (c) Short-range Lennard-Jones potential per monomer between (7,6) SWNT and poly(acrylic acid) with 20 units, poly(styrene) with 20 units, and poly(acrylated cortisol) with 5 units. (d-f) Snapshots of (d) poly(acrylic acid), (e) polystyrene, and (f) poly(acrylated cortisol) adsorbed onto (7,6) SWNT. (g) Radial distribution functions describing atom distance from surface of (7,6) SWNT for P10 adsorbed onto the SWNT surface. (h) Snapshot of P10 adsorbed on SWNT, demonstrating close proximity of styrene and acrylated cortisol and more distance acrylic acid from the SWNT surface. (i) A snapshot of progesterone (colored purple and indicated by arrow) occupying a binding site consisting of SWNT (silver), styrene (green), acrylic acid (white), and acrylated cortisol (peach).

The following heat maps were also obtained during the screening process and plot the sensor response of polymer suspended HiPCO SWNT against 100 μ M steroid. The functional form is the following:

$$\text{Response} = \frac{I - I_0}{I_0} \quad (4-2)$$

Each heat map plots the response of a single group of chiralities, as obtained from spectral deconvolution. Blue indicates a fluorescence increase, or ‘turn-on,’ whereas red indicates a fluorescence decrease, or ‘turn-off.’

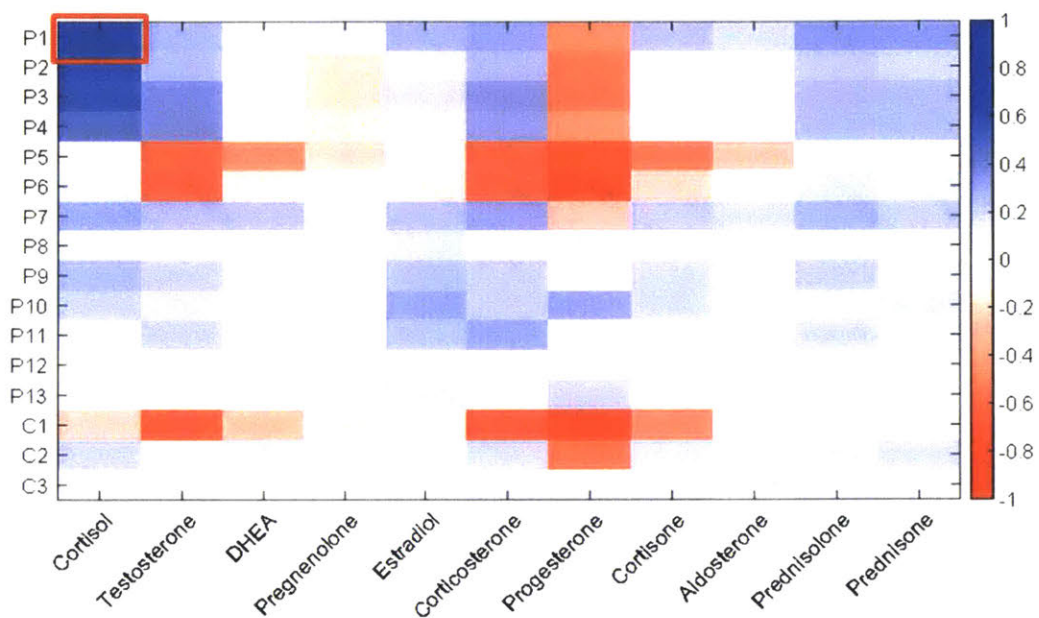


Figure 4-13: Composite (8,3) and (6,5) fluorescence response heat map. P1-(6,5) is marked with a red box. The selective response of P1-(6,5) to cortisol is boxed in red.

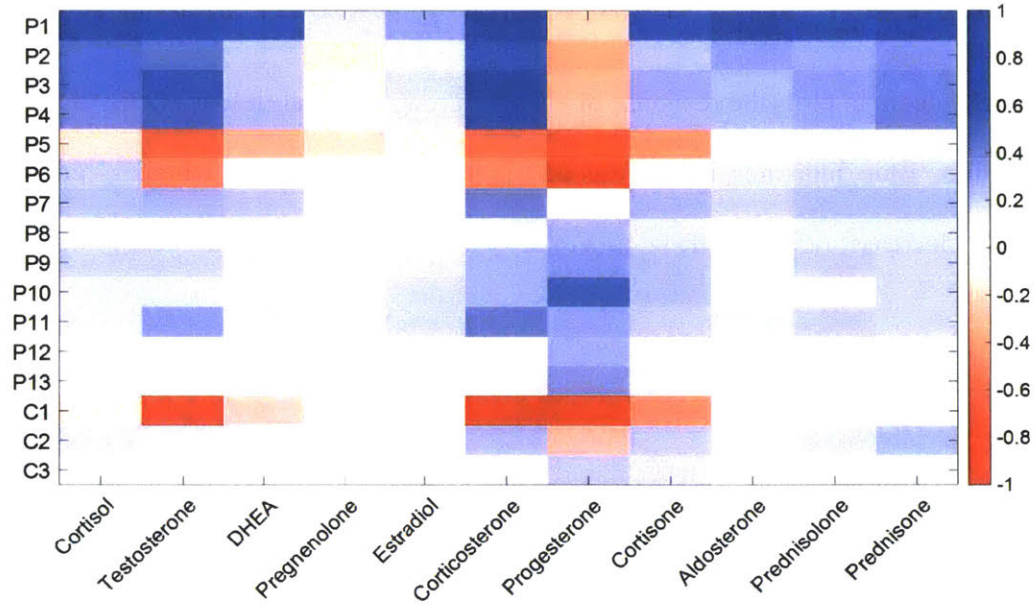


Figure 4-14: (7,5) fluorescence response heat map.

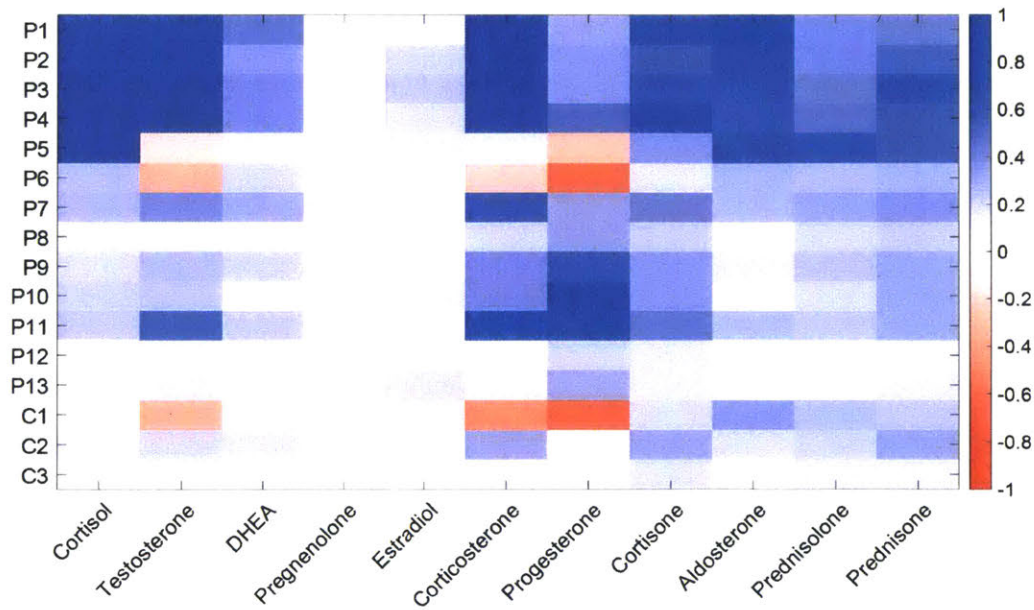


Figure 4-15: (10,2) fluorescence response heat map.

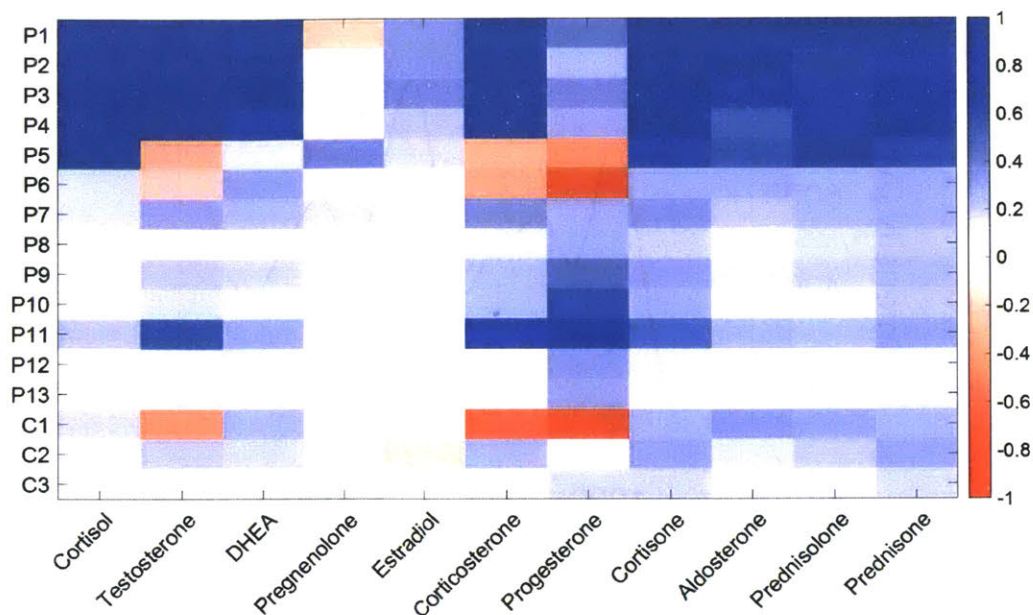


Figure 4-16: (12,1) fluorescence response heat map.

Hydrogel Characterization. To provide a biocompatible interface and a localizable implant that can be queried at any time *in vivo*, the progesterone sensor was tested in a variety of hydrogel materials (Figure 4-18a). Hydrogels have been made using a variety of materials, including polyacrylamide, PEG, poly(acrylic acid), poly(vinyl pyrrolidone), and alginate.⁶⁶ To choose the hydrogel, solution phase SWNT were mixed with the uncrosslinked polymers, and the responses to 100 μM progesterone were measured. Without progesterone, PEG has the least effect on baseline fluorescence, indicating the best preservation of the CoPhMoRe phase (Figure 4-18b). The other polymers induce larger intensity and/or wavelength shifts. Furthermore, only the samples with PEG and PVP have identical responses to 100 μM progesterone as the sensor in 1x PBS (Figure 4-18c). For these reasons, PEG was chosen as the encapsulating material for the progesterone sensor (Figure 4-17).

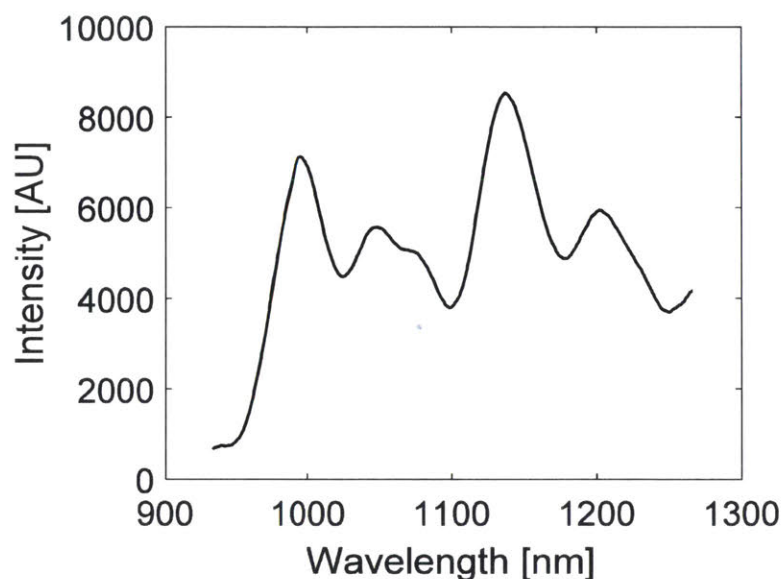


Figure 4-17: Fluorescence spectrum of P10-suspended HiPCO SWNT encapsulated in PEGDA hydrogel. The hydrogel was fabricated from a solution 10 wt% PEGDA in 1x PBS and 10 mg/L SWNT before cross-linking and swelling.

The functionality of the sensor in the hydrogel was verified through several tests. The hydrogel was exposed to alternating cycles of 0 and 100 μM progesterone in 1x PBS (Figure 4-18d). The hydrogel exhibits a stable and reversible response with a constant baseline. The stable baseline allows perturbations in fluorescence to be attributed to changes in analyte concentration rather than sensor artefacts. The sensor hydrogel's fluorescence response was also calibrated against progesterone (Figure 4-18e). After being equilibrated in 10% mouse serum in 1x PBS, the sensor still responds to 100 μM progesterone (Figure 4-18f). The magnitude of the response was lower at 12%, but reversibility was maintained. The lower response in the biological environment suggests the presence of interfering molecules that reduce sensor sensitivity. Nevertheless, these interfering molecules may be avoided with strategic placement of the sensor. For example, implanting the hydrogel in the interstitial space as opposed to intravascularly avoids proteins such as albumin, which non-specifically binds to a number of surfaces.⁷⁷ As indicated by the excitation-

emission map, the most sensitive chiralities in the hydrogel are still the (10,2), (9,4), and (7,6), as in solution phase (Figure 4-18g).

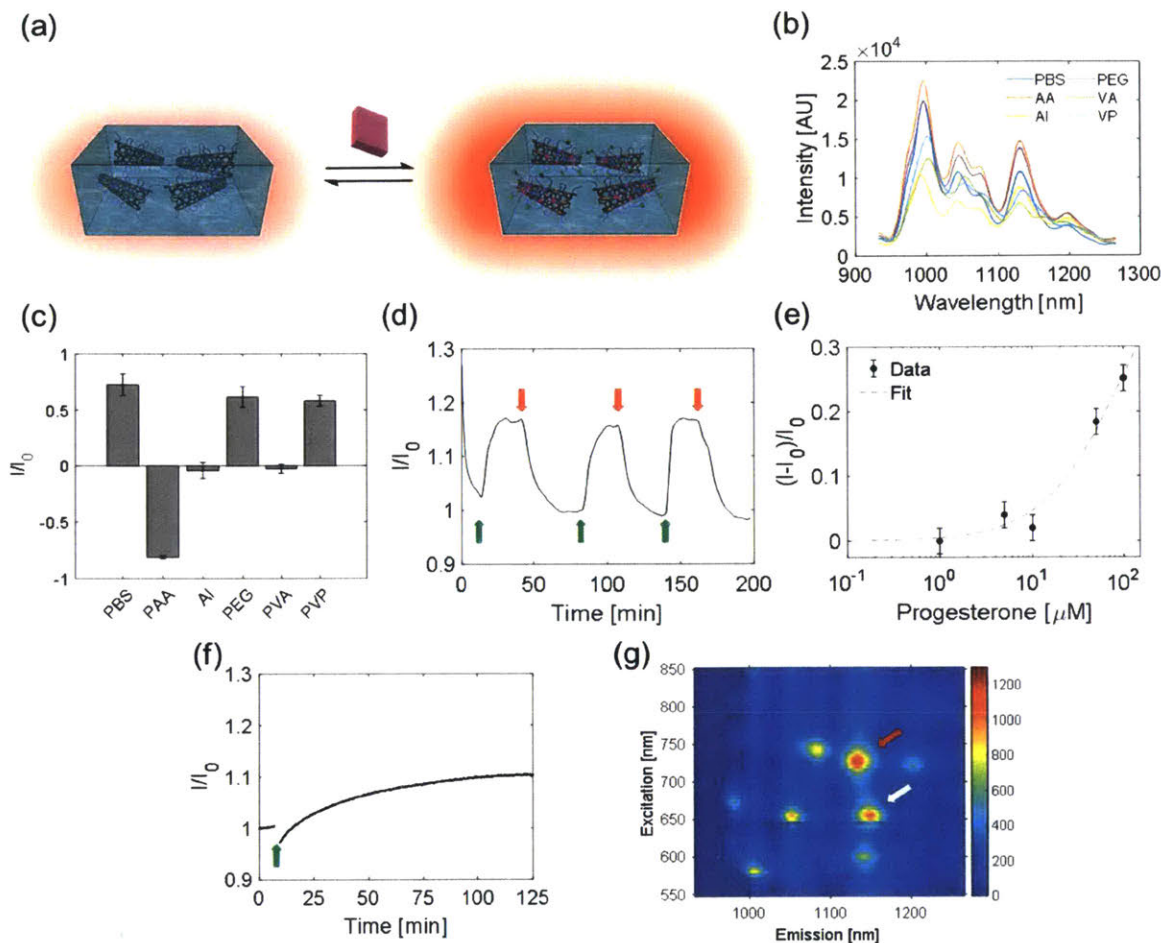


Figure 4-18: Hydrogel formulation, selection, and performance. (a) SWNT were encapsulated into PEGDA hydrogels, into which analytes diffuse and modulate fluorescence intensity. (b) Fluorescence spectrum of the progesterone sensor in 1x PBS and other commonly used hydrogel polymers before crosslinking. The degree of polymer interaction with SWNT can be seen by the shifting fluorescence spectrum. Among the different hydrogel components, PEG perturbed the sensor baseline fluorescence the least. (c) Sensor response to 100 μM when also incubated with hydrogel materials. Of the polymers tested, PEG and poly(vinyl pyrrolidone) preserved the sensor response compared to PBS. (d) Progesterone sensor encapsulated in PEGDA hydrogel exposed to varying cycles of 0 (red arrows) and 100 μM (green arrows) progesterone, showing a stable and reversible response of 18%. (e) Calibration curve of the progesterone sensor hydrogel. (f) The progesterone sensor hydrogel is functional in 10% mouse serum. (g) Excitation-emission plots show that the (9,4) and (7,6) chiralities are most sensitive to progesterone, marked in red and white, respectively.

The hydrogel-encapsulated SWNT exhibit a lower magnitude of response to progesterone at 30% versus the 60% observed in solution phase. Several contributions may exist. First, as the hypothesized mechanism involves displacement of the suspending polymer on the SWNT surface,

the crosslinked hydrogel matrix may reduce sensor sensitivity by constraining the movements of the suspending polymer. Second, the free radicals produced during hydrogel fabrication may have chemically altered the suspending polymer on the SWNT, which were produced using RAFT polymerization and are living.

***In vivo* proof of concept.** As a proof of concept of *in vivo* measurements of progesterone with the CoPhMoRe sensor, hydrogels with and without a dialysis bag were implanted subcutaneously into mice. Analytes would be able to pass freely into and out of the hydrogel through contact with the interstitial fluid.

Sensor hydrogels implanted without dialysis bags were deactivated upon implantation in a time dependent manner (Figure 4-21a). Compared to hydrogels subjected to the same sterilization procedure but not implanted, hydrogels that were implanted into a mouse, extracted, and tested *in vitro* were completely insensitive to 100 μ M progesterone after two hours. Conversely, when extracted within 2 hours and tested outside the mouse, hydrogels inside of 6-8 kDa dialysis bags still responded to 100 μ M progesterone with the same magnitude as the control. After 24 hours in the mouse, the hydrogel was only partially deactivated.

The deactivation of the hydrogel suggests the presence of an interfering molecule *in vivo* that either chemically alters or binds irreversibly to the CoPhMoRe site. Given that the sensor functions in mouse serum, the interferents are likely inflammatory molecules released at the implantation site during surgery. Furthermore, the kinetics of deactivation with dialysis bag over 24 hours suggest that at least one of the interferents has a molar mass on the order of 5 kDa. A number of different molecules are released in the acute inflammatory response, including cytokines, protein fragments, reactive oxygen and nitrogen species, etc.⁷⁸ To rule out biofouling of the bulk hydrogel as the deactivation mechanism, the zwitterionic component 2-

methacryloyloxyethyl phosphorylcholine (MPC) was added to the hydrogel formulation, verified to work *in vitro*, and again found to be deactivated after implantation into mice (Figure 4-19). The strong non-fouling attributes of MPC in PEG hydrogels have been reported in previous studies,⁷⁹ and the deactivation suggests that biofouling is not the predominant mechanism. To determine the presence of any chemical modification, FTIR measurements were performed on the hydrogels (Figure 4-21b). Due to the low mass concentration, the SWNT and the suspending polymers are not visible in the IR spectra (Figure 4-20). However, the bulk hydrogel spectra before and after sensor deactivation are identical. Therefore, chemical modification of the bulk hydrogel is not the primary mechanism of deactivation. Precise identification of the interferents will be the subject of future work.

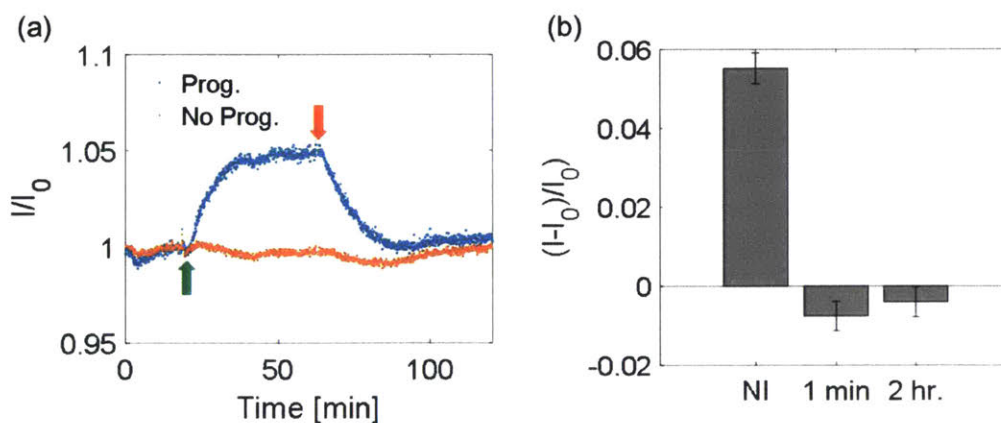


Figure 4-19: Fluorescence response of P10-SWNT encapsulated in hydrogels with 50 mg/mL 2-methacryloyloxyethyl phosphorylcholine (MPC) and 75 mg/mL PEGDA 8000 to 100 μ M progesterone. (a) Hydrogels were confirmed to respond to progesterone upon introduction of 100 μ M progesterone (green arrow) and confirmed to be reversal after changing the concentration to 0 μ M progesterone (red arrow). (b) Non-implanted (NI) controls were compared to hydrogels that had been implanted 1 minute or 2 hours and explanted.

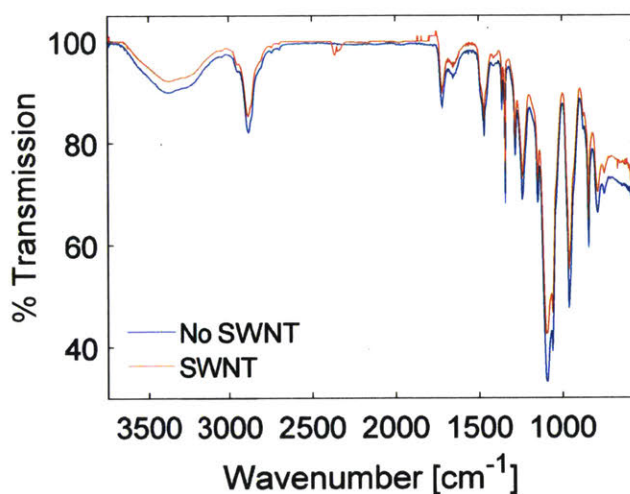


Figure 4-20: FTIR Spectra comparing hydrogels with and without SWNT. Due to their low concentration in the hydrogels, SWNT were not visible.

Nevertheless, the delay of deactivation by using a 6-8 kDa dialysis bag permitted a 24-hour window in which our sensor could be tested *in vivo*. The response profile to 100 μM progesterone *in vitro* was measured (Figure 4-21c). The equilibrium response was 27% and leveled out after 3 hours.

Two dialysis bags – one incubated in 100 μM progesterone and another incubated in 0 μM progesterone for three hours – were implanted simultaneously in multiple mice to test the short-term functionality of the sensors *in vivo* (Figure 4-21d-e). The *in vivo* trial exploited the reversibility of the sensor by measuring a decrease in fluorescence as progesterone diffuses out from the hydrogel. The sensor incubated in buffer served as a control to measure any perturbations in sensor due to the change in environment from buffer to interstitial fluid. In each trial, the sensor incubated in progesterone showed a higher decrease in fluorescence relative to its paired control (Figure 4-21f). Over three mice, the sensor response was $22.1 \pm 6.6\%$, and the control was $7.4 \pm 3.7\%$. The difference was statistically significant with a one-tailed p-value of 0.016 (Figure 4-21g).

The reversal monitoring demonstrates functionality of the sensor while working in the time constraint of deactivation. In its current form, the sensor will only function in the first day when implanted *in vivo*. The eventual application is long-term monitoring of steroids, so the interferent will be identified in future work. Therefore, the sensor formulation will be modified to mitigate the deactivation, as well as to decrease the limit of detection to target physiological values of progesterone. Physiological concentrations of cortisol and progesterone in typical people are lower than the dynamic range of the sensor. Cortisol exists between 0-500 nM,¹⁵ while progesterone can range from 0 to 800 nM depending on the status of pregnancy.^{80,81}

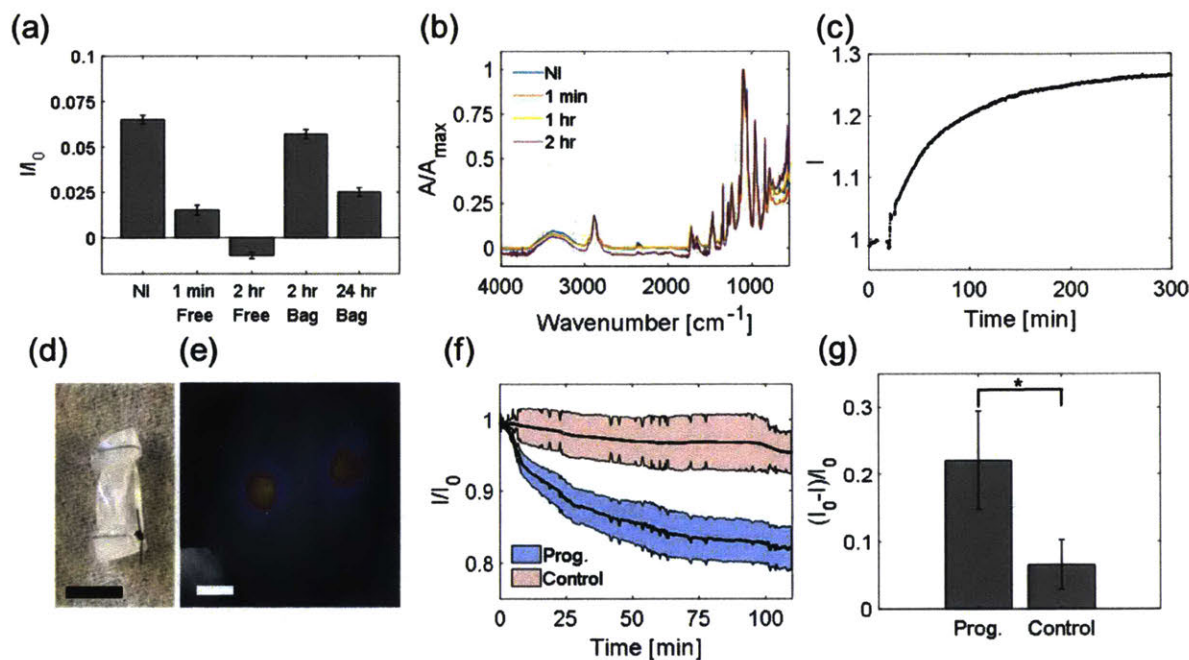


Figure 4-21 : Proof of concept of *in vivo* steroid sensor monitoring. (a) Response of sensor hydrogels to 100 μM progesterone outside of mice. The hydrogels were implanted subcutaneously either directly or inside of 6-8 kDa dialysis bags for varying durations of time and subsequently extracted. Direct implantation leads to deactivation over time, while the use of a dialysis bag slows the deactivation. (b) FTIR spectra do not show any changes in chemical functionalities of the bulk hydrogel material with implantation time. (c) Response of hydrogel inside of dialysis bags to 100 μM progesterone. (d) Hydrogels inserted into 6-8 kDa dialysis bags (scale = 5 mm). (e) Two hydrogels inside of dialysis bags implanted simultaneously in the dorsal subcutaneous space of SKH1-E mice (scale = 10 mm). One dialysis bag was incubated in 100 μM progesterone, while the other was incubated in the control buffer. (f) The dialysis bag incubated in progesterone shows a more intense fluorescence decrease over the control bag, as progesterone diffuses outside of the sensor hydrogel. The colored area represents the S.E.M. (n=3). (g) The trend was reproducible in 3 mice, with $p < 0.02$.

Conclusions and Future Work

In total, these experiments demonstrate both the feasibility and efficacy of the development process that originates with CoPhMoRe library synthesis and discovery, characterization, insertion into a biocompatible interface, and *in vivo* measurement. Hence, this work underscores a new strategy for *in vivo* bioanalyte monitoring and motivates further development to broaden the classes of measured biomarkers and their measurable concentrations. In the steroid space, future research avenues exist. To permit long-term monitoring of progesterone, the sensor deactivation mechanism will be elucidated, and interfering molecules will be identified. Additionally, the limit of detection of the progesterone sensor will be decreased to enable monitoring of the entire dynamic range of the analyte. Furthermore, the tunability of the template steroid system and hydrogel formulations will be further explored to construct sensors for other steroid hormones. In this way, several unique sensors for a range of bioanalytes can be constructed to enable multiplexed biomarker measurements to compose a comprehensive evaluation of an individual's health.

References

- (1) Fernandez-Real, J.-M.; Pugeat, M.; Emptoz-Bonneton, A.; Ricart, W. Study of the effect of changing glucose, insulin, and insulin-like growth factor-I levels on serum corticosteroid binding globulin in lean, obese, and obese subjects with glucose intolerance. *Metabolism* **2001**, *50* (10), 1248–1252 DOI: <https://doi.org/10.1053/meta.2001.25647>.
- (2) de Kloet, E. R.; Vreugdenhil, E.; Oitzl, M. S.; Joëls, M. Brain Corticosteroid Receptor Balance in Health and Disease*. *Endocr. Rev.* **1998**, *19* (3), 269–301 DOI: 10.1210/edrv.19.3.0331.
- (3) Nock, B.; Feder, H. H. Neurotransmitter modulation of steroid action in target cells that

- mediate reproduction and reproductive behavior. *Neurosci. Biobehav. Rev.* **1981**, *5* (4), 437–447 DOI: [https://doi.org/10.1016/0149-7634\(81\)90014-2](https://doi.org/10.1016/0149-7634(81)90014-2).
- (4) Barnes, P. J.; Adcock, I.; Spedding, M.; Vanhoutte, P. M. Anti-inflammatory actions of steroids: molecular mechanisms. *Trends Pharmacol. Sci.* **1993**, *14* (12), 436–441 DOI: [https://doi.org/10.1016/0165-6147\(93\)90184-L](https://doi.org/10.1016/0165-6147(93)90184-L).
- (5) Sapolsky, R. M.; Romero, L. M.; Munck, A. U. How Do Glucocorticoids Influence Stress Responses? Integrating Permissive, Suppressive, Stimulatory, and Preparative Actions. *Endocr. Rev.* **2000**, *21* (1), 55–89 DOI: 10.1210/edrv.21.1.0389.
- (6) Litwack, G. Steroid Hormones. In *Human Biochemistry*; Litwack, G. B. T.-H. B., Ed.; Academic Press: London, 2018; pp 467–506.
- (7) Honour, J. W. Diagnosis of Diseases of Steroid Hormone Production, Metabolism and Action. *J. Clin. Res. Pediatr. Endocrinol.* **2009**, *1* (5), 209–226 DOI: 10.4274/jcrpe.v1i5.209.
- (8) Miller, W. L.; Auchus, R. J. The Molecular Biology, Biochemistry, and Physiology of Human Steroidogenesis and Its Disorders. *Endocr. Rev.* **2011**, *32* (1), 81–151 DOI: 10.1210/er.2010-0013.
- (9) Kotłowska, A. Application of Steroid Hormone Metabolomics in Search of Biomarkers in Clinical Research. *Drug Dev. Res.* **2012**, *73* (7), 381–389 DOI: 10.1002/ddr.21028.
- (10) Hartmann, K.; Koenen, M.; Schauer, S.; Wittig-Blaich, S.; Ahmad, M.; Baschant, U.; Tuckermann, J. P. Molecular Actions of Glucocorticoids in Cartilage and Bone During Health, Disease, and Steroid Therapy. *Physiol. Rev.* **2016**, *96* (2), 409–447 DOI: 10.1152/physrev.00011.2015.
- (11) Almeida, M.; Laurent, M. R.; Dubois, V.; Claessens, F.; O'Brien, C. A.; Bouillon, R.;

- Vanderschueren, D.; Manolagas, S. C. Estrogens and Androgens in Skeletal Physiology and Pathophysiology. *Physiol. Rev.* **2016**, *97* (1), 135–187 DOI: 10.1152/physrev.00033.2015.
- (12) Dobruch, J.; Daneshmand, S.; Fisch, M.; Lotan, Y.; Noon, A. P.; Resnick, M. J.; Shariat, S. F.; Zlotta, A. R.; Boorjian, S. A. Gender and Bladder Cancer: A Collaborative Review of Etiology, Biology, and Outcomes. *Eur. Urol.* **2016**, *69* (2), 300–310 DOI: <https://doi.org/10.1016/j.eururo.2015.08.037>.
- (13) Kim, C.; Cushman, M.; Kleindorfer, D.; Lisabeth, L.; F. Redberg, R.; M. Safford, M. A Review of the Relationships Between Endogenous Sex Steroids and Incident Ischemic Stroke and Coronary Heart Disease Events. *Current Cardiology Reviews*. pp 252–260.
- (14) Bansal, R.; Singh, R. Exploring the potential of natural and synthetic neuroprotective steroids against neurodegenerative disorders: A literature review. *Med. Res. Rev.* **2018**, *38* (4), 1126–1158 DOI: 10.1002/med.21458.
- (15) Lee, M. A.; Bakh, N.; Bisker, G.; Brown, E. N.; Strano, M. S. A Pharmacokinetic Model of a Tissue Implantable Cortisol Sensor. *Adv. Healthc. Mater.* **2016**, *5* (23), 3004–3015 DOI: 10.1002/adhm.201600650.
- (16) Iqbal, M. J.; Dalton, M.; Sawers, R. S. Binding of Testosterone and Oestradiol to Sex Hormone Binding Globulin, Human Serum Albumin and other Plasma Proteins: Evidence for Non-Specific Binding of Oestradiol to Sex Hormone Binding Globulin. *Clin. Sci.* **1983**, *64* (3), 307 LP – 314.
- (17) Dorin, R. I.; Pai, H. K.; Ho, J. T.; Lewis, J. G.; Torpy, D. J.; Urban, F. K.; Qualls, C. R. Validation of a simple method of estimating plasma free cortisol: Role of cortisol binding to albumin. *Clin. Biochem.* **2009**, *42*, 64–71 DOI: 10.1016/j.clinbiochem.2008.09.115.
- (18) Falkenstein, E.; Tillmann, H. C.; Christ, M.; Feuring, M.; Wehling, M. Multiple actions of

- steroid hormones--a focus on rapid, nongenomic effects. *Pharmacol. Rev.* **2000**, *52* (4), 513–556.
- (19) Gupta, S. K.; Dubé, M. P. Exogenous cushing syndrome mimicking human immunodeficiency virus lipodystrophy. *Clin. Infect. Dis.* **2002**, *35* (6), E69-71 DOI: 10.1086/342562.
- (20) Napier, C.; Pearce, S. H. S. Current and emerging therapies for Addison's disease. *Curr. Opin. Endocrinol. Diabetes Obes.* **2014**, *21* (3), 147–153 DOI: 10.1097/MED.0000000000000067.
- (21) LeMoult, J.; Joormann, J. Depressive rumination alters cortisol decline in Major Depressive Disorder. *Biol. Psychol.* **2014**, *100*, 50–55 DOI: <https://doi.org/10.1016/j.biopsycho.2014.05.001>.
- (22) Yahyavi, S. T.; Zarghami, M.; Naghshvar, F.; Danesh, A. Relationship of cortisol, norepinephrine, and epinephrine levels with war-induced posttraumatic stress disorder in fathers and their offspring . *Revista Brasileira de Psiquiatria* . scielo 2015, pp 93–98.
- (23) Steen, N. E.; Methlie, P.; Lorentzen, S.; Dieset, I.; Aas, M.; Nerhus, M.; Haram, M.; Agartz, I.; Melle, I.; Berg, J. P.; et al. Altered systemic cortisol metabolism in bipolar disorder and schizophrenia spectrum disorders. *J. Psychiatr. Res.* **2014**, *52*, 57–62 DOI: 10.1016/j.jpsychires.2014.01.017.
- (24) World Health Organization. Depression and other common mental disorders: global health estimates. *World Heal. Organ.* **2017** DOI: CC BY-NC-SA 3.0 IGO.
- (25) Dalirirad, S.; Steckl, A. J. Aptamer-based lateral flow assay for point of care cortisol detection in sweat. *Sensors Actuators B Chem.* **2019**, *283*, 79–86 DOI: <https://doi.org/10.1016/j.snb.2018.11.161>.

- (26) Bouchard, P. Progesterone and the progesterone receptor. *J. Reprod. Med.* **1999**, *44* (2 Suppl), 153–157.
- (27) Dinny Graham, J.; Clarke, C. L. Physiological action of progesterone in target tissues. *Endocrine Reviews.* 1997.
- (28) Siegel, R. L.; Miller, K. D.; Jemal, A. Cancer statistics, 2018. *CA. Cancer J. Clin.* **2018** DOI: 10.3322/caac.21442.
- (29) Govindasamy, M.; Subramanian, B.; Wang, S.-F.; Chinnapaiyan, S.; Jothi Ramalingam, R.; Al-lohedan, H. A. Ultrasound-assisted synthesis of tungsten trioxide entrapped with graphene nanosheets for developing nanomolar electrochemical (hormone) sensor and enhanced sensitivity of the catalytic performance. *Ultrason. Sonochem.* **2019**, *56*, 134–142 DOI: <https://doi.org/10.1016/j.ultsonch.2019.03.021>.
- (30) Sharma, P.; Allison, J. P. The future of immune checkpoint therapy. *Science (80-.).* **2015**, *348* (6230), 56 LP – 61 DOI: 10.1126/science.aaa8172.
- (31) Michot, J. M.; Bigenwald, C.; Champiat, S.; Collins, M.; Carbonnel, F.; Postel-Vinay, S.; Berdelou, A.; Varga, A.; Bahleda, R.; Hollebecque, A.; et al. Immune-related adverse events with immune checkpoint blockade: a comprehensive review. *Eur. J. Cancer* **2016**, *54*, 139–148 DOI: <https://doi.org/10.1016/j.ejca.2015.11.016>.
- (32) Weber, J. S.; Dummer, R.; de Pril, V.; Lebbé, C.; Hodi, F. S.; Investigators, for the M.-20. Patterns of onset and resolution of immune-related adverse events of special interest with ipilimumab. *Cancer* **2013**, *119* (9), 1675–1682 DOI: 10.1002/cncr.27969.
- (33) Bornstein, S. R.; Allolio, B.; Arlt, W.; Barthel, A.; Don-Wauchope, A.; Hammer, G. D.; Husebye, E. S.; Merke, D. P.; Murad, M. H.; Stratakis, C. A.; et al. Diagnosis and Treatment of Primary Adrenal Insufficiency: An Endocrine Society Clinical Practice Guideline. *J. Clin.*

- Endocrinol. Metab.* **2016**, *101* (2), 364–389 DOI: 10.1210/jc.2015-1710.
- (34) Nieman, L. K. Diagnosis of Cushing’s Syndrome in the Modern Era. *Endocrinol. Metab. Clin.* **2018**, *47* (2), 259–273 DOI: 10.1016/j.ecl.2018.02.001.
- (35) Ungaro, R.; Mehandru, S.; Allen, P. B.; Peyrin-Biroulet, L.; Colombel, J.-F. Ulcerative colitis. *Lancet* **2017**, *389* (10080), 1756–1770 DOI: [https://doi.org/10.1016/S0140-6736\(16\)32126-2](https://doi.org/10.1016/S0140-6736(16)32126-2).
- (36) Cruz-Topete, D.; Cidlowski, J. A. One Hormone, Two Actions: Anti- and Pro-Inflammatory Effects of Glucocorticoids. *Neuroimmunomodulation* **2015**, *22* (1–2), 20–32 DOI: 10.1159/000362724.
- (37) Law, T. Y.; Nguyen, C.; Frank, R. M.; Rosas, S.; McCormick, F. Current concepts on the use of corticosteroid injections for knee osteoarthritis. *Phys. Sportsmed.* **2015**, *43* (3), 269–273 DOI: 10.1080/00913847.2015.1017440.
- (38) Sathish, V.; Martin, Y. N.; Prakash, Y. S. Sex steroid signaling: Implications for lung diseases. *Pharmacol. Ther.* **2015**, *150*, 94–108 DOI: <https://doi.org/10.1016/j.pharmthera.2015.01.007>.
- (39) Porcu, P.; Barron, A. M.; Frye, C. A.; Walf, A. A.; Yang, S.-Y.; He, X.-Y.; Morrow, A. L.; Panzica, G. C.; Melcangi, R. C. Neurosteroidogenesis Today: Novel Targets for Neuroactive Steroid Synthesis and Action and Their Relevance for Translational Research. *J. Neuroendocrinol.* **2016**, *28* (2) DOI: 10.1111/jne.12351.
- (40) Tan, M. H. E.; Li, J.; Xu, H. E.; Melcher, K.; Yong, E. Androgen receptor: structure, role in prostate cancer and drug discovery. *Acta Pharmacol. Sin.* **2014**, *36*, 3.
- (41) Chia, K.; O’Brien, M.; Brown, M.; Lim, E. Targeting the Androgen Receptor in Breast Cancer. *Curr. Oncol. Rep.* **2015**, *17* (2), 4 DOI: 10.1007/s11912-014-0427-8.

- (42) Perkins, M. S.; Toit, R. L.; Africander, D. Hormone therapy and breast cancer: emerging steroid receptor mechanisms. *J. Mol. Endocrinol.* **2018**, *61* (4), R133–R160 DOI: 10.1530/JME-18-0094.
- (43) Gatti, R.; Antonelli, G.; Prearo, M.; Spinella, P.; Cappellin, E.; De Palo, E. F. Cortisol assays and diagnostic laboratory procedures in human biological fluids. *Clin. Biochem.* **2009**, *42* (12), 1205–1217 DOI: <https://doi.org/10.1016/j.clinbiochem.2009.04.011>.
- (44) Kaushik, A.; Vasudev, A.; Arya, S. K.; Pasha, S. K.; Bhansali, S. Recent advances in cortisol sensing technologies for point-of-care application. *Biosens. Bioelectron.* **2014**, *53*, 499–512 DOI: 10.1016/j.bios.2013.09.060.
- (45) Singh, A.; Kaushik, A.; Kumar, R.; Nair, M.; Bhansali, S. Electrochemical Sensing of Cortisol: A Recent Update. *Appl. Biochem. Biotechnol.* **2014**, *174* (3), 1115–1126 DOI: 10.1007/s12010-014-0894-2.
- (46) Klouda, J.; Barek, J.; Nesměrāk, K.; Schwarzová-Pecková, K. Non-Enzymatic Electrochemistry in Characterization and Analysis of Steroid Compounds. *Crit. Rev. Anal. Chem.* **2017**, *47* (5), 384–404 DOI: 10.1080/10408347.2017.1318694.
- (47) Gugoasa, L. A.; Staden, R.-I. S. Advanced Methods for the Analysis of Testosterone. *Current Medicinal Chemistry*. pp 4037–4049.
- (48) Campuzano, S.; Yáñez-Sedeño, P.; Pingarrón, J. M. Electrochemical bioaffinity sensors for salivary biomarkers detection. *TrAC Trends Anal. Chem.* **2017**, *86*, 14–24 DOI: <https://doi.org/10.1016/j.trac.2016.10.002>.
- (49) Takase, M.; Murata, M.; Hibi, K.; Huifeng, R.; Endo, H. Development of mediator-type biosensor to wirelessly monitor whole cholesterol concentration in fish. *Fish Physiol. Biochem.* **2014**, *40* (2), 385–394 DOI: 10.1007/s10695-013-9851-1.

- (50) Cook, C. J. Real-time measurements of corticosteroids in conscious animals using an antibody-based electrode. *Nat. Biotechnol.* **1997**, *15* (5), 467–471 DOI: 10.1038/nbt0597-467.
- (51) Cook, C. J. Glucocorticoid feedback increases the sensitivity of the limbic system to stress. *Physiol. Behav.* **2002**, *75* (4), 455–464 DOI: [https://doi.org/10.1016/S0031-9384\(02\)00650-9](https://doi.org/10.1016/S0031-9384(02)00650-9).
- (52) Sunwoo, S. H.; Lee, J. S.; Bae, S.; Shin, Y. J.; Kim, C. S.; Joo, S. Y.; Choi, H. S.; Suh, M.; Kim, S. W.; Choi, Y. J.; et al. Chronic and acute stress monitoring by electrophysiological signals from adrenal gland. *Proc. Natl. Acad. Sci.* **2019**, *116* (4), 1146 LP – 1151 DOI: 10.1073/pnas.1806392115.
- (53) Iverson, N. M.; Barone, P. W.; Shandell, M.; Trudel, L. J.; Sen, S.; Sen, F.; Ivanov, V.; Atolia, E.; Farias, E.; McNicholas, T. P.; et al. In vivo biosensing via tissue-localizable near-infrared-fluorescent single-walled carbon nanotubes. *Nat. Nanotechnol.* **2013**, *8* (11), 873–880 DOI: 10.1038/nnano.2013.222.
- (54) Kruss, S.; Landry, M. P.; Vander Ende, E.; Lima, B. M. a; Reuel, N. F.; Zhang, J.; Nelson, J.; Mu, B.; Hilmer, A.; Strano, M. Neurotransmitter detection using corona phase molecular recognition on fluorescent single-walled carbon nanotube sensors. *J. Am. Chem. Soc.* **2014**, *136* (2), 713–724 DOI: 10.1021/ja410433b.
- (55) Kruss, S.; Salem, D. P.; Vuković, L.; Lima, B.; Vander Ende, E.; Boyden, E. S.; Strano, M. S. High-resolution imaging of cellular dopamine efflux using a fluorescent nanosensor array. *Proc. Natl. Acad. Sci.* **2017**, *114* (8), 1789–1794 DOI: 10.1073/pnas.1613541114.
- (56) Zhang, J.; Landry, M. P.; Barone, P. W.; Kim, J.-H.; Lin, S.; Ulissi, Z. W.; Lin, D.; Mu, B.; Boghossian, A. A.; Hilmer, A. J.; et al. Molecular recognition using corona phase

- complexes made of synthetic polymers adsorbed on carbon nanotubes. *Nat. Nanotechnol.* **2013**, 8 (12), 959–968 DOI: 10.1038/nnano.2013.236.
- (57) Zhang, J. Q.; Boghossian, A. A.; Barone, P. W.; Rwei, A.; Kim, J. H.; Lin, D. H.; Heller, D. A.; Hilmer, A. J.; Nair, N.; Reuel, N. F.; et al. Single Molecule Detection of Nitric Oxide Enabled by d(AT)(15) DNA Adsorbed to Near Infrared Fluorescent Single-Walled Carbon Nanotubes. *J. Am. Chem. Soc.* **2011**, 133 (3), 567–581 DOI: 10.1021/ja1084942.
- (58) Giraldo, J. P.; Landry, M. P.; Kwak, S. Y.; Jain, R. M.; Wong, M. H.; Iverson, N. M.; Ben-Naim, M.; Strano, M. S. A Ratiometric Sensor Using Single Chirality Near-Infrared Fluorescent Carbon Nanotubes: Application to in Vivo Monitoring. *Small* **2015**, 11 (32), 3973–3984 DOI: 10.1002/smll.201403276.
- (59) Bisker, G.; Dong, J.; Park, H. D.; Iverson, N. M.; Ahn, J.; Nelson, J. T.; Landry, M. P.; Kruss, S.; Strano, M. S. Protein-targeted corona phase molecular recognition. *Nat. Commun.* **2016**, 7 DOI: 10.1038/ncomms10241.
- (60) Bisker, G.; Bakh, N. A.; Lee, M. A.; Ahn, J.; Park, M.; O’Connell, E. B.; Iverson, N. M.; Strano, M. S. Insulin Detection Using a Corona Phase Molecular Recognition Site on Single-Walled Carbon Nanotubes. *ACS Sensors* **2018**, 3 (2), 367–377 DOI: 10.1021/acssensors.7b00788.
- (61) Bisker, G.; Ahn, J.; Kruss, S.; Ulissi, Z. W.; Salem, D. P.; Strano, M. S. A mathematical formulation and solution of the CoPhMoRe inverse problem for helically wrapping polymer corona phases on cylindrical substrates. *J. Phys. Chem. C* **2015**, 119 (24), 13876–13886 DOI: 10.1021/acs.jpcc.5b01705.
- (62) Salem, D. P.; Landry, M. P.; Bisker, G.; Ahn, J.; Kruss, S.; Strano, M. S. Chirality dependent corona phase molecular recognition of DNA-wrapped carbon nanotubes. *Carbon N. Y.* **2016**,

97, 147–153 DOI: <https://doi.org/10.1016/j.carbon.2015.08.075>.

- (63) Salem, D. P.; Gong, X.; Liu, A. T.; Koman, V. B.; Dong, J.; Strano, M. S. Ionic Strength-Mediated Phase Transitions of Surface-Adsorbed DNA on Single-Walled Carbon Nanotubes. *J. Am. Chem. Soc.* **2017**, *139* (46), 16791–16802 DOI: 10.1021/jacs.7b09258.
- (64) Zhang, J.; Kruss, S.; Hilmer, A. J.; Shimizu, S.; Schmois, Z.; De La Cruz, F.; Barone, P. W.; Reuel, N. F.; Heller, D. A.; Strano, M. S. A Rapid, Direct, Quantitative, and Label-Free Detector of Cardiac Biomarker Troponin T Using Near-Infrared Fluorescent Single-Walled Carbon Nanotube Sensors. *Adv. Healthc. Mater.* **2014**, *3* (3), 412–423 DOI: 10.1002/adhm.201300033.
- (65) Park, M.; Strano, M. S. Molecular Probe Adsorption to Estimate Nanoparticle Surface Area. *Prep.*
- (66) Iverson, N. M.; Bisker, G.; Farias, E.; Ivanov, V.; Ahn, J.; Wogan, G. N.; Strano, M. S. Quantitative tissue spectroscopy of near infrared fluorescent nanosensor implants. *J. Biomed. Nanotechnol.* **2016**, *12* (5), 1035–1047 DOI: 10.1166/jbn.2016.2237.
- (67) Bisker, G.; Iverson, N. M.; Ahn, J.; Strano, M. S. A Pharmacokinetic Model of a Tissue Implantable Insulin Sensor. *Adv. Healthc. Mater.* **2015**, *4* (1), 87–97 DOI: 10.1002/adhm.201400264.
- (68) Hishiya, T.; Shibata, M.; Kakazu, M.; Asanuma, H.; Komiyama, M. Molecularly Imprinted Cyclodextrins as Selective Receptors for Steroids. *Macromolecules* **1999**, *32* (7), 2265–2269 DOI: 10.1021/ma9816012.
- (69) Manickam, P.; Pasha, S. K.; Snipes, S. A.; Bhansali, S. A Reusable Electrochemical Biosensor for Monitoring of Small Molecules (Cortisol) Using Molecularly Imprinted Polymers. *J. Electrochem. Soc.* **2017**, *164* (2), B54–B59 DOI: 10.1149/2.0781702jes.

- (70) Farber, S.; Green, B. S.; Domb, A. J. Selective 17- β -estradiol molecular imprinting. *J. Polym. Sci. Part A Polym. Chem.* **2009**, *47* (20), 5534–5542 DOI: 10.1002/pola.23604.
- (71) Özgür, E.; Yılmaz, E.; Şener, G.; Uzun, L.; Say, R.; Denizli, A. A new molecular imprinting-based mass-sensitive sensor for real-time detection of 17 β -estradiol from aqueous solution. *Environ. Prog. Sustain. Energy* **2012**, *32* (4), 1164–1169 DOI: 10.1002/ep.11718.
- (72) Kellens, E.; Bové, H.; Conradi, M.; D’Olieslaeger, L.; Wagner, P.; Landfester, K.; Junkers, T.; Ethirajan, A. Improved Molecular Imprinting Based on Colloidal Particles Made from Miniemulsion: A Case Study on Testosterone and Its Structural Analogues. *Macromolecules* **2016**, *49* (7), 2559–2567 DOI: 10.1021/acs.macromol.6b00130.
- (73) Ramström, O.; Ye, L.; Mosbach, K. Artificial antibodies to corticosteroids prepared by molecular imprinting. *Chem. Biol.* **1996**, *3* (6), 471–477 DOI: [https://doi.org/10.1016/S1074-5521\(96\)90095-2](https://doi.org/10.1016/S1074-5521(96)90095-2).
- (74) Cheong, S. H.; McNiven, S.; Rachkov, A.; Levi, R.; Yano, K.; Karube, I. Testosterone Receptor Binding Mimic Constructed Using Molecular Imprinting. *Macromolecules* **1997**, *30* (5), 1317–1322 DOI: 10.1021/ma961014l.
- (75) Choi, J. H.; Strano, M. S. Solvatochromism in single-walled carbon nanotubes. *Appl. Phys. Lett.* **2007**, *90* (22), 223114 DOI: 10.1063/1.2745228.
- (76) Weisman, R. B. Chapter 5 Optical spectroscopy of single-walled carbon nanotubes. In *Carbon Nanotubes: Quantum Cylinders of Graphene*; Saito, S., Zettl, A. B. T.-C. C. of C. M. S., Eds.; Elsevier, 2008; Vol. 3, pp 109–133.
- (77) Adamczyk, Z.; Nattich-Rak, M.; Dąbkowska, M.; Kujda-Kruk, M. Albumin adsorption at solid substrates: A quest for a unified approach. *J. Colloid Interface Sci.* **2018**, *514*, 769–

790 DOI: <https://doi.org/10.1016/j.jcis.2017.11.083>.

- (78) Dang, T. T.; Nikkhah, M.; Memic, A.; Khademhosseini, A. Polymeric Biomaterials for Implantable Prostheses. In *Natural and Synthetic Biomedical Polymers*; Kumbar, S. G., Laurencin, C. T., Deng, M. B. T.-N. and S. B. P., Eds.; Elsevier: Oxford, 2014; pp 309–331.
- (79) Herrick, W. G.; Nguyen, T. V.; Sleiman, M.; McRae, S.; Emrick, T. S.; Peyton, S. R. PEG-Phosphorylcholine Hydrogels As Tunable and Versatile Platforms for Mechanobiology. *Biomacromolecules* **2013**, *14* (7), 2294–2304 DOI: 10.1021/bm400418g.
- (80) Dunning, M. B.; Fischbach, F. *Nurses' Quick Reference to Common Laboratory & Diagnostic Tests*, 5 ed.; China, 2010.
- (81) Booth, M.; El Garf, T. A. R. Plasma Progesterone Concentration During the Third Trimester of Diabetic Pregnancy. *BJOG An Int. J. Obstet. Gynaecol.* **1974**, *81* (10), 768–776 DOI: 10.1111/j.1471-0528.1974.tb00378.x.

Chapter 5 : Formulation of Hydrogel-Encapsulated Single Walled Carbon Nanotube Sensors Implants to Modulate Inflammation and Foreign-Body Response

This chapter is adapted from a manuscript in preparation for submission.

Introduction

Single-walled carbon nanotubes (SWNT) have increasingly been utilized for *in vivo* biological applications, including drug delivery and biosensors.¹ Depending on the application, SWNT have been employed as injectable liquids or as solid hydrogel implants.²⁻⁵ Various extents of cellular toxicity have been reported based on SWNT synthesis method,⁶ wrapping,^{7,8} and cell type.⁸⁻¹⁰ Few studies, however, have studied the effect of formulation on *in vivo* SWNT toxicity. In this study, we study the tissue responses of five SWNT hydrogel formulations implanted subcutaneously in SKH1-E mice.

As an emerging nanomaterial for biological applications, a central question regarding SWNT has been their biocompatibility. It is important to note, however, that SWNT comprise a family of materials characterized by different diameters, lengths, and methods of synthesis, all of which have important effects on the biocompatibility.¹¹ Historically, SWNT toxicity has been evaluated in *in vitro* systems. It has been found that the synthesis method influences toxicity by changing the impurities from the process, namely the metal catalysts. For example, to produce SWNT, the HiPCO process utilizes Fe catalysts,¹² while the CoMoCAT process uses CoMo catalysts.¹³ Residual catalysts have been shown to drastically alter SWNT cytotoxicity.⁶

Furthermore, SWNT length has been shown to alter its biodistribution properties, with shorter, individualized SWNT (<300 nm) able to be cleared by the kidneys and larger SWNT aggregates inducing granuloma formation and phagocytosis.¹⁴ Furthermore, the SWNT corona has been reported to alter SWNT cytotoxicity. Dong et al. reported that SDS and SDBS-wrapped SWNT reduced 1321N1 human astrocytoma cell viability, while sodium cholate and DNA-wrapped SWNT did not affect cell viability or proliferation.⁸ Given the heterogeneity of cellular responses and SWNT functionalization methods, the toxicity of each unique SWNT construct may have to be considered individually if used in direct contact with tissues.

While a useful preliminary step,¹⁵ cellular toxicity may not always reflect *in vivo* tissue responses to a compound because of heterogeneous cell populations *in vivo*,¹⁰ different effective doses and exposure times due to *in vivo* systems being open as opposed to closed as in cell culture,¹⁶ and chemical transformation of the material upon introduction into the body.¹⁷ Thus, direct testing in the *in vivo* environment, reflecting the intended route, dose, and location of administration, is critical.

In recent years, SWNT have become commonly used *in vivo*. Iverson et al. delivered DNA-wrapped SWNT via tail vein injection into mouse livers to detect the onset of inflammatory events.⁴ The authors also implanted SWNT encapsulated in alginate hydrogels subcutaneously, where they remained for 400 days. Histological analysis showed minimal inflammation at the implantation site. Williams et al. and Harvey et al. encapsulated DNA-wrapped SWNT into dialysis bags and implanted them into intraperitoneally.^{18,19} Jena et al. delivered DNA-wrapped SWNT into the liver to detect endolysosomal lipid flux in the liver.²⁰ Our group has previously utilized DNA-wrapped SWNT encapsulated in PEGDA hydrogels in various marine organisms for biologging purposes.⁵ High-resolution ultrasound found that changes in tissue architecture

were minimal in the catshark and eel, but histological analysis found evidence of a foreign body reaction in the turtle.

These studies together show the potential of SWNT to be used in various *in vivo* applications. However, even when tissue responses were reported, these studies did not explore the modification of tissue responses based on changes in SWNT formulation. Given the heterogeneity of toxic responses observed based on SWNT factors and biomaterials in general,^{11,21} there is a potential of maintaining SWNT function while minimizing adverse tissue responses based on careful formulation of the delivery vehicle.

In this study, five hydrogel formulations were implanted into SKH1-E mice. Formulation parameters included SWNT concentration, hydrogel cross-linking density, and SWNT wrapping. Tissue samples around the implant were collected at various times and characterized in terms of the inflammatory infiltrate and thickness of fibrous capsule formation. From these results, design rules to formulate SWNT delivery systems for minimal tissue responses were formulated. Furthermore, the effect of tissue responses on SWNT sensor functionality were characterized.

Methods and Materials

Materials. Raw single walled carbon nanotubes (SWNT) were purchased from NanoIntegris (Batch HR27-104). Poly(ethylene glycol) diacrylate (PEGDA) ($M_n = 8000$) was purchased from Alfa Aesar, while PEGDA $M_n = 1000$ was purchased from Sigma Millipore. Unless otherwise noted, the remaining reagents were purchased from Sigma Millipore.

Synthesis and Characterization of Hydrogels. SWNT were encapsulated in PEGDA hydrogels matrix using a modified version of a previously reported protocol.²² PEGDA (100 mg/L), SWNT (25 mg/L) and 2-hydroxy-4'-(2-hydroxyethoxy)-2methylpropiophenone (0.175 mg/mL for PEGDA

8000 or 1.75 mg/mL for PEGDA 1000) were mixed in 1x PBS and placed into a mold glass mold. The mixture was held under a nitrogen atmosphere for 15 minutes and subsequently crosslinked under 365 nm UV light (UVP Blak-Ray XX-15BLB, 15 W) for 60 minutes. The solid hydrogels were incubated in 1x PBS with regular buffer replacements for at least 5 days to remove unencapsulated SWNT and unreacted reagents. Formulations are listed in Table 37.

Hydrogel pore sizes were estimated using a swelling protocol previously reported. The mass of the swollen hydrogel and a dehydrated hydrogel were measured. Equations (5-1)-(5-3) were used to estimate the pore size:²³

$$Q = \frac{m_{\text{swollen}}}{m_{\text{dry}}} = \alpha^{-1} \quad (5-1)$$

$$\bar{M}_c^{-1} = \frac{2}{\bar{M}_n} - \frac{(\bar{v}/V) [\ln(1-\alpha) + \alpha + \chi\alpha^2]}{\alpha^{1/3} - (2/\theta)\alpha} \quad (5-2)$$

$$\xi = \alpha^{-1/3} \left(\frac{2C_\infty l^2 \bar{M}_c}{M_0} \right)^{1/2} \quad (5-3)$$

where Q is the hydrogel mass swelling ratio, m is mass, where \bar{M}_c is the molecular weight between cross links, \bar{M}_n is the molecular weight of the precursor polymers, \bar{v} is the specific volume of the polymer (=0.903 mL/g), V is water's specific volume (=18.01 mL/mol), χ is the Flory-Huggins parameter (=0.3765),²⁴ θ is the functionality of PEGDA (=4), ξ is the average pore size, C_∞ is the Flory characteristic ratio (=6.9), l is the length of carbon-carbon bonds (=0.154 nm), and M_0 is the molar mass of the monomeric unit (=44.05 g/mol).

Fluorescence imaging on hydrogels was conducted with a 2D InGaAs camera (Princeton Instruments) coupled to a Nikon AF Micro-Nikkor 60 mm 4/2.8D lens. The hydrogels were excited by a 785 nm Invictus laser (Kaiser). The optical window from 1075 – 1200 nm was monitored

using a 1075 nm longpass filter and 1200 nm shortpass filter (Edmund Optics). Sensor responses to progesterone were tested by placing hydrogels in 6-well plates and exposed to varying concentrations of progesterone.

Table 37: Hydrogel Formulations

Gel	SWNT (mg/L)	PEGDA (g/mol)
1	SM8-3 (25 mg/L)	8000
2	(AAAT) ₇ (25 mg/L)	8000
3	SM8-3 (25mg/L)	1000
4	Blank	8000
5	Blank	1000

Mouse surgeries and tissue collection. All procedures were reviewed and approved by the Committee of Animal Care. Hydrogels were autoclaved prior to implantation. Female 7 week old mice (Charles River Laboratory and Jackson Labs) were anesthetized using 2% isoflurane gas. Once unresponsive, the implantation sites were sterilized using alternating washes with iopovidone and 70% ethanol repeated thrice. Hydrogels were implanted subcutaneously in the dorsal side of the animal. Two hydrogels would be implanted at a time. Implantation sites were sutured using vicryl stitches (Ethicon).

At the appropriate time point (1, 7, 14, or 28 days), mice were euthanized by CO₂ asphyxiation. Tissue samples were collected around the hydrogel implantation sites and a control surgical wound site without a hydrogel to give a surgical baseline. Tissues were fixed in 10% formalin and subjected to H&E staining for histological analysis.

Analysis of degradation products. Hydrogels were autoclaved and incubated in 1x PBS at 37°C. Buffers were collected and replaced at 1, 7, 14, and 28 days. The samples were frozen until further use. The samples were lyophilized and reconstituted in a 5x smaller volume to concentrate the samples. A drop of each sample was placed and dried on a glass slide, which were then characterized using Raman spectroscopy and FTIR spectroscopy. The remaining sample was characterized using ¹H NMR. Gel permeation chromatography was also performed using an Agilent Infinity 1260 equipped with a PL Aquagel-OH 30 column. The mobile phase was 0.2 M NaNO₃ and 0.01 M NaH₂PO₄ eluted at a flowrate of 0.5 mL/min. Samples were filtered through a 0.22 μm membrane prior to the run.

Results and Discussion

Table 37 summarizes the five hydrogel formulations evaluated in this work, chosen to evaluate tissue responses when the hydrogels possess differences in SWNT concentration, SWNT wrapping, pore size, and compressive modulus. Previous *in vitro* studies have examined cellular toxicity in the presence of SWNT and have reported different results depending on synthesis method and associated impurities in the raw SWNT material,⁶ SWNT corona,^{7,8} and cell type.^{8,9} For example, while SDS and SDBS-wrapped HiPCO SWNT were shown to be toxic to 132N1 human astrocytoma cells, utilizing sodium cholate or ssDNA-wrapped SWNT eliminated such adverse reactions.⁸ The disparate results among the same cell type indicate that each SWNT suspension may need to be tested individually to determine cellular toxicity. Furthermore, A549 and NHBE cells, both primary human lung epithelial cells, exhibited different toxic responses when exposed to dipalmitoylphosphatidylcholine-wrapped HiPCO-SWNT, indicating that particle toxicity is not universal among different cell types.^{11,25} The wide range of cellular responses may

indicate that the *in vivo* response to implanted SWNT may also be need to evaluated in each type of implantation site, whether that be subcutaneous, intramuscular, etc.

The interaction of hydrogel materials with tissue has been a widely investigated topic in the literature, and we point readers to the excellent reviews written on this subject.^{26–28} Conversely, there have been relatively few studies that have examined the use of hydrogels as an implantation vehicle for SWNT and the effects of formulation on overall functionality. We examined the use of two different molecular weight PEGDA hydrogels. As shown in Figure 5-1, the PEGDA 1000 hydrogels have a modulus of 180 kPa and a pore size of 4 nm, while the PEGDA 8000 hydrogels have a modulus of 120 kPa and a pore size of 20 nm. The *in vivo* foreign body response has been shown to be more severe in the case of stiffer PEGDA hydrogels.²⁹ However, stiffer hydrogels also lead to smaller pore sizes, which may increase the efficiency of nanoparticle encapsulation and consequently decrease the rate of product release upon degradation of the hydrogel scaffold.

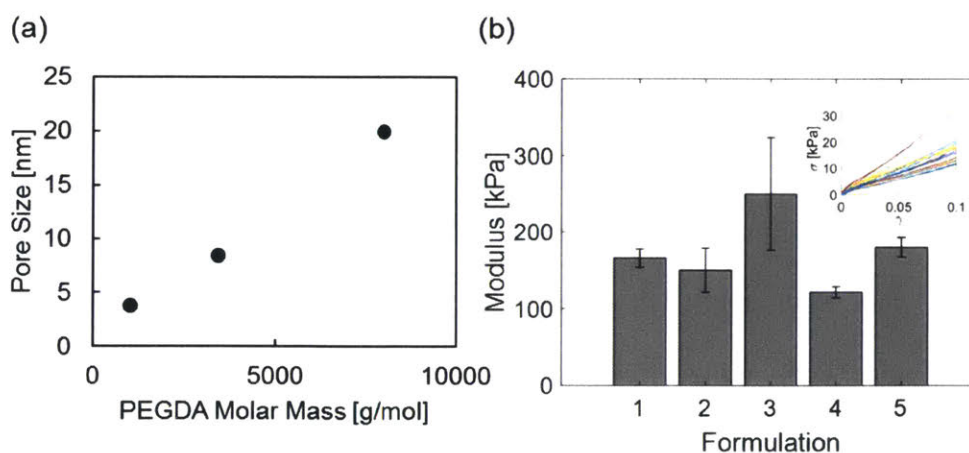


Figure 5-1: (a) Hydrogel pore sizes obtained via swelling experiments. (b) Compressive moduli of hydrogels obtained from the linear regions of dynamic mechanical analysis (inset).

Tissue responses to the five hydrogel formulations were evaluated and scored according to several criteria, including the inflammatory cellular infiltrate at and around the implant site, fibrosis, edema, neovascularization, and the presence of multi-nucleated giant cells (MNGCs). The

identity of the cells surrounding the implant indicate tissue tolerance of the implant, as well as the progression of healing.³⁰ In the classical wound healing process, the first 3-4 days are characterized by acute inflammation, in which the primary cell types are neutrophils and mast cells, which attempt to phagocytose the material. They also release degranulation molecules for the degradation of foreign material and cytokines for the progression of later stages of inflammation. Following acute inflammation, neutrophils are replaced with macrophages, which release ROS and attempt to phagocytose any foreign material. If the material is too large, as is the case with many implants, macrophages fuse and form giant cells. Furthermore, a fibrous capsule around an implant if it is not degraded. In the case of poorly biocompatible materials, deviations from the classical wound healing response may result, which may manifest itself in the presence of different cell types at a delayed or accelerated timelines.³¹ Furthermore, the ultimate thickness of the fibrous capsule surrounding an implant directly also indicates how well the tissue tolerates the implant.²¹ Taken together over time, inflammatory infiltrate and fibrous capsule thickness provide several criteria to quantify local tissue response to implants.

H&E-stained tissues are shown in Figure 5-3 and Figure 5-4, and the inflammation scores are summarized in Figure 5-5. Among all five formulations, we observed a sequence of cellular morphologies consistent with the classical wound healing responses, with neutrophils early and macrophages later (Figure 5-5a-b). Neutrophilic density around the implant revealed two significant trends. First, more densely crosslinked hydrogels led to a faster resolution of acute inflammation, as can be seen by comparing the scores of formulations 1-3 at day 14. Furthermore, at the same time point, the SWNT prolonged the acute inflammatory response (gels 1-2 vs. 4 and gel 3 vs. 5). This was observed by the external appearance of the wounds, with obvious tissue response persisting at day 7 in formulations 1-2 that was absent in formulation 3 (Figure 5-2). By

day 28, however, all five hydrogel formulations showed a similar amount of inflammation at the site. These differences may be explained by the differences in crosslink density of the hydrogels, with smaller pore-sized hydrogels encapsulating SWNT more efficiently and releasing less degradation products. One important observation is that at the early time points, gel 1 had the highest amount of acute inflammation, possibly a consequence of the wrapping. Gel 1 contained poly(acrylic acid-*ran*-styrene)-wrapped SWNT, while gel 2 contained (AAAT)₇-wrapped SWNT, indicating that the corona also influences the inflammatory response, possibly due to imperfect encapsulation of the SWNT and/or release of loosely bound wrapping molecules from the gel.

As expected, fibrosis generally increased over time, as the fibrotic capsule became more organized and better defined (Figure 5-5c), while edema and acute inflammation decreased as a function of time (Figure 5-5a-b,d). Neovascularization showed a maximum at day 7, with a gradual decrease in all formulations with time (Figure 5-5e). Neutrophils were most numerous around the implant sites at days 1 and 7 for all formulations. By day 28, acute inflammation, fibrosis, edema, and neovascularization were of similar levels in all formulations. MNGCs were present in low numbers and not in all animals and time points.



Figure 5-2: Images of mice implanted with PEGDA 8000 and PEGDA 1000 hydrogels. Mice with PEGDA 8000 hydrogels showed observable swelling in the vicinity of the implants at day 7, whereas none were noticed with the PEGDA 1000 hydrogels.

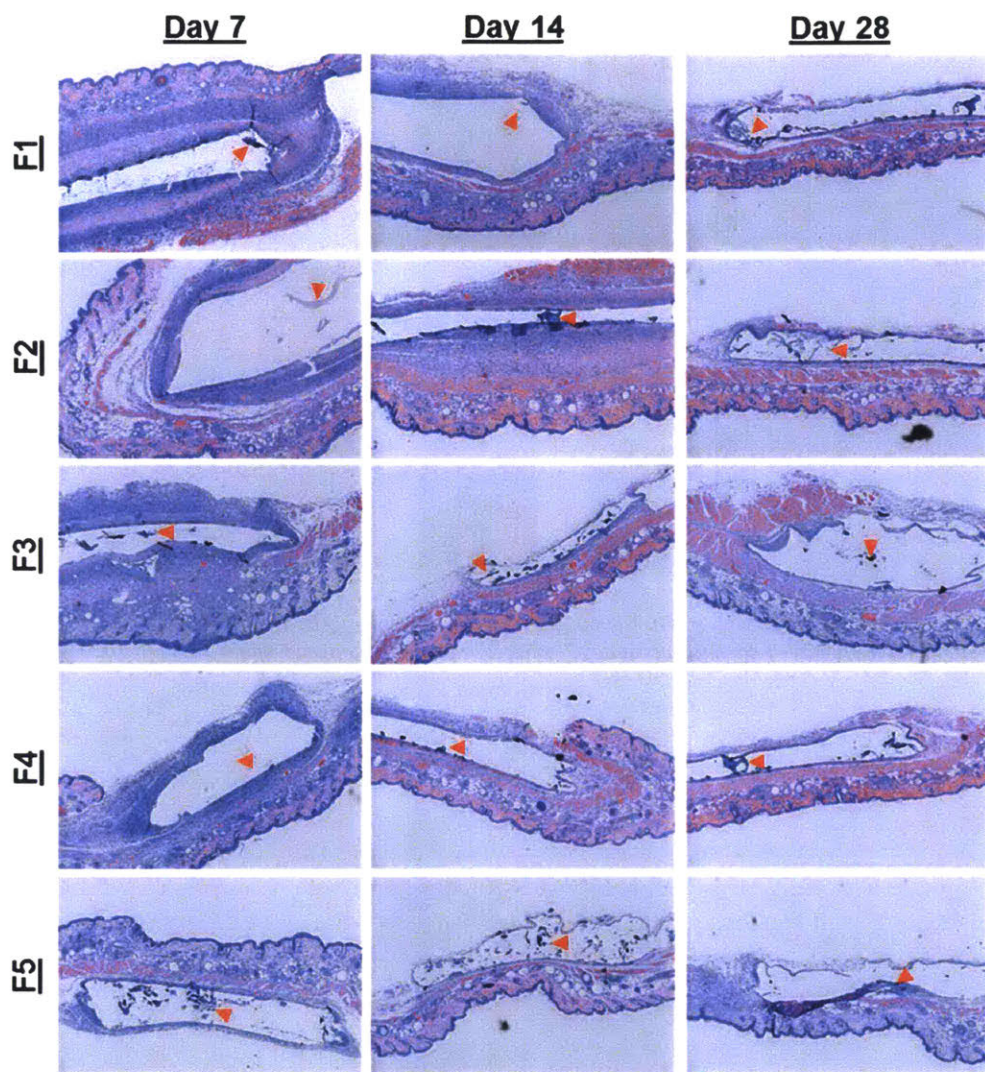


Figure 5-3: H&E stained tissue samples of SKH1-E taken from implant sites of hydrogels. Hydrogels of formulations 1-5 were explanted days 1, 7, 14, and 28. The hydrogel itself or locations of the hydrogels are marked by arrows. In all formulations, we see heavy neutrophilic infiltration on day 1, with less on day 14, and resolution by day 28. The severity of acute inflammation is higher in formulations 1 and 2 compared to 4 and formulation 3 relative to formulation 5. Formulation 3, however, has neutrophils than formulations 1 and 2. All formulations show an increase in, edema, neovascularization, and fibrosis with time. Images were taken at 20x magnification, and gels are indicated by red arrows. Magnification is 4x.

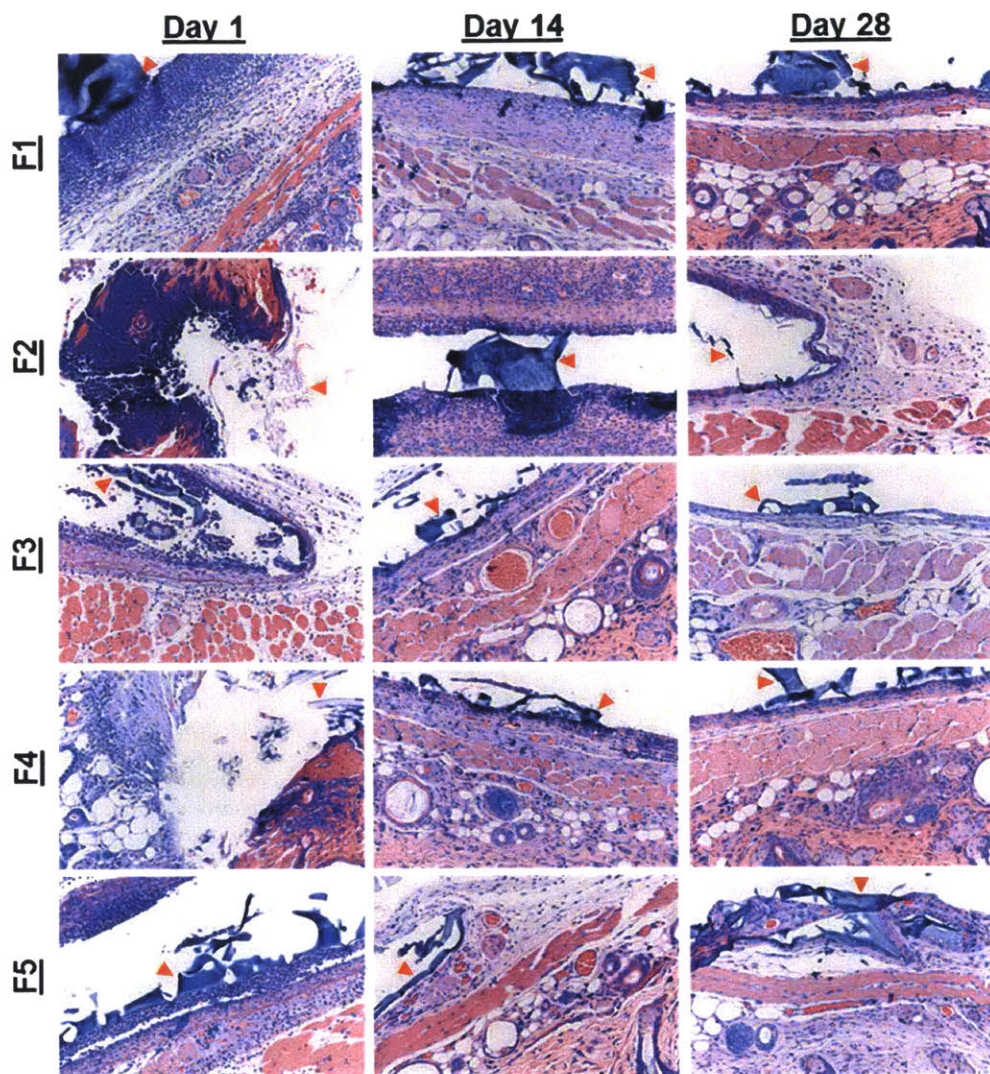


Figure 5-4: H&E stained tissue samples of SKH1-E taken from implant sites of hydrogels. Magnification is 20x.

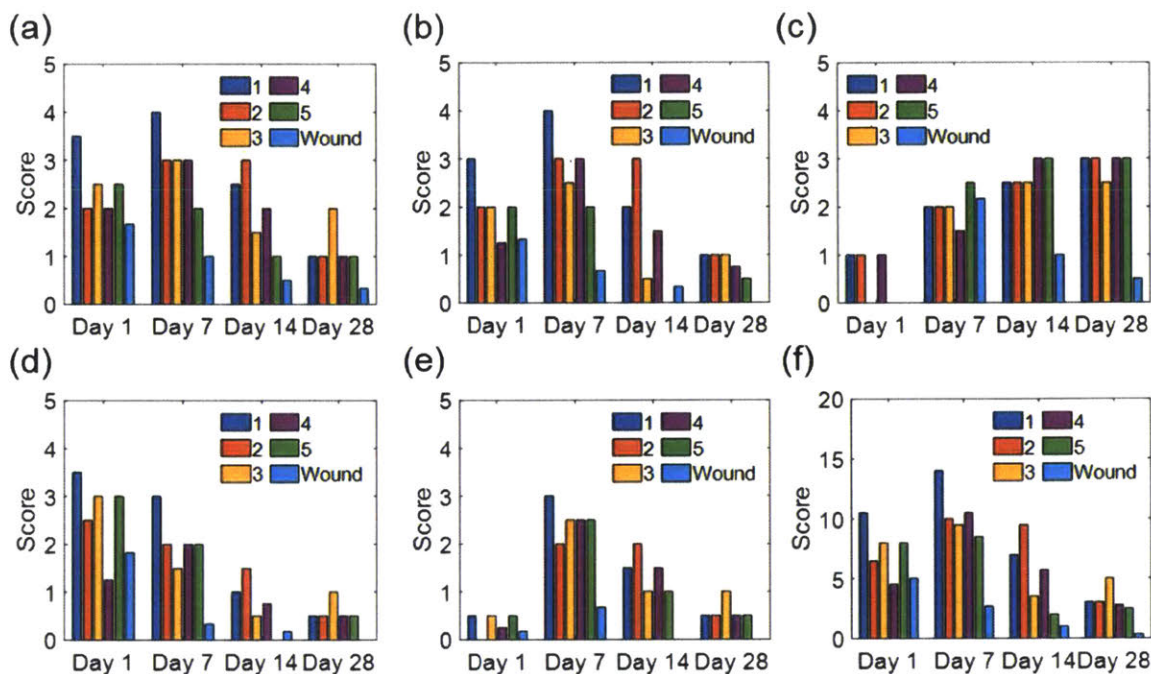


Figure 5-5: Tissue response scores for the (a) implant site, (b) tissue surrounding the implant, (c) fibrosis, (d) edema, (e) neovascularization, and (f) total adverse tissue reaction. The inflammation at and surrounding the implant site, edema, and neovascularization were rated on a scale of 0 to 4: 0 is absent, 1 is minimal, 2 is mild, 3 is moderate, and 4 is severe. Fibrosis was rated on a scale of 1 to 3, with 1 being only a mild fibrous encirclement, 2 being moderate or poorly organized fibrous encirclement, and 3 being a well-organized and epithelioid histiocytic cap. The total adverse tissue reaction was obtained by summing all the components except fibrosis. Fibrosis was omitted from the total because fibrosis limits the inflammatory response and promotes healing, thus being a positive outcome rather than adverse.

Masson's trichrome staining was performed to visualize the fibrous capsule formed around the implants (Figure 5-6 and Figure 5-7). We observed that at day 7, we see the beginning of fibrous capsular formation in the implant and surrounding the implant, with more organized fibrosis in formulations 3, 4, and 5. These indicate that healing is occurring more quickly in hydrogels without SWNT, as well in hydrogels with SWNT having smaller pore sizes. By day 28, we see that the fibrous capsule has fully encircled the implant in all formulations. These results are consistent with the H&E staining, which was expected given the role macrophages and fibroblasts play in capsule formation.

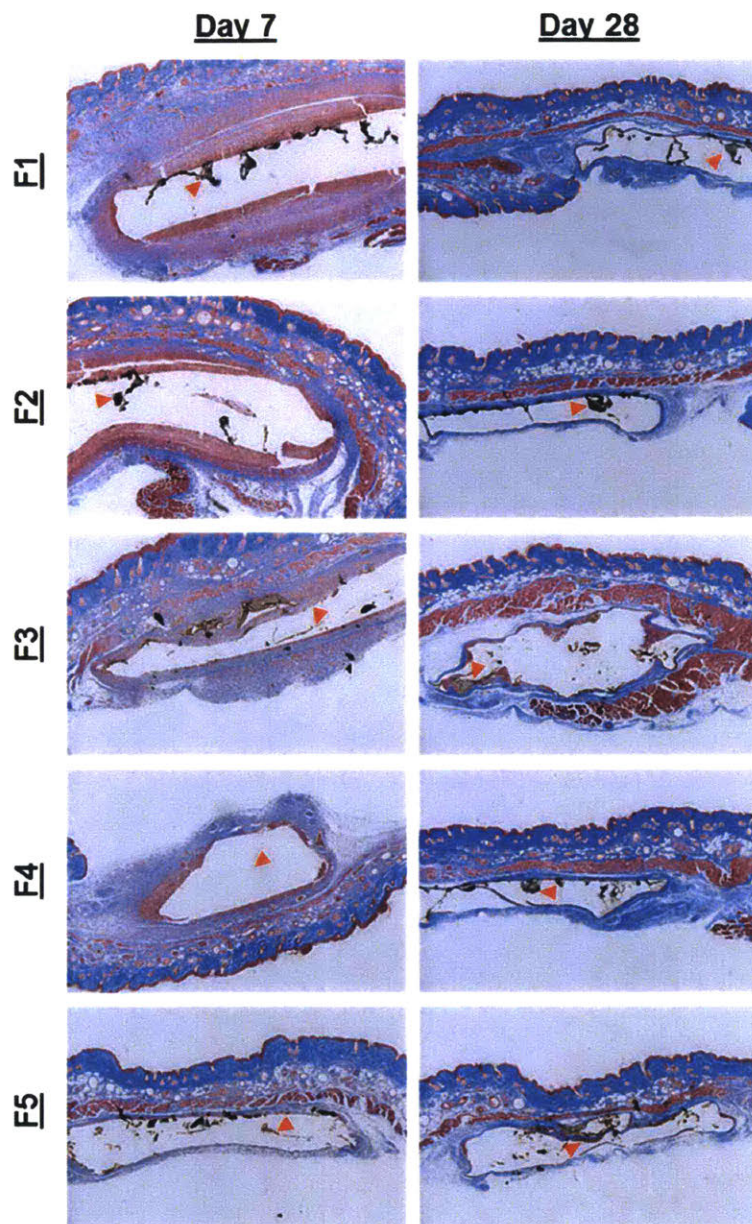


Figure 5-6: Masson's Trichrome stained tissue samples imaged at 4x magnification. The progression of healing can be seen by observing the regions of blue, representing fibrous tissue, increasing from day 7 to day 28. Formulations 3-5 appear to have slightly more organized fibrous regions at day 7 compared to formulations 1 and 2, indicating faster healing with smaller pore sizes, as well as lower SWNT concentrations.

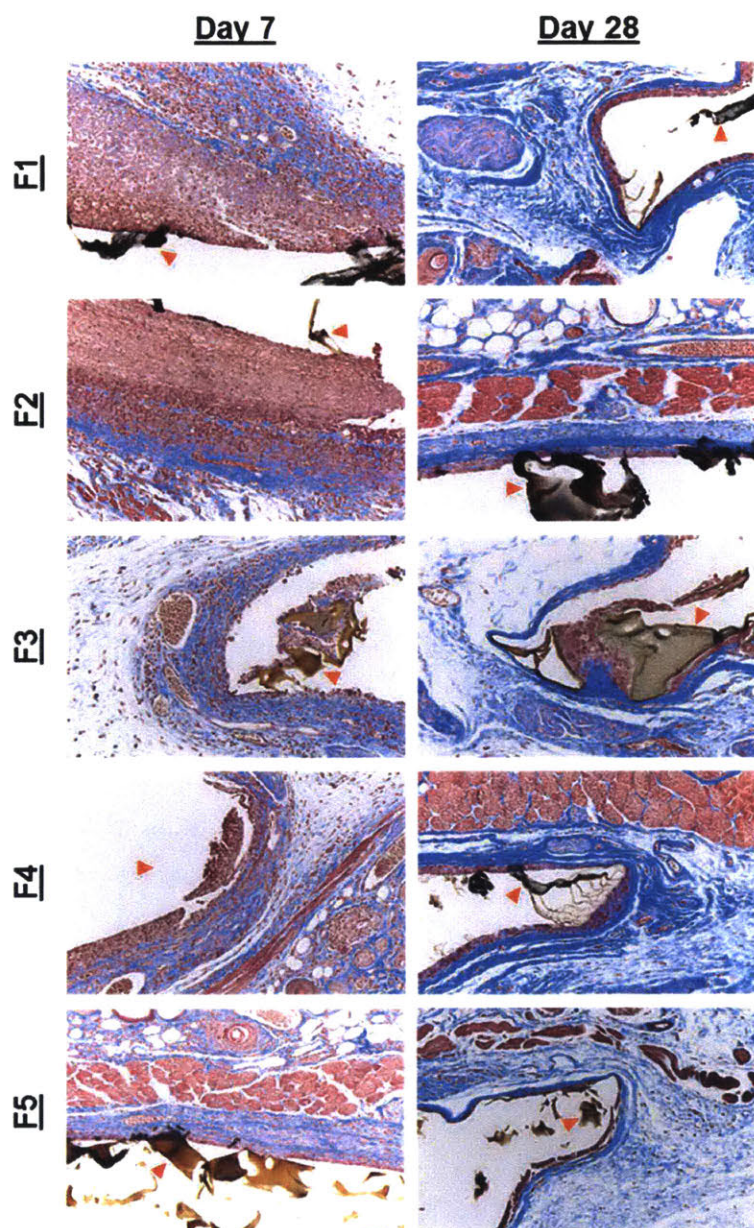


Figure 5-7: Masson's Trichrome stained tissue samples imaged at 20x magnification

The degradation products were monitored by taking aliquots of buffer in which hydrogels were incubated at 37°C. Possible products include individually wrapped SWNT, SWNT aggregates, free wrapping polymer, and degradation products of the hydrogel matrix and/or wrapping polymer. Aliquots were taken at 1, 7, and 12 days. GPC was used to detect any polymeric

degradation productions. Degradation products were not concentrated enough to be detected by GPC, even after concentration of the products with a lyophilization and reconstitution step. Furthermore, SWNT were also not detected in incubation buffer using Raman spectroscopy.

All together, these results suggest design considerations when formulating SWNT-encapsulated hydrogels. Cellular responses are highly dependent on SWNT wrappings, as was shown when comparing formulations 1 and 2. Furthermore, SWNT concentration is another important parameter, as shown when comparing formulations 1 and 2 to 4, as well as formulation 3 to 5. Nevertheless, comparisons between formulations 1 and 3 indicate that changing the physical parameters of the hydrogel such as cross-link density may reduce the overall release of degradation products, leading to a better-tolerated implant.

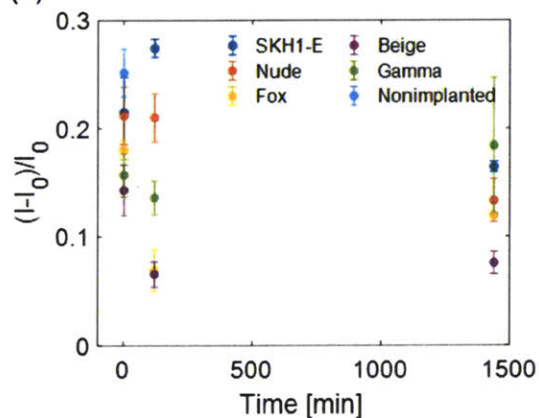
Inflammatory cells release reactive molecules that serve to deactivate pathogens and digest residual materials.³¹ To determine if this inflammatory response interferes with the function of a SWNT sensor implant irreversibly, formulation 1 hydrogels were implanted in five lines of mice with different populations of functional inflammatory cells (Figure 5-8a). The hydrogels were explanted at a given time between 0 and 24 hours, incubated in 1x PBS to remove any reversibly binding analytes, and challenged with 100 μ M progesterone. The responses were evaluated in terms of the maximum magnitude of sensor response and the time constant to reach 66% of the maximum response. The results for the mice are summarized in (Figure 5-8b-c). In general, the maximum sensitivity of the hydrogels to progesterone decreased upon and the kinetics of responsivity slowed with longer implantation times. Given the time scale of the implantation (~24 hours), acute inflammation would be the active tissue response because of the surgical procedure, even in the case of a completely inert implant. Though the mice lines had unique populations of functional immune cells, there was no clear trend in the extent to which the sensors were

deactivated or slowed. It is important to note, however, that they all had functional neutrophils and monocytes, which would be active at this time scale.³⁰ Neutrophils release degranulation molecules which has the potential to chemically alter the SWNT corona and thus the recognition capability of the nanoparticle.³¹ Furthermore, protein fragment adhesion occurs almost immediately upon implantation, which may clog the porous hydrogel, effectively increasing the time required for analyte diffusion into the hydrogel.²¹ This may have further consequences on the sensitivity as well, in that individual SWNT are entrapped at specific locations in the hydrogel, which may end up inaccessible to the analyte and effectively be trapped in an unresponsive state. All together, the time dependence of these data, despite working in serum and an incubation period in buffer to remove reversibly bound interfering molecules, suggest that the progression of inflammation may in fact disrupt sensor functionality.

(a)

	Gamma	Beige	Fox	Nude	SKH1-E
B Cells	-	-	-	+	+
T Cells	-	-	-	-	+
Dendritic Cells	-	+	+	+	+
Macrophages	-	+	+	+	+
Natural Killer Cells	-	-	+	+	+
Hemolytic Complement	-	+	+	+	+
Neutrophils	+	+	+	+	+
Monocytes	+	+	+	+	+

(b)



(c)

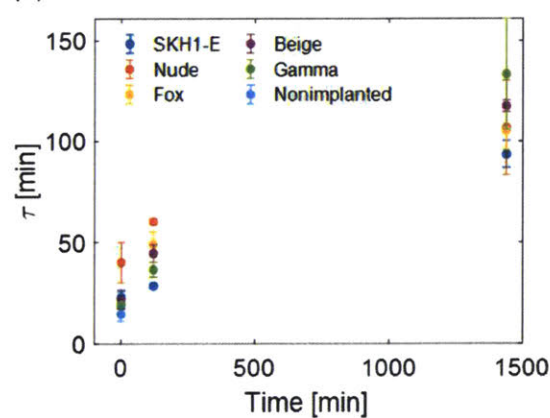


Figure 5-8: (a) Summary of the functional and dysfunctional inflammatory cells in five mice lines used in this study. Hydrogel sensors were implanted for a time period (1 min, 2 hours, 24 hours), explanted, and tested outside the mice against 100 μ M progesterone. (b) The maximum sensitivity decreased with increasing implantation time in general. (c) For all mice lines, the kinetics of response slowed with longer implantation time.

Conclusions and Future Work

In this work, tissue responses were tracked in response to hydrogel formulations, and the deactivation of SWNT sensor functionality during the acute inflammatory response was demonstrated. Future work will examine further hydrogel formulations beyond PEGDA hydrogels to observe the chemical dependence of the scaffolding material on the tissue response. With a

larger collection of hydrogel formulation data, an optimal hydrogel may be chosen that best extends the longevity of SWNT sensors *in vivo*.

References

- (1) Li, Z.; de Barros, A. L. B.; Soares, D. C. F.; Moss, S. N.; Alisaraie, L. Functionalized Single-Walled Carbon Nanotubes: Cellular Uptake, Biodistribution and Applications in Drug Delivery. *Int. J. Pharm.* **2017**, *524* (1), 41–54.
- (2) Galassi, T. V.; Jena, P. V.; Shah, J.; Ao, G.; Molitor, E.; Bram, Y.; Frankel, A.; Park, J.; Jessurun, J.; Ory, D. S.; et al. An Optical Nanoreporter of Endolysosomal Lipid Accumulation Reveals Enduring Effects of Diet on Hepatic Macrophages in Vivo. *Sci. Transl. Med.* **2018**, *10* (461), eaar2680.
- (3) Williams, R. M.; Lee, C.; Galassi, T. V.; Harvey, J. D.; Leicher, R.; Sirenko, M.; Dorso, M. A.; Shah, J.; Olvera, N.; Dao, F.; et al. Noninvasive Ovarian Cancer Biomarker Detection via an Optical Nanosensor Implant. *Sci. Adv.* **2018**, *4* (4), eaaq1090.
- (4) Iverson, N. M.; Barone, P. W.; Shandell, M.; Trudel, L. J.; Sen, S.; Sen, F.; Ivanov, V.; Atolia, E.; Farias, E.; McNicholas, T. P.; et al. In Vivo Biosensing via Tissue-Localizable near-Infrared-Fluorescent Single-Walled Carbon Nanotubes. *Nat. Nanotechnol.* **2013**, *8* (11), 873–880.
- (5) Lee, M. A.; Nguyen, F. T.; Scott, K.; Chan, N. Y. L.; Bakh, N. A.; Jones, K. K.; Pham, C.; Garcia-Salinas, P.; Garcia-Parraga, D.; Fahlman, A.; et al. Implanted Nanosensors in Marine Organisms for Physiological Biologging: Design, Feasibility, and Species Variability. *ACS Sensors* **2019**, *4* (1), 32–43.

- (6) Chowdhury, I.; Duch, M. C.; Gits, C. C.; Hersam, M. C.; Walker, S. L. Impact of Synthesis Methods on the Transport of Single Walled Carbon Nanotubes in the Aquatic Environment. *Environ. Sci. Technol.* **2012**, *46* (21), 11752–11760.
- (7) Heister, E.; Neves, V.; Lamprecht, C.; Silva, S. R. P.; Coley, H. M.; McFadden, J. Drug Loading, Dispersion Stability, and Therapeutic Efficacy in Targeted Drug Delivery with Carbon Nanotubes. *Carbon N. Y.* **2012**, *50* (2), 622–632.
- (8) Dong, L.; Joseph, K. L.; Witkowski, C. M.; Craig, M. M. Cytotoxicity of Single-Walled Carbon Nanotubes Suspended in Various Surfactants. *Nanotechnology* **2008**, *19* (25), 255702.
- (9) Jin, H.; Heller, D. A.; Strano, M. S. Single-Particle Tracking of Endocytosis and Exocytosis of Single-Walled Carbon Nanotubes in NIH-3T3 Cells. *Nano Lett.* **2008**, *8* (6), 1577–1585.
- (10) Kumar, V.; Sharma, N.; Maitra, S. S. In Vitro and in Vivo Toxicity Assessment of Nanoparticles. *Int. Nano Lett.* **2017**, *7* (4), 243–256.
- (11) Gao, Z.; Varela, J. A.; Groc, L.; Lounis, B.; Cognet, L. Toward the Suppression of Cellular Toxicity from Single-Walled Carbon Nanotubes. *Biomater. Sci.* **2016**, *4* (2), 230–244.
- (12) Chiang, I. W.; Brinson, B. E.; Huang, A. Y.; Willis, P. A.; Bronikowski, M. J.; Margrave, J. L.; Smalley, R. E.; Hauge, R. H. Purification and Characterization of Single-Wall Carbon Nanotubes (SWNTs) Obtained from the Gas-Phase Decomposition of CO (HiPco Process). *J. Phys. Chem. B* **2001**, *105* (35), 8297–8301.
- (13) Monzon, A.; Lolli, G.; Cosma, S.; Mohamed, S. B.; Resasco, D. E. Kinetic Modeling of the SWNT Growth by CO Disproportionation on CoMo Catalysts. *Journal of Nanoscience and Nanotechnology*. 2008, pp 6141–6152.
- (14) Kolosnjaj-Tabi, J.; Hartman, K. B.; Boudjemaa, S.; Ananta, J. S.; Morgant, G.; Szwarc, H.;

- Wilson, L. J.; Moussa, F. In Vivo Behavior of Large Doses of Ultrashort and Full-Length Single-Walled Carbon Nanotubes after Oral and Intraperitoneal Administration to Swiss Mice. *ACS Nano* **2010**, *4* (3), 1481–1492.
- (15) Shrivastava, R.; Delomenie, C.; Chevalier, A.; John, G.; Ekwall, B.; Walum, E.; Massingham, R. Comparison of in Vivo Acute Lethal Potency and in Vitro Cytotoxicity of 48 Chemicals. *Cell Biol. Toxicol.* **1992**, *8* (2), 157–170.
- (16) Almeida, J. P. M.; Chen, A. L.; Foster, A.; Drezek, R. In Vivo Biodistribution of Nanoparticles. *Nanomedicine* **2011**, *6* (5), 815–835.
- (17) Ravindran, S.; Suthar, J. K.; Rokade, R.; Deshpande, P.; Singh, P.; Pratinidhi, A.; Utekar, R. K. and S. Pharmacokinetics, Metabolism, Distribution and Permeability of Nanomedicine. *Current Drug Metabolism*. 2018, pp 327–334.
- (18) Harvey, J. D.; Jena, P. V.; Baker, H. A.; Zerze, G. H.; Williams, R. M.; Galassi, T. V.; Roxbury, D.; Mittal, J.; Heller, D. A. A Carbon Nanotube Reporter of MicroRNA Hybridization Events in Vivo. *Nat. Biomed. Eng.* **2017**, *1* (4).
- (19) Williams, R. M.; Lee, C.; Galassi, T. V; Harvey, J. D.; Leicher, R.; Sirenko, M.; Dorso, M. A.; Shah, J.; Olvera, N.; Dao, F.; et al. Noninvasive Ovarian Cancer Biomarker Detection via an Optical Nanosensor Implant. *Sci. Adv.* **2018**, *4* (4), eaaq1090.
- (20) Jena, P. V; Roxbury, D.; Galassi, T. V; Akkari, L.; Horoszkó, C. P.; Iaea, D. B.; Budhathoki-Uprety, J.; Pipalia, N.; Haka, A. S.; Harvey, J. D.; et al. A Carbon Nanotube Optical Reporter Maps Endolysosomal Lipid Flux. *ACS Nano* **2017**, *11* (11), 10689–10703.
- (21) Swartzlander, M. D.; Barnes, C. A.; Blakney, A. K.; Kaar, J. L.; Kyriakides, T. R.; Bryant, S. J. Linking the Foreign Body Response and Protein Adsorption to PEG-Based Hydrogels Using Proteomics. *Biomaterials* **2015**, *41*, 26–36.

- (22) Iverson, N. M.; Bisker, G.; Farias, E.; Ivanov, V.; Ahn, J.; Wogan, G. N.; Strano, M. S. Quantitative Tissue Spectroscopy of near Infrared Fluorescent Nanosensor Implants. *J. Biomed. Nanotechnol.* **2016**, *12* (5), 1035–1047.
- (23) Peppas, N. A.; Hilt, J. Z.; Khademhosseini, A.; Langer, R. Hydrogels in Biology and Medicine: From Molecular Principles to Bionanotechnology. *Adv. Mater.* **2006**, *18* (11), 1345–1360.
- (24) Pedersen, J. S.; Sommer, C. Temperature Dependence of the Virial Coefficients and the Chi Parameter in Semi-Dilute Solutions of PEG. *Prog. Colloid Polym. Sci.* **2005**, *130*, 70–78.
- (25) Herzog, E.; Byrne, H. J.; Casey, A.; Davoren, M.; Lenz, A.-G.; Maier, K. L.; Duschl, A.; Oostingh, G. J. SWCNT Suppress Inflammatory Mediator Responses in Human Lung Epithelium in Vitro. *Toxicol. Appl. Pharmacol.* **2009**, *234* (3), 378–390.
- (26) Caló, E.; Khutoryanskiy, V. V. Biomedical Applications of Hydrogels: A Review of Patents and Commercial Products. *Eur. Polym. J.* **2015**, *65*, 252–267.
- (27) Saboktakin, M. reza; Tabatabaei, R. M. Supramolecular Hydrogels as Drug Delivery Systems. *Int. J. Biol. Macromol.* **2015**, *75*, 426–436.
- (28) Dimatteo, R.; Darling, N. J.; Segura, T. In Situ Forming Injectable Hydrogels for Drug Delivery and Wound Repair. *Adv. Drug Deliv. Rev.* **2018**, *127*, 167–184.
- (29) Blakney, A. K.; Swartzlander, M. D.; Bryant, S. J. The Effects of Substrate Stiffness on the in Vitro Activation of Macrophages and in Vivo Host Response to Poly(Ethylene Glycol) based Hydrogels. *J. Biomed. Mater. Res. Part A* **2012**, *100A* (6), 1375–1386.
- (30) Klopfleisch, R.; Jung, F. The Pathology of the Foreign Body Reaction against Biomaterials. *J. Biomed. Mater. Res. Part A* **2017**, *105* (3), 927–940.
- (31) Selders, G. S.; Fetz, A. E.; Radic, M. Z.; Bowlin, G. L. An Overview of the Role of

Neutrophils in Innate Immunity, Inflammation and Host-Biomaterial Integration. *Regen. Biomater.* 2017, 4 (1), 55–68.

Chapter 6 : Conclusions and Future Work

This thesis explored the design, synthesis, and application space of Corona Phase Molecular Recognition sensors (CoPhMoRe) for *in vivo* steroid monitoring for various applications, including human health monitoring and aquatic organism biologging. This thesis represents a significant expansion of the CoPhMoRe technique to different classes of analytes, the steroids, and to different environments, including aquatic organisms and rodents. In particular, this thesis is significant in the use of custom-synthesized polymers as SWNT wrappings, as opposed to more commonly and commercially available wrappings, such as DNA, RNA, and phospholipid-PEGs. Through the exploration of the relationship between wrapping structure and sensor functionality, some rational corona phase design rules have been elucidating to streamline later sensing efforts. Furthermore, the thesis has laid out a theoretical framework for sensor fabrication, involving the formulation of a mathematical model, followed by an iterative process of synthesizing and testing sensors.

In Chapter 2, we formulated a mathematical model describing compartmental concentrations of cortisol in the human body. The modeled compartments included the adrenal gland, blood, adipose, muscle, and brain. The peak values of cortisol predicted by the model were verified by comparison to reported values in the medical literature. Other features were also verified, including the relative proportions of free vs. protein-bound cortisol and the diurnal pattern. The model was used to predict values in both healthy patients and Cushing's disease patients. Furthermore, a theoretical sensor placed in the adipose interstitial space was tuned against the mathematical model, and a working parameter set describing sensor geometry, binding site concentration, binding equilibrium, and kinetics were obtained. The same sensor was found to operate well in both the healthy and the Cushing's disease patients.

Future work may add several layers of sophistication to the model. Additional compartments may be added, including the liver, stomach, pancreas, etc. where cortisol may act to mobilize macromolecules for metabolism. Furthermore, the model may serve as a basis of other steroid hormone pharmacokinetic models, such as progesterone, testosterone, and others. In the case of new steroids, specific compartments would have to be added depending on the relevant biochemistry of the steroid (e.g. the testicles for testosterone and the ovaries for progesterone).

In Chapter 3, we explored the feasibility of applying CoPhMoRe sensors to the field of aquatic organism biologging using seven species of aquatic organisms, including teleost fish, catsharks, sharks, and turtles at Oceanografic in Valencia, Spain. A portable and inexpensive Raspberry Pi-based imaging system was fabricated for this study, to enable fluorescence images to be obtained outside of a spectroscopy laboratory. We developed basic protocols for SWNT-hydrogel intramuscular implantation into these animals, and explored the relationship between fluorescence signal extraction and sensor implantation depth. We also explored the effect of tissue pigmentation on the ability to extract signal. Furthermore, we utilized a living eel, turtle, and catshark for biocompatibility studies and observed minimal changes in tissue architecture in the eel and catshark via high resolution ultrasound. Conversely, the eel's wound did not fully heal, and histological analysis indicated a foreign body reaction. Nevertheless, those animals, as well as goldfish at MIT, showed no quantifiable differences in movement or behavior with and without the implant.

The positive results of the study warrant future exploration. To meet the demands of biologging, a wearable or implantable fluorescence device coupled directly to the hydrogels should be fabricated. Intensity-based sensing, as is often performed with CoPhMoRe sensors, is subject to a number of artefacts when taken outside the laboratory environment. In addition to the chemical

changes of interest, fluorescence intensity is often modulated in response to excitation incident power, movement, and background brightness. To minimize the effects of these external factors, direct mounting of the hydrogel onto the excitation/photodetector platform would be ideal. Furthermore, miniaturization into a wearable or implantable form factor provides a scalable option that would allow animals to roam freely in their environments without the need to confine their movements.

In Chapter 4, we described a novel CoPhMoRe sensor for steroids based on a templated steroid approach. Copolymers of styrene, acrylic acid, and acrylated cortisol were synthesized, pinned onto SWNT, and screened against a panel of steroids chosen for their physiological and therapeutic significance. Tuning of polymer composition elucidated design rules that facilitated targeting of different steroids. Two constructs selective for cortisol and progesterone were synthesized, and the progesterone sensor was successfully translated into an implantable hydrogel form factor. After further encapsulation of the hydrogel into a membrane, the sensor was shown to be functional within an SKH1-E mouse in the first day.

In Chapter 5, tissue responses to the progesterone sensor were explored as a function of formulation of the hydrogel scaffold. Five species of mice immunocompromised to varying degrees were utilized to determine which cell populations may be contributing to sensor deactivation. All hydrogels in all mice were found to decrease in sensitivity and increase in response time with longer implantation times, indicating that the neutrophils involved in the acute inflammatory response may contribute to sensor deactivation. Furthermore, through histological analysis of cellular morphologies at various time points after hydrogel implantation, it was discovered that hydrogels with smaller pore sizes led to faster healing. Together, these data

indicate that hydrogel formulation may be a viable way of utilizing a sensor *in vivo* that may otherwise have been poorly tolerated by the tissue.

This thesis has laid a foundation for steroid hormone sensing *in vivo*. In future work, the sensitivity range of the cortisol and progesterone sensors has to be decreased in order to reach physiological concentrations. In their current form, they can capture only the high end of the physiological range. A new sensor discovery process may not be necessary, as increased detection limits may be accomplished using single-molecule fluorescence spectroscopy. The templating strategy outlined in Chapter 4 may be a viable strategy for the fabrication of sensors for new analytes. For example, other steroids may be targeted by changing the template steroid molecule from a cortisol to some other steroid molecule. Furthermore, the lifetime of the sensor may be extended by employing the formulation strategies discovered in Chapter 5. If the sensor lifetime is extended beyond the 1 hour demonstrated in Chapter 5, other experiments can be conducted to test the sensor in novel ways, including sensor response to exogenous administration of and endogenous production of progesterone.